**UNIVERSITY OF VERONA**

DEPARTMENT OF NEUROLOGICAL, NEUROPSYCHOLOGICAL, MORPHOLOGICAL AND MOVEMENT SCIENCES

DOCTORAL SCHOOL OF SCIENCE ENGINEERING AND MEDICINE

DOCTORAL PROGRAM IN NEUROSCIENCE

XXIV CYCLE

# A MULTIMODAL IMAGING APPROACH FOR QUANTITATIVE ASSESSMENT OF EPILEPSY

S.S.D. MED/26

Coordinator: Prof. Michele Tinazzi

Supervisor: Prof. Paolo Manganotti

PhD Candidate: Silvia Francesca Storti

# Contents

# Abbreviations

| | |
|---|---|
| **AAS** | averaged artifact subtraction |
| **AIC** | Akaike information criterion |
| **APB** | abductor pollicis brevis |
| **AR** | autoregressive model |
| **BCG** | ballistocardiogram |
| **BEM** | boundary element method |
| **BET** | brain extraction tool |
| **BOLD** | blood oxygenation level dependent |
| **CBF** | cerebral blood flow |
| **CMT** | continuous Morlet wavelet transformation |
| **DMN** | default mode network |
| **ECD** | equivalent current dipole |
| **ECG** | electrocardiogram |
| **EEG** | electroencephalography |
| **eLORETA** | exact LORETA |
| **EMF** | electromotive force |

| | |
|---|---|
| **EMG** | electromyogram |
| **EPI** | echo planar imaging |
| **ERD** | event related desynchronization |
| **ERS** | event related synchronization |
| **ESI** | electrical source imaging |
| **FDM** | finite difference method |
| **FDR** | false discovery rate |
| **FENICA** | algorithm fully exploratory network ICA |
| **FFT** | fast Fourier transform |
| **FIR** | finite impulse response |
| **fMRI** | functional magnetic resonance imaging |
| **FN** | false negative |
| **FOV** | field of view |
| **FP** | false positive |
| **FSL** | FMRIB software library |
| **FWE** | family wise error |
| **FWHM** | full width at half maximum |
| **GF** | "canonical" model |
| **GFT** | "canonical" model plus its temporal partial derivative |
| **GFTD** | "canonical" model plus its temporal and dispersion derivatives |
| **GLM** | general linear model |
| **GSW** | generalized spike and wave |
| **hdEEG** | high density electroencephalography |

| | |
|---|---|
| **HRF** | hemodynamic response function |
| **ibHRF** | individual-based hemodynamic response function |
| **IC** | independent component |
| **ICA** | independent component analysis |
| **IED** | interictal epileptiform discharges |
| **LCMV** | linear constrained minimum variance |
| **LD** | linear distributed approaches |
| **LORETA** | low-resolution electromagnetic tomography algorithm |
| **MEG** | magnetoencephalography |
| **MELODIC** | multivariate exploratory linear decomposition into independent components |
| **MNI** | Montreal Neurological Institute |
| **MNLS** | minimum norm least square |
| **MRI** | magnetic resonance imaging |
| **MUSIC** | multiple signal classification |
| **nAIC** | the lowest mean-Akaike value for the active pixels |
| **PCA** | principal component analysis |
| **PET** | positron-emission tomography |
| **PICA** | probabilistic independent component analysis |
| **PST** | peristimulus time |
| **RSN** | resting state network |
| **SD** | standard deviation |
| **sLORETA** | standardized LORETA |
| **SM1** | sensory motor area |

| | |
|---|---|
| **SMA** | supplementary motor area |
| **SMAC** | spherical head model with anatomical constraint |
| **SNR** | signal to noise ratio |
| **SOHIA** | selection of optimal HRF and image analysis |
| **SPM** | statistical parametric mapping |
| **TBI** | traumatic brain injury |
| **TDSep** | temporal decorrelation source separation |
| **TE** | echo time |
| **TH** | threshold value |
| **TLE** | temporal lobe epilepsy |
| **TN** | true negative |
| **TP** | true positive |
| **TR** | repetition time |
| **WMN** | weighted minimum-norm least squares |
| **WRSS** | weighted residual sum of squares |

# Sommario

Le tecniche di coregistrazione elettroencefalogramma-risonanza magnetica funzionale (EEG-fMRI) ed EEG ad alta densità (hdEEG) consentono di mappare attivazioni cerebrali anomale evocate da processi epilettici. L'EEG-fMRI è una tecnica di imaging non invasivo che permette la localizzazione delle variazioni del livello di ossigenazione nel sangue presente nelle regioni irritative (segnale BOLD). Diversamente, l'analisi di sorgente stima, a partire da un potenziale elettrico misurato sullo scalpo (EEG), la densità di corrente della sorgente elettrica a livello corticale producendo una plausibile localizzazione del dipolo nelle regioni irritative. Lo scopo di questa tesi è quello di sviluppare un approccio multimodale attraverso l'uso di dati di coregistrazione EEG-fMRI e hdEEG al fine di localizzare l'attività epilettica e verificare l'affidabilità sia dell'attivazione BOLD che della localizzazione della sorgente.

Nel ***Capitolo I*** si introduce il concetto di approccio multimodale. Il capitolo è suddiviso principalmente in due parti: la prima descrive la tecnica di coregistrazione EEG-fMRI e la seconda la tecnica di localizzazione della sorgente in epilessia. La prima parte consiste in una breve analisi delle basi fisiologiche del dato di coregistrazione EEG-fMRI, nella descrizione di tecniche di registrazione simultanea e nell'introduzione del metodo convenzionale di analisi dei dati. Sono inoltre descritti problemi tecnici, problemi di sicurezza, modalità di scansione e strategie di rimozione degli artefatti EEG. È quindi presentata una panoramica sullo stato dell'arte delle coregistrazioni EEG-fMRI con discussione dei problemi aperti riguardanti l'analisi convenzionale. La seconda parte introduce i principi di base della stima delle sorgenti da dati hdEEG ed i loro limiti.

Il primo capitolo fornisce un quadro generale, mentre i due capitoli suc-

cessivi sono dedicati ad introdurre approcci di tipo diverso. Nell'analisi convenzionale di dati EEG-fMRI, l'apparizione di eventi interictali (IED) guida l'analisi dei dati fMRI. Il neurologo identifica gli intervalli degli eventi IED, che sono rappresentati da un'onda quadra, e successivamente questo protocollo viene convoluto con una risposta emodinamica (HRF) canonica per la costruzione di un modello o *regressore* da impiegare nell'analisi con modelli lineari generalizzati (GLM). I problemi principali dell'analisi convenzionale consistono nel fatto che essa non è automatica, ossia soffre di soggettività nella classificazione degli IED, e che, se la scelta dell'HRF non è ottimale, l'attivazione può essere sovra o sotto stimata. Il nuovo metodo proposto integra nell'analisi GLM convenzionale due nuove funzioni: il regressore basato sul segnale EEG (***Capitolo II***), e l'individuazione di una risposta emodinamica individual-based (ibHRF) (***Capitolo III***).

Nel ***Capitolo IV*** le prestazioni del nuovo metodo per l'analisi di dati EEG-fMRI sono validate su dati in silico. A questo scopo sono stati creati dati fMRI simulati per testare la scelta dell'HRF ottima tra cinque modelli: quattro standard ed un modello HRF individual-based. Le prestazioni del metodo sono state valutate utilizzando come selezione il criterio di Akaike. Le simulazioni dimostrano la superiorità del nuovo metodo rispetto a quelli convenzionali e mostrano come la variazione del modello HRF influisce sui risultati dell'analisi statistica.

Il ***Capitolo V*** introduce un criterio automatico volto a separare le componenti del segnale fMRI relative a network interni dal rumore. Dopo il processo di decomposizione probabilistico delle componenti indipendenti (PICA), si seleziona il numero ottimale di componenti applicando un nuovo algoritmo che tiene conto, per ciascuna componente, dei valori medi delle mappe spaziali di attivazione seguito da passaggi di clustering, segmentazione ed analisi spettrale. Confrontando i risultati dell'identificazione visiva dei network neuronali con i risultati di quella automatica, l'algoritmo mostra elevata accuratezza e precisione. In questo modo, il metodo di selezione automatica permette di separare ed individuare i network in stato di riposo, riducendo la soggettività nella valutazione delle componenti indipendenti.

Nel ***Capitolo VI*** sono descritti il design sperimentale e l'analisi dei dati reali. Il capitolo illustra i risultati di dodici pazienti epilettici, concentrandosi sull'attività BOLD, sulla localizzazione della sorgente e sulla concordanza con il quadro clinico del paziente. Lo scopo è quello di applicare un approccio multimodale che combini tecniche non invasive di acquisizione ed

analisi. Sequenze di EEG standard e fMRI sono acquisite nel corso della stessa sessione di scansione. L'analisi dei dati EEG-fMRI è eseguita utilizzando l'approccio GLM tradizionale, il nuovo approccio e l'analisi PICA. La sorgente dell'attività epilettica è stimata a partire da tracciati EEG a 256-canali. L'attivazione BOLD è confrontata con la ricostruzione della sorgente EEG. Questi risultati sono infine confrontati con l'attività epilettica definita da EEG standard ed esiti clinici.

La combinazione di tecniche multimodali ed i loro rispettivi metodi di analisi sono strumenti utili per creare un workup prechirurgico completo dell'epilessia, fornendo diversi metodi di localizzazione dello stesso focolaio epilettico. L'approccio non invasivo di integrazione multimodale di dati EEG-fMRI e hdEEG sembra essere uno strumento molto promettente per lo studio delle scariche epilettiche.

# Summary

Electroencephalography-functional magnetic resonance imaging (EEG-fMRI) coregistration and high density EEG (hdEEG) can be combined to noninvasively map abnormal brain activation elicited by epileptic processes. EEG-fMRI can provide information on the pathophysiological processes underlying interictal activity, since the hemodynamic changes are a consequence of the abnormal neural activity generating interictal epileptiform discharges (IEDs). The source analysis estimates the current density of the source that generates a measured electric potential and it yields a plausible dipole localization of irritative regions. The aim of this thesis is to develop a multimodal approach with hdEEG and EEG-fMRI coregistration in order to localize the epileptic activity and to verify the reliability of source localization and BOLD activation.

In ***Chapter I*** the multimodal approach is introduced. The chapter is divided in two main parts: the first is based on EEG-fMRI coregistration and the second on the source localization in epilepsy. The first part consists of a brief review of the physiologic basis of EEG and fMRI and the technical basics of simultaneous recording, examining the conventional method for EEG-fMRI data. Technical challenges, safety issues, scanning modalities and EEG artifact removal strategies are also described. An overview of the state of EEG-fMRI is presented and the open problems of conventional analysis are discussed. The second part introduces the basic principles of the source estimation from EEG data in epilepsy and their limitations.

The first chapter provides a general framework. The next two are devoted to introduce different approaches. Conventional analysis of EEG-fMRI data relies on spike-timing of epileptic activity: the neurologist identifies the intervals of the IEDs events, as represented by a square wave; this protocol is then

convolved with a canonical hemodynamic response function (HRF) to construct a model for the general linear model (GLM) analysis. There are limitations to the technique, however. The conventional analysis is not automatic, suffers of subjectivity in IEDs classification, and using a suboptimal HRF to model the BOLD response the activation map may result over or under estimated. The novel method purposed integrates in the conventional GLM two new features: the regressor based on the EEG signal (***Chapter II***) and the individual-based hemodynamic response function (ibHRF) (***Chapter III***).

In ***Chapter IV*** the performance of the novel method of EEG-fMRI data was tested on in silico data. Simulated fMRI datasets were created and used for the choice of the optimal HRF among five models: four standard and an individual-based HRF models. The performance of the method was evaluated using the Akaike information criterion as selection. Simulations would demonstrate the superiority of the novel method compared with the conventional ones and assess how the variations in HRF model affect the results of the statistical analysis.

***Chapter V*** introduces an automatic criterion aiming to separate in fMRI data the signal related to an internal network from the noise. After the decomposition process (probabilistic independent component analysis [PICA]), the optimal number of components was selected by applying a novel algorithm which takes into account, for each component, the mean values of the spatial activation maps followed by clustering, segmentation and spectral analysis steps. Comparing visual and automatic identification of the neuronal networks, the algorithm demonstrated high accuracy and precision. Thus, the automatic selection method allows to separate and detect the resting state networks reducing the subjectivity of the independent component assessment.

In ***Chapter VI*** experimental design and analysis on real data are described. The chapter focuses on BOLD activity, source localization and agreement with the clinical history of twelve epileptic patients. The scope is to apply a multimodal approach combining noninvasive techniques of acquisition and analysis. Standard EEG and fMRI data were acquired during a single scanning session. The analysis of EEG-fMRI data was performed by using both the conventional GLM, the new GLM and the PICA. Source localization of IEDs was performed using 256-channels hdEEG. BOLD localizations were then compared to the EEG source reconstruction and to the expected epileptic activity defined by standard EEG and clinical outcome.

The combination of multimodal techniques and their respectively methods of analysis are useful tools in the presurgical workup of epilepsy providing different methods of localization of the same epileptic foci. Furthermore, the combined use of EEG-fMRI and hdEEG offers a new and more complete approach to the study of epilepsy and may play an increasingly important role in the evaluation of patients with refractory focal epilepsy.

# Introduction

Epilepsy is a disorder of cerebral function, and it can or not have a discernible brain structural correlate. The feature of partial seizures is the presence of abnormal electrical activity that originates from the epileptic foci, i.e. a small cluster of neurons with increased excitability. Unfortunately, this localization is difficult because the rapid spread of its activity can be far from the lesion. Although structural brain imaging has added much to their evaluation, functional localization remains essential.

Functional magnetic resonance imaging (fMRI), positron emission tomography (PET) and magnetoencephalography (MEG) alone have not sufficient temporal resolution to distinguish the origin of a spike or seizure. Differently, the electroencephalography (EEG) as brain functional measure remains the most important and most commonly applied diagnostic tool. The recent combination of the neurophysiological and imaging technique, such as EEG-fMRI coregistration and high density EEG (hdEEG) improves the process of presurgical evaluation of epileptic patients mapping their abnormal brain activations.

Combined recordings as in EEG-fMRI have the dual advantage offered by the high temporal resolution of EEG and the spatial resolution obtained with neuroradiological exams. By using the EEG signal as a reference for fMRI maps, this technique opens a new avenue for investigating the brain activity. The BOLD activations cased by interictal spikes represent the irritative zone which is spatially related to the ictal zone. The limitation of the EEG-fMRI is that it provides an indirect BOLD measures of the brain electrical activity. In some cases the localization of the irritative zone is difficult because of multiple active areas; in other cases it is not possible to detect BOLD activations related to interictal epileptiform discharge (IED) activity, at least

using conventional analysis. Nonetheless, these limitations can be exceeded by the application of multimodal and comparative analysis approaches.

The advent of hdEEG acquisition systems with more than 64 channels can overcome the low spatial resolution of conventional 16-32 channel-EEG systems improving the estimation of the electric sources from scalp recording (electrical source imaging [ESI]). ESI can directly measure neuronal activity solving the EEG inverse problem via different strategies, e.g. dipole localization or distributed source imaging. Furthermore, combination of hdEEG and MRI data can also improve the localization of brain structure responsible for epileptic activity.

ESI and simultaneous EEG-fMRI are complementary methods for exploring epileptic activity. fMRI shows a complex network of focal hemodynamic changes related to interictal activity with high spatial resolution, whereas ESI temporally identifies the regions involved during the spike event. An area where EEG and fMRI integration and ESI have considerable clinical relevance is in the presurgical evaluation of epileptic patients: in many patients with drug-resistant focal seizures undergoing epilepsy surgery, standard magnetic resonance imaging scans fail to visualize a clear epileptic source, making preliminary invasive stereo EEG analysis necessary. Simultaneous EEG and fMRI recording and hdEEG offer a less invasive alternative, since they provide valuable information to localize the brain regions generating interictal epileptiform activity. In patients, who are not candidates for any surgical treatment, a multimodal approach allows a better investigation of the complex physiopathological mechanisms of that epilepsy.

The aims of the thesis are two. First, to identify the localization of the epileptic foci using combined functional and electrophysiological modalities of registration. Specifically, to evaluate the integrative use of hdEEG and EEG-fMRI techniques in order to reduce the invasive examinations. Second, to quantify performance of new multimodal approaches of analysis compared with the conventional ones in order to improve the identification of activated area. The specific methodological purposes aim to solve the main limitations of the conventional general linear model (GLM) analysis on EEG-fMRI data and to solve the problem of component selection in the independent component analysis (ICA) on fMRI data. To this purpose an automatic approach was introduced to integrate the EEG and the fMRI analysis and improve IEDs identification and a method was developed to select a number of ICA components that corresponds with the effective number of resting state net-

works (RSNs).

A noninvasive approach with multimodal integration of EEG-fMRI and hdEEG that combines two different methods to localize the same epileptic foci appears to be a very promising tool in the study of epileptic discharges.

Chapter 1

# EEG-fMRI Analysis and ESI in Epilepsy

In drug-resistant epilepsy, i.e. when the pharmacological therapy fails to control sufficiently the seizures, and focal epilepsy, i.e. when the seizure comes from a single area of the brain, the patient is a potential candidate for epilepsy surgery, which beneficial effects are related to the localization of the epileptic foci. Noninvasive imaging such as electroencephalography-functional magnetic resonance imaging (EEG-fMRI) or high density EEG (hdEEG), separately considered, are widely used to investigate abnormal neural activity in relation to blood oxygenation level dependent (BOLD) activity and electrical activity, respectively.

EEG-fMRI recording offers advantages in terms of temporal and spatial resolution of brain activity. It can provide information on the pathophysiological processes underlying interictal activity, since the hemodynamic changes are a consequence of the abnormal neural activity generating interictal epileptiform discharges (IEDs).

Differently from standard EEG, hdEEG is a recording method that relies on numerous electrodes to increase spatial sampling. Also, hdEEG can be combined with realistic head models and used in source analysis to determine the generators of IED.

To date, few researchers have been able to demonstrate a correspondence between the EEG-fMRI signal and the electrical sources [Vulliemoz et al., 2009, 2010b, Siniatchkin et al., 2010], given that the generators of the EEG and the BOLD signals do not always completely overlap. A recent review

of the combined use of EEG-fMRI coregistration and EEG source analysis for event localization in epilepsy reported promising perspectives for these strategies [Vulliemoz et al., 2010a].

When these techniques can not accurately localize deeper brain activity, the neurosurgeon uses an invasive technique: the intracerebral EEG (stereo EEG). Stereo EEG acquires intracranial data using multilead depth electrodes. It localizes the origin of the ictal discharges and captures the role of the surrounding regions in order to avoid postoperative permanent neurological deficit. In literature there are some examples of good spatial concordance between BOLD changes and intraoperative recording of the epileptiform foci [Benar et al., 2002, Salek-Haddadi et al., 2003], between EEG source localization and surgical outcome [Brodbeck et al., 2011] or EEG source localization, EEG-fMRI and stereo EEG [Benar et al., 2006].

## 1.1 Correlation between BOLD and neural activity

In the 1990s, a rapid development of non invasive structural and functional brain imaging methods has occurred. The fMRI, in particular, introduced the hemodynamic aspect in response to an electrical event. In detail, the fMRI measures the hemodynamic response induced by the neural activity and permits to display the active brain regions associated to a process. fMRI does not directly measure neural activity but the changes in oxygenation and blood flow. The advantages of fMRI include high spatial resolution (order of mm) and whole brain coverage. Moreover, fMRI combined with standard neurophysiological stimulation techniques can provide important clinical insights on epileptic patients.

Conversely, EEG measures with high temporal resolution (order of ms) the scalp neural activity generated by brain current sources which produce a current dipole moment in each tissue volume [Niedermeyer and Lopes da Silva, 2004]. When activated neurons generate time-varying electrical currents (transmenbrane currents). There are two types of neuronal activation: first, the fast depolarization of neuronal membranes that creates the action potential and, second, the slower changes in membrane potential due to synaptic activation (excitatory or inhibitory) and mediated by the neurotransmitter systems. The neurons that mainly contribute to the EEG are

the pyramidal neurons of the cortex with dendrites oriented towards to the cortical surface. When activated, these neurons are akin to "current dipoles", which activity can be measured by electrodes on the scalp surface [Lopes da Silva, 2002, Lopes da Silva and van Rotterdam, 2005]. In particular, the cortex modulated by gyri and sulci has neurons with dendrites parallel or perpendicular to the skull. EEG depends only to dipole moment vectors normal to the scalp electrodes, i.e. the strength depends on the angle between the source dipole and the scalp. In EEG only the synchronized activities are detected, whereas non-phase locked sources are deleted. The EEG signal is the weighted sum of all sources in time and the weighting function contains geometric and conductive characteristics of the head volume conductor. By using the weighted function the projection of the sources can be calculated (forward problem). Unfortunately, the estimation of the function is head-model dependent. The inverse problem, instead, can be solved mapping back the measured signal on the scalp surface to the source configuration inside the brain. Because of non-uniqueness, an infinite number of estimates could have generated the electric potential vector [Isaev and Supin, 1985]. For decades the EEG has been used to study and characterize pathophysiological processes in the brain, but it has showed a limited ability to localize activity in a deep brain region until the advent of hdEEG.

Used separately, EEG and fMRI provide low spatial (EEG, order of cm) or temporal (fMRI, order of s) resolution, when combined they have complementary features. Used simultaneously, EEG and fMRI is a powerful and non-invasive method to investigate the spatiotemporal mechanisms of abnormal brain activity and to precisely define the irritative zone.

The relationship between neuronal physiology and the observed BOLD activity is still unclear. It is only partially understood. To determine their relationship invasive studies on monkeys and other animals were conducted, whereas neural physiological studies in human were also conducted but less invasive. Several studies identified a coupling between blood flow and metabolic rate [Magistretti and Pellerin, 1999], i.e. the blood supply which provides the nutrients for brain metabolism. Other studies suggested that the increase in cerebral blood flow (CBF) following neural activity is not causally related to the metabolic demands of the brain region, but rather is driven by the presence of neurotransmitters [Yang and Iadecola, 1996, Bonvento et al., 2000]. The BOLD signal also depends on local factors such as blood volume, blood flow, and blood oxygenation and on global factor such as heart beat [Glover

et al., 2000, Liston et al., 2006, Lund et al., 2006] and respiration [Windischberger et al., 2002]. Research results so far suggest a predominantly linear coupling between BOLD and neuronal activity. Ogawa et al. [2000] demonstrated a linear relationship between somatosensory-evoked potentials and BOLD signals for brief stimulation durations. Rees et al. [2000] and Heeger et al. [2000] demonstrated a linear correlation between BOLD contrast in humans and averaged spike rate in a monkey cortical area during stimulation with nearly identical stimuli. A linear relationship was also observed in anesthetized monkeys where single-unit responses were acquired simultaneously with BOLD signals inside the MR scanner [Logothetis et al., 2001]. Logothetis and Pfeuffer [2004] suggested that the BOLD signal is not as well correlated to a single unit activity, but correlates better with the local field potentials, which includes membrane potential fluctuations, oscillations, and postsynaptic and presynapic events. Kim et al. [2004] found an approximated linear coupling between BOLD and neuronal activity in cat, only if a relatively large activity area is considered.

In a human study a similarly linear regression was suggested [Formaggio et al., 2008b]. A combined EEG-fMRI was used to determine the possible correlation between topographical movement-related EEG changes in brain oscillatory activity recorded from EEG electrodes over the scalp and BOLD cortical responses in motor area during finger movement. A negative linear correlation between BOLD and event related desynchronization (ERD) was found contralaterally. Nevertheless, these findings must be interpreted carefully because the fMRI signal is not a direct measure of synaptic activities or action potentials of cortical neurons; it results from the BOLD effect characterized by a limited temporal resolution [DeYoe et al., 1994, Ugurbil, 1997, Ogawa et al., 1998].

## 1.2 EEG-fMRI coregistration in epilepsy

EEG-fMRI simultaneously measures neuronal processes and provides the localization of the seizure. These technologies were combined by [Ives et al., 1993] and are widely used in studies of epileptic patients to localize epileptogenic foci [Ossenblok et al., 1999, Baudewig et al., 2001, Lemieux et al., 2001a,b, Benar et al., 2002, Archer et al., 2003, Aghakhani et al., 2004, Gotman et al., 2005, Kobayashi et al., 2006, Jacobs et al., 2007, Laufs et al., 2007, Rodionov et al., 2007, Manganotti et al., 2008, Li et al., 2009, Luo

et al., 2010, Cosottini et al., 2010]. The results have been corroborated in several important reviews [Menon and Crottaz-Herbette, 2005, Ritter and Villringer, 2006, Rosenkranz and Lemieux, 2010].

Three different methods of acquisition were employed: triggered, interleaved and continuous EEG-fMRI methods. In the *triggered* EEG-fMRI method, the EEG is acquired in the absence of scanning, while the patient is in the magnet. The functional scanning is manually triggered after identification of interictal spikes in the EEG record using the information that BOLD response has a $5 \pm 7$ s lag after the electrical activity [Ives, 1995, Warach et al., 1996, Seeck et al., 1998, Krakow et al., 1999, Patel et al., 1999, Symms et al., 1999]. The main limitation is that you are not sure to begin the fMRI sequence during the peak of the hemodynamic response function (HRF). Other researchers use *interleaved* EEG-fMRI methods. The fMRI acquisition starts 2-3 s after the event and is controlled by the timing of the experimental paradigm. It is used to study other types of EEG phenomena as evoked potentials and spontaneous activity [Huang-Hellinger et al., 1995, Bonmassar et al., 1999, Lovblad et al., 1999]. Both the triggered and interleaved methods show some limitations. In the triggered method, changes in the EEG can not be seen during fMRI scanning and the MR image contrast typically does not reach equilibrium until $3 \pm 4$ volumes after initiation of the scan [Goldman et al., 2000], when the first volumes are the most important. In the interleaved method, data are acquired using stimuli displaced in time, and the EEG can not be used as a direct reference function for fMRI signal maps. More recently, a *continuous* technique allows to acquire simultaneously EEG and fMRI signals. This type of acquisition introduces common artifacts on MR images and on EEG, that can be filtered off-line [Goldman et al., 2000, Mulert and Lemieux, 2010]. The MR artifacts on images are caused by electrodes, wires and the EEG system inside the magnet room near the scanner. Variations in the local properties of the field can cause intensity variations across the image, such as the brightening of the center of the image compared to the periphery. Another problem is the radio-frequency emission of the EEG system that can be solved by shielding the system. Differently, the EEG artifacts are caused by movement of the leads themselves within the static field of the magnet that induces an electromotive force (EMF) in a wire loop (ballistocardiogram [BCG] artifact). In addition, the switching magnetic field, applied during image acquisition, induces an EMF in the electrode leads and in a wire loop.

Fig. 1.1 shows the EEG-fMRI coregistration system. The patient is inside the magnet room and is asked to lie still in the scanner (resting state condition) with closed eyes. From the MRI recording unit the radiologist acquires the MR images. The patient wears an EEG cap and the cap is connected to the MR compatible amplifier. The common MR-compatible EEG cap has 16 or 32 channels and in more recently systems also 64 channels, whereas 256 MR-compatible systems are still prototypes. The EEG MR-compatible amplifier has large dynamic range to avoid that the amplifier saturates during the fMRI acquisition. Data are transmitted from amplifier via optic fiber cable to the EEG recording unit (pc) located outside the scanner room. The feature of this system, differently from a standard EEG, is that the amplifier is MR compatible.

### 1.2.1 EEG artifacts inside a magnet

During EEG-fMRI acquired simultaneously, EEG is obscured by artifacts induced by both the static and the time-variant fields of the MR scanner. By Lenz's Law, in a wire loop perpendicular to the static field direction, the electromotive force (EMF) is proportional to the cross sectional area of the wire loop and to the rate of change of the perpendicular magnetic field (dB/dt):

$$\xi = -d\Phi(B)/dt \tag{1.1}$$

In detail, the EMF can be induced in fixed conductor loops in rapidly changing gradient fields as well as in moving conductor loops in the static magnetic field [Lemieux et al., 1997]. In the first case, the radio-frequency pulses and the gradient switching, required for MRI, may induce voltages that obscure the EEG signal (*gradient artifact*) [Ives et al., 1993, Huang-Hellinger et al., 1995]. This gradient artifact can be reduced minimizing the area comprised by loops of wires. In the second case, pulsatile motion related to the heart beat in the static field causes the *BCG artifact* [Ives et al., 1993, Muri et al., 1998, Goldman et al., 2000]. Further, introduction of EEG equipment into the scanner potentially can disturb the homogeneity of the magnetic field and distort the resulting MR images [Ives et al., 1993, Goldman et al., 2000].

The gradient artifact has high amplitudes in the range of several mV (EEG is in the range of $\mu$V), is periodic with multiple spectral lines in the Fourier Spectrum and contains components in the EEG frequency range (Fig.

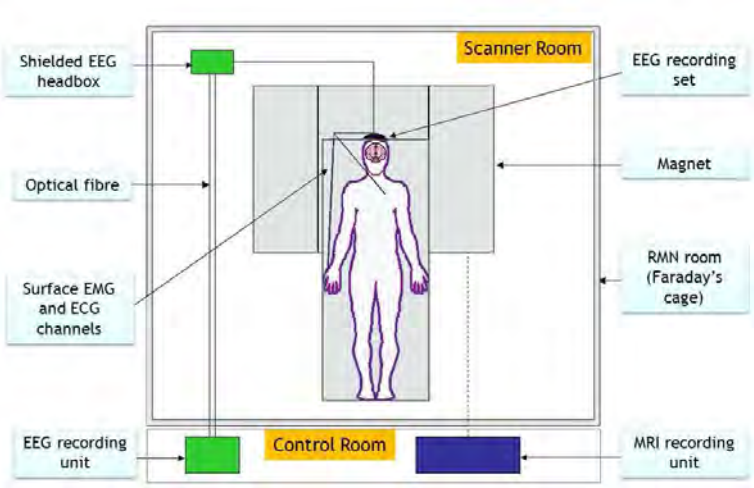


**(a)**

**(b)**

**Figure 1.1:** (a) EEG-fMRI setup. (b) EEG-fMRI equipment.

1.2a). It can not be removed by conventional low-pass or band pass filters because of the large power in the EEG frequency band. The EEG corrupted by the gradient artifact can be filtered by average subtraction in the temporal domain [Niazy et al., 2005] or in frequency domain [Hoffmann et al., 2000]. In the average-subtraction method, a gradient artifact template, computed by averaging N gradient artifact occurrences, is subtracted from each individual artifact, followed by adaptive noise cancellation in order to remove residual artifact components (Fig. 1.2b). Differently, frequency domain filtering consists in determining the spectrum of the artifact template and subsequently correcting the signal power spectrum by setting artifact frequencies to zero. However, this approach can affect EEG, since its band may overlap. In 1999,

Felblinger et al. [1999] estimated the individual responses of the Gx, Gy, Gz gradients and subtracted the sum of these responses from the EEG signal. In Allen et al. [2000], principal component analysis (PCA) was introduced in order to capture temporal variations in the artifact. The algorithm was applied to generate an optimal set of basis functions that best described the temporal variations of the artifacts. These basis functions were then fitted and subtracted from the EEG to reduce the artifacts. Sijbers et al. [1999] estimated the power spectrum of the gradient artifact and used this template to remove the gradient artifact through adaptive filtering techniques. More recently, an interesting method based only on average subtraction was developed [Goncalves et al., 2007]. The algorithm preliminarily estimates the MR sequence timing parameters, in order to correct misalignments between EEG and fMRI data, and then removes gradient artifact by subtracting an artifact template calculated both on slice and on volume acquisitions.

Our group developed a novel method, based on the average-subtraction approach, to remove gradient artifact, able to preserve EEG integrity and adapt to any dataset avoiding MRI trigger, using complexity-free mathematical procedures. The novelties of this method are the iteratively average subtraction and the tuning of the artifact to be subtracted, for each slice, by linear regression. Moreover, this method offers a practical solution as it does not require hardware solutions such as synchronizing the EEG and MRI systems or altering imaging sequence and collecting data at very high sampling rate [Sartori et al., 2009] (Appendix A).

The EMF also produces on EEG electrodes the BCG artifact caused by cardiac pulse-related movements of the electrodes during the acquisition, which increases with the static field strength and can cover the EEG signal fluctuation (Fig. 1.2c). Its frequencies are approximately 10 Hz and below [Allen et al., 1998, Bonmassar et al., 2002]. There are three causes of this artifact. First, the movement of the electrodes and scalp due to expansion and contraction of scalp arteries between the systolic and diastolic phases [Allen et al., 1998, Muri et al., 1998, Goldman et al., 2000, Ellingson et al., 2004]. Second, fluctuation of the Hall voltage due to pulsatile changes of the blood in the arteries [Muri et al., 1998]. Finally, the small cardiac-related movement of the body [Sijbers et al., 2000]. The methods to eliminate the BCG are based on averaged artifact subtraction (AAS) or adaptive filtering techniques. In AAS, a BCG artifact template is estimated first detecting the QRS peaks in the electrocardiogram (ECG) signal and then by averag-

ing over the intervals of EEG signal. The template is then subtracted from the individual raw EEG epochs [Allen et al., 1998]. The method has been subsequently modified. To compensate the slow changes in the BCG artifact, Goldman et al. [2000] assign weights to the EEG segment that vary inversely with the temporal displacement from the current sample. Because of the non-stationarity of the ECG signal, others apply adaptive filtering techniques which uses the correlations between a reference ECG channel and the EEG channels to estimate the contribution of the BCG artifact in the EEG signal. The template is then subtracted from the raw EEG [Sijbers et al., 2000, Bonmassar et al., 2002]. Differently from these two techniques, more recently the independent component analysis (ICA) has been used for removing BCG artifacts from EEG [Srivastava et al., 2005]. The ICA decomposition found from five to six components related to the BCG artifact. The spectral power analysis, applied before and after removal of the components, showed a reduction at frequencies related with the artifact.

## 1.3 Conventional analysis of EEG-fMRI data in epilepsy

The EEG-fMRI coregistration is a suitable technique to study IED activity. IEDs are composed of spikes, fast electrographic transients lasting less than 70 ms, and slow waves that probably represents a period of refractoriness. In the conventional analysis of EEG-fMRI data the appearance of IEDs drives the analysis on fMRI data. Conventional analysis of EEG-fMRI data relies on spike-timing of epileptic activity: the neurologist identifies the intervals of the IED events, as represented by a square wave; this protocol is then convolved with a canonical HRF to construct a model, *regressor* or *design matrix*, for the general linear model (GLM) analysis. Differently, the ictal EEG is long lasting and does not show different states of rest-active conditions: the ictal events are limited, in most of cases are unpredictable and may have safety problems. There are limitations to this analysis, however. First, because it is impossible to predict when epileptic discharges will occur, few IEDs will usually appear during the few minutes of fMRI recording; this hampers the possibility to detect BOLD signal changes [Salek-Haddadi et al., 2006]. Second, because of the volume conductor, deep epileptic discharge cannot be captured by scalp EEG. The first our approaches to analyze the EEG-fMRI data were to treat

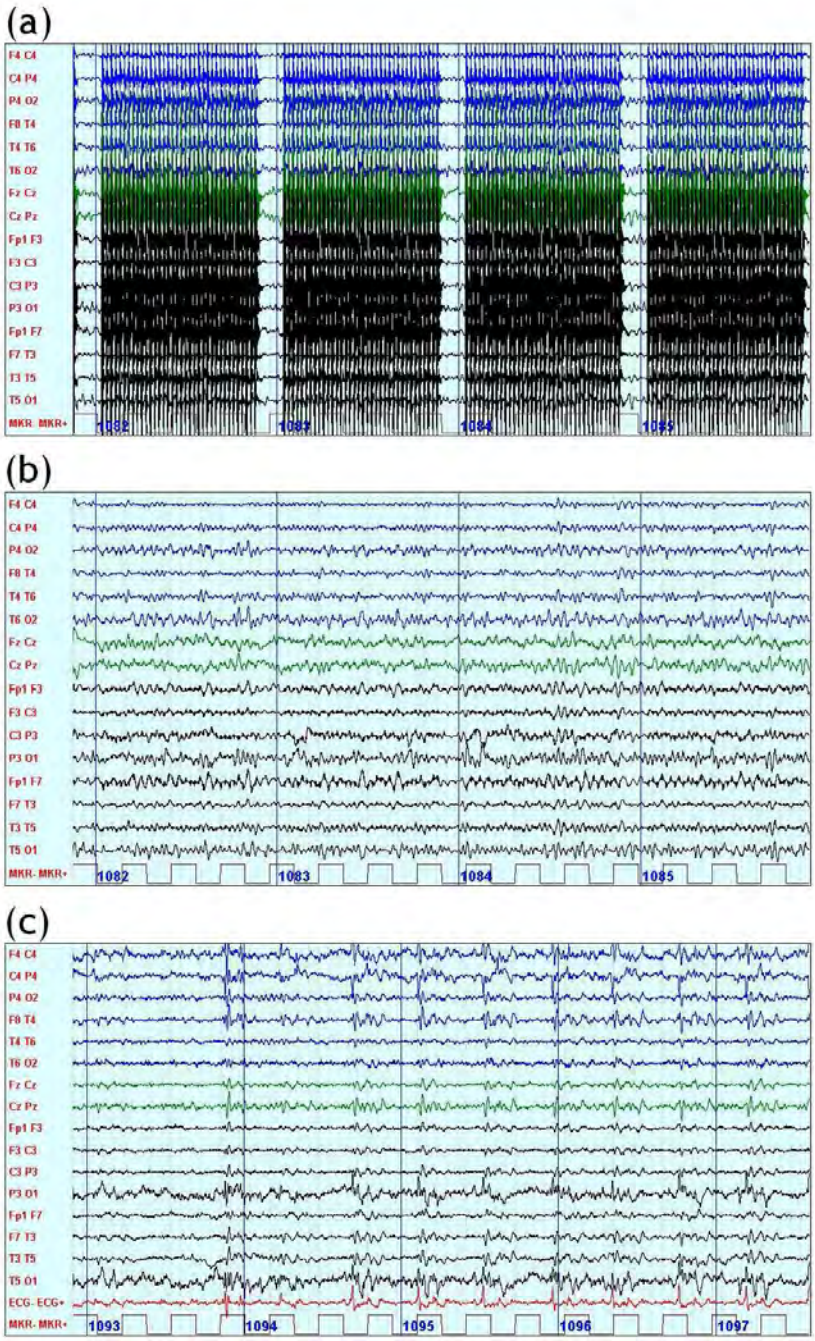


**Figure 1.2:** (a) Raw EEG signal acquired inside the MR scan. (b) Signal after gradient artifact subtraction. (c) EEG acquired inside the MR scan affected by BCG artifact. The signal was pass band-filtered between $1.6 - 30$ Hz, gain $= 150\ \mu V/cm$. The time windows are of 15 s.

the data separately [Avesani et al., 2008, Formaggio et al., 2008b, Manganotti et al., 2008] as described above. The studies are somewhat limited because the advantages of the simultaneous recordings have not really been exploited: the analysis does not combined the two measurement modalities.

### 1.3.1 fMRI preprocessing

The main goal of fMRI preprocessing is to reduce non-task- or non-event- related variability in the data before the analysis. The basic preprocessing steps are: slice scan time correction, motion correction, temporal filtering, spatial smoothing, registration and normalization. To correct for the different slice acquisition times, a slice scan time correction can be used with different interleaved scanning order [Huettel et al., 2004]. Head motion can introduce false BOLD activity if correlated to stimulus. Therefore, to reduce the effect of head motion the data are realigned using rigid-body transformation. Movement correction can be either before or after slice timing correction. For interleaved data acquisition slice timing correction must be used first, for sequential data acquisition movement correction first (Fig. 1.3).

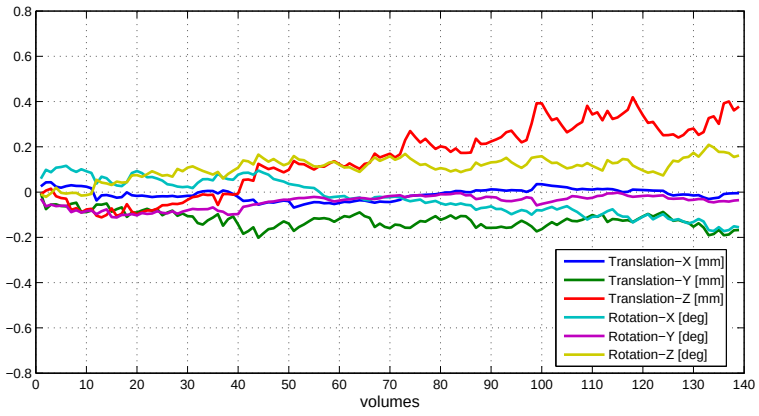


**Figure 1.3:** Example of rigid body motion parameters - 3 translations, 3 rotations. Translation (mm) or rotation (degrees).

Typical time course shows also a slow background signal (scanner drift, noise from physiological source as respiratory and cardiac cycles and residual movement). These slowly varying signals can be removed by a high-pass filter

(Fig. 1.4a,b). The spatial filter adjusts voxel intensities with a weighted average of neighbour voxels (the weighting is typically Gaussian). It requires a convolution with a Gaussian kernel (full width at half maximum [FWMH] typically about twice the voxel size). The advantage is that it increases signal to noise ratio (SNR) but reducing spatial resolution. Smoothing can spread activations across sulci and increase partial-volume effects (averaging across different tissues) (Figs. 1.4c, 1.5).

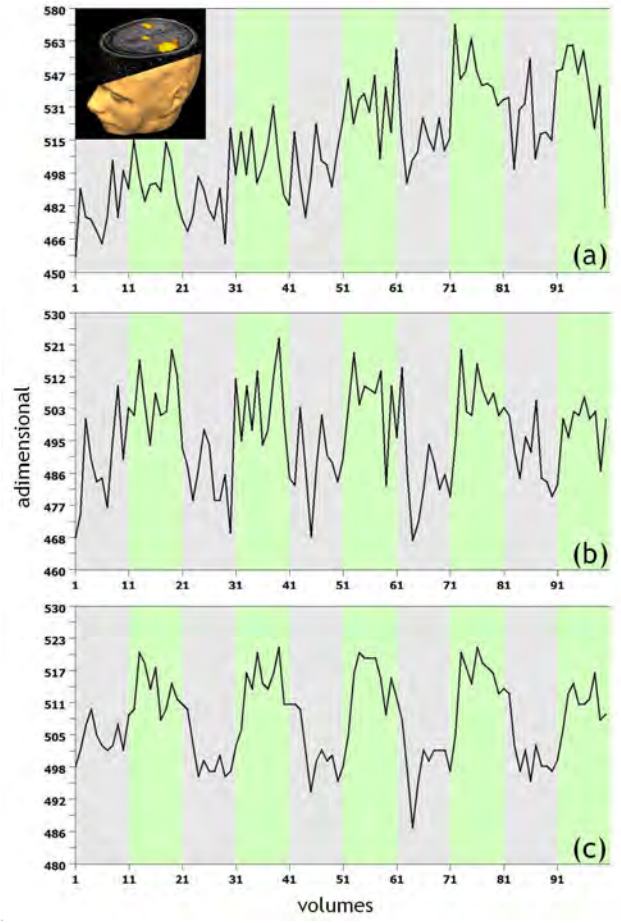


**Figure 1.4:** a) FMRI time course acquired during square-wave movement at 26 s on and 26 s off, b) after highpass filtering with cut-off of 0.008 Hz and c) after spatial smoothing (FWHM = 6 mm).

Registration optimizes parameters (translations and rotations) that describe

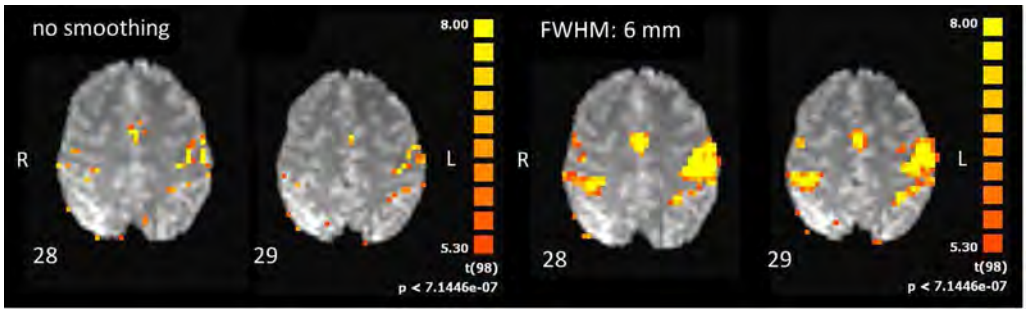


**Figure 1.5:** Effect of spatial smoothing on a single subject during a right-hand motor task. The small activations disappear and near activations join.

rigid body transformation between source and reference images; transformation re-samples according to determined transformation. The anatomical space can be standardized in a common space, e.g. Talaraich or Montreal Neurological Institute (MNI). The atlas of Talaraich and Tournoux is based on a single subject (60 years, female, cadaver) and it is related to the Brodmann coordinates [Talairach and Tournoux, 1988]. Differently, the MNI space is a combination of many MRI scans on normal controls. The normalization allows generalization of results to larger population, improves comparison with other studies, provides coordinate space for reporting results and enables averaging across subjects. Since the template is derived from normal brains, transformations can lead to inappropriate image distortion at the site of a lesion. Brains to be normalized has regions of signal intensity that are different compared to the corresponding region of the template. Therefore, normalization may distort the lesion extension of a patient.

### 1.3.2 General linear model

The quantitative analysis of the BOLD signal allows to detect and delineate cerebral areas active after a specific stimulus or task. Bandettini et al. [1992] demonstrated that the time course, obtained with a long-echo time (TE) gradient-echo planar imaging (EPI), is an effective tool in localizing brain function in humans. The brain regions activated by a specific task can be recognized by calculating the correlation coefficient of the data with respect to a reference waveform, followed by formation of a cross-correlation image

[Bandettini et al., 1993] or by using the GLM approach [Friston et al., 1995] and assuming a model to describe the HRF, that is the expected shape of the BOLD response due to stimulus presentation.

In the GLM analysis, for each voxel, the observed response vector of fMRI data ($y \in R^{N\times 1}$ with $N$ equal to the number of the acquired volumes), is expressed in terms of a linear combination of explanatory variables, contained in the known matrix ($X \in R^{N\times M}$ with $M$ equal to the number of the unknown regression coefficients), commonly called design matrix, via the unknown parameter vector ($\beta \in R^{M\times 1}$), plus an error term ($\epsilon \in R^{N\times 1}$):

$$y = X \cdot \beta + \epsilon. \tag{1.2}$$

The theoretical basis of GLM in fMRI analysis can be found in [Friston et al., 1995]. The design matrix $X$ is crucial for the results of the study. Its first column is a vector of ones and the second column contains values, at acquisition time points $n = 1, 2, \ldots, N$, equal to the convolution of the stimulus function, $u(n)$, with the impulse response, $HRF(n)$, representing the hemodynamic response function:

$$X(n) = [1(n) \;\; u(n) \otimes HRF(n)] \tag{1.3}$$

where $\otimes$ denotes the convolution operation. Additional columns are eventually present when the time and dispersion derivatives of the HRF are introduced. The external stimulus function $u(n)$ is known since it depends on the experimental set-up, with values equal to 1 or 0 denoting the presence or absence of a stimulus, respectively.

### HRF modeling

In response to specific stimuli or an EEG event, the fMRI signal takes few seconds to increase, reaches its peak between 5 and 7 s and then recovers to baseline in 12 s. After that there is a signal undershoot up to 30 s after the onset of the stimulus. This response to the impulse is referred to as the HRF. In epileptic patients, it describes the dynamic process of the BOLD signal evoked by an interictal event.

***Dip.*** The shape of the HRF shows a slight initial signal decrease (Fig. 1.6). Some researchers suggested that an initial negative dip before the positive peak of BOLD response correlates with measured local decreases in tissue

oxygen concentration probably with an increase of the local metabolism during neuron activation [Malonek and Grinvald, 1996, Kim et al., 2000]. The negative initial dip of the BOLD response occurs within 1-2 s after electrical response and can not be captured when the fMRI acquisition has long time repetition (TR). In addition it is only observed using scanners with high magnetic fields of at least 3 T or superior where the SNR is more high [Menon and Goodyear, 1999, Menon and Kim, 1999].

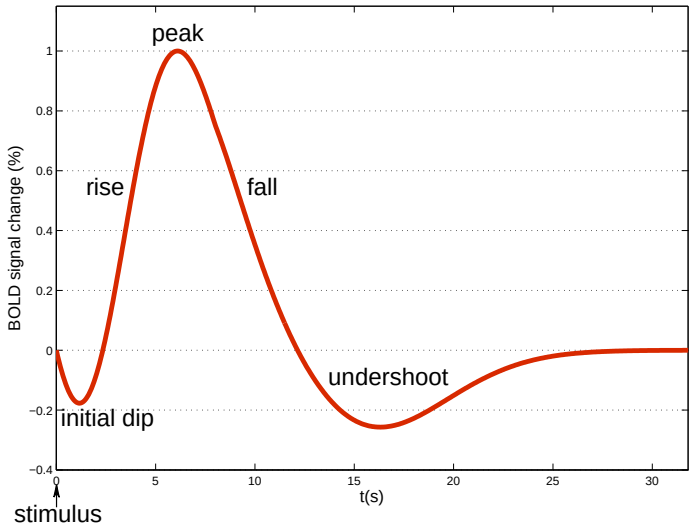


**Figure 1.6:** Typical hemodynamic response measured by fMRI after a stimulus. It shows a negative initial dip, a positive BOLD response and a negative undershoot.

***HRF shape.*** The nature of the HRF has been extensively studied and different models were purposed: models based on a gamma function [Cohen, 1997, Lange and Zeger, 1997], combination of gamma functions [Friston et al., 1998], Gaussian model [Rajapakse et al., 1998], spline-like functions [Gossl et al., 2001a,b], models using a basis set such as Fourier sines and cosines [Lange and Zeger, 1997, Ardekani et al., 1999], finite impulse response [Goutte et al., 2000], canonical HRF plus temporal and dispersion derivatives [Friston et al., 2007], models based on deconvolution methods [Glover, 1999, Warach et al., 2000, Lu et al., 2006, 2007], and Bayesian methods [Marrelec and Benali, 2001, Marrelec et al., 2003, Woolrich et al., 2004]. Briefly, the most used HRF models are here introduced.

The simplest HRF model is the *gamma variate function* that is used in the AFNI software [Cox, 1996], (Fig. 1.7a):

$$h_{gamma}(t) = \left(\frac{t}{bc}\right)^{b} \cdot e^{\left(b-\frac{t}{c}\right)}, \tag{1.4}$$

where t is the time in seconds, b = 8.6 and c = 0.547. The parameters b and c are estimated from a dataset of visual flash stimuli [Savoy et al., 1994, Cohen, 1997] using the Levenberg-Marquardt algorithm. The time to the peak of the gamma density is 4.7 s, and the approximate FWHM is 3.8 s.

The *Glover function* is used in the FMRISTAT software (http://www.math.mcgill.ca/keith/fmristat), (Fig. 1.7a):

$$h_{glover}(t) = \left(\frac{t}{d_1}\right)^{a_1} \cdot e^{-\left(\frac{t-d_1}{b_1}\right)} - c\left(\frac{t}{d_2}\right)^{a_2} \cdot e^{-\left(\frac{t-d_2}{b_2}\right)}, \tag{1.5}$$

where t is the time in seconds, $d_1 = a_1 b_1$ is the time to peak, $d_2 = a_2 b_2$ is the time to the undershoot, and $a_1 = 6$, $a_2 = 12$, $b_1 = b_2 = 0.9$, $c = 0.35$. The parameters $a_1$, $a_2$, $b_2$, $b_2$, and $c$ are fitted from brief auditory events datasets [Glover, 1999, Worsley et al., 2002]. This HRF function is modeled as the difference of two gamma density functions. The time to the peak of the first gamma density (positive) is 5.4 s, the approximate FWHM of the first gamma density is 5.2 s, the time to the peak of the second gamma density (negative) is 10.8 s, the approximate FWHM of the second gamma density is 7.35 s, and the coefficient c of the second gamma density is 0.35.

*SPM's canonical HRF* is used in the SPM (Statistical Parametric Mapping, www.fil.ion.ucl.ac.uk/spm/) software package (Fig. 1.7a). The canonical HRF is a "typical" BOLD impulse response characterized by two gamma functions, one modelling the peak and one modelling the undershoot:

$$h_{spm}(t) = \frac{l_1 h_1 t^{(h_1-1)} e^{-l_1 t}}{gamma(h_1)} - c \cdot \frac{l_2 h_2 t^{(h_2-1)} e^{-l_2 t}}{gamma(h_2)}, \tag{1.6}$$

where $t$ is the time in seconds, $gamma(h)$ is the standard gammavariate, and $l_1 = l_2 = 1$, $h_1 = 6$, $h_2 = 16$. The time to the peak of the first gamma density is 5 s, the approximate FWHM of the first gamma density (positive) is 5.3 s, the time to the peak of the second gamma density (negative) is 15.8 s, the approximate FWHM of the second gamma density is 9.2 s, and the coefficient c of the second gamma density is 1/6.

To allow variations about the canonical form, the partial derivatives of

the canonical HRF with respect to, for example, its peak delay and dispersion parameters can be added as further basis functions. The temporal derivative can capture differences in the latency of the peak response (*Canonical HRF and its derivatives*). In SPM, it is created from the finite difference between a canonical HRF and a canonical shifted by one second. The dispersion derivative can capture small differences in the duration of the peak response (Fig. 1.7b) [Friston et al., 2007]. In [Henson, 2001], different HRFs showed different fMRI activities suggesting that a linear combination of several temporal basis functions can be used to account for delays and dispersions in the HRF. The stimulus function is convolved with each of the basis functions to give a set of regressors. In Fig. 1.8 an example of different activation maps using canonical HRF and canonical HRF with its derivatives is described.
The most flexible HRF models are the *finite impulse response* (FIR) and *Fourier basis sets* (Fig. 1.7c,d), which make minimal assumptions about the shape of the response. FIR functions increase the degrees of freedom used in the design matrix and allow less powerful statistical tests. The FIR set consists of contiguous boxcar functions of finite peristimulus time (PST), each lasting $T/K_{FIR}$ s, where T is the duration of HRF and $K_{FIR}$ the number of functions of the basis set. The Fourier set consists of a constant and $K_F$ sine and $K_F$ cosine functions of harmonic periods $T, T/2, ..., T/K_F$ s. Then, linear combinations of the FIR or Fourier basis functions can capture any shape of response, compared to the canonical HRF, whose shape is fixed [Friston et al., 2007]. To model the BOLD signal of the epileptic patients more flexible HRF models such as the Fourier set were used [Salek-Haddadi et al., 2006].

### HRF modeling in epilepsy

As described in literature, in response to an IED activity the HRF shows an high degree of variability in shape presumably due to the vasculature of different regions [Bagshaw et al., 2004, Lu et al., 2006, Salek-Haddadi et al., 2006, Lemieux et al., 2008].

Many researchers studied the shape of the HRF in epileptic patients. Two reviews showed that about the 30% of EEG-fMRI coregistrations had no BOLD activation or discordant BOLD activation with the clinical epileptic activity and the clinical outcome [Aghakhani et al., 2006, Salek-Haddadi et al., 2006]. A possible explanation for this result is the used of a standard

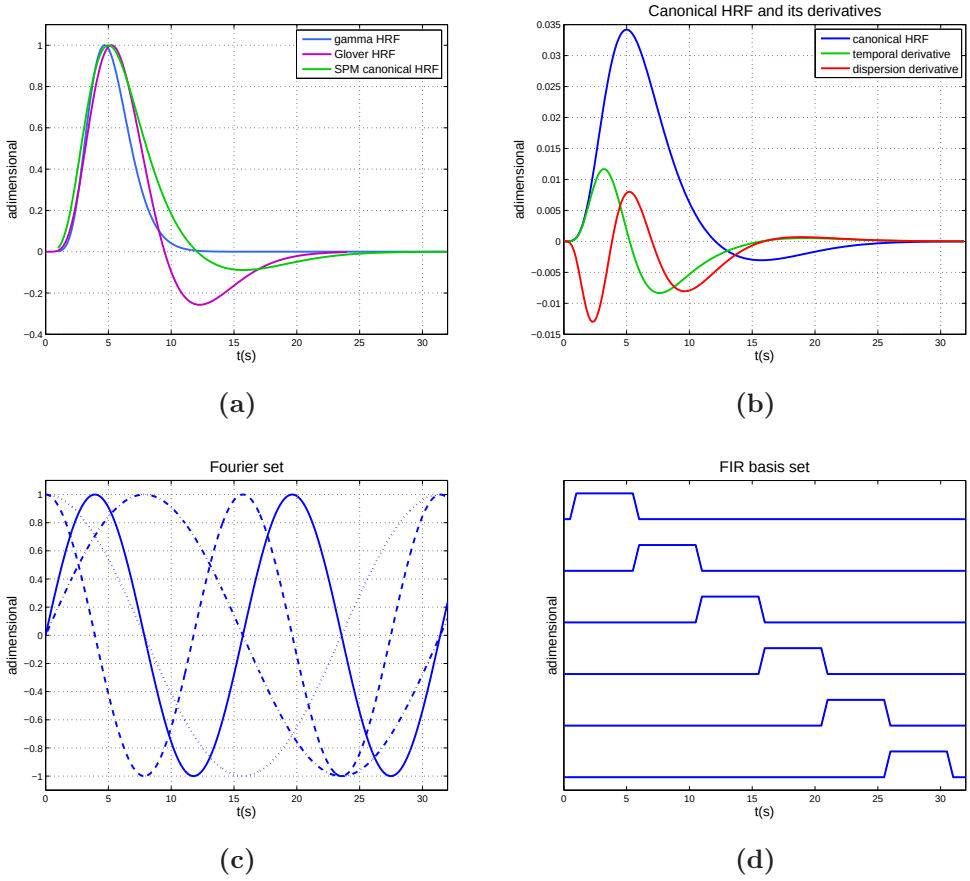


**Figure 1.7:** (a) Gamma, Glover, and SPM canonical HRFs. The three HRFs have almost the same time to peak, and the shapes are very similar before peak time. After peak time the Glover HRF has a deeper undershoot. The three HRFs are scaled to have a maximum amplitude of 1 [Lu et al., 2006]. (b) Canonical HRF (blue) and its temporal (green) and dispersion (red) derivatives. (c) Fourier basis set, $K_F = 4$. (d) FIR basis set, $K_{FIR} = 6$.

HRF model instead of a specific HRF estimated on the epileptic region.

The first attempt to create a modified hemodynamic response was to hypothesize that the HRF can be arise before the EEG event. In fact long-lasting hemodynamic changes were observed occurring several minutes before the interictal event [Weinand et al., 1997, Baumgartner et al., 1998, Federico et al., 2005, Makiranta et al., 2005]. Hawco et al. [2007] suggested that neu-

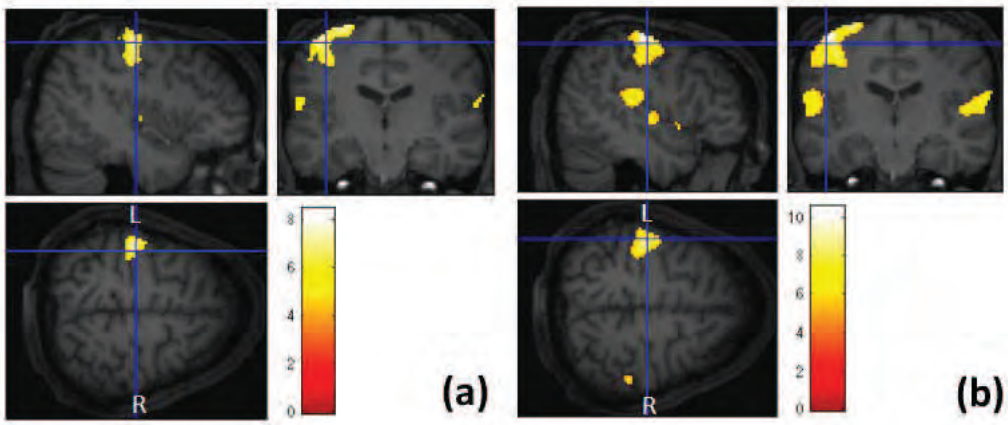


**Figure 1.8:** fMRI map obtained on a healthy subject during a motor task (right hand movement). The activation maps were generated by GLM (SPM software) with p-value corrected for multiple comparison, family wise error (FWE) ($p < 0.05$). A large activation in the left primary motor area (MI) and supplementary motor area (SMA) was observed using both canonical HRF (a) and canonical HRF with its derivatives (b). An activation in the right motor area and right cerebellum was also found by using only the canonical HRF with its derivatives (b).

ronal changes can occur several seconds before the EEG surface event, but that these changes are not visible on the scalp. Therefore, they peaked the HRF at seven different times (two before the spike onset, -3 and -1 s, and five after, 1, 3, 5, 7 and 9 s). For each patient, seven activation maps were generated using Boynton HRF with these peaks. Using the deconvolution method [Cox, 1996, Warach et al., 2000] an HRF for each significant activation for all data sets was calculated (no deactivations were considered).

Using a voxel-based approach that merges deterministic and pattern recognition methods for the analysis of EEG-fMRI data in patients with epilepsy, Lu et al. [2007] estimated HRF by deconvolution on a training data set to be used together with the GLM approach on an independent data set. The HRFs, in response to sensory or cognitive stimuli, differ in epileptic patients compared to healthy subjects. The limitations of this approach are principally related to the intrinsic problems affecting deconvolution: the linear assumption underlying convolution is often an approximation; the deconvolution is an ill-posed problem when no constraints on the HRF are assumed,

as in this case, and when data are affected by high measurement errors. The beta parameters of the model and the parameters that describe the HRF are simultaneously estimated. The method returns inaccurate estimates and this is reflected on HRF.

Grouiller et al. [2010] proposed an HRF based on a limited set of gamma functions. The parameters (the time scaling factor and the time of onset on the standard HRF) were identified to maximize the number of activated and deactivated voxels assuming that the optimal HRF was that highlighted the strongest activation. But this choice may not always be the optimal.

***Negative HRFs.*** Some researchers observed an inverted HRF both in studies of EEG alpha rhythm [Laufs et al., 2003, Moosmann et al., 2003] that in studies on epilepsy [Stefanovic et al., 2004, 2005, Hamandi et al., 2008]. Even if the underlying mechanics is not completely understood, a decrease in neuronal activity seems to be related to a decrease in the BOLD response. Some studies hypothesized a vascular origin of the negative response with an association between reduction in cerebral blood flow and decreases in oxygen consumption [Harel et al., 2002, Kannurpatti and Biswal, 2004]. The deactivation might represent vascular "steal" phenomenon or might be related to the disruption of neurovascular coupling [Shmuel et al., 2002, Gotman, 2008, Mangia et al., 2009].

In case of epileptic spikes, anticausal EEG-fMRI correlation could indicate that the observed spikes is only "the tip of iceberg", caused by a period of temporal neural synchronization of the network, in a stream of any synchronous pathological activity associated with epilepsy [Hawco et al., 2007, Ullsperger and Debener, 2010].

***Earlier HRFs.*** Many hypothesis were investigated about the existence of earlier HRFs. A likely explanation is an increase in synaptic activity preceding the spike [Logothetis et al., 2001]. As described by [Makiranta et al., 2005], early BOLD responses might reflect electrical processes invisible on the EEG (e.g. if generated from deep regions). Also Jacobs et al. [2009] observed early increases in the BOLD signal associated with focal spikes. They suggested that this early BOLD activity is the result of IED occurring some seconds before the measured EEG event but that these changes are not visible on the scalp.

The BOLD signal can appear earlier than the EEG event [Hawco et al.,

2007, Rathakrishnan et al., 2010] or later [Lemieux et al., 2008]. In this case the sensitivity of EEG-fMRI analysis can be improved with the used of HRF peaking at different time onset (e.g. from -9 to +9 s around the spike). Also Moeller et al. [2008] found an HRF with negative onset of 3-6 s prior the onset of generalized spike and wave (GSW).

Recently, Masterton et al. [2010] studied patients with benign childhood rolandic epilepsy and found that the shape of the averaged BOLD response was different to the canonical HRF, including earlier onset and positive time-to-peak, and a more pronounced signal decrease. The estimated HRF was calculated, first applying a FIR basis set, then choosing for each subject the individual response estimate from the most significant voxel within the cluster of voxels located closely to the face area. Finally, the group response shape was estimated by averaging the individual responses.

### 1.3.3 Open problems in GLM

In spite of its current limitations, EEG-fMRI coregistration in epilepsy has yielded promising results [Gotman et al., 2006, Laufs and Duncan, 2007] and the BOLD activation has been usually detected in agreement with the supposed epileptogenic area [Benar et al., 2006, Zijlmans et al., 2007].

In the conventional GLM analysis, the neurologist is able to visually identify IEDs. The convolution of these EEG events with a model of the fMRI response, i.e., the HRF, provides the regressor for the GLM analysis (Fig. 1.9). Maps showing regions of significant IED-related change were obtained through voxel-wise fitting of the model and application of appropriate statistical thresholds [Lemieux et al., 2001b, Benar et al., 2002, Salek-Haddadi et al., 2003, Hamandi et al., 2004, Gotman et al., 2006].

Unfortunately, this method shows two limits. First, the method is not automatic causing subjectivity in IEDs classification. Second, the using of a standard HRF in the GLM framework can introduce errors in extension and localization of the active area. In particular the shape and latency of the HRF evoked by IED are variable [Benar et al., 2002, Lemieux et al., 2008, Lu et al., 2006]. Although several studies have suggested that a single HRF model may be suboptimal [Aguirre et al., 1998], the widely used approach adopts for all subjects a fix HRF to describe the expected shape of the BOLD response due to stimulus presentation.

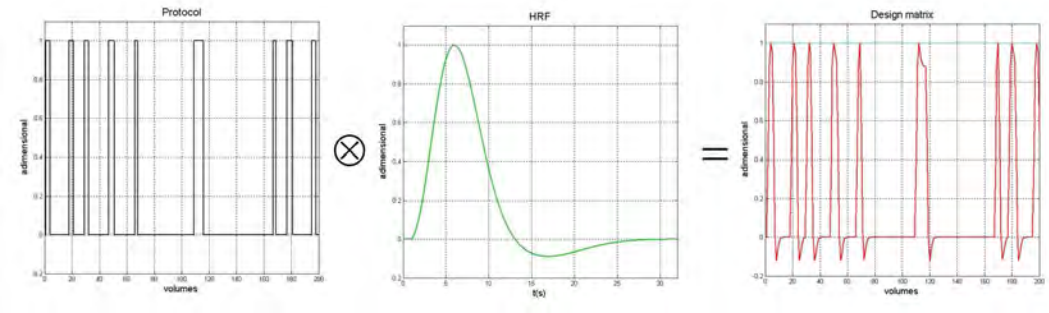


**Figure 1.9:** Design matrix construction: convolution between the protocol based on the EEG events and the HRF.

### First: IED selection

To solve the problem of the visual identification of the EEG event (square-wave protocol), different solutions based on the correlation between the EEG and fMRI data were purposed. Reference functions related to the interictal spikes were extracted from the EEG and compared to the fMRI signal [Ives et al., 1993, Warach et al., 1996, Lemieux et al., 2001b, Gotman et al., 2004, Liston et al., 2006, Zijlmans et al., 2007].

Recently, ICA, a technique able to separate statistically independent components from a mixture of data, was also applied to EEG data and a single component due to IED activity was identified by visual inspection [Jann et al., 2008]. Luo et al. [2010] used a procedure to analyzed EEG-fMRI data based on the temporal correlation between a channel of raw EEG and each independent component with the same time window. Subsequently, each type of IED was imaged using GLM. The method wanted to solve the foci localization for patients with complex and multiple discharges, not identified by the usual GLM.

Unfortunately, fMRI data consist of different slices recorded separately whereas the EEG data are instantaneous measures and multiple EEG events may occur during a TR. For these reasons integrating the data is not simple.

### Second: Use of standard HRFs

The widely used approach adopts the same HRF for all subjects undergoing a given experimental protocol. However, several studies examining the vari-

ability in BOLD response have suggested that a single HRF model may be suboptimal, since HRF differs both among people and scans. When optimal HRF across subjects (intersubject variability) was compared, the shape of the response was highly variable [Aguirre et al., 1998], while less variability in HRF was observed from a single subject collected across sessions, and even less variability in the responses collected within a single session (intrasubject variability) [Huettel et al., 2004]. Lindquist and Wager [2007] showed that neuronal activity produces changes in multiple aspects of the HRF shape, such as height, time to peak and width. They introduced a technique based on superposition of three inverse logit functions (the first describing the rise following activation, the second the decrease and undershoot and the third the stabilization) to construct a seven-parameters model, which balances interpretability and flexibility of the HRF model. The onset and peak latencies of the HRF provide information about the timing of activation for a brain area and the width provides information about the duration of activation. In this simulation study, the parameters were inferred at each voxel of brain volume using nonlinear fitting procedure, thus requiring high time-computational efforts [Lindquist and Wager, 2007]. Using the same HRF for each subject neglects hemodynamic response variability and could lead to false negatives and to false positives [Bonakdarpour et al., 2007]. Inclusion of derivative terms of the HRF into the model can alleviate such differences on the first level. However, it ignores the potential for amplitude bias induced by model mismatched due to variable hemodynamic delays and is not helpful for second level random effect analysis [Calhoun et al., 2004].

### 1.3.4 Independent component analysis

EEG-fMRI is widely used to investigate the hemodynamic correlates of spontaneous brain rhythms, i.e. the resting state networks (RSNs) [Mantini et al., 2007]. In case of 'resting state' condition, a state of a spontaneous and endogenous brain activity not intentionally induced externally nor voluntarily generated by the subject, the BOLD signal fluctuations reflect the baseline activity of the brain [Mulert and Lemieux, 2010]. In resting state condition the brain rhythms fluctuate in amplitude producing a modulation in the BOLD signal. The posterior alpha rhythm is associated to the visual system [Berger, 1929, Lopes da Silva et al., 1997], the temporal tau-rhythm to the auditory system [Tiihonen et al., 1991] and the rolandic alpha and beta

rhythms to the sensorimotor system [Gastaut, 1952, Salenius et al., 1997]. All are attenuated or not present during a task (e.g. the alpha rhythm is attenuated with eyes opening [Storti et al., 2010]).

Although the role of these networks has yet to be understood, their modifications are object of study in some pathologies such as in the Alzheimer's disease or other impaired brain functions [Mulert and Lemieux, 2010]. Epileptic events affect the activity of the default mode network (DMN) [Salek-Haddadi et al., 2003, Gotman et al., 2005, Hamandi et al., 2006]. Decreasing activity of DMN was observed both in generalized and focal epileptic activity [Kobayashi et al., 2006, Laufs et al., 2006] and may describe impaired consciousness.

During a task, the most common method used to analyze the fMRI data is the hypothesis-driven, voxel-based statistical method such as correlation method [Bandettini et al., 1993] and GLM [Friston et al., 1995]. However, GLM and correlation methods are not able to identify this spontaneous activity.

In the absence of a paradigm design, a useful alternative is a multivariate approach/analysis such as ICA. This important technique of data-driven analysis can be applied to solve the problem of blind source separation of signals by dividing the imaging data into several spatial patterns or independent activation maps. With this method, fMRI can be analyzed in the absence of spatial bounds or a priori knowledge about the time course of activation of the different components [McKeown et al., 1998]. ICA can extract task-related as well as physiologically-relevant non-task-related components and artifactual components. Furthermore, it is extremely useful for identifying IED-related activity [Moeller et al., 2011] and the RSNs of neuronal activity as regions involved in motor function, visual and auditory processing, memory, executive functioning and the DMN.

In detail, ICA separates statistically independent components (ICs) from a mixture of data [Jutten and Herault, 1988, Comon, 1994, Bell and Sejnowski, 1995]. Achieving maximal independence in time or space yields two types of ICA: the temporal ICA attempts to find temporally ICs with associated spatial maps, whereas the spatial ICA, most widely used in fMRI, attempts to find spatially independent components with associated time-courses [Calhoun et al., 2001]. fMRI data set is represented as a space-time matrix $\widetilde{X}$ (with $\widetilde{X} \in \Re^{N \times M}$), having in its $M$ columns the $N$-dimension time series measured in the $M$ voxels. $\widetilde{X}$ matrix information is modeled by

a linear combination of $N$ statistically ICs (the "sources") arranged as $N$-dimension rows of matrix $S$ (Fig. 1.10a). Thus the relationship between $\widetilde{X}$ and the independent components, matrix $S$, can be written as:

$$\widetilde{X} = AS \tag{1.7}$$

where $A$ is the square mixing matrix (with $A \in \Re^{N \times N}$ and $N$ the number of underlying ICs). The nth column of $A$ consists of the time-course associated with the nth row of $S$. The matrix $A$ may be estimated using several algorithms. Typical algorithms for ICA use centering, whitening (usually with the eigenvalue decomposition) and dimensionality reduction as preprocessing steps in order to simplify and reduce the complexity of the problem for the actual iterative algorithm. The inverse matrix of $A$, $W = A^{-1}$, is computed and the spatial components are estimated from:

$$\hat{S} = W\widetilde{X} \tag{1.8}$$

where $\hat{S} \in \Re^{N \times M}$ is a good approximation of the sources $S$ and $W \in \Re^{N \times N}$ is the unmixing matrix. Each component thus consists of a spatial map [McKeown et al., 1998]. The maximum number of ICs the ICA method can extract equals the number of time points in the data [McKeown et al., 1998]. Infomax [Amari et al., 1995, Bell and Sejnowski, 1995] and the FastICA [Hyvarinen, 1999] algorithms solve the aforementioned linear equation. The Infomax maximizes the information transferred from inputs through a non-linear neural network transfer function, whereas the FastICA maximizes independence among estimated ICs, which is achieved via maximization of negentropy, a measure of deviation from Gaussian distributions. There are two main limitations about traditional spatial ICA. First, neglecting the role of noise can cause inaccurate estimation of true dimension of independent sources, leading to so called overfitting phenomena, i.e. the separating matrix estimated by ICA fails completely in separating the true source signals. Second, there is no statistical processing available, i.e. it is not possible to apply a test for significance to the source estimates within the framework of null-hypothesis testing and the conversion in z scores does not show a statistical meaning [McKeown et al., 1998]. It can only represent how far the voxel intensities differ from the mean voxel intensity.

The probabilistic independent component analysis (PICA) method, implemented in FMRIB Software Library (FSL, www.fmrib.ox.ac.uk/fsl) and

used in this thesis, is an extension of classical spatial ICA framework and estimates sources by maximizing non-Gaussianity in terms of negentropy [Beckmann and Smith, 2004]. The novelty of PICA is the introduction of a non-square mixing matrix in the presence of Gaussian noise in the model: data are assumed to be generated from a set of statistically independent non-Gaussian sources corrupted by additive Gaussian noise, so that (Eq. 1.7) becomes:

$$X = AS + \eta \tag{1.9}$$

where $X = \bar{X} - \mu$ with $\bar{X} = \widetilde{X} + \eta + \mu$, $\mu$ defines the mean intensity of all voxels (assuming zero-mean sources) and $\eta \sim N(0, \Sigma^2)$ (Fig. 1.10b). The mixing matrix $A$ is estimated from the data using the Maximum Likelihood estimation [Beckmann and Smith, 2004] and, given $A$, the maximum likelihood source estimates ($S$) are obtained using generalized least squares. $A$ is now a $N \times K$ mixing matrix with $K \leq N$ (the number $K$ of sources is less than the size $N$ of data) and $S$ is a $K \times M$ matrix. The noise element introduced into the PICA model allows statistical processing by noise estimation and the z scores displayed are based on the estimated standard error of the residual noise.

The PICA decomposition can be made using Multivariate Exploratory Linear Decomposition into Independent Components (MELODIC) toolbox. After data reduction by means of principal component analysis (PCA), the number of dimensions (with waveforms and spatial maps) were estimated for each subject using the Laplace approximation to the Bayesian evidence of the model order [Minca, 2000, Beckmann and Smith, 2004]. The maps were thresholded at a posterior probability threshold of p>0.5 [Beckmann and Smith, 2004]. A threshold of z scores was finally used for visualization of the IC maps. Negative z scores indicate voxels whose fMRI signals are opposite modulated to the IC waveform.

### 1.3.5 Open problems in ICA

Three main methodological problems are present in-handling ICA results. First, the analysis, each time it is performed, can induce some changes in the estimated ICs, caused probably either by the assumption of statistical independence that may not hold for the data, or by the additive noise that can cause modification in the solution [Ylipaavalniemi and Vigario, 2008].

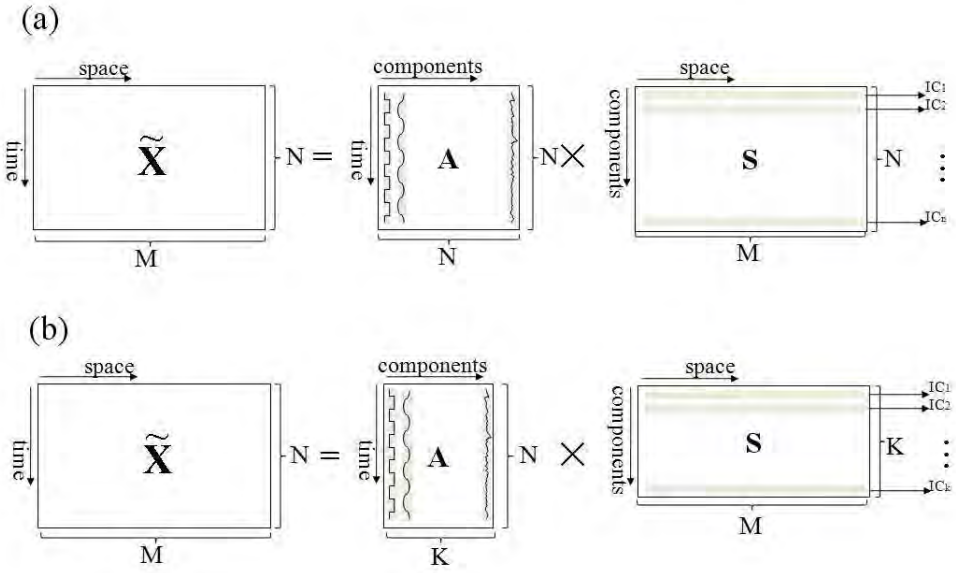


**Figure 1.10:** a) Spatial ICA of fMRI data. The columns of square mixing matrix $A$ are the time-courses and the independent components are the rows of matrix S. b) PICA of fMRI data. The matrix $A$ is a rectangular matrix and the number of components $K$ is less than the size $N$ of data.

Second, the ICA algorithm is able to extract only a number of components defined a priori and the components are not ranked during the decomposition [Boly et al., 2008], therefore the dimensionality of fMRI data for ICA could be unfortunately overestimated, leading to an excessive number of components with dissociated sources or underestimated discarding information. In this case it is not possible to separate the phenomena of interest [Beckmann, 2001]. The last issue is how to identify and isolate the spontaneous networks and to discard non neuronal noise such as scanner instability, environment noise, head movements and physiological fluctuation (cardiac and respiratory cycles).

ICA is implemented in many available algorithms to identify the source signals [McKeown et al., 2003, Ylipaavalniemi and Vigario, 2008]: Infomax [Amari et al., 1995, Bell and Sejnowski, 1995], JADE [Cardoso and Souloumiac, 1989, 1993], FastICA [Hyvarinen, 1999], that use higher order statistics, and also decorrelation methods belong to Molgedey and Schuster [1994] and Ziehe and Muller [1998].

In the literature several methods were also developed to order the output components. FSL uses the percentage of total variance explained by each single component. However, the percentage of variance generated by neural signals differs across subjects, multiple runs in the same subject, repeated applications of an ICA algorithm to a single dataset and can be even lower than the percentage of variance generated by noise. Alternatively, Lu and Rajapakse order the ICs either according to kurtosis or by incorporating a priori information as constrain [Lu and Rajapakse, 2003]; McKeown [2000] suggests an hybrid method to separate the task-related components from the artifactual sources, but employing a priori hypothesis to guide the analysis; Formisano et al. [2002] propose three measures for each IC to solve the selection problem: kurtosis of the component's distribution of the voxel values ranking according to descending values, the degree of spatial clustering of its suprathreshold voxels and one-lag serial correlation of its time course. In Brain Voyager software it is available a method that provides a classification of ICs as BOLD network through a 11 parameters representation (IC-fingerprint): kurtosis, skewness, spatial entropy, degree of clustering, one-lag serial autocorrelation, temporal entropy, power contribution in five range bands [De Martino et al., 2007]. This solution is also employed in patients with focal epilepsy [Rodionov et al., 2007]. However, despite an automatic classification of ICs as BOLD components, the visual identification by an expert neurologist is needed. Finally, a different approach applicable to periodic fMRI paradigms, i.e. not for resting state, uses for ranking the power component of the fundamental task frequency, quantified by Fourier transform of ICs [Moritz et al., 2003]. Algorithm fully exploratory network ICA (FENICA), introduced in the context of ICA group analysis, explores spatial consistent resting state networks over a group of subjects neither requiring a priori template definition nor visual inspection nor single-subject component selection [Schopf et al., 2010]. The disadvantage is that the algorithm cannot be applied in individual clinical setting such as epilepsy, where it is strictly necessary to identify the ICA components related to the epileptic activity of each patient.

## 1.4 Electrical source imaging in epilepsy

The simple analysis of the scalp EEG and their potential maps can not provide information about the number, location and orientation of the deep generators and the highest activity of some scalp electrodes does not always demonstrate that the activities are located there. The inverse solution methods have just this scope [Fender, 1987, Brunet et al., 2011].

The electrical source imaging (ESI), performed by solving the associated inverse problem, can estimate the localization within the brain volume of the electric source(s) generating an IED that can be recorded with scalp electrodes [Scherg and Von Cramon, 1985, Liu et al., 1998, Babiloni et al., 2003, Michel et al., 2004]. ESI involves numerous scalp electrodes, hdEEG (Fig. 1.11), and realistic head models derived from structural MRI.

Unfortunately, the problem is fundamentally ill posed: there are infinitive possible generator locations and configurations that give the same potential distribution over the surface of a volume conductor [Nurez and Srinivasan, 2006]. In addition, a wrong model of individual geometry and conductivity of the brain and a limited number of EEG channels can influence the estimate of the sources. HdEEG technology was developed to enhance the poor spatial information content of the EEG activity. In this case the inverse solutions benefit from a large number of electrodes.

There are several source localization strategies to solve the inverse problem and to estimate the currents in the brain that produce a measured electric field. They can be grouped in two main approaches: the equivalent current dipole (ECD) model, where the signals are assumed to be generated by few focal sources and the linear distributed (LD) approaches, which consider that the dipoles are regularly distributed in cerebral volume according to a 3D grid and where all possible source locations are simultaneously considered [Michel et al., 2004, Sanei and Chambers, 2007, He et al., 2011].

The best fit solution differs from the source inversion algorithm used, so to remedy this problem many source algorithms were usually applied. The assumption about the number of electrodes, geometric and anatomical properties, conductive volume and focus characteristics can enhance the precision of the inverse solution [Michel et al., 2004, Michel and Murray, 2011].

Both the ECD and LD methods were widely used in epilepsy [Ebersole, 1994, Michel et al., 2004, Plummer et al., 2008, Brodbeck et al., 2009, Holmes et al., 2010, Brodbeck et al., 2011, Lai et al., 2011, Michel and Murray, 2011].

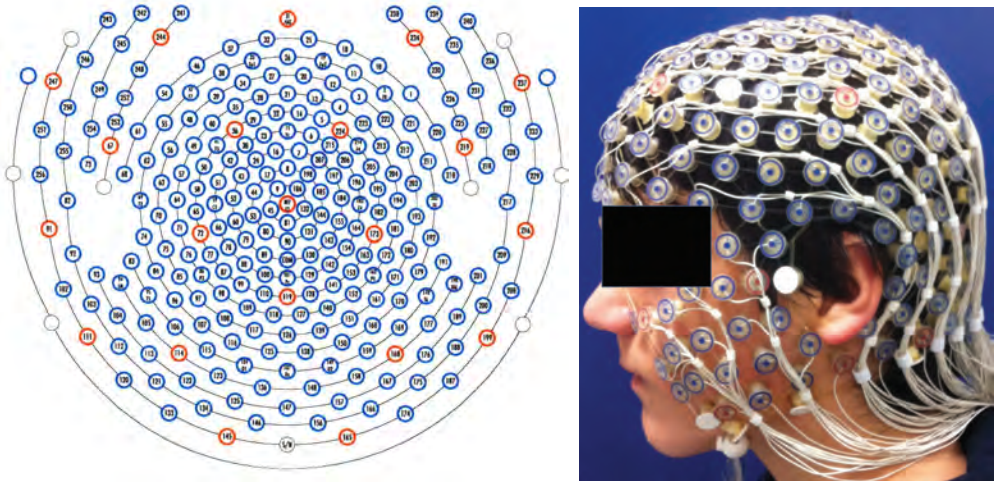

(a) (b)

**Figure 1.11:** (a) 256-channel HydroCel Geodesic Sensor Net. (b) HdEEG cap.

### 1.4.1 Equivalent current dipole model

According to the ECD approach, the sources are a number of discrete electric dipoles located in a 3D space, where each dipole is described by six parameters: three for its location, two for its orientation, and one for its amplitude. This approach assumes the underlying neuronal sources to be focal. The a priori assumption is that a small number of current sources in the brain can adequately model the surface EEG measurements. To obtain a unique solution, the number of unknown parameters has to be less than or equal to the number of independent measurements (*overdetermined*). To determine the best location of the sources, the squared error between the surface electric potential map generated by dipoles using a certain forward model and the actual measured potential map is calculated. Non linear optimization methods based on directed search algorithms are usually used to obtain all possible locations and orientations of the sources [Uutela et al., 1998].

The estimation of the inverse solution can be obtained by using: *dipole fitting methods* [Scherg, 1990], *linear constrained minimum variance* (LCMV) beamformers [Van Veen et al., 1997], the *multiple signal classification* (MUSIC) [Mosher and Leahy, 1998] with the scope to solve the problem of how

to choose the locations of a dipole model within a head volume that give the best projection onto the signal EEG space. ECD models have some limits in estimating in advance the number of dipoles and localizing extended sources, i.e. the center of mass of the cortical activity is localized, but the distribution and the extension of the activity remain to be determined [He et al., 2011].

### 1.4.2 Linear distributed approaches

When the number of dipole sources is not available, the 3D grid of solution points is considered as a possible location of a brain activity source. As the number of unknown dipole moments is much greater than the number of EEG electrodes, the LD approach is *underdetermined* [Hamalainen and Ilmoniemi, 1994, Sanei and Chambers, 2007].

#### The forward problem

The forward equation gives scalp electric potential differences as a function of current density and is expressed as:

$$\Phi = LJ, \tag{1.10}$$

where $\Phi$ is a $N \times 1$ known matrix of measurements of scalp electric potential differences, in which the coordinates of measurement points are given by Cartesian position vectors: $J = (j_1^T, j_2^T, \ldots, j_M^T)^T$ is a $(3M) \times 1$ matrix of current densities with $j_\beta^T = (j_{x\beta}, j_{y\beta}, j_{z\beta})^T$ and $\beta = 1 \ldots M$ at $M$ point within the brain volume and $L$, $N \times (3M)$ matrix, is a transfer matrix or *lead field matrix* and $\alpha^{th}$ row of the matrix is $(l_{\alpha 1}^T, l_{\alpha 2}^T, \ldots, l_{\alpha M}^T)$ with $l_{\alpha\beta} = (l_{x\alpha\beta}, l_{y\alpha\beta}, l_{z\alpha\beta})^T$.

#### The inverse problem

The inverse problem is used to convert measured electric potentials into current densities of the sources. The inverse problem is ill-posed because an infinity of different source configurations can produce the same EEG scalp distribution. For noise-free measurements the estimation of the dipole source configuration $\hat{J}$ is provided by the solution of the linear system:

$$\hat{J} = T\Phi, \tag{1.11}$$

where $\Phi$ is the measured EEG potential distribution and $T$, $(3M)\times N$ matrix, is the generalized inverse of the transfer function $L$ in which each jth column describes the potential distribution generated on the scalp electrodes by the jth unitary dipole. It must satisfy:

$$LT = H_N, \tag{1.12}$$

where $H_N$ is defined as $N \times N$ *average reference operator*:

$$H_N = I_N - \frac{1}{N} 1_N 1_N^T \tag{1.13}$$

with $I_N$ $N \times N$ identity matrix, and $1_N$ $N \times 1$ matrix of ones. This is a underdetermined linear system, in which the number of unknowns, dimension of the vector $\hat{J}$ is greater than the number of measurements $\Phi$ of about one order of magnitude. The relationship between the "true" $J$ and the estimated $\hat{J}$ is given by:

$$\hat{J} = RJ, \tag{1.14}$$

where $R = TL$ is the *resolution matrix*. If the matrix $R = I$, the current density can be estimate exactly. The solution of the Eq. 1.11 is given by computing pseudoinverse according to the following expressions:

$$T = W^{-1}L^T(LW^{-1}L^T)^+, \tag{1.15}$$

where $(LW^{-1}L^T)^+$ denotes the Moore-Penrose pseudoinverse of $(LW^{-1}L^T)$ and $W$ is $(3N)\times(3N)$ a symmetric weight matrix. Because the solution (Eq. 1.15) satisfies the measurement equation $\Phi = LJ$ exactly, the solution is not robust to the measurement contaminated by observation noise. To avoid this effect the following Tikhonov regularization parameter ($\alpha > 0$) can be considered:

$$T = W^{-1}L^T(LW^{-1}L^T + \alpha H)^+; \tag{1.16}$$

this parameter represents the relative weight between the data fitting error and prior terms.

The lead field matrix $L$ represents the contribution of each elementary dipole to the potential recorded on the scalp surface and requires a solution to the well-known Poisson equation [Steele, 1996], where the EEG potential differences $\Phi$ on the scalp surface $\partial\Omega$ are the manifestation of a source distribution $\rho(A/m^3)$ in the brain:

$$\nabla \cdot (\sigma \nabla \Phi) = -\rho, \tag{1.17}$$

where $\sigma$ is the conductivity of the head volume $(\Omega m)^{-1}$. Despite the possible use of a priori knowledge about the nature of the source distribution or overall physiology of the brain or the status of the subject, determining $\rho$ is an ill-posed problem [Kandaswamy et al., 2008].

### Particular inverse solutions

In the field of LD approaches, various imaging strategies were developed to obtain the "optimal" source estimation introducing biophysical and physiological constraints. Different source models attempt a total inversion as in the Eq. 1.15.

The first inverse solution of a distributed model was the *minimum norm least square* (MNLS) *solution* introduced in MEG by [Hamalainen and Ilmoniemi, 1984]. MNLS corresponds to Eq. 1.15 with $W = I_{(3M)}$.

Since the minimum norm solutions favored superficial sources and misplaced deep sources, a *weighted minimum-norm least squares* (WMN) solution was later developed to avoid the intrinsic bias toward superficial current [Pascual-Marqui et al., 1994, Gorodnitsky et al., 1995, Grave de Peralta and Gonzalez, 1998]. To assign larger weights to deeper sources the matrix $W$ in Eq. 1.15 is now expressed as:

$$W = \Omega \otimes I_3, \tag{1.18}$$

where $\otimes$ is the Kronecker product and $\Omega$ a $M \times M$ matrix which elements are: $\Omega_{\beta\beta} = \sqrt{\sum_{\alpha=1}^{N} l_{\alpha,\beta}^T l_{\alpha,\beta}}$, with $\beta = 1 \ldots M$. These solutions achieve lower localization error than the MNLS, but their errors are still significant.

Another algorithm widely used is the *low-resolution electromagnetic tomography algorithm* (LORETA) [Pascual-Marqui et al., 1994, 1999]. LORETA minimizes the squared norm of the Laplacian of the weighted 3D current-density vector field. It incorporates the "smoothness assumption" selecting the inverse solution of the measured data with the smoothest distribution in space [Ossenblok and Spekreijse, 1991]. In detail, the solution produces a image with a certain degree of dispersion of a point source conserving the location of maximal activity ($\mathrm{mA}/mm^3$). LORETA was widely used in the last years to localize the EEG generator [Park et al., 2002, Mulert et al., 2004]

and specifically the IED generator. The matrix $W$ in Eq. 1.15 is expressed as:

$$W = (\Omega \otimes I_3)B^T B(\Omega \otimes I_3), \tag{1.19}$$

where the matrix $B$ implements a discrete spatial Laplacian operator and its inverse $B^{-1}$ implements a discrete spatial smoothing operator. LORETA chooses a weighting matrix capable of depth compensation, but the solution obtained is rather smooth or in "low-resolution". LORETA shows to have more accuracy if there is a large number of active sources, and if no information is available about the position of the electrical generators [Mulert and Lemieux, 2010]. In addiction it has good accuracy in localizing deep sources. Development of LORETA are *standardized LORETA* (sLORETA [Pascual-Marqui, 2002]) and *exact LORETA* (eLORETA [Pascual-Marqui, 2007]). sLORETA has no localization bias in the presence of measurement noise and biological noise; eLORETA has exact, zero error localization in the presence of measurement and structured biological noise.

Another inverse solution is the *Local Autoregressive Average* (LAURA) [Grave de Peralta and Gonzalez, 2002]. LAURA selects the source configuration that better mimics the biophysical behavior of electric vector fields. The estimated activity at one point depends on the activity at neighboring points according to electromagnetic laws (i.e. the strength of the source declines with the inverse of the squared distance of the potential field). LORETA and LAURA are analogous to WMN but allows for additional constraints on the source covariance.

The *FOCal Underdetermined System Solver* (FOCUSS) repeats the procedure of the WMN method, recursively adjusting the weighting matrix until most elements of the solution become nearly zero, thus achieving a localized solution. However, the final solution depends on the assumed initial current distribution.

EPIFOCUS [Grave de Peralta and Gonzalez, 2002] shows a high spatial accuracy in cases where a single, dominant source with a certain spatial extent can be assumed [Lantz et al., 2001, 2003a,b, Michel et al., 2004]. The advantages of these LD approaches is that no prior specifications of the source model are necessary. Nonetheless the spatial resolution depends on several parameters (anatomical information, depth, orientation, and number of sensors).

### 1.4.3 Head models

The source imaging method requires a head model on which the inverse problem is solved and a finite number of solution points for which the electric current is estimated. There are two types of head models: simple spherical models and realistic head shape models. In the first case, the head is approximated to a sphere with uniform conductivity properties creating a non realistic model. In the second case, the MRI has to be available for the patient and the segmentation is necessary to extract the brain surface and the gray matter. In addition, the head surface has to be geometrically described and the electrode position (measured using 3D digitizers) has to be landed on the surface by using landmarks specially labeled in the MRI.

To describe the head surface many methods were proposed. The *boundary element method* (BEM) [Meijs et al., 1987] uses triangulations of the interface between compartments of equal isotropic conductivities as a geometric model; the *finite element method* (FEM) [Bertrand et al., 1991, Awada et al., 1997] includes the whole volume and allows to consider individual, anisotropic conductivities for each element and projective methods in which the unknown potential field is expanded in terms of basis functions [Gonzalez Andino et al., 1989, Mosher et al., 1999]. Because of the computational efforts the application of these methods in clinical studies is unfortunately not used. A widely used method is the approximation of the head as multiple concentric spheres and the solution of the inverse problem in these spheres (spherical head model with anatomical constraint [SMAC]) [Spinelli et al., 2000]. In detail, Spinelli et al. solve the inverse problem on a spherical head model, but defining the solution points on the brain limits and calculating the lead field matrix for this solution space. The MRI is mapped to the spherical system by transformation operations. Through this transformation the inverse problem can be calculated analytically by a spherical model, but the solutions are calculated for the MRI that constrains the inverse solution space according to the anatomy. The solution points generated by the integration of EEG source and MRI are restricted to the gray matter for each patient. The localization of the EEG source in the brain of the patient and not in a standard template is useful to compare the epileptic foci with the anatomical lesion and coregister the result with other imaging techniques.

### 1.4.4 Open problems in source localization

The main limitation of the source localization is that it can be biased by a low number of electrodes [Michel et al., 2004]: as explain in Fig. 1.12, increasing the number of electrodes (from 30 to 256 channels) the localization of the epileptic area can be improved.

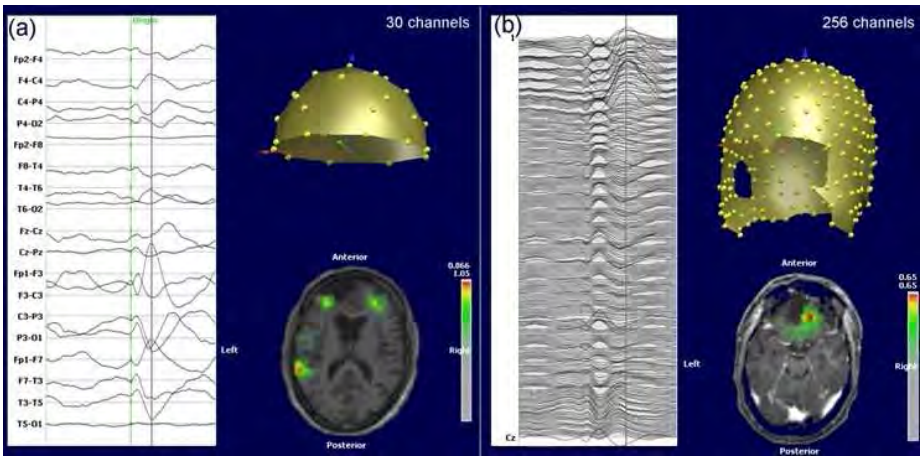


**Figure 1.12:** Difference between source localization on a epileptic patient using a) 30 channels, 10-20 system and b) 256-EGI channels.

The direct use of the source localization results for the presurgical evaluation can be a risk if no supplementary information is provided (e.g. EEG-fMRI, MEG and invasive EEG). In order to generate more specific spatial constraints and reduce the solution space, new approaches that combine fMRI and EEG were also applied. The BOLD activation clusters can be used as "seeding points" for the dipoles [Babiloni et al., 2003], even if a main limitation is that some electrical generators can not be observed in the fMRI analysis. In fact the cerebral activity can be found only with the EEG or only with the fMRI or with both. The first case can happen when a short lasting neural activity is not able to evoke a measurable hemodynamic response function. In the second case, a hemodynamic response could be evoked by a long-lasting neuronal activity but with a slow shift of the electrical baseline that can not be detected.

EEG source localization accuracy is also affected by many factors regarding the forward problem. First, a wide range of the conductivity values has been reported in literature and it is difficult to individualize these values and a more accurate volume conductor model is required for the accurate

source localization. Second, an accurate coordinate transformation is needed to register the electrodes coordinates with the head.

Chapter 2

# Automatic EEG Method

The evaluation of patients with epilepsy is one of the areas where EEG and fMRI integration has considerable clinical relevance for localizing the brain regions generating interictal epileptiform activity.

The conventional analysis of EEG-fMRI data is based on the visual identification of the IEDs on scalp EEG. The convolution of these EEG events, represented as stick functions, with a model of the fMRI response, i.e. the hemodynamic response function, provides the regressor for the GLM analysis of fMRI data. However, the conventional analysis is not automatic and suffers of subjectivity in IEDs classification.

Here, a fully automatic method is described using ICA followed by time-frequency analysis of the identified components to detect IED activity to be used as a regressor in GLM. The underlying rationale is that epileptic discharges correspond to high-frequency activity of synchronized neurons and they differ from that of normal brain activities and other noise background. EEG signal due to IED is reconstructed and its wavelet power is used as a regressor in GLM. The method was validated on simulated data and applied on real data set in [Formaggio et al., 2011].

## 2.1 Conventional approaches

In the study of spontaneous EEG activity without a task condition, EEG signal is used to derive the input for GLM. Several methods were proposed for this purpose. The first applications of EEG-fMRI addressed the study of subclinical epileptic discharges [Salek-Haddadi et al., 2003, Gotman et al., 2004, 2006]: in order to find regions of BOLD change linked to the discharges, these events were marked by visual inspection of the EEG data recorded in the scanner, to create a series of identical impulses functions (delta functions) to be convolved with a canonical HRF to obtain the regressor for GLM. This method was then applied in [Manganotti et al., 2008], while in a different study, [Formaggio et al., 2008b], EEG and fMRI were integrated by means of a correlation analysis. However, both the studies suffer of some limitations: in the former study a conventional approach based on visual identification was used, while, in the latter one, signals were simultaneously recorded but their correlation analysis was performed as if they were recorded in separate sessions.

## 2.2 Unconventional approaches

Recently, some authors proposed unconventional methods to analyzed EEG-fMRI data that allow to integrate the two signals, previously considered separately [Debener et al., 2006, Scheeringa et al., 2008, Ritter et al., 2009].

Debener et al. [2006] proposed the integration of EEG and fMRI recordings on a single-trial level in cognitive processing. ICA was used to decompose EEG signal into ICs and one or several ICs, that reflect task-related EEG activity, were used to obtain single-trial EEG amplitudes. Finally, convolution of these single-trial amplitudes with the HRF takes into account the temporal evolution of the fMRI signal.

Scheeringa et al. [2008] investigated in which areas the BOLD signal correlated with frontal theta power changes in a resting state condition applying ICA on band-pass filtered (2-9 Hz) EEG data. The component that best matched the mid-frontal scalp topography associated with the frontal theta rhythm was selected. A time-frequency analysis on this component was applied and the time course of the frequency bin was used with the highest overall power to create a regressor to model spontaneous fluctuations in frontal theta power.

Similarly, Ritter et al. [2009] acquired EEG-fMRI data in subjects that performed a bimanual motor task. Blind source separation was applied to the EEG data using Temporal Decorrelation Source separation (TDSep). EEG of motor channels (C3 and C4) and all TDSep sources were time-frequency decomposed using wavelet analysis to obtain power time courses for all frequencies. TDSep sources with alpha and beta spectral powers correlating best with the motor task were identified. For the EEG signal of C3 and C4 channels and TDSep sources, peak frequencies in alpha and beta were estimated, convolved with the HRF and used as regressors in the GLM.

Also in epilepsy new approaches were introduced to process EEG-fMRI data [Jann et al., 2008, Marques et al., 2009]. The ICA was used to decomposed the EEG signal and separate epileptiform activity from normal phycological brain activity and artifacts. Components concordant with interictal activity were selected by a neurophysiologist and the model based on those components was then used as regressor.

Differently, LeVan et al. [2010] decomposed by ICA the fMRI data and used a deconvolution method to identified IED-related components by detecting time courses with a significant HRF time-locked to the IEDs. Individual HRF amplitudes were then calculated for each IED. Components with a significant HRF/IED amplitude correlation were compared to the presumed epileptogenic focus in the GLM analysis.

Recently, a new approach was purposed by [Grouiller et al., 2011] to understand why many studies of EEG-fMRI coregistration showed an absence of IED during the acquisition. An average of IED recorded outside the magnet was correlated with the EEG recorded inside frame by frame and the time course of the correlation coefficient was used as regressor for the GLM. In patients with inconclusive conventional results, BOLD activations were obtained with the new method and then validated with intracranial EEG and/or resection area in patients who were seizure free after surgery.

### 2.2.1 Wavelet analysis in EEG-fMRI coregistration

Our first attempt to integrate the EEG power as regressor in the GLM analysis is described in [Storti et al., 2010]. In this study EEG-fMRI was used to determine the possible correlation between topographical movement-related EEG changes in brain oscillatory activity recorded from EEG electrodes over the scalp and fMRI cortical responses in healthy subjects over motor areas

during finger movement. EEG were recorded in 12 subjects during eyes-closed condition inside a 3 T MR scanner. For EEG data analysis, a time-frequency approach was applied to measure time by varying the energy in a signal at a given frequency band by the convolution of the EEG signal with a wavelet family in the alpha and beta bands. The correlation between the BOLD signal associated with the EEG regressor provides that sensory motor region is a source of the EEG.

EEG activity recorded from the human brain at rest oscillates in various frequency bands including theta ($4-7$ Hz), alpha ($8-12$ Hz), beta ($13-30$ Hz) and gamma ($30-50$ Hz) ranges. Movement preparation typically suppresses, with a decrease in power, the cortical oscillations in both alpha and beta rhythms starting more than 1 s before the onset of finger or hand movement over sensorimotor areas [Pfurtscheller and Aranibar, 1979, Leocani et al., 1997, Erbil and Ungan, 2007] (Fig. 2.1). Upon movement completion, the EEG recording shows an alpha event-related desynchronization (ERD) followed a brief "rebound" beta event-related synchronization (ERS) over various cortical regions [Salmelin and Hari, 1994]. ERD indicates oscillations in cortical activation and ERS reflects a cortical idling state [Pfurtscheller, 1992]. These pre-movement and post-movement power changes correspond to the somatotopic organization of the primary sensorimotor cortex. The regional activation of cortical areas with a decrease in power has been associated with the term "EEG desynchronization", whereas brain activation produces spontaneous synchronization of fast rhythms with high amplitudes [Steriade and Amzica, 1996].

In Storti et al. [2010] topographical and temporal changes were investigated in brain oscillatory activities correlated to the BOLD activity recorded during an EEG-fMRI coregistration. To do so EEG signal was recorded simultaneously to a 3T fMRI signal while healthy subjects inside the scanner did a hand motor task. To calculate the spectral EEG response to hand movement, wavelet analysis was used, choosing the best compromise between temporal and frequency resolution. To detect the instantaneous interaction between EEG recordings acquired under two experimental conditions (at rest and during active movement) a continuous Morlet wavelet transformation (CMT) was applied. After this, the wavelet energy was used as regressor of GLM in fMRI analysis.

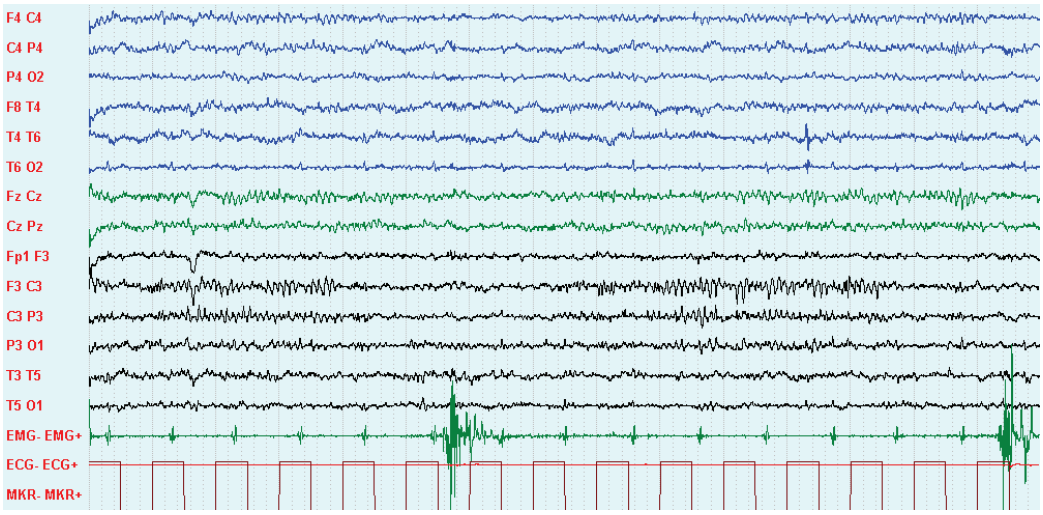


**Figure 2.1:** EEG signal acquired during a finger movement. The signal was pass band-filtered between $1.6-30$ Hz, gain $= 150\ \mu V/cm$. The EMG signal (green) has a gain of 200 $\mu V/cm$. The time window is of 15 s.

### Subjects and experimental paradigm

Data were recorded in twelve healthy subjects (seven men and five women), whose ages ranged from 21 to 34 years (mean: 32.08, standard deviation [SD]: 5.76). All subjects were right-handed. While lying inside the MRI chamber the subjects performed a motor task. This task consisted of synchronous opening and closing of the right hand at a frequency of 1 Hz (metronome paced) for 26.1 s alternating with rest periods of equal duration. During fMRI acquisition, 100 volumes of 2610 ms were acquired, alternating five activations and five control cycles (rest), resulting in about 5 min of EPI recording. Five epochs of EEG data starting one volume (2610 ms) before the active condition and one volume consecutive (epochs of 2*TR) were extracted.

### EEG data acquisition and analysis

The EEG was acquired using a MR compatible EEG amplifier (SD MRI 32, Micromed, Treviso, Italy) and a cap providing 32 Ag/AgCl electrodes positioned according to a 10/20 system (impedance was kept below 10 $k\Omega$). To remove pulse and movement artifacts during scanning two of these electrodes were used to record the ECG and electromyogram (EMG). The EMG electrode was placed on the right abductor pollicis brevis (APB) muscle. The

reference was placed anterior to Fz, and the ground posterior to Fz as in other studies [Formaggio et al., 2008a,b, Manganotti et al., 2008] using the same system. To ensure subjects' safety, the wires were carefully arranged to avoid loops and physical contact with the subject. To minimize the variability in the EEG artifacts due to the MR sequence and avoid wire movement caused by mechanical vibration the wires rested on foam pads. EEG data were acquired at the rate of 1024 Hz using the software package SystemPlus (Micromed, Treviso, Italy). To avoid saturation, the EEG amplifier had a resolution of 22 bits with a range of ± 25.6 mV. An anti-aliasing hardware band-pass filter was applied with a bandwidth between 0.15 and 269.5 Hz.

The EEG analysis was performed by using functions implemented in Matlab 7 (The Mathworks Inc., Natick, MA) (Fig. 2.2a). The EEG artifact induced by the magnetic field gradient was digitally removed off-line using an adaptive filter (Micromed). The EEG artifact associated with pulsatile blood flow, BCG, was also digitally removed offline using a simple averaging procedure [Allen et al., 1998]. Reference-free recordings were then obtained by calculating the local average reference using the software EEGLAB, a Matlab toolbox [Delorme and Makeig, 2004]. A notch filter (50 Hz) and a baseline correction were also applied to all channels. Two subjects' data were excluded from the analysis owing to poor quality EEG recordings. Five epochs of EEG data starting one volume (2610 ms) before the active condition and one volume consecutive (epochs of 2*TR) were extracted. EEG epochs with ocular, muscular and other types of artifact were preliminarily identified and then rejected.

Time-frequency data were assessed using wavelet-based analysis. To divide the continuous-time function into wavelets a CMT was used. Unlike Fourier transform, CMT constructs a time-frequency representation of a signal that offers a time and frequency localization. The Morlet $\psi(t)$ is a function of time t consisting of a complex exponential modulated by a Gaussian envelope. It has a Gaussian distribution in both time and frequency domains. This "mother" wavelet was used to build a set of daughter wavelets by translating $\psi(t)$ in time, and by dilating or contracting $\psi(t)$. The operation, served to adjust the mean frequency and also the spread of the daughter wavelet.

The wavelet transform is the inner-product of the wavelet function with the signal s(t). A family of Morlet wavelets was first constructed at 1 Hz frequency intervals ranging from 8 to 30 Hz. Each wavelet has a Gaussian distribution in the time (SD: $\sigma_t$) and frequency domains (SD: $\sigma_f$) around the

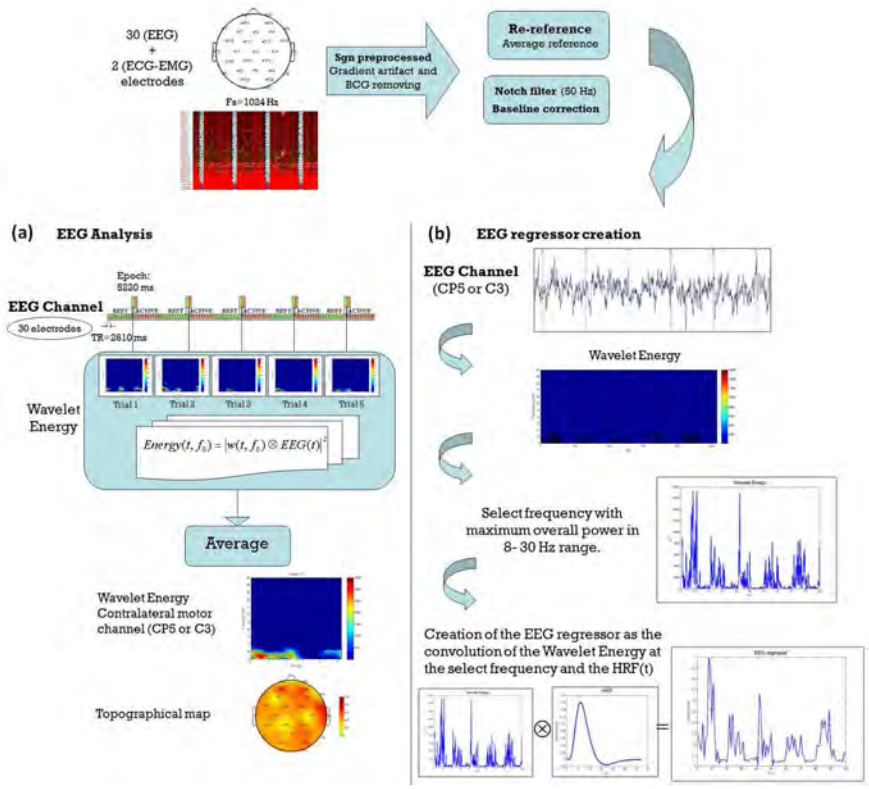


**Figure 2.2:** Schematic representation of the different steps in EEG analysis (a) and in EEG-fMRI analysis (b).

center frequency $f_0$ [Tallon-Baudry et al., 1997]:

$$\omega(t, f_0) = (\sigma_t\sqrt{\pi})^{-1/2} exp\left(\frac{-t^2}{2\sigma_t^2}\right) exp(2i\pi f_0 t) \tag{2.1}$$

with

$$\sigma_f = \frac{1}{2\pi\sigma_t}. \tag{2.2}$$

This function depends on a parameter, the number of oscillations $f_0/\sigma_f$; which has to be chosen by the user. Our wavelet family was computed using a ratio of 20 oscillations. To compute the time varying energy in a frequency band the recorded signal s(t) was then convolved with the corresponding set of functions generated by the mother wavelet. The convolution can be computed by using fast Fourier transform (FFT). Normally, the output is a

real function except when the mother wavelet is complex. The power spectrum calculated from the result of convolution can be represented by [Tallon-Baudry et al., 1997]:

$$E(t, f_0) = |\omega(t, f_0) \otimes s(t)|^2 \tag{2.3}$$

The wavelet energy for all five epochs and for all 30-EEG electrodes was computed using Matlab and then these five epochs of 5220 ms were averaged for further processing. At the end the wavelet trend for EEG recording channels selected for each subject (CP5 or C3) was examined. These channels were chosen because they were over the sensorimotor area contralateral to the movement. The additional topographic plots were constructed with the EEGLAB toolbox. The topographical maps allowed us to verify the energy distribution for all channels on the whole scalp at one specific time-point (under the two conditions). The time-point from the individual subject's scalogram was chosen and it differed for each subject. Because movement preparation and execution produce ERD over the sensorimotor area at 10 and 20 Hz [Leocani et al., 1997], the frequency bands chosen for these maps were the upper alpha (10-12 Hz) and beta (13-30 Hz) for the two conditions. The grand-average scalogram and the grand mean topographic maps were also computed for the ten subjects whose data were analyzed.

A two-ways ANOVA was computed in Matlab within subjects and across subjects for alpha and beta bands both in the contralateral and ipsilateral hemisphere. The two factors are the condition (rest: 0-2610 ms versus active: 2610-5220 ms) and the subject (ten subjects for the contralateral hemisphere and three for the ipsilateral one). The electrodes providing informative data over the region of activation in the contralateral motor area were CP5 or C3 and T4 in the ipsilateral side. For the statistical test, a p value of $< 0.05$ was considered significant. Using EEG-fMRI analysis, described in the paragraph "Combining EEG-fMRI signals", activation of the ipsilateral sensory motor area (SM1) was obtained only in three subjects. For this reason, the statistical comparison between the ipsilateral and contralateral hemisphere was not performed.

### fMRI data acquisition and analysis

MRI data were acquired on a 3T MR scanner (MAGNETOM Allegra, Siemens, Erlangen, Germany) equipped with EPI capability, a standard tran-

sient/receive head coil and foam cushions to minimize head movement. For each subject a T1-weighted anatomical scan was acquired (160 slices, TR = 2300 ms, time echo (TE) = 3 ms; scanning matrix 256 × 256, field of view (FOV) = 192 × 192; slice thickness of 1 mm; sagittal slice orientation). Functional images were acquired with a T2-weighted EPI sequence (36 slices, TR = 2600 ms, TE = 30 ms, 64 × 64 matrix, FOV = 192 × 192, slice thickness of 3 mm; voxel size = 3 × 3 × 3 mm, axial slice orientation). In the protocol, 100 volumes were acquired, alternating five activations and five control cycles. At the onset of each fMRI acquisition, the scanner emitted a trigger signal that was recorded by the EEG system and used as a volume marker.

The functional data were analyzed using BrainVoyager (QX 1.9, Brain Innovation, Maastricht, The Netherlands). Preprocessing of functional MRI included three-dimensional motion correction, slice scan time correction (linear interpolation), linear trend removal by temporal high pass filtering (three cycles in a time course) and transformation into Talairach coordinate space [Talairach and Tournoux, 1988]. Neither spatial nor temporal smoothing was used. In each subject, activated voxels were identified with a single-subject GLM approach for time series data [Friston et al., 1995]. To account for the hemodynamic delay, the boxcar waveform representing the rest and task conditions was convolved with an empirical HRF [Friston et al., 1998]. Brain activation was detected by comparing the signal intensity of task performance images (ON) with that of resting images (OFF) based on the changes in local BOLD signals. Images acquired during the ON condition were compared with images acquired from the same location during the OFF condition on a pixel-to-pixel basis with Student t-test. Z-score maps representing brain activation were generated. The results were displayed on parametric statistical maps in which the pixel z value is expressed on a colorimetric scale. Individual statistical maps were thresholded at $p < 0.05$ (corrected for multiple comparisons: Bonferroni). The statistical functional maps (z maps) were then superimposed on the respective structural scans to localize significantly activated areas.

In addition to individual subject analysis, a fixed-effect analysis (ten subjects) was used to calculate a GLM for the entire group of subjects. Group activation maps were thresholded at $p < 0.05$ (Bonferroni-corrected) and were superimposed on the (Talairach-transformed) structural scan for a representative subject.

### Combining EEG-fMRI signals

A time-frequency analysis of power was applied on the time series of the selected channel (Cp5 or C3). For the selected channel the time course of one frequency bin was used to form a regressor. This was done by selecting from the frequency bins, centered around 8 and 30 Hz, the one with the maximal power (alpha rhythm). The maximum was based on the average power in these frequency bins over the total recording session. The entire time series for the selected frequency bin ($f_0$) was extracted to form the basis for the regressor.

For the correlation with the fMRI data, the regressor $E(t, f_0)$ was convolved with the canonical two gamma HRF provided by Brain Voyager and down-sampled to the temporal resolution of the fMRI data (TR = 2.61 s). This signal was used as predictor for the BOLD signal in fMRI analysis (Fig. 2.2b). As single subject regressor, the waveforms represented by wavelet energy fluctuations along the movement protocol were generated and subsequently the regressor was used to predict the BOLD response that have been acquired currently from the same subject [Debener et al., 2006]. Single subject activation maps were calculated by using the voxel-wise student's t-test to identify activated voxels (p-value $\leq 0.002$). In addition a fixed-effect group analysis was applied ($p \leq 0.002$).

## Results

### fMRI results

The distribution of BOLD activations in fMRI recording during hand movement was similar to that described in the literature. fMRI images showed significant BOLD activation ($p < 0.05$, Bonferroni) in the supplementary motor area (SMA), and contralateral and ipsilateral SM1. These activations were statistically consistent ($p < 0.05$, Bonferroni) across all the subjects.

In the single subject analysis, activation clusters in the contralateral SM1 were consistent for all subjects. In subjects Nos. 1, 2, 3, 4, 5, 7, 8, and 9 GLM analysis showed wide activation in SMA. In subjects Nos. 1, 3, 5, 7, and 9 the statistical t-map showed a significant activation clusters also in ipsilateral SM1. Subjects Nos. 6 and 10 had no activation in ipsilateral SM1 and in SMA (see fMRI maps, Figs. 2.3 and 2.4).

In the group analysis (fixed effect analysis), fMRI showed significant

BOLD activation ($p < 0.05$, Bonferroni) in SMA, and SM1 and also in ipsilateral cerebellum (Fig. 2.5).

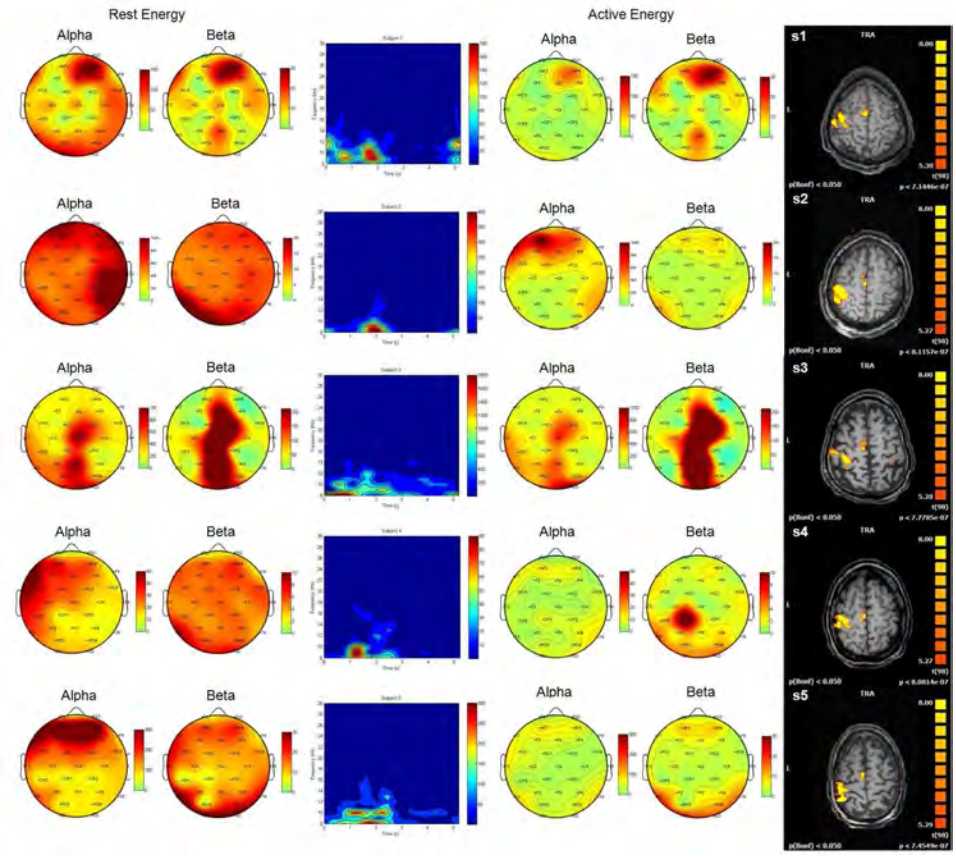


**Figure 2.3:** Individual time-frequency plots for subjects 1-5 (blue areas indicate low power values whereas red areas show high power) and their alpha (10-12 Hz) and beta (12-30 Hz) topographies obtained under the two experimental conditions: at rest and during active movement. On the right side the transaxial images show activation of the SM1 in the left hemisphere for each subject (images in neurological convention). The colorbar shows the z score scale.

### EEG results

EEG results generally agreed with the pattern of BOLD activation in the contralateral and ipsilateral motor areas as reported in an our previous study

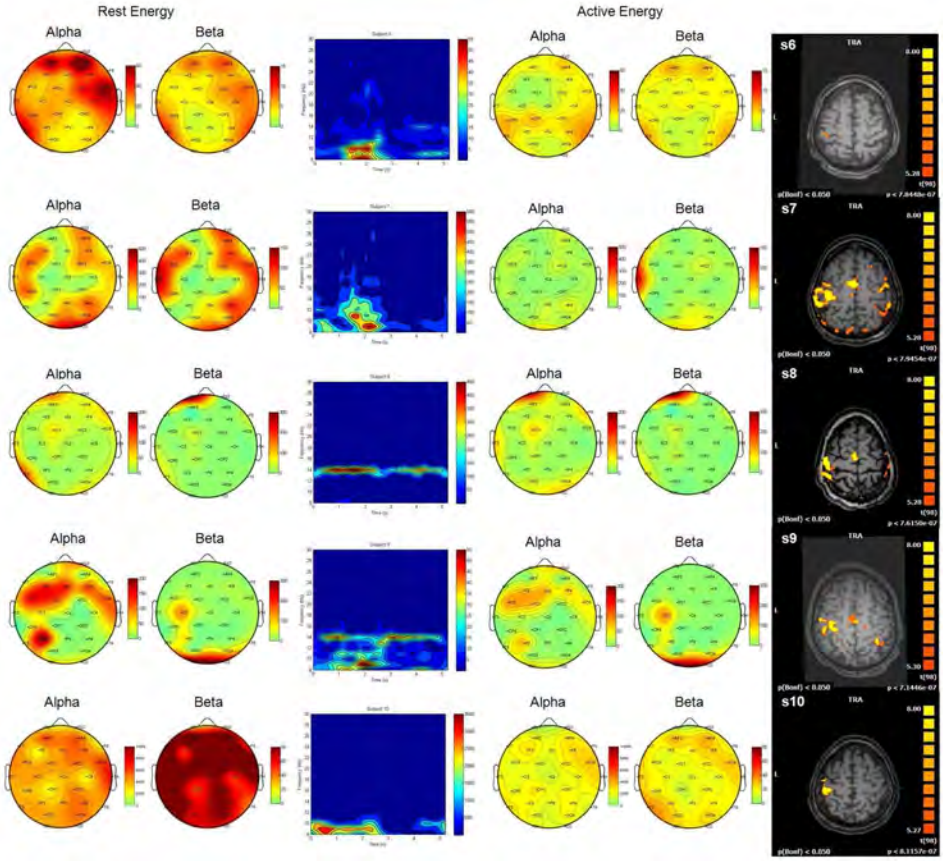


**Figure 2.4:** Individual time-frequency plots for the subjects 6-10 (blue areas indicate low power values whereas red areas show high power) and their alpha (10-12 Hz) and beta (12-30 Hz) topographies obtained under the two experimental conditions: at rest and during active movement. The transaxial images on the right show activation of the SMI in the left hemisphere for each subject (images in neurological convention). The colorbar shows the z score scale.

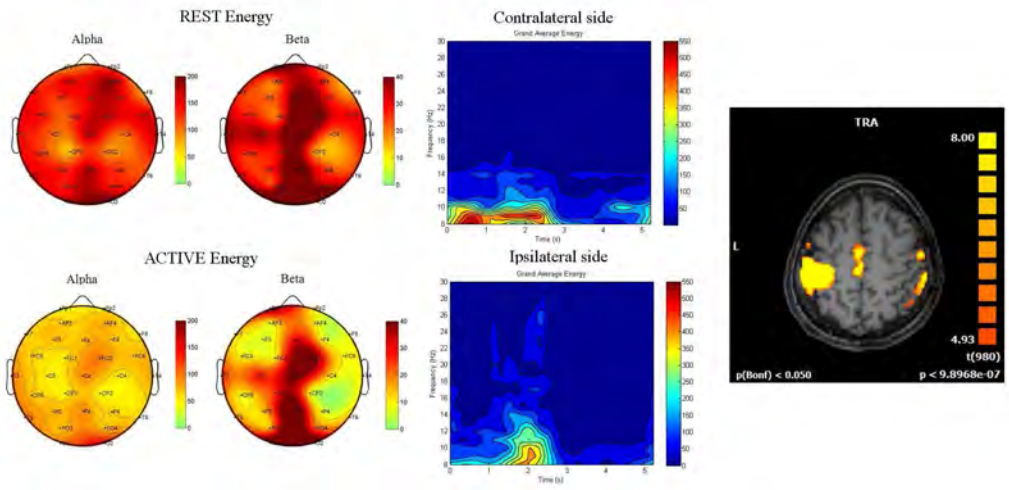


**Figure 2.5:** In the center, grand-average time-frequency energy plot for the ten subjects recorded from EEG electrodes over the contralateral sensorimotor cortex, CP5 or C3 (top wavelet image) and over the ipsilateral sensorimotor cortex, T4 (bottom wavelet image) in the rest condition (from 0 to 2610 ms) and during active movement (from 2610 to 5220 ms). On the left, alpha (10-12 Hz) and beta (12-30 Hz) topographies from the rest condition (t = 1300 ms) and from the active condition (3900 ms). On the right fMRI group analysis (neurological convention).

[Formaggio et al., 2008b]. The individual EEG data showed that the motor task invariably activated the contralateral central-temporal electrodes over the SM1. The scalograms showed a common trend, although temporal dynamics differed, and energy values, especially those in the alpha range, changed rapidly from rest to the active condition (Figs. 2.3 and 2.4). Changes in time-frequency energy from rest to active condition in the alpha (10-12 Hz) and beta (13-30 Hz) frequency bands were prominent over the central parietal and central temporal areas contralateral to the movement (see the topographical maps, Figs. 2.3 and 2.4). Alpha maps showed a decrease in energy distribution from rest to the active condition located especially in the electrodes over the sensorimotor area contralateral to the movement.

In beta maps the effect was less perceptible over the electrodes of interest whereas it was topographically more restricted to temporal and posterior areas; except for subjects Nos. 2, 7, 8, and 10 in whom there was a significant difference between conditions in CP5 and C3. Despite the technical problems

related to filtering and MRI artifacts, in all subjects central temporal electrodes were especially sensitive to the EEG changes and were close to the activated cortical areas corresponding to Brodmann areas 4 and 3, 1 and 2 of the hand representation over the cortex.

The most clearly visible feature in the contralateral grand-averaged scalogram was that alpha and beta energy decreased from rest to active condition (0 - 2610 vs 2610 - 5220 ms) (Fig. 2.5). Associated with the hand movement there was an increase of energy over the contralateral electrodes (CP5 and C3, half time of rest block), while in t = 3900 ms (half time of active block) the energy decreased significantly in alpha band especially over contralateral and ipsilateral electrodes as represented in the topographical maps.

In the contralateral hemisphere the alpha and beta energy for CP5 or C3 differed significantly both across subjects (alpha: $F = 20.01$, $df = 9$, $p < 0.05$; beta: $F = 7.69$, $df = 9$, $p < 0.05$) and within subjects (alpha: $F = 8.37$, $df = 1$, $p < 0.05$; beta: $F = 12.11$, $df = 1$, $p < 0.05$). In the ipsilateral hemisphere the alpha energy for T4 differed significantly in alpha and beta band (Across subjects. Alpha: $F = 5.95$, $df = 2$, $p < 0.05$; Beta: $F = 32.56$, $df = 2$, $p < 0.05$; Within subjects. Alpha: $F = 14.66$, $df = 1$, $p < 0.05$; Beta: $F = 26.2$, $df = 1$, $p < 0.05$).

As shown in the statistical results, during the movement an asymmetry in the modulation of EEG oscillations with an energy decrease for the active versus the rest condition was obtained, mostly on the left hemisphere contralateral to the finger abduction. This asymmetry is only a trend because it was not possible to compare contralateral vs ipsilateral side using a statistical analysis due to the low number of subjects (3) which activated ipsilateral SM1 in EEG-fMRI analysis.

### EEG-fMRI results

Alpha rhythm was chosen since it was most intensely modulated by motor task and since it was identified over both hemispheres. As expected, alpha rhythm was suppressed during hand movement and reappeared during rest; the power of this rhythm is inversely correlated to the motor task. As a consequence, voxels that are activated during motor task will tend to be deactivated during periods of desynchronization. The negative correlations between alpha rhythm and BOLD signal are shown in Fig. 2.6 with the respective wavelet time courses. The fMRI maps based on alpha energy re-

gressor are very similar to the maps obtained with the previous fMRI block analysis.

Confirming earlier findings during fMRI block analysis, eight out of ten subjects showed a negative correlation between the BOLD signal and the wavelet energy in motor areas. In subjects Nos. 1, 2, 3, 4, and 7 GLM analysis showed activation in SMA. In subjects Nos. 2, 5, and 7 the statistical z-map showed a significant activation clusters also in ipsilateral SM1. Subjects Nos. 6 and 10 had no activation in ipsilateral SM1 and in SMA. The number of voxels of the region of interest in each subject is reported in Table 2.1.

**Table 2.1:** Number of voxels of the region of interest in each subject in EEG-fMRI analysis. Ipsilateral (i) and contralateral (c) refer to the hemispheric side with respect to the hand moved.

| **Subject** | **No. of voxels** | | |
|---|---|---|---|
| | **SM1c** | **SM1i** | **SMA** |
| **1** | 555 | 0 | 179 |
| **2** | 4591 | 38 | 152 |
| **3** | 957 | 0 | 144 |
| **4** | 7072 | 0 | 367 |
| **5** | 195 | 52 | 17 |
| **6** | 553 | 0 | 0 |
| **7** | 6522 | 895 | 1251 |
| **8** | 0 | 0 | 0 |
| **9** | 0 | 0 | 0 |
| **10** | 735 | 0 | 0 |

In the group analysis (fixed effect analysis), fMRI showed significant BOLD activation ($p < 0.002$) in SMA, and contralateral SM1 and also in ipsilateral cerebellum (Fig. 2.6).

### Discussion

Using combined EEG-fMRI, useful new information was obtained on the temporal and topographical changes in brain oscillatory activity in the alpha and beta frequency bands during voluntary movement. Current knowledge on the sites of BOLD activity was also extended as the possible sources generating these rhythms. While healthy subjects did the motor task inside the scanner, EEG recordings showed a movement-related alpha and beta rhythm desynchronization over the bilateral sensorimotor area predominantly on the

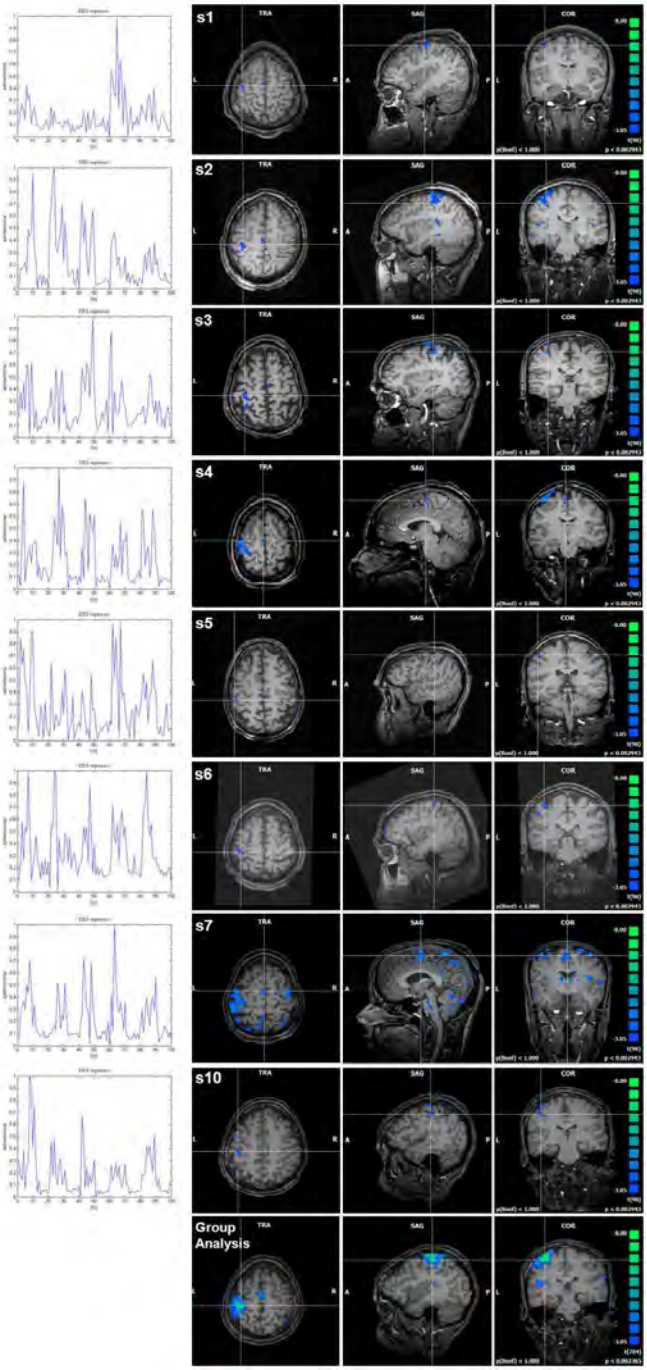


**Figure 2.6:** EEG-fMRI results: single subject ( BOLD activation in 8 out of 10 subjects) and group analysis. The colorbar on the right indicates the statistical z scores. The wavelet time course, on the left, was strongly anti-correlated with the motor areas.

side contralateral to the movement. Despite the technical problems related to filtering and MRI artifacts we were able to detect brain oscillatory changes during hand movements and map this activity.

In this study, the EEG-fMRI method based on CMT, used for data analysis, provided excellent temporal localization, more accurate than that obtained by analyzing frequency alone. A time-frequency representation based on CMT of EEG data was used to identify stimulus-induced amplitude modulations in oscillatory activities.

When fMRI showed BOLD activation in sensorimotor areas energy in the alpha and beta bands of the EEG signal decreased significantly. Despite using a 3T MR scanner, which produces a large BCG, we could easily detect the temporal energy changes in oscillatory activity during movement. These findings are supported by studies showing that BOLD activity correlates with activity in the alpha and beta EEG frequency bands [Babiloni et al., 2005, Brookes et al., 2005, Formaggio et al., 2008b]. A study, combining fMRI and EEG during finger abduction [Parkes et al., 2006], reported that the BOLD activity in the postcentral sulcus is related to post-movement beta rebound. Unlike Parkes et al., in this study, EEG recordings showed reliable, consistent alpha and beta suppression during the finger movements in the fMRI recording. As documented by the topographical maps, in most subjects a reliable suppression of both rhythms correlating with the BOLD activation was noted.

The wavelet-based analysis had several other advantages. It clearly showed the pattern of energy development while two fMRI volumes (during the two conditions) were acquired and distinguished the temporal changes over a motor electrode on the contralateral and ipsilateral sides. A decrease of wavelet energy could be the result of the involvement of a larger neural network or cell assemblies in information processing. These findings could suggest that activity in primary sensorimotor areas increases when the motor task begins and decreases when it ends. The increase in BOLD signal with a decrease in EEG alpha and beta energy mainly in the contralateral motor areas suggests that the mean rate of synaptic activity measured at baseline increased in the local neuronal population during the movement. Using a multitrial wavelet analysis of EEG, the temporally components related to the finger movement were previously studied, then the information derived from EEG recordings were used to inform the analysis of fMRI data recorded for the same motor task. The localization of the alpha band generators using EEG-fMRI did not

require assumptions on the number of dipoles, their geometry and spatio-temporal smoothness. So using this technique we were able to identify the cortical regions that temporally correlated with the EEG. The correlation between the BOLD signal associated with the EEG regressor provides further evidence that sensory motor region is a source of the EEG.

Despite the filtering, topographic maps are probably sensitive to MRI artifacts and different MRI effects may affect the EEG maps. Gradient effects can induce a diffuse EEG signal increase that may mask slight EEG changes during a motor task [Menon and Crottaz-Herbette, 2005]. Hand movements themselves could induce slow activity over the scalp electrodes that is more evident under a gradient effect. Generally, because the BCG artifact becomes larger from occipital to the frontal sites [Allen et al., 1998] it could have affected responses in frontal regions in most of our subjects. After we subtracted MRI artifacts the brain oscillatory activity nevertheless persisted during both experimental conditions, rest and active movement.

Overall our findings in this study and our previous study [Formaggio et al., 2008b] suggest that investigating the correlation between brain oscillatory activities and BOLD activity recorded during fMRI recording is a suitable method for studying movement in healthy subjects and in patients. Using combined EEG-fMRI in healthy subjects is an important research tool that provides new information on the neural activity underlying the hemodynamic changes. The results of EEG-fMRI combination for the evaluation of the underlying neural correlates were reported in terms of fine functional cortical topography (fMRI) and fine time course of the activation (EEG) and related modulation of alpha rhythms. These findings must nevertheless be interpreted carefully because the fMRI signal is an indirect measure of synaptic activities or action potentials from cortical neurons.

During EEG signal processing, quantifying wavelet energy - a measure indicating the degree of synchronization in brain rhythm generators - helps to clarify possible sources of movement-related brain activation. Using the time course of the oscillatory activity, information on the relationship between EEG recordings and the fMRI results was provided. This relationship is quantitatively described by fMRI activation maps, obtained using a regression analysis. This new approach enables the study of dynamic properties of motor processing relating to hemodynamic response.

In healthy subjects, fMRI topographic maps closely correlate with EEG energy findings. In the study of functional deficits, the wavelet-based tech-

nique could help to analyze brain responses more reliably and may also tell us more about their dynamics.

## 2.3 Automatic EEG method in epilepsy

A similar approach was adopted to develop an automatic method for data analysis of epileptic patients. Differently from the above method, the approach was adapted to study the low frequency instead of high frequency EEG and ICA decomposition was introduced to detect IED activity to be used as a parametric modulator in fMRI analysis [Formaggio et al., 2011]. The method consists of four steps, as shown in Fig. 2.7:

**1. Selection of components.** The relationship between EEG recorded at sampling time from $M$ positions $\mathbf{EEG}(t) = [EEG_1(t), \ldots, EEG_M(t)]^T$ (with $\mathbf{EEG} \in \Re^{M\times 1}$) and $N$ independent components $\mathbf{s}(t) = [s_1(t), \ldots, \mathbf{s}_N(t)]^T$ (with $\mathbf{s} \in \Re^{N\times 1}$) can be written as:

$$\mathbf{EEG}(t) = \mathbf{A} \cdot \mathbf{s}(t) \tag{2.4}$$

where $\mathbf{A}$ is the mixing matrix (with $\mathbf{A} \in \Re^{M\times N}$). Assuming that the number of sources ($N$) is equal to the number of recorded signals ($M$), the independent components $\mathbf{y}(t) = [y_1(t), \ldots, y_N(t)]^T]$ (with $\mathbf{y} \in \Re^{N\times 1}$), representing a good approximation of sources, were obtained by:

$$\mathbf{y}(t) = \mathbf{W} \cdot \mathbf{EEG}(t) \tag{2.5}$$

where $\mathbf{W} = \mathbf{A}^{-1}$. Each component was described on the basis of a spatial pattern (map), representing its spatial distribution, and of a time course, representing its temporal evolution. Components related to IED were selected based on their power because, typically, IEDs activity is higher in amplitude than background activity and has high power. We used a time-frequency representation by wavelet analysis because of the non-stationarity of the signal. The time-frequency power of each component was then averaged along time, and the frequency value with the maximal power was evidenced. These values were represented in a histogram, and components that exceeded mean value ±SD were selected as IED components.

**2. Reconstruction of EEG signal.** After the IED components have been selected, they were back projected to obtain the reconstructed EEG signal

due to interictal epileptiform discharges, $\mathbf{IED}(t)$ according to:

$$\mathbf{IED}(t) = \mathbf{W}^{-1}\mathbf{Z}\mathbf{y}(t) \tag{2.6}$$

where $\mathbf{Z}$ is a diagonal matrix having $z_{ii}$ element equal to 1 if the i-th component was selected, to 0 otherwise. In this way, the unselected components were eliminated from the EEG recordings, and the reconstruction of the EEG signal due to IED was completed.

**3. Selection of channel and wavelet analysis.** To automate the selection of the EEG channel to be used for building the EEG regressor, we compared the reconstructed EEG signal (IED) with the original one (EEG) by computing the cross correlation between them. The IED channel with the highest correlation coefficient was selected, and its time-frequency power spectrum was estimated using wavelet analysis. For each epoch (TR), its maximum value was evaluated and used to build the power signal $P(t)$, i.e. a series of impulses at times of maxima with amplitude equal to the maxima values of power. The number of impulses in $P(t)$ obviously corresponds to the number of volumes.

**4. Construction of EEG regressor.** The power time series $P(t)$ was convolved with the HRF:

$$\mathbf{EEGreg}(t) = \int_0^\infty P(\tau)HRF(t-\tau)d\tau \tag{2.7}$$

**EEGreg** was used as a predictor for the BOLD signal in GLM analysis.

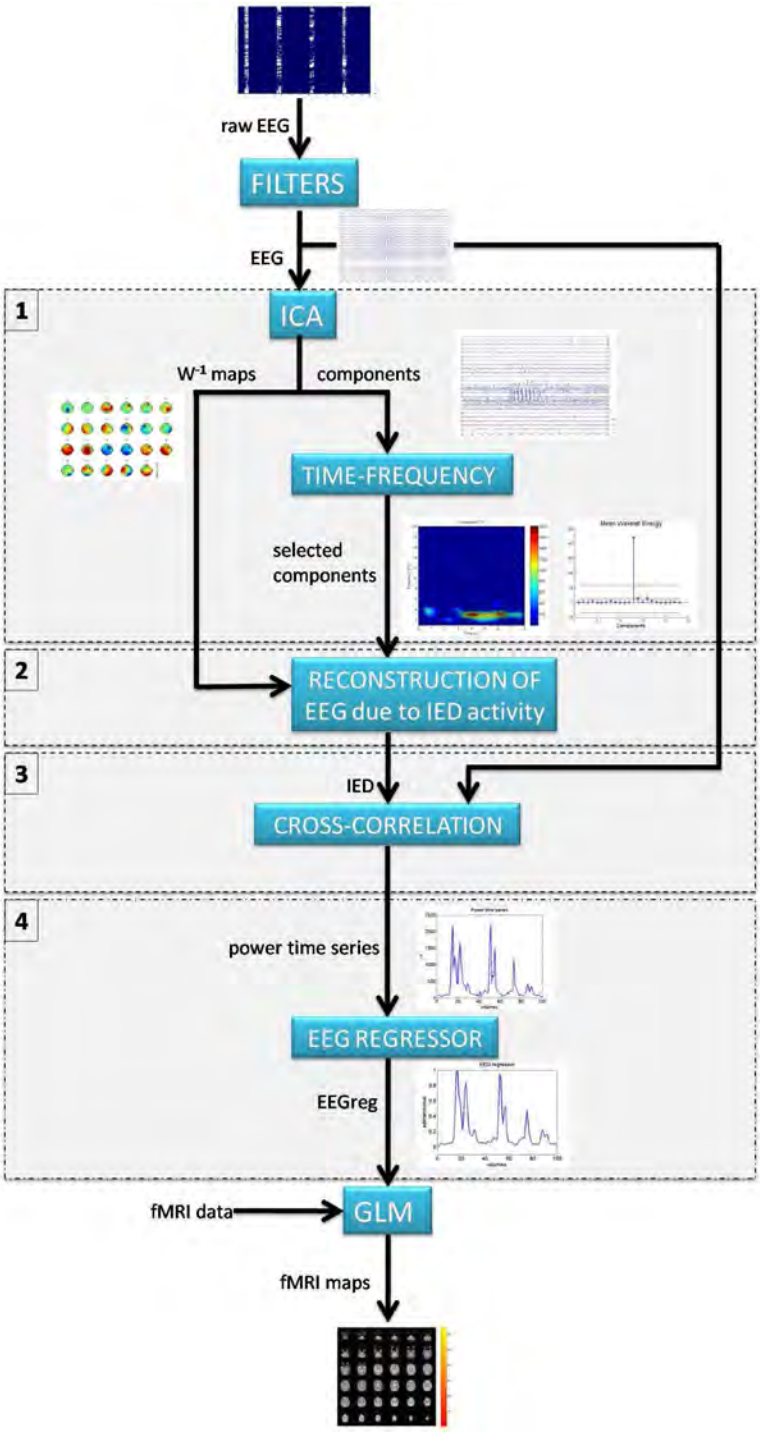


**Figure 2.7:** A schematic representation of the different steps in EEG-fMRI analysis. Step 1: Selection of the components; Step 2: Reconstruction of EEG signal; Step 3: Selection of the channel and wavelet analysis; Step 4: Construction of EEG regressor.

Chapter 3

# Individual-based HRF

In EEG-fMRI data, the variability of the HRF to epileptic neural activity is a crucial point in the GLM analysis. In this chapter, a method for selecting subject-specific HRFs is purposed on the basis of the performance of five models: four standard HRFs with fixed parameters, plus an additional individually adapted HRF model.

Since HRF may vary in several physiopathological conditions the major aim was to investigate the impact of a subject-specific HRF to describe the differences in hemodynamic response functions across epileptic patients versus the use of a standard HRF model. Since it is not possible to infer which is the best HRF model by looking at the activation maps, we developed a novel method and implemented a procedure to optimize in each patient the choice of HRF model from a set of four standard HRFs and a individual-based HRF (ibHRF). Starting from a general template with flexible shape, we chose to model B HRF using the simple gamma function and GF by the sum of two gamma functions with fixed parameters. We also included GF HRF and its first temporal and dispersion derivatives [Friston et al., 1998]. In ibHRF five-parameters were estimated, constructing a model which balances the accuracy of estimates and flexibility of the HRF model.

## 3.1 HRF models

Instead of postulating a model for HRF, we selected an optimal model out of five candidates. The general template for all models is derived from [Handwerker et al., 2004] and continuously differentiable. In discrete domain the HRF is sampled at time points $k = 1, 2, \ldots, K$:

$$HRF(k) = HRF_1(k) + HRF_2(k) \tag{3.1}$$

$$HRF_1(k) = \begin{cases} a_1 \cdot [(k - \delta_1)/\tau_1]^2 \cdot [exp(1 - ((k - \delta_1)/\tau_1))]^2 & \text{if } k > \delta_1 \\ 0 & \text{otherwise} \end{cases}$$

$$HRF_2(k) = \begin{cases} -a_2 \cdot [(k - \delta_2)/\tau_2]^2 \cdot [exp(1 - ((k - \delta_2)/\tau_2))]^2 & \text{if } k > \delta_2 \\ 0 & \text{otherwise} \end{cases}$$

where $k$ is the time point; $a_1$ and $a_2$ are the magnitude of the peak and undershoot terms, respectively; $\tau_1$ and $\tau_2$ are related to the width, peak height and time to peak; $\delta_1$ and $\delta_2$ to the time-to-onset. The times of occurrence of the positive ($k_{max}$) and negative ($k_{min}$) peaks are:

$$k_{max} = \delta_1 + \tau_1 \qquad k_{min} = \delta_2 + \tau_2 \tag{3.2}$$

To simulate a continuous physiological curve, the two gamma functions were connected at time point $\delta_1 + 1.51 \cdot \tau_1 = \delta_2$, i.e. the second inflection point of the positive function. The vector of model parameters is: $[a_1, a_2, \tau_1, \tau_2, \delta_1]^T$. The HRF has been modelled in fMRI using several models. Among them, the most commonly used (a simple gamma function [Boynton et al., 1996], difference of two gamma functions and two gamma functions and its temporal and dispersion derivatives [Friston et al., 1998]) are here considered. The first two models derive from the general template (Eq. 3.1) by properly setting parameter values.

*Model 1.* The sometimes called "Boynton" (B) model [Boynton et al., 1996], i.e. a single gamma function. The parameter values of Eq. 3.1 were fixed to $a_1 = 0.167, a_2 = 0, \tau_1 = 5.2, \tau_2 = 0, \delta_1 = 1.1$.

*Model 2.* The "canonical" model (GF), i.e. two gamma functions [Friston et al., 1998], one modelling the peak and one modelling the undershoot typically found in the measured hemodynamic response. The parameter values of Eq. 3.1 were fixed to $a_1 = 0.16, a_2 = 0.0147, \tau_1 = 5.2, \tau_2 = 8, \delta_1 = 0.8$.

*Model 3.* It is obtained by adding to the "canonical" model its temporal partial derivative (GFT).

*Model 4.* It is obtained by adding to the "canonical" model its temporal and dispersion derivatives (GFTD). The HRF is modelled as a linear combination of respectively two or three regressors. Incorporating the derivative terms allows to describe shape variations of the actual response: the time derivative and the dispersion derivative account for (small) variations in the latency of the peak response and in the width of the response, respectively [Friston et al., 1998]. Including temporal and dispersion derivatives is one of the most common method to capture variation in the HRF.
Differently from models $1 - 4$, the following parametric model, solving a nonlinear optimization problem, is here introduced to add more flexibility in the reconstruction of complex shape response.

*Model 5.* The ibHRF, where the parameters of Eq. 3.1 were estimated for each subject, following the steps shown in Fig. 3.1. The vector of model parameters is: $[a_1, a_2, \tau_1, \tau_2, \delta_1]^T$. Model parameters were estimated by weighted nonlinear least squares (Levenberg-Marquardt algorithm) on a limited number of preselected voxels identified as active by GLM analysis using HRF models 1, 2, 3, and 4 with a stringent statistical test (t-contrast with Bonferroni correction, p-value $< 0.05$). The following initial values were used: $[a_1 = 0.16, a_2 = 0.0147, \tau_1 = 5.2, \tau_2 = 8, \delta_1 = 0.8]$. Of note that the above models were not used to identify the brain regions involved in the stimulation, but only to limit the estimation of the subject-specific hemodynamic process to a subset of voxels with similar degree of signal change and time courses that have significant on-off modification: to avoid that this procedure introduces any bias, the "template" was based on voxels identified as active by all the four HRF models.
Estimates with $a_1 > a_2$ (physiological condition) and acceptable precision (coefficients of variation for all parameters lower than 100%) were selected and average values of parameters were used to create ibHRF (Fig. 3.1).
GLM analysis was applied five times to all voxels of each data set, by using respectively, B, GF, GFT, GFTD, and ibHRF models. The design matrix

contains one, two or three regressors: the first is the protocol convolved with B, GF or ibHRF; the second one is related to the use of time derivative of GF and the third regressor is related to the use of dispersion derivative of GF (the derivative with respect to $\tau$ in Eq. 3.1).

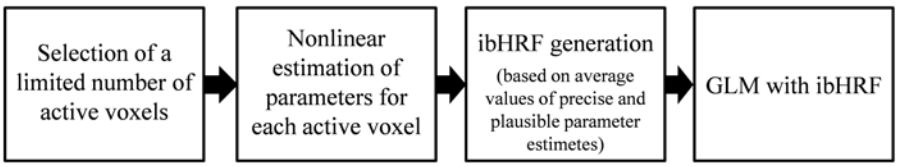


**Figure 3.1:** Schematic representation of the different steps in ibHRF estimation.

## 3.2 Selection of optimal HRF

To make a parsimonious choice among the candidate regressors (matrix $X$) obtained from the models $1-5$, the Akaike information criterion (AIC) was used. AIC is based on the minimization of the Kullback-Leibler distance and allows to implement the principle of parsimony, i.e. choose the model which is best able to describe the data with the minimum number of parameters. More than two models can be compared and the model which has the smallest AIC value is assumed to be the best [Landaw and DiStefano, 1984, Cobelli et al., 2001]. Under weighted least squares with uncorrelated, Gaussian errors, the criterion is [Turkheimer et al., 2003]:

$$AIC = Nlog(WRSS) + 2M + \frac{2M(M+1)}{(N-M-1)} \tag{3.3}$$

where $N$ is the number of volumes, $M$ is the number of parameters estimated by weighted minimum least squares [Friston et al., 1995], and $WRSS$ is the weighted residual sum of squares.

## 3.3 Implementation

The novel method has been developed in a software tool implemented in Matlab environment and called SOHIA (Selection of Optimal HRF and Im-

age Analysis) [Storti et al., 2009, Manganotti et al., 2012]. It includes five fundamental steps that are repeated iteratively for each HRFs:

1. *Building the design matrix*: the matrix $X$ is obtained by convolving a chosen HRF (B, GF, GFT, GFTD, ibHRF) with the stimulus function discretized on the same HRF grid.

2. *Building the weight matrix*: $W$ matrix is obtained by estimating GLM parameters without weights and, after, by identifying the autoregressive model (AR) of noise on the unweighted residuals (Appendix B).

3. *Parameter estimation*: $\beta s$ are estimated by linear least squares. Precision of the parameter estimates is evaluated from the inverse of the Fisher information and expressed as percent coefficient of variation; i.e., $SD(\hat{\beta})/\hat{\beta} \times 100$, where $\hat{\beta}$ is the vector of the parameter estimates.

4. *Statistical analysis*. To recognize the active voxels a t-contrast statistical test with False Discovery Rate (FDR) correction is used (q-value $\leq 0.05$). This choice reduces the numbers of voxel hypothesis and improves the power to detect activated voxels inside the brain and uncovered by the mask [Logan and Rowe, 2004]. After FDR correction the t value is expressed on a colorimetric scale in a t-map, representing brain activation.

5. *Akaike coefficient and selection of the optimal HRF model*: for each subject, steps $1-4$ are automatically repeated for all voxels and AIC is calculated for the five HRF models. Average AIC value is obtained from the active voxels, and the lowest value identifies the optimal model, i.e. the most parsimonious choice among the five HRF models.

## 3.4 Discussion

Generally, a brief neural event produces an HRF that peaks approximately $5-7$ s after neural response and is followed by an undershoot that lasts as long as 30 s [Friston et al., 2007]. In patients with epilepsy different hemodynamic shapes were observed. In this particular case, the choice of hemodynamic response is crucially important in obtaining clinically reliable information. Because of the importance of an individual tuning of HRF model parameter values, we have developed a software tool, SOHIA using ibHRF for a

correct characterization of HRF essential for an accurate prediction of the time-course behavior.

To conduct the analysis in an efficient manner, estimation of the HRF is performed on several selected voxels and based on them an unique HRF model is derived for each subject. This method improves upon the conventional approach providing an individual-based estimate. It could be easily extended to detect intra-subject variability, by using it at individual-region level. This procedure causes higher computational time than our method (order of magnitude: hours vs minutes) and different criterion to evaluate the results. At the moment, the vast majority uses standard HRFs, but here an accurate modeling of HRF shape were designed to improve the model fitting in the GLM framework. While the standard HRF models are clearly a simplification of the underlying biology, the ibHRF can be modelled on physiological intrinsic information of the fMRI time series.

Our method selects the optimal HRF model using AIC, which allows to identify the most parsimonious description of the BOLD signal. AIC not only rewards goodness of fit, but also includes a penalty that is an increasing function of the number of estimated parameters and discourages overfitting [Akaike, 1974]. Alternative criteria exist to compare the performance of different models. Among them, the F-test was widely used in fMRI analysis [Sachs, 2004]. The F-test is a frequently used hypothesis-test. It uses the difference of $WRSS$ of two models ($M_1$ and $M_2$), the number $N$ of data points and the number $P$ of free parameters. Only two nested models can be compared based on the number $F$, with

$$F = \frac{(WRSS_1 - WRSS_2)(P_2 - P_1)}{WRSS_2/(N - P_2)}. \tag{3.4}$$

The alternative (more complex) model is $M_2$, the simpler model $M_1$ (null hypothesis). $N - P$ is the number of the degrees of freedom [Cobelli et al., 2000]. F-test and AIC are based on different theoretical approaches and can result in different model selection. In particular, F-test needs to specify the significance level, which is often arbitrary set to 0.05 and the chosen value may obviously affect the choice of the optimal model [Glatting et al., 2007]. In addition, comparison among more than two models requires multiple F-tests, and thus to address issues inherent to any multiple testing [Jezzard et al., 2001]. Unfortunately the F-test can only be applied to compare models of different orders. The HRF models B, GF and ibHRF have the same num-

ber of parameters to be estimated, thus limiting applicability of the F-test. It is of note that, even if not often used in fMRI, the use of AIC criterion is not completely new in this field since it has been considered e.g. to estimate the dimensionality of data for principal component analysis [Cordes and Nandy, 2006], to find the optimum scale of drift in a modified GLM modeling approach in wavelet domain under Bayesian framework [Luo and Puthusserypady, 2008], and to estimate the order of the Near-Neighbourhood Autoregressive with exogenous variable model [Riera et al., 2004]. However, to the best of our knowledge, the present work is probably the first attempt to use AIC criterion for an automatic model selection between five HRF models.

Chapter 4

# Assessment on in Silico Data

In this chapter the performance of the novel method of analysis of EEG-fMRI proposed in Chapter 3 is tested on in silico data. Nineteen simulated fMRI dataset are created and used for the choice of the optimal HRF among five models: four standard and an individual-based HRF models. The data sets 1-4 reproduce situations where HRF assumes usual patterns, whereas the data sets 5-19 reproduce situations where HRF assumes unusual patterns (i.e. as in epileptic patients). Differently, data sets 16-19 represent deactivated time courses. The performance of the method is evaluated using the AIC as selection. Simulations would demonstrate the superiority of the novel method compared with the conventional ones and assess how the variations in HRF model affect the results of the statistical analysis.

## 4.1 In silico data set

Nineteen data sets were simulated, to reproduced situations where HRF assumes both usual and unusual (i.e. as in epileptic patients) patterns. The simulated data sets represented time series consisting of 100 active pixels and 200 non active pixels. The first experimental data set was generated assuming the same experimental design used for the epileptic patients and the GF model as "true" HRF. $X$ matrix was obtained by convolving the "true" HRF with the EEG regressor created as in Chapter 2, $\mathbf{EEGreg}(t)$, and down-sampled to the temporal resolution of the fMRI data (TR), resulting in a [110 $\times$ 2] matrix, where the first column was a vector of ones and the second column was a vector of values that characterize the model trend. To simulate the response vector $Y$ of 100 active pixels, the $X$ matrix was multiplied by a vector $\beta = [\beta_1, \beta_2]^T$, where $\beta_1$ and $\beta_2$ where sampled from Gaussian distributions. Similarly for the 200 non active pixels. These values were suggested from a study made in a epileptic patient (woman, 36 years old and right-handed), and analyzed by using GLM with a GF HRF model. This study also suggested values of the variance/covariance of the Gaussian white noise added to the simulated data ($\epsilon \sim N(0, \sigma^2 V)$). In a similar way, synthetic data sets 2-4 were generated by assuming as "true" HRF, respectively B, GFT, and GFTD models, with beta parameters ($\beta_1, \beta_2$ for B; $\beta_1, \beta_2, \beta_3$ for GFT and $\beta_1, \beta_2, \beta_3, \beta_4$ for GFTD) and noise processes obtained as before.

Data sets 5-15 were generated with unusual HRFs, called $T$ and $D$ functions, to create different simulations of BOLD response. These functions do not fit exactly any of the models (1-4), and allow both the dispersion of peaks and the delay of the BOLD signal to vary as occur in a epileptic patient [Bagshaw et al., 2004, Hawco et al., 2007]. A shift in time was also introduced, to check the influence of this feature on simulation results. $D_1, D_2, D_3$, and $D_4$ differ in positive delay, whereas $D_6$, and $D_7$ in negative delay. $T_1$, $T_2$, $T_3$, and $T_4$ have different dispersions of peak, but $T_3$ and $D_1$ do not differ substantially from the standard HRF functions (Table 4.1).

Data sets 16-19 represented time series consisting of 100 deactivated pixels and 200 non deactivated pixels. They were generated with the four usual HRFs. These values were suggested from patient (man, 43 years old and right-handed).

**Table 4.1:** Parameters of T and D functions.

| **Parameters of H functions** | | | | | |
|---|---|---|---|---|---|
| | $A_1$ | $A_2$ | $\tau_1$ | $\tau_2$ | $\delta_1$ |
| $T_1$ | 0.16 | 0.0147 | 2 | 2 | 0.8 |
| $T_2$ | 0.16 | 0.0147 | 4 | 4 | 0.8 |
| $T_3$ | 0.16 | 0.0147 | 6 | 6 | 0.8 |
| $T_4$ | 0.16 | 0.0147 | 8 | 8 | 0.8 |
| | | | | | |
| $D_1$ | 0.16 | 0.0147 | 5.2 | 8 | 3 |
| $D_2$ | 0.16 | 0.0147 | 5.2 | 8 | 4 |
| $D_3$ | 0.16 | 0.0147 | 5.2 | 8 | 5 |
| $D_4$ | 0.16 | 0.0147 | 5.2 | 8 | 6 |
| $D_5$ | 0.16 | 0.0147 | 5.2 | 8 | 0 |
| $D_6$ | 0.16 | 0.0147 | 5.2 | 8 | -2 |
| $D_7$ | 0.16 | 0.0147 | 5.2 | 8 | -4 |

Parameters of $T$ and $D$, but not $T_3$ and $D_1$, differ substantially from the standard HRF functions, namely $a_1 = 0.167, a_2 = 0$, $\tau_1 = 5.2$, $\tau_2 = 0, \delta_1 = 1.1$ for B model, $a_1 = 0.16, a_2 = 0.0147$, $\tau_1 = 5.2$,$\tau_2 = 8, \delta_1 = 0.8$ for GF model.

## 4.2 Analysis

Each data set underwent to five GLM analysis, performed using the five candidate HRF models. Activated pixels were compared to the true ones, to evaluate the amount of true positive (TP) out of the original 100 active pixels and false positive (FP) out of the original 200 pixels provided by each candidate models. Finally, for each data set and for the five HRF models AIC was calculated. The number of times that each model provides the lowest mean-Akaike value for the active pixels out of the 100 simulated active pixels, denoted as nAIC, was evaluated.

## 4.3 Results

In silico data allowed us to assess the performance of GLM analysis for different choices of HRF, either standard or individually based, in situations where the true HRF has an usual shape (Data sets 1-4, Table 4.2), has an unusual shape, as in epileptic patients (Data sets 5-15, Fig. 4.1, Tables 4.3,

4.4, and 4.5), or has negative time course (Data sets 16-19, Table 4.6).

Tables 4.2 and 4.6 show that when the data were generated from either B or GF or GFT or GFTD as "true" HRF, TPs and FPs using either ibHRF or any of the standard HRFs for GLM are generally comparable.

Since $\beta$ estimates of all HRF models were precise, model selection was based on AIC only, but nAIC value sometimes fails to select the true model, in favor of standard model. However, even if a wrong model is selected, activation is correctly recovered. The likely reason is that all models are comparable given that differences in amplitude, delay and dispersion are limited, and thus a good performance is achieved whatever the model used in the GLM analysis. The choice of the optimal HRF is thus irrelevant, as expected since the data generated in these simulations have similar characteristics to those of healthy subjects [Ferretti et al., 2004, 2007].

Conversely, the potentiality of our method is evidenced by the results on in silico data sets in which pathological data were simulated. Tables 4.3, 4.4, and 4.5 show that, when data are generated with models different from the standard ones ($T_1 - T_5$ and $D_1 - D_7$ models), the nAIC value in 11 out of 11 cases effectively selects the ibHRF model and the TPs values obtained with ibHRF are superior to those obtained with standard HRFs while the FPs, widely controlled by the FDR correction ($q<0.05$) for all simulations, produces low oscillations in its number. The likely reason is that HRF substantially differs in shape from B, GF, GFT, and GFTD: the application of standard model in GLM analysis introduces significant errors causing a decrease in TP and nAIC, whereas the application of ibHRF improves TP and nAIC. This is exemplified in Fig. 4.2 where the unusual hemodynamic response function $D_1$, $D_6$ and $T_2$ is plotted against the standard HRF models B and GF and the estimated ibHRF: only this latter provides a good approximation of the "true" HRF, while standard HRFs deviate from it.

## 4.4 Discussion

In order to evaluate the performance of the purposed method, simulations were performed using as "true" HRF both models with a standard shape and models with an unusual shape, as in epileptic patients.

When data are simulated from the standard HRFs as "true" HRF, the GLM results are generally comparable for all HRFs with similar performance in terms of TPs and FPs but AIC criterion is not always able to discriminate

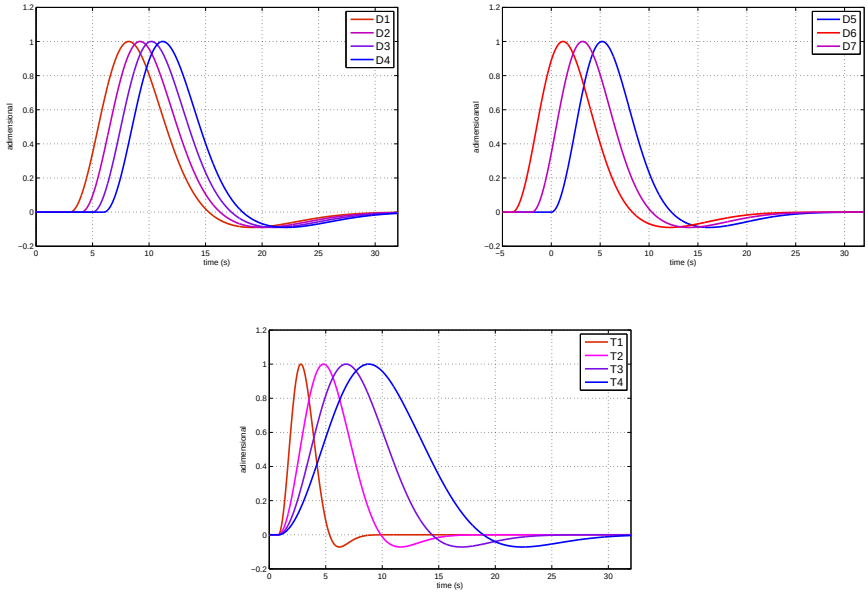


**Figure 4.1:** HRFs used to create simulated data. (a) and (b) HRF with different $\delta$ values. (c) HRF with different $\tau$ values.

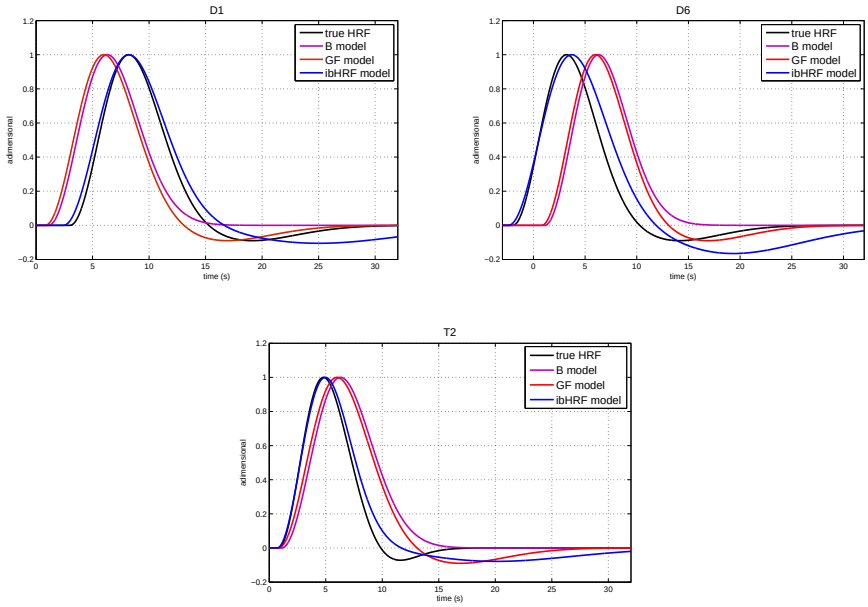


**Figure 4.2:** Effect of using standard HRF models when the "true" HRF deviates from the canonical templates.

**Table 4.2:** Results of Simulation (BOLD activation) with standard HRFs.

| | | | HRF used for GLM | | | | |
|---|---|---|---|---|---|---|---|
| | | | **B** | **GF** | **GFT** | **GFTD** | **ibHRF** |
| **"true" HRF (Activation)** | **B** | **TP** | 83 | 83 | 83 | 77 | 83 |
| | | **FP** | 0 | 0 | 0 | 0 | 0 |
| | | **nAIC** | 28 | 26 | 4 | 3 | 23 |
| | **GF** | **TP** | 76 | 77 | 76 | 61 | 80 |
| | | **FP** | 0 | 0 | 0 | 0 | 0 |
| | | **nAIC** | 27 | 27 | 2 | 2 | 23 |
| | **GFT** | **TP** | 83 | 85 | 85 | 73 | 85 |
| | | **FP** | 0 | 0 | 0 | 0 | 0 |
| | | **nAIC** | 31 | 8 | 5 | 2 | 39 |
| | **GFTD** | **TP** | 92 | 91 | 94 | 100 | 81 |
| | | **FP** | 7 | 8 | 12 | 34 | 2 |
| | | **nAIC** | 3 | 0 | 9 | 87 | 1 |

TPs out of 100 realizations, FPs out of 200 realizations and nAIC obtaining by using B, GF, GFT, and GFTD.

**Table 4.3:** Results of simulation (BOLD activation) for T functions (different values of $\tau$).

| | | | HRF used for GLM | | | | |
|---|---|---|---|---|---|---|---|
| | | | **B** | **GF** | **GFT** | **GFTD** | **ibHRF** |
| **"true" HRF (Activation)** | $\mathbf{T_1}$ | **TP** | 29 | 40 | 35 | 45 | 73 |
| | | **FP** | 0 | 0 | 0 | 0 | 0 |
| | | **nAIC** | 2 | 2 | 1 | 7 | 62 |
| | $\mathbf{T_2}$ | **TP** | 72 | 75 | 75 | 44 | 79 |
| | | **FP** | 0 | 0 | 0 | 0 | 0 |
| | | **nAIC** | 24 | 10 | 3 | 1 | 42 |
| | $\mathbf{T_3}$ | **TP** | 82 | 82 | 82 | 71 | 83 |
| | | **FP** | 0 | 0 | 0 | 0 | 0 |
| | | **nAIC** | 11 | 20 | 2 | 0 | 51 |
| | $\mathbf{T_4}$ | **TP** | 78 | 77 | 74 | 78 | 87 |
| | | **FP** | 0 | 0 | 0 | 0 | 0 |
| | | **nAIC** | 5 | 27 | 3 | 7 | 46 |

TPs out of 100 realizations, FPs out of 200 realizations and nAIC obtaining by using $T_1$, $T_2$, $T_3$, and $T_4$.

**Table 4.4:** Results of simulation (BOLD activation) for D functions (different values of positive $\delta$).

| | | | HRF used for GLM | | | | |
|---|---|---|---|---|---|---|---|
| | | | **B** | **GF** | **GFT** | **GFTD** | **ibHRF** |
| **"true" HRF (Activation)** | **$D_1$** | **TP** | 75 | 71 | 68 | 67 | 80 |
| | | **FP** | 0 | 0 | 0 | 0 | 0 |
| | | **nAIC** | 4 | 16 | 4 | 0 | 56 |
| | **$D_2$** | **TP** | 65 | 60 | 58 | 64 | 77 |
| | | **FP** | 0 | 0 | 0 | 0 | 0 |
| | | **nAIC** | 6 | 10 | 2 | 2 | 58 |
| | **$D_3$** | **TP** | 34 | 27 | 24 | 56 | 79 |
| | | **FP** | 0 | 0 | 0 | 0 | 0 |
| | | **nAIC** | 2 | 4 | 1 | 9 | 64 |
| | **$D_4$** | **TP** | 32 | 11 | 12 | 56 | 82 |
| | | **FP** | 0 | 0 | 0 | 0 | 0 |
| | | **nAIC** | 2 | 0 | 2 | 10 | 69 |

TPs out of 100 realizations, FPs out of 200 realizations and nAIC obtaining by using $D_1$, $D_2$, $D_3$, and $D_4$.

**Table 4.5:** Results of simulation (BOLD activation) for D functions (different values of negative $\delta$).

| | | | HRF used for GLM | | | | |
|---|---|---|---|---|---|---|---|
| | | | **B** | **GF** | **GFT** | **GFTD** | **ibHRF** |
| **"true" HRF (Activation)** | **$D_5$** | **TP** | 78 | 80 | 78 | 61 | 83 |
| | | **FP** | 0 | 0 | 0 | 0 | 0 |
| | | **nAIC** | 31 | 9 | 2 | 2 | 40 |
| | **$D_6$** | **TP** | 72 | 74 | 73 | 66 | 85 |
| | | **FP** | 0 | 0 | 0 | 0 | 0 |
| | | **nAIC** | 17 | 1 | 3 | 2 | 62 |
| | **$D_7$** | **TP** | 24 | 36 | 24 | 34 | 76 |
| | | **FP** | 0 | 0 | 0 | 0 | 0 |
| | | **nAIC** | 0 | 6 | 1 | 2 | 67 |

TPs out of 100 realizations, FPs out of 200 realizations and nAIC obtaining by using $D_5$, $D_5$, and $D_6$.

**Table 4.6:** Results of simulation (BOLD deactivation) with standard HRFs.

| | | | HRF used for GLM | | | | |
|---|---|---|---|---|---|---|---|
| | | | **B** | **GF** | **GFT** | **GFTD** | **ibHRF** |
| **"true" HRF (Deactivation)** | **B** | **TP** | 70 | 72 | 71 | 47 | 80 |
| | | **FP** | 0 | 0 | 0 | 0 | 0 |
| | | **nAIC** | 3 | 6 | 17 | 17 | 38 |
| | **GF** | **TP** | 65 | 70 | 70 | 35 | 77 |
| | | **FP** | 0 | 0 | 0 | 0 | 0 |
| | | **nAIC** | 10 | 2 | 7 | 10 | 48 |
| | **GFT** | **TP** | 67 | 74 | 74 | 42 | 77 |
| | | **FP** | 0 | 0 | 0 | 0 | 0 |
| | | **nAIC** | 2 | 5 | 25 | 20 | 26 |
| | **GFTD** | **TP** | 69 | 63 | 62 | 57 | 80 |
| | | **FP** | 0 | 0 | 0 | 0 | 0 |
| | | **nAIC** | 7 | 6 | 26 | 11 | 30 |

TPs out of 100 realizations, FPs out of 200 realizations and nAIC obtaining by using B, GF, GFT, and GFTD.

among them, i.e. the amount of TPs and FPs are comparable (Tables 4.2 and 4.6).

When data are simulated with models different from the standard ones, that allow both the amplitude and the delay of the BOLD signal to vary, the results obtained with ibHRF are superior to those obtained with the standard HRFs both in TPs and in nAICs (Tables 4.3, 4.4 and 4.5).

These results suggest that in subjects with canonical shape of BOLD responses, since all the candidate models are comparable, any HRF model can be indistinctly used, whereas in epileptic patients, where the data show modifications in shape and delay, the use of ibHRF model provides more reliable results. We observed that the presence of delay substantially influenced fMRI results. Including the derivative terms in some cases can improve the GLM results [Friston et al., 1998, Henson et al., 2002], but in our case it is not able to eliminate the errors caused by BOLD delay. Therefore the use in GLM analysis of only standard HRFs can decrease the amount of TP pixels, mainly in presence of a delay or an unusual shape.

Chapter 5

# Automatic Selection of ICA Components in fMRI

During a resting state condition fMRI is able to reveal coactivation of specific brain regions in distributed networks, called RSNs. ICA applied on fMRI data is often used for selecting RSNs. However, one of the major difficulties relies in the automatic selection of the ICA features related to brain activity (Chapter 1). In this chapter a method aiming to automatically separate the signal related to an internal network from the noise was developed. The image analysis was based on the probabilistic ICA as implemented in FSL software. After the decomposition process, the optimal number of components were selected by applying a novel algorithm which takes into account, for each component, the mean values of the spatial maps generated by FSL followed by clustering, segmentation and spectral analysis steps. To evaluate the performance of the suggested approach, the resting-state networks in twelve healthy subjects were investigated using resting state fMRI and a 1.5T MRI scanner. Comparing visual and automatic identification of the neuronal networks, the algorithm demonstrated high accuracy (98%) and precision (89%). The DMN was detected in most of the subjects (10/12), the occipital network in 8/12, the attention network in 7/12. Thus, our automatic selection method allows to separate and detect the RSNs reducing the subjectivity of the ICA component assessment.

## 5.1 Aim

Although ICA decomposition in fMRI is widely used to identify networks, a gold standard selection criteria to separate the ICs related to an internal network from noise-related ICs is still lacking. The existing methods, cited in Chapter 1, only rank the components, after which the neurologist must scroll each components manually. Hence the necessity to develop an automatic method of selection, able to identify signals representing networks of interest.

The aim is to determine the optimal number of ICs to describe the resting state activity by a five step algorithm, consisting of the spatial map filtering, statistical tests and spectral analysis. To verify the ability of the method, the selection of components on the basis of visual inspection vs automatic selection were compared in a data set of twelve healthy subjects.

## 5.2 Materials and methods

### 5.2.1 Data set and experimental paradigm

Data were recorded in 12 healthy subjects (mean age 29.2 $\pm$ 2.5, 7 males and 5 females). All subjects, as assessed by the Edinburgh handedness inventory [Oldfield, 1971], gave written informed consent for the study in accordance with the Declaration of Helsinki. The study was approved by the Local Ethics Committee of the University Department and Hospital.

Inside the bore of the scanner subjects laid supine on a bed with their elbows flexed at 120° and hands pronated in a relaxed position. The subject's head was stabilized with adjustable padded restraints on both sides. Subjects were told to remain as still as possible throughout the experiment. They were also instructed simply to lie still inside the scanner with their eyes closed, thinking of nothing in particular and not fall asleep.

### 5.2.2 FMRI data acquisition

Functional and anatomical images were acquired on a 1.5 T MR scanner (Symphony, Siemens, Erlangen, Germany) equipped with EPI capability and a standard transient/receive head coil. fMRI data were acquired with a T2* weighted EPI sequence: 140 or 180 volumes, 22 slices (36 slices for subjects Nos. 3 and 6), TR = 2000 ms (TR = 3200 ms for subjects Nos. 3 and 6),

TE = 50 ms, scanning matrix 64 × 64, FOV = 1350 × 1350 for subjects Nos. 3 and 6 and FOV = 1125 × 1125 for the remaining subjects, voxel size = 3.52 × 3.52 × 5.85 mm for subjects Nos. 1, 2, 4, 5, and 7, voxel size = 3.52 × 3.52 × 3.75 mm for subjects Nos. 3 and 6, voxel size = 3.52 × 3.52 × 6.08 mm for subjects Nos. 8, 9, 10, 11, and 12 in axial slice orientation. A T1-weighted anatomical scan with 144 slices (128 slices for subject No. 1; 192 slices for subject No. 6), TR = 9, TE = 3 ms, scanning matrix 512 × 512, FOV = 235 × 235, voxel size = 0.46 × 0.46 × 1 mm (subject No. 6 with voxel size = 0.46 × 0.46 × 0.09 mm) in axial slice orientation (sagittal for subject No. 6) was also acquired for each subject.

### 5.2.3 Image processing and analysis

#### Preprocessing

The functional data were preprocessed using the Multivariate Exploratory Linear Decomposition into Independent Components (MELODIC) version 3.09, part of FSL toolbox, www.fmrib.ox.ac.uk/fsl. The images were smoothed with a Gaussian kernel of full-width at half-maximum of 5 mm but without motion-correction [Bannister et al., 2001]. To correct for the different acquisition times, a slice timing correction was used. Data were then preprocessed with high-pass temporal filtering (with a cut-off of 100 s) and with the removal of non-brain structures from the echo planar imaging volumes (brain extraction tool, BET).

#### Automatic selection of the components

Starting from ICs estimated by PICA, a new method to select the optimal number of components related to internal networks was developed. This algorithm, implemented in Matlab (Mathworks, Sherborn, MA), consists of five consecutive steps: mean value evaluation and spectral analysis (steps 1-4-5) are used to reduce the number of ICs, whereas clustering and segmentation methods (steps 2-3) are used to filter the spatial maps (matrix $S$) at voxel-level. These steps, schematized in Fig. 5.1, are briefly presented in the following.

1. *Mean value evaluation (on ICs).* The method takes into account, for each component, mean values of each row of the spatial map (matrix $S$) generated by FSL. Assuming, as in PICA, that the noise has a zero-mean Gaussian

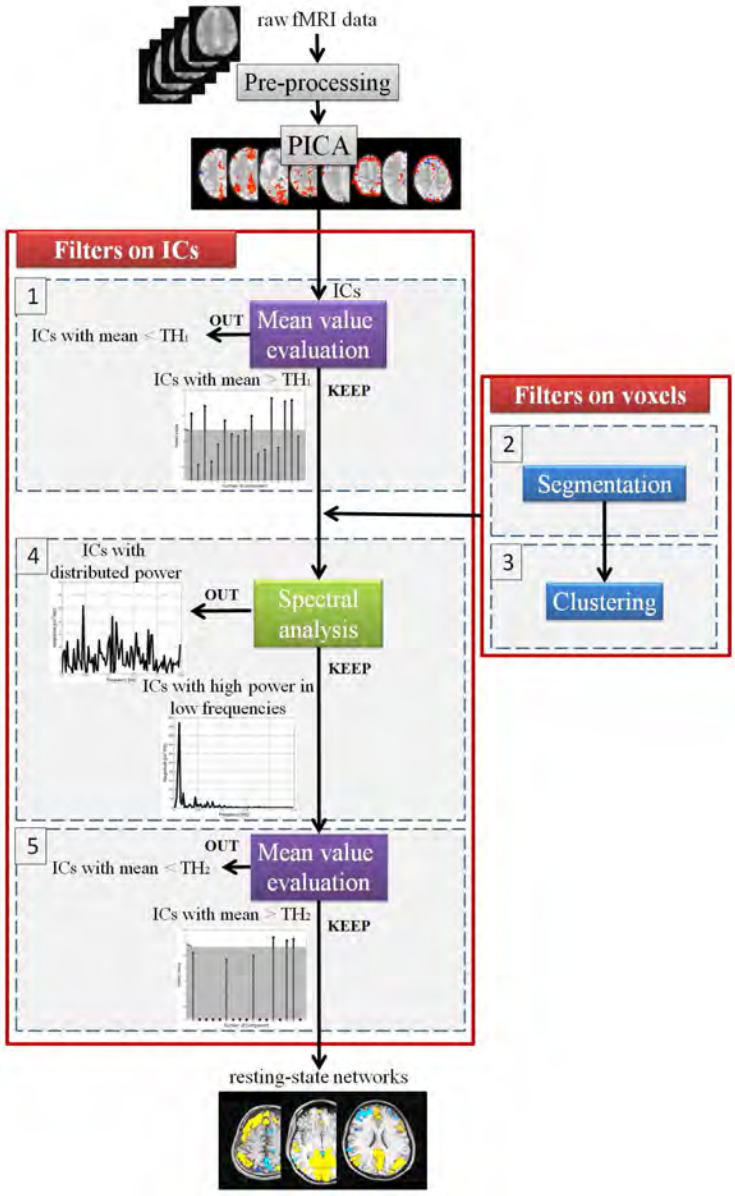


**Figure 5.1:** A schematic representation of the different steps in the method for the automatic selection of the ICA components. TH = threshold value.

distribution, the components related to the neuronal activation are expected to have mean value far from zero (Fig. 5.2abc), whereas those related to the noise to have mean value close to zero (Fig. 5.2d). The algorithm thus rejects the ICs if the mean value of the elements in the corresponding row of $S$ matrix is lower than a selected threshold, TH, evaluated for each subject as the grand average of all elements in the $S$ matrix. After this test, the ICs and, thus, the rows of $S$ matrix, are re-ordered so that rejected ICs are moved to the last positions. Thus, the matrix $S$ has a number of nonzero rows $I \leq K$ (Fig. 5.3).

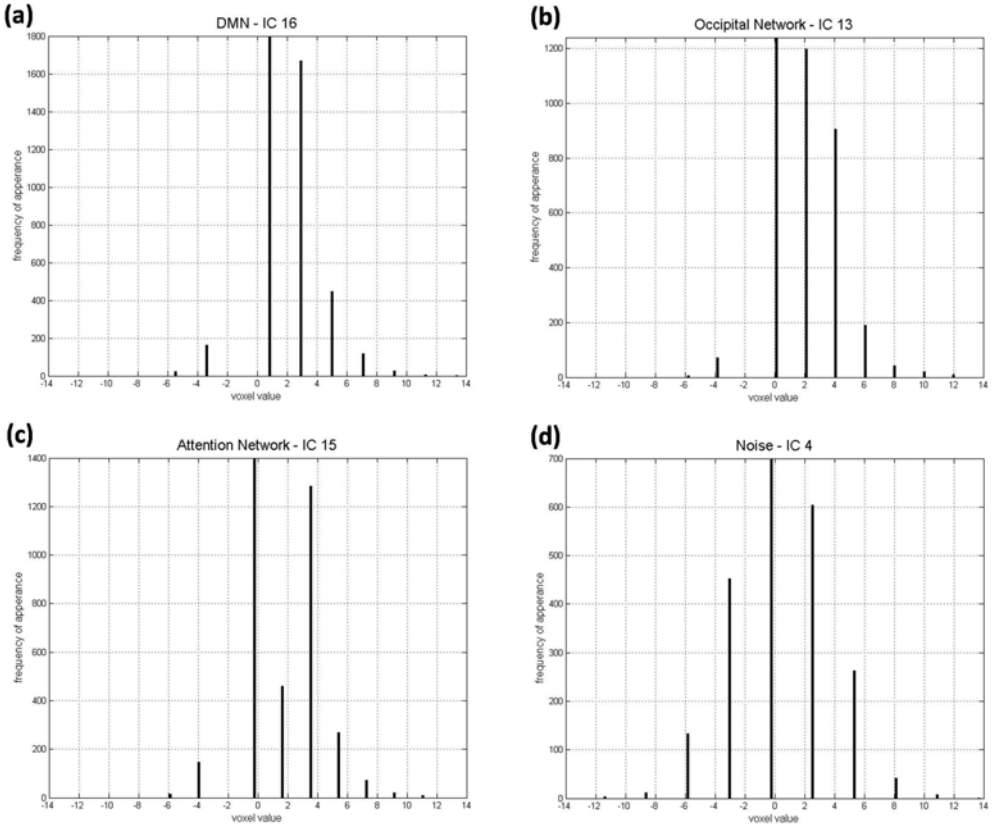


**Figure 5.2:** Subject 6. The histograms of rows of matrix S related to the DMN (a), the Occipital Network (b), the Attention Network (c), and a noisy IC (d). The x axis range from negative to positive values.

2. *Clustering (on map).* The cluster analysis, implemented by using k-means clustering algorithm [MacQueen, 1967, Golay et al., 1998, Goutte et al.,

1999], aims to eliminate those voxels that are associated with low values for each component. It works on the elements of each row of $S$, setting to zero some elements of the M columns, i.e. voxels. After creating the clusters, the algorithm eliminates the voxels that belong to the cluster with centroid nearest to zero, i.e. voxels with the lowest probability map. The initial value given to the algorithm for the number of clusters is eight. This number was empirically determined by applying the method several times to the same data, with different number of clusters. Using eight as initial number, DMN showed four activations (localized one in frontal region, two symmetrical in temporoparietal regions and one in posterior region) localized without causing further subdivisions. Since optimal initial value may depend on the data sets available, it should be checked before starting the analysis.

3. *Segmentation (on map).* PICA decomposition models the signal also in subcortical structures since the $S$ matrix includes signal from white matter and ventricles. To minimize pulsation effects from cerebrospinal fluid and restrict the activations to the gray matter, a segmentation on fMRI data was introduced, by using SPM version 8 (http://www.fil.ion.ucl.ac.uk/spm/). Voxels whose probability to belong to the white matter or cerebral-spinal fluid was at least at 90% were cancelled.

4. *Spectral analysis (on ICs).* For each component $i$, selected in step 1, the voxels $s_{i,m}$ selected in step 3 were identified. The relative fMRI time courses $x_{n,m} = a_{n,i} \cdot s_{i,m}$ , with $m = 1 \dots M$ and $n = 1 \dots N$ were baseline corrected, detrended and averaged. For each component, the FFT (using periodogram method) was then applied on the mean fMRI time course to best investigate spectral profile and study if a particular trend is present. The relative power spectral density $P_1$, $P_2$, and $P_3$ were estimated for the three ranges of interest: $P_1[0 - f_1]$, $P_2[f_1 - f_2]$ and $P_3[> f_1]$, according to Eq. 5.1:

$$P_1 = \frac{\int_0^{f_1} P_x(f)}{\int_0^a P_x(f)} df, \quad P_2 = \frac{\int_{f_1}^{f_2} P_x(f)}{\int_0^a P_x(f)} df, \quad P_3 = \frac{\int_{f_2}^a P_x(f)}{\int_0^a P_x(f)} df, \tag{5.1}$$

where $f_1$ and $f_2$ are the values closer respectively to 0.01 Hz and 0.1 Hz, $P_x(f)(\mu V^2/Hz)$ is the power spectral density and $a$ depends on acquisition parameters. Because of the different TR employed in the fMRI sequences, the frequency range and resolution was not the same for each subject (Table 5.1). Since the RSNs are characterized by slow fluctuations of functional imaging

signals between 0.01 and 0.1 Hz ($P_2$) [Cordes et al., 2000, Damoiseaux et al., 2006, De Martino et al., 2007, Mantini et al., 2007], the components with $P_2 < 50\%$ and with $P_1 + P_2 < 90\%$ were rejected. After spectral analysis, matrix $S$ has $J \leq I$ columns (i.e. components) (Fig. 5.3).

5. *Mean value evaluation (on ICs).* The assessment of the mean value is applied to all the components $J$ selected in step 4 (Fig. 5.3). In particular, the same method as in step 1 is repeated since clustering and segmentation can modify the mean value of the spatial maps (rows of $S$). After this second evaluation of the mean, the matrix $S$ has $W \leq J$ nonzero rows.

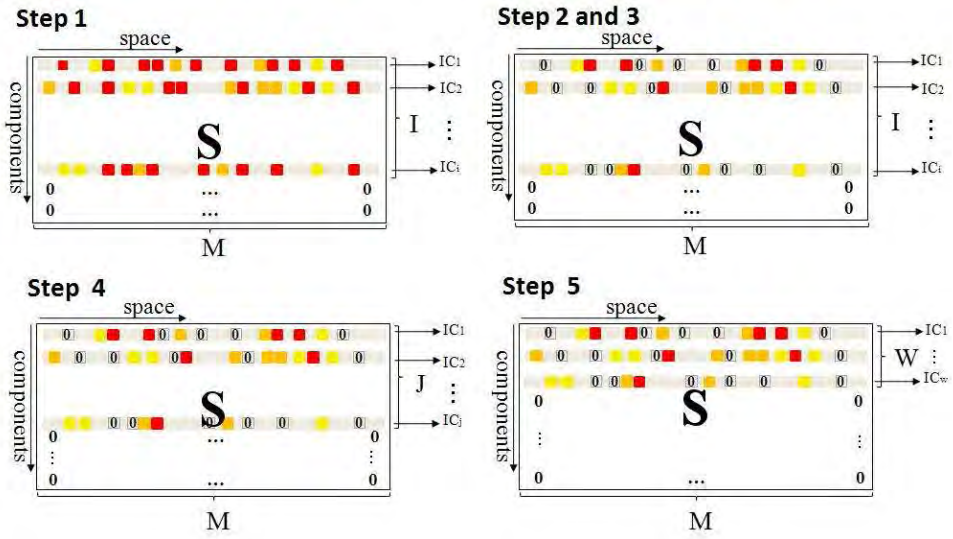


**Figure 5.3:** Schematic representation of the method applied to matrix S. Steps 1, 4 and 5 operate on the row of matrix S (setting to zero some ICs), steps 2 and 3 on the elements (setting to zero some voxels).

**Table 5.1:** Acquisition parameters and frequency ranges.

| **TR** | **slices** | **volumes** | **fs [Hz]** | **range $P_1$ [Hz]** | **range $P_2$ [Hz]** | **range $P_3$ [Hz]** |
|---|---|---|---|---|---|---|
| 2 | 22 | 180 | 0.5 | [0 − 0.0083] | [0.0083 − 0.1] | [0.1 − 0.2472] |
| 2 | 22 | 140 | 0.5 | [0 − 0.0107] | [0.0107 − 0.1] | [0.1 − 0.2464] |
| 3.2 | 36 | 140 | 0.3125 | [0 − 0.0089] | [0.0089 − 0.1004] | [0.1004 − 0.1540] |

fs = sampling frequency

**Assessment**

To quantify the ability of the method to select meaningful ICA components, RSNs identified by the automatic method were compared against those identified by an expert neurologist based on accuracy and precision defined as:

$$Accuracy = (TP + TN)/(TP + TN + FP + FN) \tag{5.2}$$

$$Precision = TP/(TP + FP), \tag{5.3}$$

where:

- true positive TP are the number of RSNs identified by an expert which are correctly recovered by the automatic method,
- false positives FP are the number of false RSNs,
- false negatives FN are the number of missed RSNs,
- true negatives TN are the components correctly rejected by the automatic method.

## 5.3 Results

Table 5.2 summarizes the performance of our method in 12 subjects: out of the N = 243 components selected by FSL, 33 are TP, i.e. the number of RSNs correctly recovered by the method, 4 are FP (subject No. 3, component no. 5; subject No. 7, component no. 17; subject No. 10, components nos. 11 and 17), 2 are FN (subject No. 2, component no. 12; subject No. 8, component no. 6), and 204 are TN. Thus, accuracy = (33+204)/(33+204+4+2) = 98% and precision = 33/(33+4) = 89%. Table 5.2 underlines that for 7 subjects out of 12 (Nos. 1, 4, 5, 6, 9, 11, and 12) the algorithm fully detects the networks identified by the neurologist. In two subjects some components visually chosen by the neurologist were not detected by our automatic method, namely the component no. 12 in subject No. 2 and the component no. 6 in subject No. 8. The component no. 12 is a Temporal-Motor Network with activation in bilateral temporal lobe and in the supplementary motor area. The component no. 6 was probably decomposed in two components (nos. 6 and 20) from FSL, in fact the mean time courses of the active voxels of these

two components had a correlation coefficient of 0.80 ($p < 0.05$). Vice versa in 3 subjects (Nos. 3, 7, and 10) the automatic method selected one or two additional components not identified as neuronal activations. These components, probably due to low quality of the signal generated for this subject, were easily identifiable, e.g. the component no. 17 in subject No. 7 was related to an activation in the ventricular regions, and disappeared by using a mask with higher probability to belong to the cerebral fluid (the probability of the mask in the method were not lowered over 90% to avoid the inclusion of cortex areas in the mask).

Starting from a variable number of ICs obtained by PICA decomposition (ranging, as indicated in Table 5.2, second column, from 15 to 26 components), the first step held 44% of components (example in Fig. 5.4), whereas after clustering, segmentation and spectral analysis only 30% were retained. In the last step, additional components were rejected, with a 15% surviving components as reported in Table 5.2, forth column. Although the number of incoming components to the algorithm varies widely from subject to subject depending on the number carried out by FSL, the algorithm performs equally well.

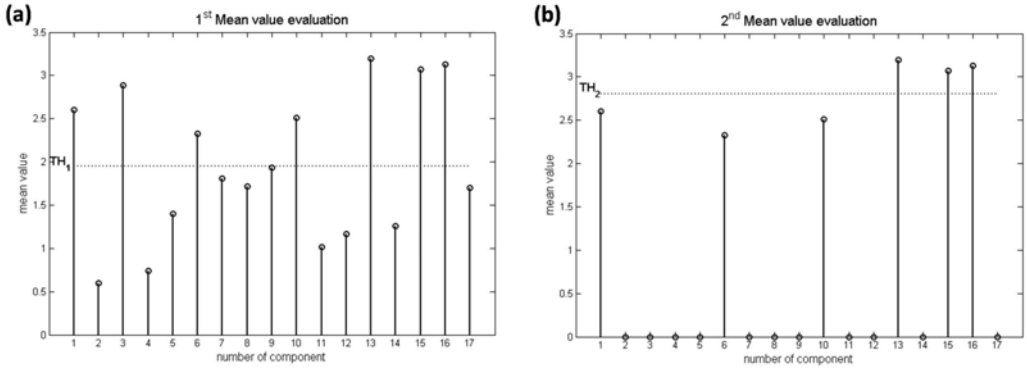


**Figure 5.4:** Subject 6. Description of the mean value for each component (17 in this subject) and the threshold values ($TH_1$ and $TH_2$ respectively) in broken black line before (a) and after (b) clustering, segmentation, and spectral analysis.

The frequency with the largest amplitude in $P_2$ was identified by spectral analysis as the dominant frequency for all RSNs, as exemplified in Fig. 5.5, that shows for subject No. 9 the power spectra of two IC time courses se-

**Table 5.2:** Comparison between the automatic and visual IC selection. 'Number of ICs' refers to the number of automatic component estimated by FSL software.

| Subjects | Number of ICs | Selected by neurologist | Selected by the automatic method | $P_1(\%)$ | $P_2(\%)$ | $P_3(\%)$ |
|---|---|---|---|---|---|---|
| **1** | 15 | 10 (DMN) | 10 | 4.85 | 86.52 | 8.63 |
| | | 13 (Occ) | 13 | 3.23 | 83.74 | 13.03 |
| **2** | 20 | 12 (Tem-Mot) | Not found | 56.28 | 40.62 | 3.11 |
| | | 15 (DMN) | 15 | 56.83 | 35.37 | 7.80 |
| | | 17 (Att) | 17 | 25.37 | 59.15 | 15.48 |
| **3** | 16 | 1 (Occ) | 1 | 6.71 | 91.51 | 1.77 |
| | | 2 (Tem-Mot) | 2 | 6.75 | 91.10 | 2.15 |
| | | Not found | 5 | 6.28 | 79.62 | 14.11 |
| **4** | 22 | 10 (DMN) | 10 | 20.27 | 74.13 | 5.59 |
| | | 11 (Occ) | 11 | 16.01 | 74.55 | 9.45 |
| | | 21 (Att) | 21 | 17.42 | 75.44 | 7.15 |
| **5** | 19 | 1 (Tem) | 1 | 12.61 | 84.10 | 3.29 |
| | | 2 (Occ) | 2 | 7.85 | 89.06 | 3.09 |
| | | 10 (Occ) | 10 | 6.58 | 73.66 | 19.76 |
| **6** | 17 | 13 (Occ) | 13 | 21.43 | 74.77 | 3.80 |
| | | 15 (Att) | 15 | 13.21 | 80.99 | 5.80 |
| | | 16 (DMN) | 16 | 6.04 | 86.53 | 7.43 |
| **7** | 19 | 14 (DMN) | 14 | 10.86 | 74.77 | 14.37 |
| | | 15 (Att) | 15 | 7.23 | 63.74 | 29.03 |
| | | Not found | 17 | 3.65 | 74.52 | 21.83 |
| **8** | 26 | 5 (Tem-Mot) | 5 | 9.08 | 75.08 | 15.84 |
| | | 6 (DMN) | Not found | 8.56 | 82.61 | 8.82 |
| | | 10 (Att) | 10 | 9.50 | 80.08 | 10.42 |
| | | 12 (Sens) | 12 | 13.99 | 71.80 | 14.21 |
| | | 20 (DMN) | 20 | 11.58 | 79.19 | 9.23 |
| **9** | 20 | 6 (DMN) | 6 | 13.19 | 79.45 | 7.37 |
| | | 8 (Occ) | 8 | 13.35 | 67.22 | 19.43 |
| **10** | 24 | 5 (Occ) | 5 | 9.77 | 84.43 | 5.80 |
| | | Not found | 11 | 5.80 | 73.39 | 20.82 |
| | | 12 (Front) | 12 | 36.24 | 52.28 | 11.48 |
| | | 14 (DMN) | 14 | 9.99 | 84.21 | 5.80 |
| | | Not found | 17 | 5.36 | 60.02 | 34.63 |
| **11** | 22 | 6 (Att) | 6 | 15.75 | 76.85 | 7.40 |
| | | 10 (DMN) | 10 | 2.17 | 87.37 | 10.46 |
| | | 14 (Att) | 14 | 10.61 | 80.00 | 9.39 |
| | | 18 (Att) | 18 | 4.37 | 84.18 | 11.45 |
| **12** | 23 | 2 (Occ) | 2 | 31.29 | 67.17 | 1.54 |
| | | 12 (Att) | 12 | 41.09 | 56.90 | 2.01 |
| | | 15 (DMN) | 15 | 23.19 | 73.32 | 3.49 |

DMN = Default Mode Network, Att = Attention Network, Occ = Occipital Network,Tem-Mot = Motor-Temporal Network, Front = Frontal Network, Sens = Sensitive Network. $P_1$, $P_2$ and $P_3$ are calculated as in Eq. 5.1.

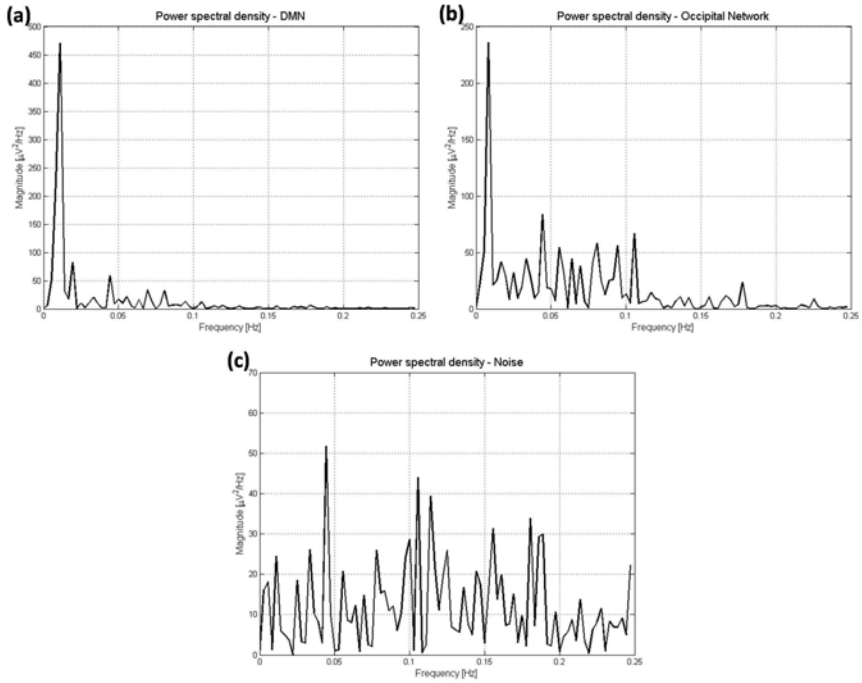


**Figure 5.5:** Subject 9. (a) and (b) Power spectral densities ($\mu V^2/Hz$) of two IC time courses selected by the algorithm: the DMN and Occipital Network after clustering and segmentation. (c) Power spectral density of a noisy-IC time course (rejected by the spectral analysis).

lected by the algorithm (DMN and Occipital Network) after clustering and segmentation, as well as the power spectrum of a noisy-IC time course rejected by the spectral analysis. Because of the wide variability of RSN time courses, it was difficult to make an objective evaluation in the time domain, whereas the FFT, applied to the time course of fMRI data, allows to observe recognizable peaks at low frequencies for the RSNs with an individual isolated and well-defined peak, for example in DMN for subjects Nos. 1, 2, and 9, and a less defined peak for subjects Nos. 4, 6, 7, 8, 10, 11, and 12, with the most percentage of power contained in $P_2$.

Summing up, the DMN was present in most of the subjects (10 of 12 subjects), the Posterior Network in 8 subjects, the Attention Network in 7, whereas the Motor-Temporal Network in 3, the Temporal Network in 1, the Sensitive Network in 1 and finally the Frontal Network in 1. Fig. 5.6 shows three selected networks of patient No. 6: the DMN, the Occipital Network

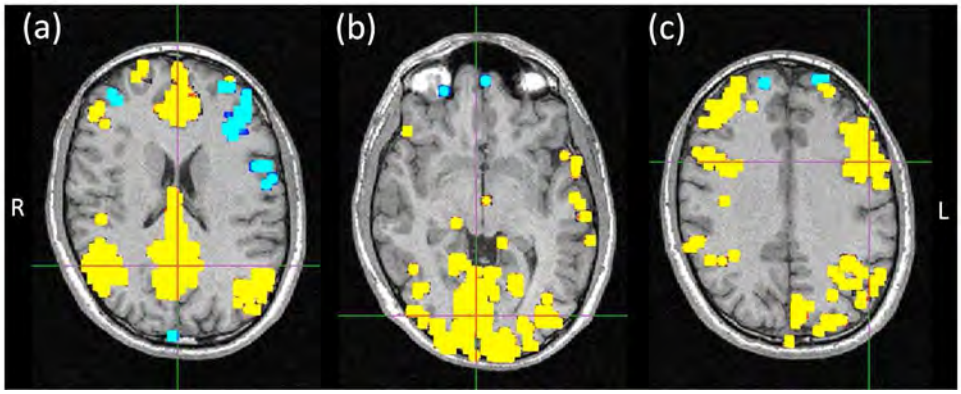


**Figure 5.6:** The DMN (a), the Occipital Network (b) and the Attention Network (c) in subject No. 6. The anatomical and functional data were registered by using affine registration on FMRIB's Linear Image Registration Tool (FLIRT), using the anatomical images as the reference. The images were visualized using the FSLView toolbox.

and the Attention Network. In healthy subjects, the first network is a baseline activity and is suspended during specific goal-directed behaviors, the second one is associated with visual processing (the subject was instructed to keep the eyes closed during the experiment) and the last one is probably due to an unconstrained behavior or a mental activity of which a subject is consciously aware.

## 5.4 Discussion

The aim of the method developed here is to allow an automatic selection of ICA components, that is usually done visually, thus eliminating the subjectivity of the selection while reducing the time of analysis of fMRI data. The method integrates time, frequency and spatial processing and results in an automatic selection procedure that is reliable, flexible and widely applicable: on our data base consisting of fMRI images of 12 healthy subjects, the algorithm demonstrated high accuracy (98%) and precision (89%) confirming its ability to automatically detect the networks identified by the neurologist. Our results are in line with previous studies confirming the presence of well-know RSNs.

Our method uses as first step the evaluation of the mean value of each row

of the spatial map. This evaluation procedure is also applied after spectral analysis as last step. The aim of this procedure is to reject the components that show mean value close to zero, i.e. related to the noisy components in agreement with the model specifications of additive Gaussian noise presence. K-means clustering and segmentation steps work for setting to zero some specific voxels. As result, the active clusters are concentrated without weak and isolated activations. Regarding the frequency analysis step, the FFT [Kiviniemi et al., 2000], the cross-correlation analysis with the prior definition of a reference region [Biswal et al., 1995], the frequency analysis of cross-correlations [Cordes et al., 2001], the coherence analysis with a user-defined seed region [Sun et al., 2004] and spectral coherence analysis without seed regions [Thirion et al., 2006] were used in this field, showing that the waveforms of these spontaneous activity patterns have prominently a low-frequency contribution and that the only frequencies less than 0.1 Hz contribute significantly to the interregional functional connectivity [Cordes et al., 2000, Laufs et al., 2003, Damoiseaux et al., 2006, De Martino et al., 2007, Mantini et al., 2007]. In order to discriminate the RSNs from the physiological fluctuation, Soldati et al. [2009] employed the spectral analysis to group-ICA time courses applying a statistical approach to assess if two classes were statistically different. Differently, we investigated the power spectra of ICs to identify the power concentrated in the range of interest [0.01-0.1Hz], founding high power in low frequency range for the RSNs as typically observed in the literature. Although some components showed high power spectrum in $P_2$, we have seen that this is not a sufficient condition to eliminate all the ICs of no interest. In fact only with the last step, i.e. the evaluation of the mean analysis applied again after the spectral analysis, we are able to complete the rejection of the ICs of no interest.

It is of note that the method requires an exact sequence of the four methods to achieve a successful result in terms of accuracy and precision. For example, moving the segmentation before the first mean value evaluation change the result. If the clustering or the segmentation were applied at the beginning of the analysis to a noisy component, which presents activities in areas not covered by the mask, the component would have a histogram different from the previous one and therefore be selected as useful by the first mean value evaluation. Therefore using this sequence of steps the performance of the method improves in term of precision and accuracy.

In MELODIC, the automatic estimation of the number of spatial maps

for each subject is useful to not subdivide the networks in different components [Beckmann and Smith, 2004]. Nevertheless, the method can be used without this pre-selection, i.e. on a number of ICs equals the number of time points in the data.

Regarding the physiological classification of the networks related to the neuronal activity, the BOLD networks could be divided in unconstrained behavior or mental activities similar to modulations induced by external stimuli and in an intrinsic activity similar to the anatomy. The origin of these networks are still an open problem. It is unclear if the fluctuations are independent from the neuronal function or if it reflects the neuronal baseline activity without task [Damoiseaux et al., 2006]. Our study confirms the presence of networks already introduced in the literature such as: DMN, the Attention Network, the Posterior Network, the Motor-Temporal Network. Marcus Raichle et al. coined "default-mode" in 2001 to describe resting state brain function demonstrating the existence of an organized, baseline default mode of brain function that is present as a baseline or default state and is suspended during specific goal-directed behaviours [Raichle et al., 2001]. This network is identified both in animals [Lu et al., 2007, Vincent et al., 2007] and in humans. DMN shows great resemblance to the brain areas found to be involved in random episodic silent thinking and is putatively associated with internal processing [Andreasen et al., 1995]. In addiction this network sustains its activity despite decreasing vigilance. The DMN component includes the posterior cingulated cortex/precuneous, the medial prefrontal cortex, and bilateral temporoparietal junctions. Laufs et al. and then Mantini et al. found a bilateral frontoparietal pattern, including intraparietal sulcus and frontal eye field, a network mediating goal-directed stimulus-response selection associated with alpha desyncronization. It is due probably to unconstrained behaviour or a metal activity of which a subject is consciously aware [Laufs et al., 2003, Mantini et al., 2007]. Recent studies of functional connectivity demonstrate the presence of a differentiation inside the DMN, linking the precuneus (site with the highest degree of interactions) and posterior cingulated cortex with visual-spatial and attention networks and the medial prefrontal cortex with the motor control circuit [Uddin et al., 2009]. Fox et al. found activations in two attentional systems that persist also in absence of external stimuli: a bilateral dorsal attention system usually involved in top-down orienting of attention and a right-lateralized ventral attention system in reorienting attention in response to salient sensory stimuli. It is

possible to make many hypothesis regarding the spontaneous activity and the possibility to seem similar to task-evocated activity. It might serve to organize the neuronal activity or as a memory of previous use or a prediction regarding the future use [Fox et al., 2006]. Finally a network dedicated to visual processing (the Occipital Network) involving the retinotopic occipital cortex and the temporal-occipital regions could be identified and the BOLD signal fluctuations associated with it are probably correlated with the EEG power variations of alpha [Mantini et al., 2007].

Showing high accuracy and precision, the proposed method allows to automate and speed up the selection of components related to the resting state networks, revealing also networks that might be difficult to identify visually. This method increases the repeatability of the RSNs selection in multi-center studies or in those studies where it is important to reduce the variability of the results produced by the subjectivity of a visual choice made by different, even if expert, neurologists.

In conclusion, although several previous studies used data-driven techniques to assess functional activity during the resting state condition, there was not a development of a selection criteria to separate the ICs related to an internal network from those related to noise. The proposed algorithm identifies the real networks or "rhythms" obtaining an adequate number of activation maps, speeding up the analysis, and reducing subjectivity in classification of the ICs.

## 5.5 Application in epilepsy

In the evaluation of epilepsy, the most common method used to analyze EEG-fMRI data is the GLM, wherein an a priori hypothesis is made on the shape of the HRF. Conversely, ICA can extract IED-related BOLD components without constraints on the HRF. The ICA was first applied to patients with epilepsy by [Rodionov et al., 2007]. The components were selected if they showed a spatial overlap with positive BOLD signal changes in the GLM analysis and a correlation of the component time courses with the model used in the GLM analysis. More recently, a new method to compare GLM and ICA results was introduced by [Moeller et al., 2011]. In this study, spatial ICA was used to extract ICs from the fMRI data, and a deconvolution method identified component time courses significantly related to the generalized

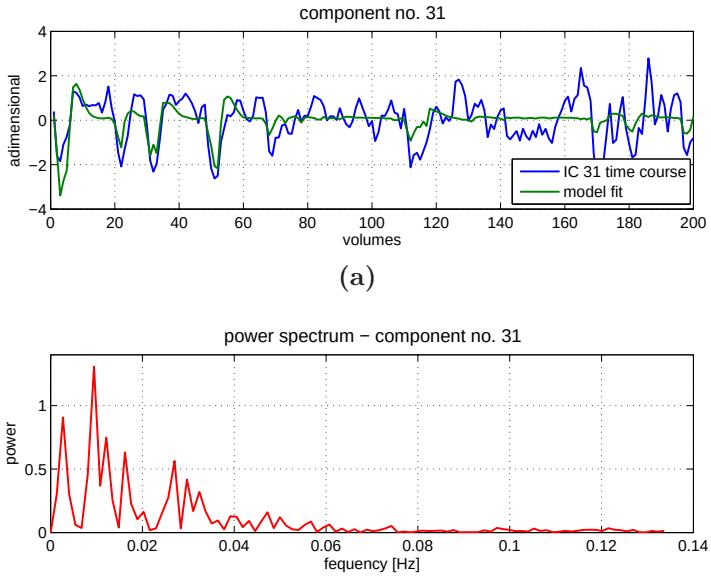


**Figure 5.7:** Patient with epilepsy. (a) The design matrix constructed in the GLM analysis (green) is fitted to the time course of a component related to the IED activity of the patient (blue). (b) Power spectrum of the IED-related IC.

EEG discharges but without imposing constraints on the HRF.

In Fig. 5.7 an example of a IED-related component time course is shown. In order to identify which component is related to the IED activity of the patient, the design matrix constructed in the GLM analysis can be fitted to the time courses of the component.

Chapter 6

# Assessment on Real Data

Here, twelve cases of pharmacoresistant epilepsy were described. Quantitative assessment was performed using a multimodal approach with hdEEG and EEG-fMRI coregistration in order to localize the epileptic activity and verify the reliability of source localization and BOLD activation. Standard EEG and fMRI data were acquired during a single scanning session. The EEG-fMRI data were analyzed using the conventional and new GLM analysis. The fMRI data were also analyzed using the PICA. Source localization of IEDs was performed using 256-channel hdEEG. BOLD localizations were then compared to EEG source reconstruction. These results were evaluated related to the expected epileptic activity defined by standard EEG and clinical outcome.

## 6.1 Patients

The study sample was twelve patients with epilepsy (seven patients with post-traumatic epilepsy, three with temporal epilepsy, one with generalized epilepsy and one with cerebral palsy). All patients gave written informed consent for the study in accordance with the Declaration of Helsinki. The study was approved by the Local Ethics Committee of the University Department and Hospital.

### 6.1.1 Post-traumatic epilepsy group

Post-traumatic epilepsy, a common complication of traumatic brain injury (TBI), occurs in 15 to 20% of patients with severe brain trauma. The risk of epilepsy is higher during the first two years after both mild and severe TBI, and it remains elevated for more than 10 years after the injury. The clinical features of seizures arising from the frontal lobe vary widely: simple focal tonic seizures with vocalization; speech arrest; fencing posture; forced head and complex focal motor activity with urinary incontinence and focal activity on the EEG. Clinical seizures are often unrelated to the severe brain lesions. And because neurosurgical treatment is generally unfeasible, correlations between EEG activity, clinical seizures and brain lesions are rarely investigated [Siegel et al., 2001].

The study sample with post-traumatic epilepsy was seven patients. Clinicopathological characteristics were roughly similar: complex partial seizures (focal) and seizure frequency (from 3 to 25 seizures per month); 5 out of 7 patients presented with cognitive and behavioral impairment; all showed focal activity, spike and slow-wave paroxysms. Paroxysmal activity predominated in the left frontal regions (5/7 patients), in the right-temporal regions (1/7) and in the left-central regions (1/7).

**Patient No. 1.** This 43-year-old man sustained severe TBI in a road accident. The first seizures developed 2 years later, with initial clonic movements of the right arm and hand, followed by right leg and orofacial automatisms of the right side of the face, deflection of the face rightward, and early loss of consciousness. MRI revealed left brain cortical and subcortical atrophy with considerable ex vacuo enlargement of the lateral ventricles. Interictal standard scalp EEG over the right hemisphere was inconstant; low voltage (8-9 Hz) EEG over the left hemisphere showed theta waves associated with

polymorphic delta waves which were more evident on the fronto-central hemisphere electrodes; specifically, high amplitude (75-120 $\mu V$) 2 Hz spike and wave discharges over the left frontal hemisphere electrodes which spread to the right hemisphere.

**Patient No. 2.** This patient suffered head trauma at age 16 years, with bleeding in the left fronto-polar and frontal regions. Two years later, the first seizure occurred during the night and was described as grand mal seizures with tonic clonic movements of the upper and lower limbs. These were followed by 2-3 episodes of cyclic clinical tonic-clonic seizures per week. Seizure occurrence eventually ceased with additional therapy. Standard EEG showed theta-wave activity in the left frontal regions with phase reversal in F3. Other seizures were characterized by abrupt loss of consciousness, fixed gaze, facial contraction and mild head version to the right.

**Patient No. 3.** At the age of 14 years, this patient suffered an accidental fall resulting in extradural hematoma and right hemiparesis which resolved (lasting 3 days). Two apparently generalized tonic-clonic seizures occurred during sleep at age 38 years, in addition to sporadic left lower limb clonic seizures during drowsiness. The patient presented no motor deficit, sensory, cognitive or behavioral impairment. Standard EEG showed slow left fronto-temporal foci (drug-resistant) associated with paroxysmal isolated elements in F7. The patient showed continuous theta activity, sometimes polymorphic delta sequences, of medium voltage on the left frontal electrodes. At the same site, isolated slow peaks were detected mainly in Fp1/F7. Rare and isolated polyspikes associated with left frontal slow waves on derivations were recorded only in stage II NREM sleep. These elements showed phase reversal in F7, without a tendency to spread, and disappeared upon awakening.

**Patient No. 4.** This patient sustained a fracture of the right cranial vault in a motorcycle accident 12 years earlier. After the accident, he fell into coma for 22 days. The front vault was removed and a prosthesis inserted. MRI findings were principally bilateral frontal lesions. He presented right-sided blindness resulting from trauma-induced lesion of the optic nerve and residual orbitofrontal asymmetry of the facial bones. Interictal standard EEG showed theta polymorphic sequences during drowsiness associated with isolated large-voltage paroxysms on the left fronto-temporal electrodes with phase reversal in F7. These elements did not tend to spread contralaterally. His history included brief attacks typically occurring in clusters and often

at night, characterized by oscillatory trunk movements, arm flexion, synchronous bi-manual automatisms, and proximal isolated movements of the lower limbs associated with loss of consciousness (Fig. 6.1).

**Patient No. 5.** This 44-year-old man suffered a head injury in a workplace accident at the age of 31 years, associated with an acute left fronto-temporo-parietal subdural hematoma, multiple brain injuries and cerebral edema resulting in right hemiplegia. The patient also presented with motor aphasia. Simple focal seizures first occurring 9 months after the accident were characterized by initial deviation of the mouth and eyes to the right, followed by clonic movements of the upper and then the lower right limb, lasting less than 1 minute, on an average of 1-2 times a year. MRI showed bilateral lesions in the frontal regions and in the left temporo-parietal regions. EEG recordings were characterized by slow theta, sometimes delta, polymorphic activity intermixed with superimposed sharp waves showing phase reversal at C3.

**Patient No. 6.** At age 19 years, this patient sustained the first and the most severe head trauma in a road accident, resulting in a left fronto-orbital lesion. Reconstruction of the front and placement of implants were performed. Four years after the accident, the patient experienced two episodes of morpheic seizures. One year later, he sustained another head injury, followed by focal and secondarily generalized seizures (starting with prolonged vocalization and quickly followed by a tonic and then a clonic phase). The last seizure occurred 4 months before the present fMRI study. MRI showed a large left frontal and an orbitofrontal poroencephalic lesion associated with significant gliosis. EEG recordings showed persistent epileptogenic foci, with theta activities intermixed with superimposed spikes and waves in the left frontotemporal regions, with maximum appearance at the F7 electrode.

**Patient No. 7.** This patient presented bilateral lesions after sustaining a work-related accident (right temporal lesion and left temporal lobe lesion). His clinical picture was characterized by temporal seizures with temporo-parietal aura characterized by auditory hallucinations ("like hearing the sea inside a seashell") followed by epigastric sensations, nausea and loss of consciousness. He sometimes experienced complex hallucinations ("like a slide series about my past life") associated with oral automatisms, head version to the right, fixed gaze and frothing at the mouth. The patient showed theta-delta activity with sharp, large-voltage morphology in the fronto-temporal

region and phase reversal at T4.

### 6.1.2 Temporal epilepsy group

Temporal lobe epilepsy (TLE) is the commonest location-related form of epilepsy accounting for more than 60-70% of focal epilepsies [Wieser, 2004]. It is a condition characterized by recurrent, unprovoked seizures originating from the medial or lateral temporal lobe. The seizures associated with temporal lobe epilepsy consist of simple partial seizures and complex partial seizures. Simple partial seizures involve small areas of the temporal lobe such as the amygdala or the hippocampus and the consciousness is not altered. Complex partial seizures cause awareness during the seizure and they can spread to involve both temporal lobes altering the ability of the patient to interact with the environment. They usually begin with a simple partial seizure, but then the seizure spreads to a larger portion of the temporal lobe resulting in impaired consciousness. Hippocampal sclerosis is the commonest pathology underlying TLE, but is detected by MRI only in around 65% of cases [Blumcke et al., 2002].

The temporal epilepsy group consists of two patients with partial seizures in the right temporal regions and a patient with a mesial temporal sclerosis and interictal activity on the right fronto-temporal lobe.

**Patient No. 8.** The patient had a drug-resistant focal epilepsy, with complex partial seizures in the right temporal regions. He underwent right temporal lobectomy 5 years ago, but he still has a persistence of seizures (1-2 times per day). Seizures were characterized by speech arrest without motor or sensory symptoms with a short duration. The recent video-stereo-EEG monitoring showed the continuous presence of epileptiform discharges, with spikes, multiple spikes and low-voltage fast activity over the posterior part of the first temporal right convolution. During the hdEEG registration the patient had two typical seizures.

**Patient No. 9.** The patient showed the first febrile seizure at 6 years old characterized of an aura with unpleasant epigastric sensation sometimes dating back to the face and complex partial seizures with break contact and large motor automatisms with arms and legs lasting 30 s. From the age of 6 years the patient showed secondarily generalized complex partial seizures, which became refractory to drug therapy. The EEG was compatible with

right fronto-temporal epileptogenic foci with phase reversal at T4. The 3T MRI showed right mesial temporal sclerosis. He underwent right temporal lobectomy 1 year ago. Now he is seizure free.

**Patient No. 10.** The patient had an idiopathic epilepsy. She showed high-amplitude spike slow wave activity and her irritative focus was localized in T4-T6. The patient had seizures with clonic movements and head and eyes version. EEG showed right frontal and temporal isolated spikes and waves. In the following years, she was treated with antiepileptic drugs. The seizures are still present in random way and some of these seizures generalized. Spikes and waves were seen over the right central-temporal regions, which were more evident during drowsiness and sleep. Theta activity over the right frontal temporal regions was also present. MRI was without evident focal lesion.

### 6.1.3 Patient with generalized epilepsy

Generalized epilepsy is a form of epilepsy characterized by generalized seizure with no apparent cause. A generalized seizure distorts the electrical activity involving the whole or a large portion of the brain, including both hemispheres.

**Patient No. 11.** This patient was suffering of drug resistant epilepsy began about 20 years ago. She had one or more seizures per day, characterized by altered state of consciousness accompanied by oral-food and gestural automatism. Sporadically she showed crisis with loss of consciousness, slowly fall to the ground and automatisms. The EEG showed isolated buffees of slow theta activity mainly in the center-right temporal electrodes with contralateral spread. The MRI was normal.

### 6.1.4 Patient with cerebral palsy

Cerebral palsy is a disorder that affects muscle tone, movement, and motor skills. It is caused by abnormal brain development or damage and can occur during pregnancy, during childbirth or after birth up to about age three. The disorders appear in the first few years of life. It affects the ability to move and to maintain balance and posture. Cerebral palsy is frequently associated with other problems, such as mental, retardation, sensory defects and epilepsy.

**Patient No. 12.** This patient was affected by cerebral palsy and secondary

epilepsy with extensive ischemic lesion over the right hemisphere involving the frontal, the central, the parietal and temporal regions. The clinical neurological examination showed a severe left hemiparesis with mild hand movement and hypertonia on the left leg. The walking was possible only with help. Mild cognitive impairment was present, but the patient was collaborative and responsive. The patient had complex partial seizure with fall, clonic movement to the left arm and loss of consciousness.

## 6.2 Data acquisition

### 6.2.1 HdEEG

HdEEG recording was performed using 256 channels (Electrical Geodesic, Inc., Eugene, OR, USA) positioned according to the international 10/20 system. The data were recorded against a vertex electrode reference (Cz) at a sampling rate of 200 or 250 Hz and filtered off-line with a band-pass filter (1-30 Hz). The patient sit in a relaxed position. The EEG recording lasted about 40 min.

### 6.2.2 EEG-fMRI data

During MRI scanning, EEG data were acquired at a sampling rate of 1024 Hz using an MR-compatible EEG amplifier (SD MRI 32, Micromed, Treviso, Italy) and a cap with 32 Ag/AgCl electrodes positioned according to a 10/20 system. To avoid saturation, the EEG amplifier had a resolution of 22 bits with a range of $\pm 25.6$ mV. An anti-aliasing hardware band-pass filter was applied with a bandwidth of $0.15 - 269.5$ Hz. To remove pulse and movement artifacts during scanning, two of the electrodes were used to record the ECG and EMG. The EMG electrode was placed on the right abductor pollicis brevis muscle. The reference was placed anterior to Fz, and the ground posterior to Fz, as previously described elsewhere [Formaggio et al., 2008b, Storti et al., 2010] for the same system.

Functional images were acquired on a 1.5 T MR scanner (Symphony, Siemens, Erlangen, Germany) equipped with EPI capability and a standard transient/receive head coil. fMRI data were acquired with a $T2^*$ weighted EPI sequence (36 slices, TR = 3700 ms, TE = 50 ms, 64 $\times$64 matrix, FOV = 256 $\times$ 256, slice thickness 3 mm; voxel size = 3 $\times$ 3 $\times$ 3 mm, axial slice

orientation). At the start of each fMRI acquisition, the scanner gave a trigger signal that was recorded by the EEG system and used as a volume marker. A T1-weighted anatomical scan (192 slices, TR = 1990 ms, TE = 3 ms; scanning matrix 512 × 512, FOV = 256 × 256; slice thickness 1 mm; sagittal slice orientation) was also acquired for each patient. Only patient No. 8 underwent a 3T fMRI scan (functional data: TR = 3000 ms, TE = 30 ms). The patients were positioned supine on a bed inside the scanner bore, with elbows flexed at 120° and hands pronated in a relaxed position; the head was stabilized on both sides with adjustable padded restraints. During fMRI acquisition, the patients were instructed to keep their eyes closed and remain as still as possible throughout the procedure. A total of 200 volumes were acquired for patient No. 1, 130 volumes for patient No. 8, 100 volumes for patient No. 10 and 140 volumes for the remaining 9 patients; the duration of one volume was 3700 ms (3000 only for patient No. 8).

## 6.3 Data analysis

### 6.3.1 Source localization

HdEEG data were analyzed using Cartool software (http://sites.google.com/site/cartoolcommunity/). The T1 anatomical images acquired before each EEG-fMRI session were used to create a realistic model of the brain for source localization. The original MRI was anisotropic. The images were converted in isotropic using Brain Voyager (Brain Innovation, Maastricht, The Netherlands) with a voxel size of $1 \times 1 \times 1\ mm^3$. In each patient, the MRI data and the solution space were restricted to the gray matter. The solution space for the distributed source model contains from a min of 3000 to a max of 3060 points uniformly distributed over the gray matter of the brain mapped onto the SMAC space [Spinelli et al., 2000]. The SMAC head model method has been successfully employed in several previous clinical and experimental studies [Michel et al., 2004, Groening et al., 2009, Siniatchkin et al., 2010, Vulliemoz et al., 2010b, Brodbeck et al., 2011] and it produces localization precisions comparable with realistic boundary element models [Guggisberg et al., 2011]. The EEG electrode positions were matched to the MR scalp surface using transformation operations such as rotation and translation according to common landmarks during both EEG and MRI acquisition.

The peak of the spike was used as a trigger for averaging in epochs of

±500 ms. Two time frames were chosen to characterize spike topography: the first, from the beginning of the spike to the time point corresponding to 50% of the rising phase as an epoch characterizing a source of the possible spike generator [Lantz et al., 2003b]; the second, at the peak of the spike indicating propagation. Special attention was paid to marking the same type of spikes as those obtained during the recordings inside the scanner. A standardized source imaging procedure, LORETA [Pascual-Marqui et al., 1994] constrained to the individual matter, was applied to the averaged spikes. The localization of the sources is measured as current density ($A/m^3$).

### 6.3.2 GLM on EEG-fMRI data

#### EEG preprocessing

The data were preprocessed using Matlab 7 (MathWorks, Natick, MA, USA) and EEGLAB 4.51 (http://sccn.ucsd.edu/eeglab/) [Delorme and Makeig, 2004]. The EEG artifact, induced by the magnetic field gradient, was digitally removed off-line using an adaptive filter [Allen et al., 2000], while the EEG artifact associated with pulsatile blood flow, ballistocardiogram, was removed using an averaging procedure [Allen et al., 1998], both of which were implemented with SystemPlus software (Micromed). Reference-free recordings were then obtained by calculating the local average reference using EEGLAB. A notch filter (50 Hz) was also applied to all channels. EEG recordings were band-pass filtered from 1 to 30 Hz using a FIR filter because all of the patients had a routine EEG recording showing focal IEDs at frequencies above 1 Hz. The signal was then baseline corrected and detrended; epochs with artifacts were visually identified and excluded from the analysis.

#### EEG regressor analysis

ICA decomposition was performed on the EEG by FastICA algorithm implemented in EEGLAB. For wavelet analysis a family of Morlet wavelets was first constructed at 1 Hz frequency intervals, ranging from 1 to 20 Hz, to study all the frequency ranges of interest using a ratio of 8 oscillations (Eqs. 2.1-2.2). These values represent the optimal compromise in time-frequency to investigate power changes.

### fMRI preprocessing

Before statistical analysis, the functional data were preprocessed using Brain Voyager QX software. The MR images were realigned to reduce the effect of head motion (three-dimensional motion correction with sinc interpolation). To correct for the different acquisition times, slice scan time correction was used in an ascending, interleaved scanning order with linear interpolation over time. The data were then preprocessed with linear trend removal to remove all drifts, and with a temporal high-pass filter (3 cycles in time course) to reduce the effect of breathing and physiological noises. The anatomical and functional data were kept in the subject's native space. The optional temporal smoothing filter was not used during Brain Voyager QX analysis, while spatial Gaussian smoothing was used with Gaussian kernel 6-mm FWHM.

### GLM analysis

Activated voxels were identified with a single-subject GLM approach for the time series data [Friston et al., 1995] using the time-information of EEG events identified by an expert neurologist and the GF HRF for the conventional analysis.

In the new analysis the preprocessed EEG and fMRI data were analyzed by using a in-house software implemented in Matlab 7 to create the EEG protocol and the ibHRF (Chapters 2 and 3). Temporal autocorrelations were accounted for by fitting an AR model. Noise was modeled as an AR process estimated from the residuals by using Yule-Walker equations (Appendix B). The partial autocorrelation plots were examined to identify the AR order. A statistical significance was found for lag 1, indicating that the AR model was appropriate for all patients, except for patient No. 3. The confidence interval for statistical significance was of 95%. The 95% confidence interval for the partial autocorrelations is at $r = \pm 2/\sqrt{N}$, with N number of volumes (Table 6.1).

Brain activation was detected by comparing the signal intensity of active images (IED activity) with that of resting images based on the changes in local BOLD signals and on the voxel-wise Student's t-test (with FDR correction according to the number of voxels related to the brain volume). Z-score maps representing brain activation were then generated. The results were displayed as parametric statistical maps, where the pixel z value is expressed on a colorimetric scale.

### 6.3.3 PICA on fMRI data

#### fMRI preprocessing

The functional data were preprocessed using MELODIC version 3.09, a part of the FSL toolbox. The images were smoothed with a Gaussian kernel of FWHM of 6 mm and motion-corrected. To correct for the different acquisition times, an interleaved slice timing correction was used. The data were then preprocessed with high-pass temporal filtering (cut-off of 100 s) and with the removal of non-brain structures from the echo planar imaging volumes (Brain Extraction Tool [BET]).

#### PICA analysis

The preprocessed data underwent a PICA decomposition using MELODIC (Eq. 1.9). The maps were thresholded at a posterior probability threshold of $p > 0.5$ [Beckmann and Smith, 2004]. A threshold of z scores was used to visualize the IC maps. A variable number of ICs was obtained by PICA decomposition (range, 13 to 35 components). The RSNs were visually chosen because the automatic method to select the optimal number of components, (Chapter 5), has not yet been set up on these data. In order to identify which components were related to a patient's IED activity, the design matrix was fitted to the time course of each component. The design matrix constructed with the block protocol was used for patients Nos. 2, 6, 7, and 8 (patients without BOLD activation with the new method) and patient No. 5 (too noisy data to estimate the ibHRF), whereas the design matrix with the new regressor was used for patients Nos. 1, 3, 4, 9, 10, 11, and 12. Components significantly related to the IED activity (IC time courses with significant signal changes time-locked to the IED activity) were identified with an F-test ($p < 0.05$).

## 6.4 Results

Clinical information and results for each patient are summarized in Tables 6.2 and 6.3. A heterogeneous population was studied to explore methodological issues. The group of post-traumatic epilepsy patients was consistent in its number with some clinico-pathological correlations, whereas the rest of patients was heterogeneous.

BOLD signal changes obtained with the new GLM method were observed in 4 out of 7 post-traumatic patients in whom IEDs were recorded (patients Nos. 1, 3, 4, and 6; patient No. 6 only with the EEG regressor). The activation was improved in patients Nos. 3 and 4 using the new method instead of the conventional GLM. In patient No. 1 the sites of localization were the same but more focal. In patient No. 6 the sites of localization were confirmed. Patients Nos. 2, 5 and 7 had no BOLD activity. In some patients the IEDs inside the magnet were not very frequent and of limited duration, which subsequently created difficulties in the off-line analysis. On hdEEG, focal source localization correlated with BOLD activation in patients Nos. 1, 3, and 6.

In the remaining patients (patients Nos. 8, 9, 10, 11, and 12), GLM detected significant modifications in 4 out of 5 patients (patients Nos. 9, 10, 11, and 12) in according with the source localization. Patient No. 8 had no BOLD activity. The activation was improved in patients Nos. 9, 10, and 12 using the new method instead of the conventional GLM. In patient No. 11 the localizations of the activation were confirmed. All these patients obtained a source localization of the epileptic activity concordant with the clinical pictures.

AIC results, for the GF and the ibHRF identified on twelve patients, are summarized in Table 6.1. GF model provided the most parsimonious fit in 2 patients (Nos. 9 and 11) and ibHRF in 5 patients (Nos. 1, 3, 4, 10, and 12) in which the comparison is possible. In patients Nos. 9 and 11 the activation maps obtained with the EEG regressor and GF or ibHRF are comparable. As expected, extension and location of the activation map depend on the EEG regressor and on the HRF model used (especially in patients Nos. 1, 3, 4, 10, and 12).

PICA identified IED-related activity in 7 out of 12 patients (patients Nos. 1, 3, 4, 6, 8, 11, and 12). DMN was not always detected (patients Nos. 1, 5, 10, 11, and 12).

Because of the different natures of the source and BOLD activation (electrical and hemodynamic), the completely spatial matching of results was not always respected but a good closeness was detected. There are some reasons for a possible lack of perfect spatial concordance: in these patients the structural imaging relives abnormal brain regions that not in all cases corresponds to the focus.

### 6.4.1 Post-traumatic epilepsy group

**Patient No. 1.** HdEEG activity showed sequences of spike and wave complexes over the left fronto-central regions lasting more than 10 s (Fig. 6.2a). The source localization showed a defined localization over the rolandic areas compatible with focal EEG activity (Fig. 6.2b). EEG activity inside and outside the magnet showed a high amplitude over the left fronto-polar electrodes, with a phase reversal over the frontal and central electrodes (Fig. 6.3a). The results of wavelet transform showed the preponderance of component no. 13 (Fig. 6.3b), and the channel F3, related to patient's IED activity, was selected for the construction of EEG regressor (Fig. 6.28a). The conventional and new GLM analysis showed prominent BOLD activation over the left central cortical areas (rolandic and sylvian) adjacent to the brain damage and anterior to the ventricular enlargement and over the SMA during the spikes and wave discharges as compared to the resting state. A deactivation in the left frontal and parietal regions, not observed in the source analysis, was also obtained, FDR ($q<0.05$) (Fig.6.3c). Fig. 6.3c showed a good agreement between the conventional and the new method even if the last produced a weaker activation, probably due to the modulation in amplitude of the EEG protocol compared to the block protocol (Fig. 6.28a). The selection of ICs detected five useful components from among 34. Components nos. 12 and 31 were IED-related ICs: the first was positively correlated with the new GLM design matrix ($F = 3.77$, $p<0.0246$) and the second negatively ($F = 50.95$, $p<0.0000$) (Fig. 5.7); component no. 23 represented the occipital network; components nos. 15 and 19 the lesion-related ICs. The DMN was not detected (Fig. 6.3d).

**Patient No. 2.** HdEEG showed slow-wave activity in the perilesional frontal and prefrontal regions, consistent with the head trauma (Fig. 6.4a). The source localization showed a defined localization over the frontal region (Fig. 6.4b). The EEG acquired inside the scanner showed predominant left frontal activity (Fig. 6.5a). Component with higher wavelet power was the no. 13 (Fig. 6.5b). The EEG derived from this component showed that the IED activity was predominant on Fp1 channel according to the original EEG, indeed this channel was selected for the construction of the EEG regressor. The EEG-fMRI activation maps showed no significant activation, probably due to the short duration of sequences characterized by IED activity, FDR ($q<0.05$) (Fig. 6.5c). The PICA decomposition estimated 35 components, four of which

were related to internal processes: the DMN (component no. 34); the temporal network, a network primarily including the bilateral superior temporal cortex, corresponding to the auditory-phonological system (component no. 30); and two components related to the lesion area (components nos. 2 and 19). No IED-related IC was identified (Fig. 6.5d).

**Patient No. 3.** HdEEG data acquisition lasted 40 minutes; during drowsiness the patient showed activity with a maximal amplitude over the left central and frontal regions (Fig. 6.6a). The source localization showed left frontal mesial activity (Fig. 6.6b). The EEG acquired inside the magnet showed predominant activity over the left frontal electrodes, with a phase reversal at F7 (Fig. 6.7a). The results of wavelet transform showed the preponderance of component no. 6 (Fig. 6.7b), and the channel F7, related to patient's IED activity, was selected for the construction of the EEG regressor (Fig. 6.28b). The conventional GLM analysis identified a cluster in the frontal-central area; whereas the new analysis identifies also a cluster in the left frontal area close to the lesional zone and a deactivated cluster in the left frontal area, FDR ($q<0.05$) (Fig. 6.7c). The fMRI sequence was acquired in the awake state. Differently from BOLD activation localized in the perilesional area, the electric source was located on the left side in the awake state but more mesial in the drowsiness state. The PICA decomposition estimated 18 components, four of which were related to internal processes: the DMN (component no. 14) and the attention network (components no. 8). The component related to IED-activity are components nos. 15 and 16, the component no. 15 significantly correlated with the new design matrix, $F = 6.23$, $p<0.0003$ (Fig. 6.7d).

**Patient No. 4.** HdEEG showed high activity over the right frontal electrodes, as confirmed by the source analysis (Fig. 6.8a,b). EEG inside the MR scanner showed high activity on the frontal electrodes. The patient underwent two continuous EEG-fMRI sessions. During the first fMRI scanning, a spontaneous critical episode lasting about 41 s was recorded; it was characterized by arm lifting and flexion, synchronous bi-manual automatisms, and ended with extension and repositioning of the limbs on the chest. Isolated synchronous movements of the lower limbs occurred towards the middle of the critical episode (Fig. 6.1). The first delta rhythmic sequences and later muscle and motion artifacts suddenly appeared in the right frontal lobe. During attenuation of the motor phenomena, delta sequences were recorded in

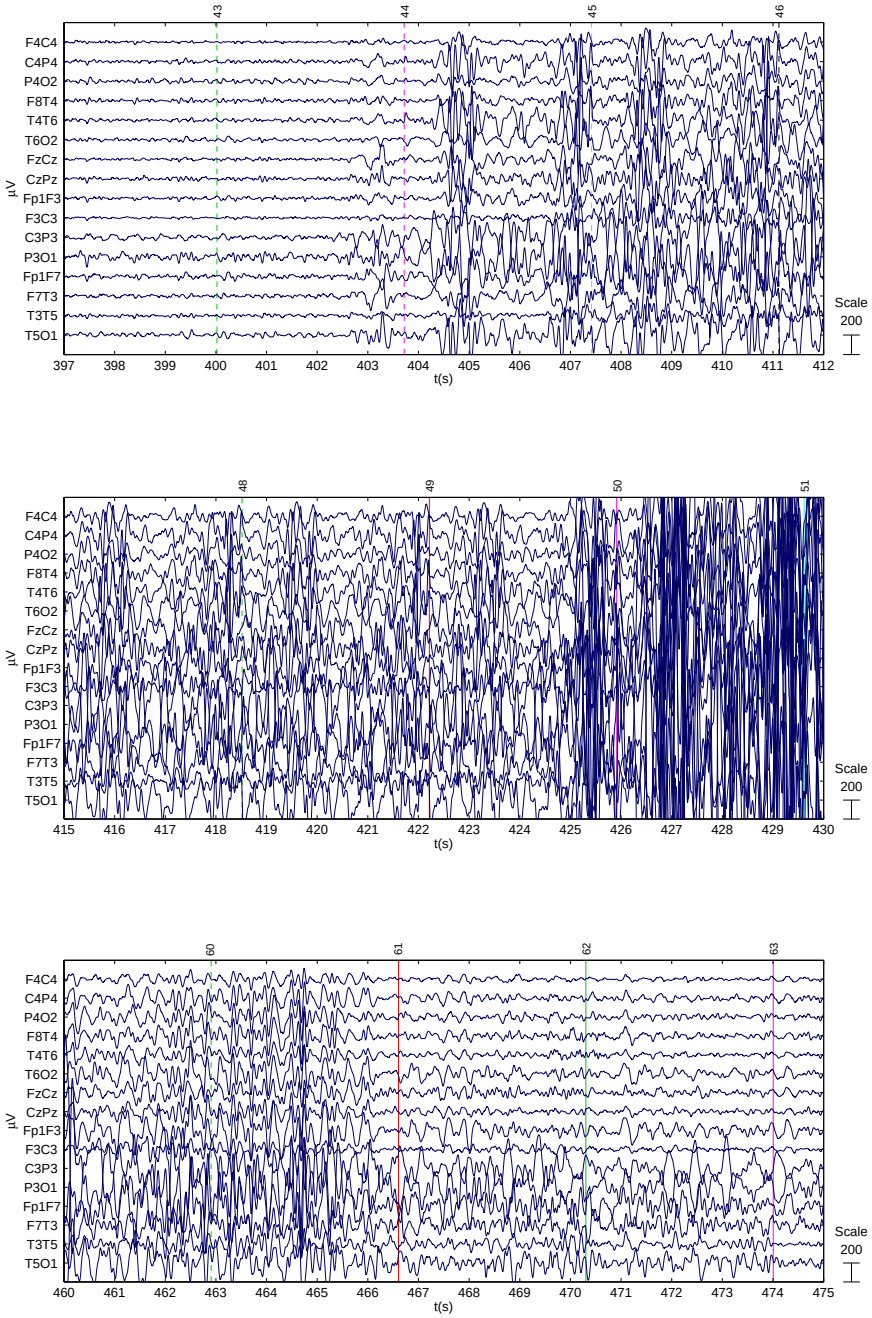


**Figure 6.1:** Patient No. 4. Seizure recorded during the first fMRI scanning.

the left frontal regions. The second fMRI scan was recorded during interical events and used for the analysis (Fig. 6.9a). The results of wavelet transform showed the preponderance of component no. 8 (Fig. 6.9b), and the channel F7, related to patient's IED activity, was selected for the construction of the EEG regressor (Fig. 6.28c). The new analysis compared with the conventional one showed high BOLD activity perilesional and localized over the frontal area, FDR ($q<0.001$) (Fig. 6.9c). The PICA decomposition estimated 20 components, three of which were selected: one related to IED activity that positively correlated with the new GLM design matrix, $F = 6.39$, $p<0.0022$ (component no. 7); one related to the DMN (component no. 16); and one related to the area of the lesion (component no. 10) (Fig. 6.9d).

**Patient No. 5.** HdEEG showed high activity over the left central posterior electrodes (Fig. 6.10a). The source was precisely localized over the left residual rolandic area (Fig. 6.10b). EEG acquired inside the scanner showed slow activity in the left motor area, with phase reversal at C3 (Fig. 6.11a). The results of wavelet transform showed the preponderance of component no. 17 (Fig. 6.11b), and the channel C3, related to patient's IED activity, was selected for the construction of the EEG regressor. No BOLD activity was measured with conventional and new analysis GLM analysis, FDR ($q<0.05$) (Fig. 6.11c). The PICA decomposition estimated 21 components, two of which related to the area of the lesion (components nos. 11 and 15) were selected. No DMN or IED-related IC was identified (Fig. 6.11d).

**Patient No. 6.** HdEEG was recorded in the waking state and at initial drowsiness. HdEEG showed high activity over the left fronto-central-temporal area (Fig. 6.12a). The source analysis showed two focal sources near the lesion: one frontal and more anterior and the other more toward the left side (Fig. 6.12b). EEG inside the magnet showed a slow sequence on the left fronto-temporal electrodes, particularly over F7 (Fig. 6.13a). The results of wavelet transform showed the preponderance of components nos. 5, 6, 7, 13, 16, and 17 (Fig. 6.13b), and the channel F7, related to patient's IED activity, was selected for the construction of the EEG regressor. EEG-fMRI showed two main changes: the first was characterized by more anterior activation in the frontal area and the second by more lateralized deactivation in the left frontal area, FDR ($q<0.001$). The new GLM analysis created using the EEG regressor without ibHRF confirmed the conventional one. The ibHRF was not calculated because of noisy fMRI signal (Fig. 6.13c). PICA decom-

position estimated 19 components, five of which were selected: components nos. 1 and 10 were significantly IED-related ICs; the first was negatively ($F=9.73$, $p<0.0001$) and the second positively ($F=23.54$, $p<0.0000$) correlated with the conventional GLM design matrix; component no. 16 was the DMN; components nos. 2 and 3 were lesion-related ICs (Fig. 6.13d).

**Patient No. 7.** HdEEG showed maximal amplitude over the right temporal electrodes (Fig. 6.14a). The source analysis showed a focal source localized in the right temporal lobe (Fig. 6.14b). The EEG acquired inside the magnet showed predominant activity over the right temporal regions (T4) (Fig. 6.15a). The results of wavelet transform showed the preponderance of component no. 21 (Fig. 6.15), and the channel T4, related to patient's IED activity, was selected for the construction of the EEG regressor (Fig. 6.28d). According to the GLM analysis, the BOLD activity showed an activation in the right temporal lobe and other sparse activations, whereas the new analysis did not show any activations, FDR ($q<0.05$) (Fig. 6.15c). The PICA decomposition estimated 13 components, three of which were selected: the attention network (component No. 2), the occipital network (component No. 1), and the DMN (component No. 9). No IED-related IC was identified (Fig. 6.15d).

### 6.4.2 Temporal epilepsy group

**Patient No. 8.** HdEEG showed maximal amplitude over the right temporal electrodes (Fig. 6.16a). The source analysis showed a focal source localized in the right temporal lobe (Fig. 6.16b). The EEG acquired inside the magnet showed predominant activity over the right temporal regions (Fig. 6.17a). The results of wavelet transform showed the preponderance of component no. 20 (Fig. 6.17b), and the channel T4, related to patient's IED activity, was selected for the construction of EEG regressor. No BOLD activity was measured with conventional and new GLM analysis, FDR ($q<0.05$) (Fig. 6.17c). The PICA decomposition estimated 26 components, six of which were selected: one related to IED activity (component No. 15, no significant correlation with the conventional GLM design matrix), one related to the area of the lesion (component no. 22), the occipital network (component No. 5), the DMN (component No. 24), the motor network (component No. 6), and the attention network (component no. 26) (Fig. 6.17d).

**Patient No. 9.** HdEEG showed maximal amplitude over the right temporal

electrodes (Fig. 6.18a). The source analysis showed a focal source localized in the right temporal lobe (Fig. 6.18b). The EEG acquired inside the magnet showed predominant activity over the right temporal regions (Fig. 6.19a). The results of wavelet transform showed the preponderance of components nos. 8 and 22 (Fig. 6.19b), and the channel T6, related to patient's IED activity, was selected for the construction of the EEG regressor (Fig. 6.29a). The conventional EEG-fMRI analysis identified a negative BOLD cluster in the right temporal lobe, the new analysis EEG-fMRI showed a focal BOLD activity in the right temporal lobe compatible with mesial temporal sclerosis, FDR ($q<0.05$) (Fig. 6.19c). The PICA decomposition estimated 26 components, two of which were selected: the occipital network (component No. 23) and the DMN (component No. 25). No IED-related IC was identified (Fig. 6.19d).

**Patient No. 10.** HdEEG showed maximal amplitude over the right frontal temporal regions; more evident during drowsiness and sleep (Fig. 6.20a). The source analysis showed a focal source localized in the frontal lobe during the rising phase and also a source localized in the right temporal lobe during the propagation (Fig. 6.20b). The EEG acquired inside the magnet showed predominant activity over the right temporal regions (Fig. 6.21a). ICA decomposition highlighted the components nos. 3, 4, 7, and 9 (Fig. 6.21b). T4 was the channel which better describes the IED activity, therefore it was used as regressor (Fig. 6.29b). The new GLM analysis showed significant activations over the frontal and the right temporal regions according to the spatial distribution of her IED activity. There were differences in the regions obtained using the conventional analysis, which in particular was not able to identify the frontal activation, FDR ($q<0.05$) (Fig. 6.21c). The PICA decomposition estimated 21 components, one of which was selected: the occipital network (component No. 14). No DMN or IED-related IC was identified (Fig. 6.21d).

### 6.4.3 Patient with generalized epilepsy

**Patient No. 11.** HdEEG showed high amplitude over the right central-temporal electrodes (Fig. 6.22a). The source analysis showed three sources localized in the right parietal lobe, in the right frontal lobe and in the left temporal region (Fig. 6.22b). The EEG acquired inside the magnet showed predominant activity over the right central-temporal regions (Fig. 6.23a). The

results of wavelet transform showed the preponderance of components nos. 3 and 4 (Fig. 6.23b), and the channel C4, related to patient's IED activity, was selected for the construction of the EEG regressor (Fig. 6.29c). The conventional and the new EEG-fMRI analysis identified BOLD activations in the right temporal lobe, in the SMA, in the right posterior regions and in the left temporal lobe, FDR ($q<0.05$) (Fig. 6.23c). The PICA decomposition estimated 23 components, one of which was selected: the IED related activity (component No. 18), which was positively correlated with the new GLM design matrix, $F = 31.81$, $p<0.0000$. No DMN was identified (Fig. 6.23d).

### 6.4.4 Patient with cerebral palsy

**Patient No. 12.** HdEEG showed high amplitude over the right temporal electrodes (Fig. 6.24a) and a diffused activity over the left temporal lobe (Fig. 6.25a). The source analysis showed a main source localized in the right temporal lobe (Fig. 6.24b) and diffused activity in the contralateral side (Fig. 6.25b). The standard EEG had a high-amplitude rhythmic activity at 4-5 Hz over the right central temporal electrodes (Fig. 6.26a). During the recording his activity rapidly diffused over the contralateral central and temporal electrodes with long sequence of spikes and slow waves complexes (Fig. 6.26b). ICA decomposition pointed out the preponderance of component no. 14 (Fig. 6.26c) and component no. 11 (Fig. 6.26d). The first was responsible for the channel T4, while the second one for the channel T3 (Fig. 6.29d). fMRI maps showed several activations: in perilesional regions with a diffusion over the parieto-temporal regions contralateral to the lesion. Differently from the conventional analysis that only produced one activation map; the two EEG regressors, derived from the two components, produced different fMRI activation maps. The new analysis is able to distinct the two activities generating the different activation maps (Fig. 6.27a). The PICA decomposition was repeated twice. The first analysis created 17 components, three of which were selected: two IED related activity (component no. 5) that correlated with the design matrix constructed from the EEG component no. 14 ($F = 39.73$, $p<0.0000$), and component no. 6 ($F = 5.80$, $p<0.0038$); one component related to the lesion area (component no. 8). No DMN was identified. The second analysis creates 17 components, three of which were selected: two IED related activity (component no. 6) that positively correlated with the design matrix constructed from the EEG component no. 11 ($F = 83.24$,

p<0.0000), and component no. 4 (F = 36.16, p<0.0000); one component related to the lesion area (component no. 7). No DMN was identified (Fig. 6.27b).

## 6.5 History, practical issues and pitfalls

Our recent experience on EEG-fMRI consists of a heterogeneous group of 34 patients with epilepsy. Patients were selected for the EEG-fMRI resting state protocol on the basis of frequent spiking. In these patients changes in BOLD signal were observed in 24 out of 34 patients in whom IEDs were recorded. In 83%, these were concordant with expected epileptic activity defined by EEG and clinical outcome. The remaining 10 patients had no significant BOLD activity because of either technical problems or no interictal epileptiform EEG activity inside the scanner. During the EEG-fMRI session some patients did not show an high-amplitude activity inside the magnet whereas the analysis required that the activity was present alternately during the exam. A possible explanation is that the IED activity could be affected by the state of the patient inside the magnet or even by possible influences of the magnetic field. Some of these cases are reported in some of our publications [Avesani et al., 2008, Manganotti et al., 2008, Del Felice et al., 2009, Borelli et al., 2010, Formaggio et al., 2011].

Twelve patients of them (reported in this thesis) were selected to underwent a hdEEG registration in order to observe if a correlation with the BOLD activity was present or if the source localization could provide more information when the EEG-fMRI did not show any activation. To validate these methods of analysis, repeated measurements on the same patient in different sessions would be needed. Repeated measures are easy to acquire on hdEEG: the 256-electrode cap is fast to use and the stress on the patient is low. The picture is more complex as regards the fMRI session because of the difficult availability of the magnet for research studies, but mainly because the registration process is stressful for the majority of the patients we selected. For these reasons we would prefer to increase the number of patients rather than repeat the entire exam in the same patient.

**Table 6.1:** Mean AIC of active voxels and number of active voxels obtained with the conventional and the new method.

| pt | $\rho$ values | | | | | corr | active voxels | | AIC | |
|---|---|---|---|---|---|---|---|---|---|---|
| | conv | | new | | | FDR | conv | new | conv | new |
| | pre | post | pre | post | r | | | | | |
| **Post-traumatic epilepsy group** | | | | | | | | | | |
| **1** | 0.4015 | 0.0095 | 0.405 | 0.010 | ±0.1414 | <0.05 | 2601 | 429 | 2800.6 | 2769.2 |
| **2** | 0.4314 | 0.00382 | – | – | ±0.169 | <0.05 | 0 | – | – | – |
| **3** | 0.1198 | n.a. | 0.1212 | n.a. | ±0.169 | <0.05 | 127 | 308 | 1755.3 | 1739.6 |
| **4** | 0.2157 | -0.0052 | 0.2089 | -0.0008 | ±0.169 | <0.05 | 5666 | 14084 | 1758.1 | 1740.1 |
| **5** | 0.203 | 0.0055 | – | – | ±0.169 | <0.05 | 0 | – | – | – |
| **6** | 0.1828 | -0.0052 | 0.1860* | -0.0039* | ±0.169 | <0.001 | 4721 | 3955* | 1364.7 | – |
| **7** | 0.2891 | 0.0293 | 0.2915 | 0.0299 | ±0.169 | <0.05 | 319 | 0 | 1362.2 | – |
| **Temporal epilepsy group** | | | | | | | | | | |
| **8** | 0.3069 | 0.0343 | – | – | ±0.1754 | <0.05 | 0 | – | – | – |
| **9** | 0.4516 | 0.0106 | 0.462 | 0.008 | ±0.169 | <0.05 | 19 | 994 | 1726.9 | 1826.1 |
| **10** | 0.2776 | 0.0027 | 0.2757 | 0.0071 | ±0.2 | <0.05 | 5 | 63 | 1212.2 | 907.0 |
| **Patient with generalized epilepsy** | | | | | | | | | | |
| **11** | 0.267 | 0.0093 | 0.2642 | 0.012 | ±0.169 | <0.05 | 2942 | 2883 | 1773.5 | 1783.5 |
| **Patient with cerebral palsy** | | | | | | | | | | |
| **12** | 0.2687 | 0.0063 | 0.237 | 0.002 | ±0.169 | <0.05 | 4529 | 26834 | 1739.0 | 1727.1 |

pt = patient; $\rho$ values = coefficient of autoregressive model, order 1 (Appendix B); conv = conventional analysis; new = new analysis; pre = before application AR(1) to the error term (correlation values); post = after the application of AR(1) to the error term; r = confidence intervals (95%); corr = BOLD correction; FDR = false discovery rate; AIC = Akaike information criterion; n.a. = not applied; * = only EEG regressor applied without ibHRF.

**Table 6.2:** Clinical profiles

| pt | age | sex | trauma | $1^{st}$ seizure | drugs | EEG | p.r. | lesion | imaging | IED localization ESI | IED localization EEG-fMRI |
|---|---|---|---|---|---|---|---|---|---|---|---|
| **Post-traumatic epilepsy group** | | | | | | | | | | | |
| **1** | 43 | M | car accident | 2 years | VPA 550 mg/die, ZNS 325 mg/die, LEV 4000 mg/die, OXC 2100 mg/die, PB 100 mg/die | low voltage on the fronto-central hemisphere electrodes | F3 | left brain damage | left cerebral atrophy, poroencephalic lesions and gliosis | left frontal and central regions | activation of left central region, SMA and deactivation of the frontal cortex |
| **2** | 32 | M | car accident | 2 years | VPA 2500 mg/die, OXC 1800 mg/die | slow waves activity in left frontal regions | F3 | bilateral frontal brain lesions | left frontopolar poroencephalic cysts with atrophy and gliosis | frontal lobe | no BOLD activation |
| **3** | 46 | M | accidental fall | 24 years | LEV 2000 mg/die | slow left fronto-temporal foci | F7 | left frontal extradural hematoma | left frontal poroencephalic cyst | left frontal-mesial lobe (drowsiness) | left frontal-central lobe |
| **4** | 27 | M | motorcycle accident | 1 year | CBZ 1400 mg/die, ZNS 475 mg/die, PB 125 mg/die | theta polymorphic sequences on the left fronto-temporal electrodes | F7 | fracture of the right frontal cranium | alteration of signal intensity on the left but mainly right frontal lobes | right front lobe | frontal lobe |
| **5** | 44 | M | work accident | 9 months | OXC 1800 mg/die, LEV 500 mg/die, PB 100 mg/die | slow theta and delta sequences with isolated components with sharp morphology | C3 | left fronto-temporo-parietal acute subdural hematoma, multiple brain lesions and cerebral edema | left temporo-occipital poroencephalic cyst, hypodense areas in bilateral frontal and left temporo-parietal regions | left central posterior electrodes | no BOLD signal |
| **6** | 57 | M | car accident | 4 years | PHT 400 mg/die, Clonazepam 2 mg/die | theta slow sequences on left fronto-temporal electrodes | F7 | fracture of the left frontal cranium | large poroencephalic lesion in the left frontal and fronto-orbital areas with gliosis | left frontal-central-temporal lobe | activation in frontal area and deactivation in left frontal area |
| **7** | 57 | M | accidental fall | 1 year | OXC 1800 mg/die | theta-delta activity on the fronto-temporal areas | T4 | right skull fracture, right acute subdural hematoma and bitemporal lesions | pore cavity of the brain with atrophy and gliosis perifocal and expansion bilaterally of the ex-vacuo temporal ventriculi | right temporal lobe | no BOLD signal |

pt=patient; $1^{st}$ seizure = first seizure from injury; p.r.= phase reversal of EEG

**Table 6.3:** Clinical profiles.

| pt | age | sex | EEG | p.r. | imaging | IED localization | |
|---|---|---|---|---|---|---|---|
| | | | | | | ESI | EEG-fMRI |
| **Temporal epilepsy group** | | | | | | | |
| **8** | 34 | M | multiple spikes and low-voltage fast activity over the posterior part of the first temporal right convolution | T4 | right temporal lobectomy 5 years ago | right temporal lobe | no BOLD signal |
| **9** | 31 | M | slow sequence theta and sometimes delta EEG on the right fronto-temporal lobe | T4 | mesial temporal sclerosis | right temporal lobe | right temporal lobe |
| **10** | 25 | F | spikes and waves over the right central temporal regions; more evident during drowsiness and sleep | T4-T6 | MRI without evident focal lesion | right temporal and frontal lobe | right temporal and frontal lobe |
| **Patient with generalized epilepsy** | | | | | | | |
| **11** | 45 | F | isolated buffees of slow theta activity mainly on the center-right temporal electrodes with contralateral spread | – | normal MRI | right temporal and posterior regions | bilateral temporal regions, right posterior region and SMA |
| **Patient with cerebral palsy** | | | | | | | |
| **12** | 29 | M | high amplitude rhythmic activity at 4-5 Hz over the right central temporal electrodes | T4 | extensive ischemic lesion over the right hemisphere involving the frontal, the central, the parietal and temporal regions | bilateral temporal regions | bilateral temporal regions |

pt = patient; $1^{st}$ seizure = first seizure from injury; p.r.= phase reversal of EEG

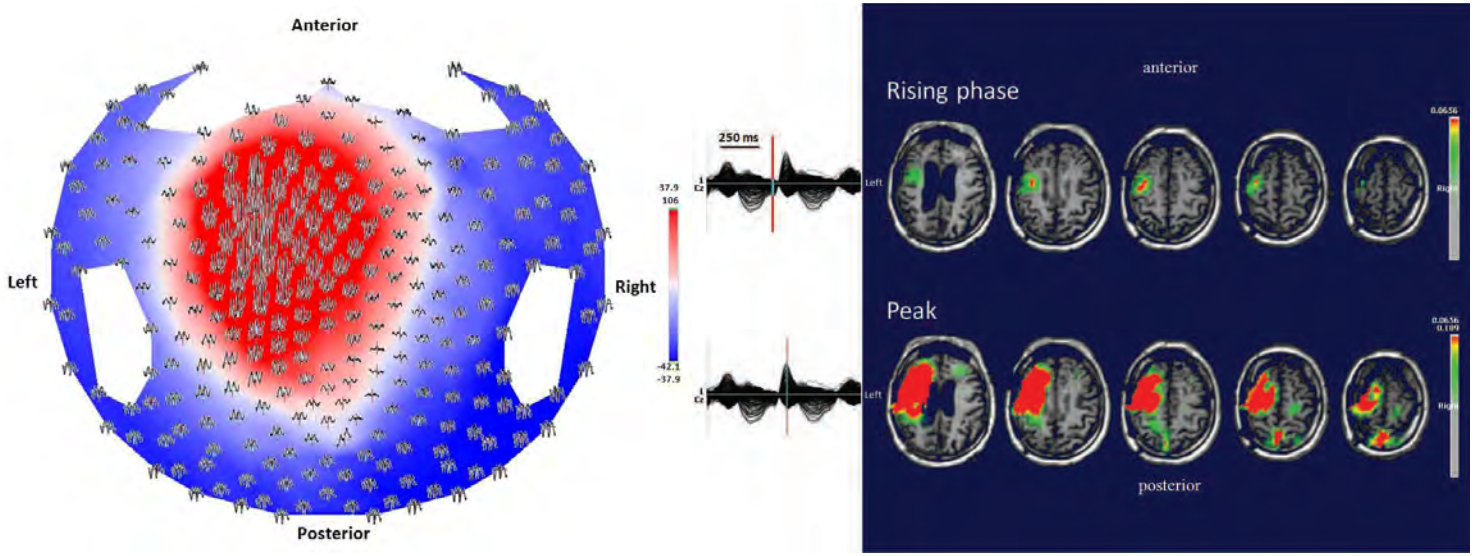


(a) (b)

**Figure 6.2:** Patient No. 1. (a) HdEEG signal visualized according to the projected locations of the scalp electrodes (spike average). The representation of the potential is set at the maximum value of the global field power. (b) HdEEG source analysis results. On the left, 256-channel EEG traces with a duration of 1 s (spike average). The global field power is used for the onset (red line). On the right, EEG source imaging in the rising phase of the peak and at the peak. The maximum of the estimated source of the average interictal spike is indicated in red.

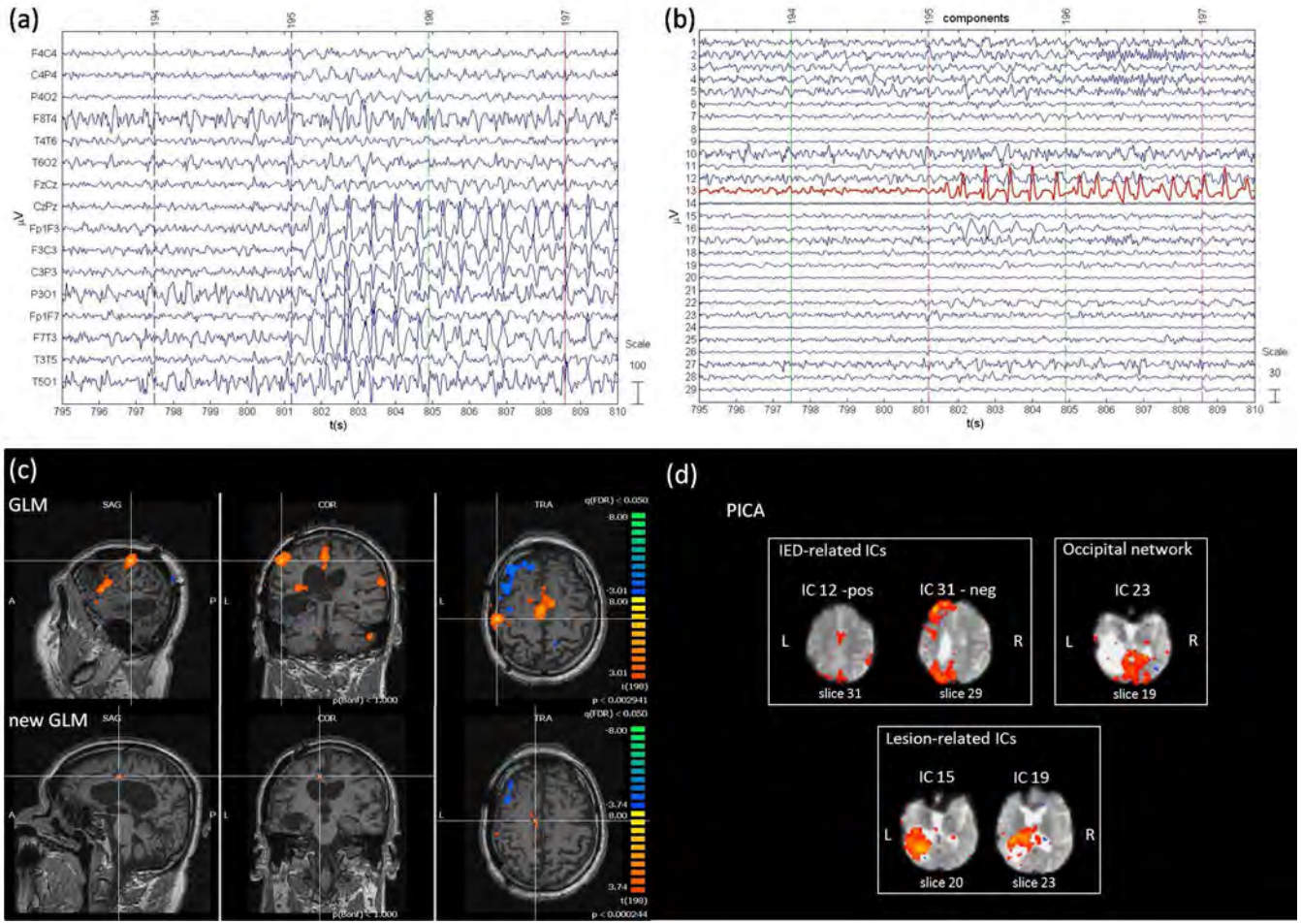


**Figure 6.3:** Patient No. 1. (a) EEG acquired during fMRI scanning after preprocessing. (b) EEG components obtained by ICA decomposition. EEG component no. 13 was selected. (c) EEG-fMRI results from the conventional (up) and new (down) GLM analysis (FDR, p<0.05). (d) EEG-fMRI results from the PICA analysis.

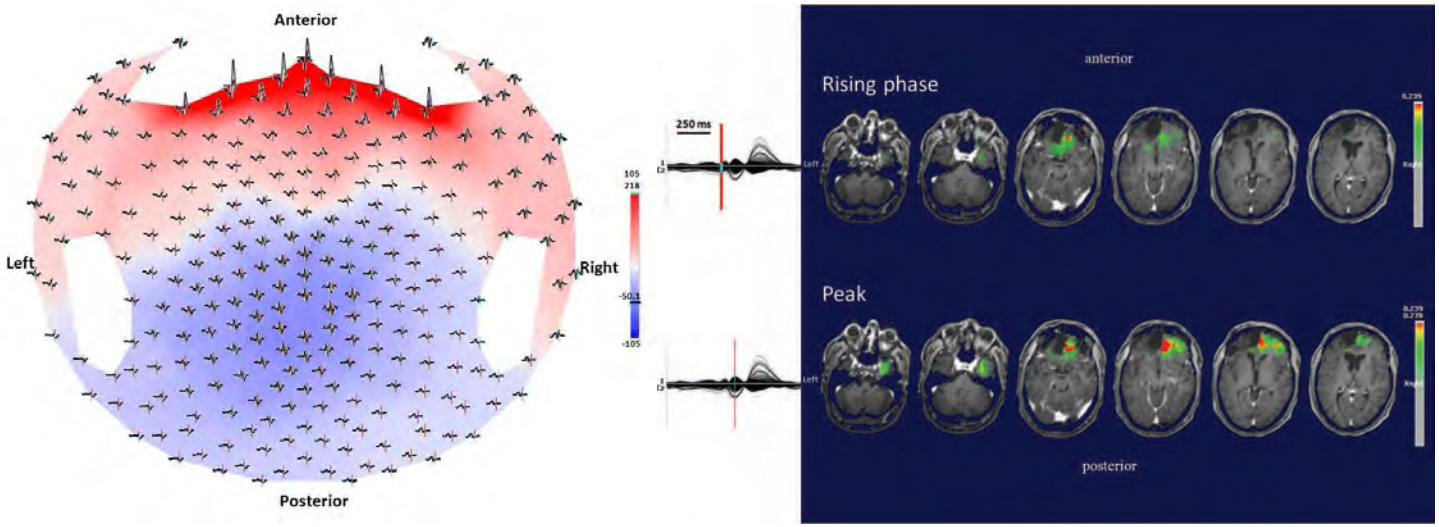


**Figure 6.4:** Patient No. 2. (a) HdEEG signal visualized according to the projected locations of the scalp electrodes (spike average). The representation of the potential is set at the maximum value of the global field power. (b) HdEEG source analysis results. On the left, 256-channel EEG traces with a duration of 1 s (spike average). The global field power is used for the onset (red line). On the right, EEG source imaging in the rising phase of the peak and at the peak. The maximum of the estimated source of the average interictal spike is indicated in red.

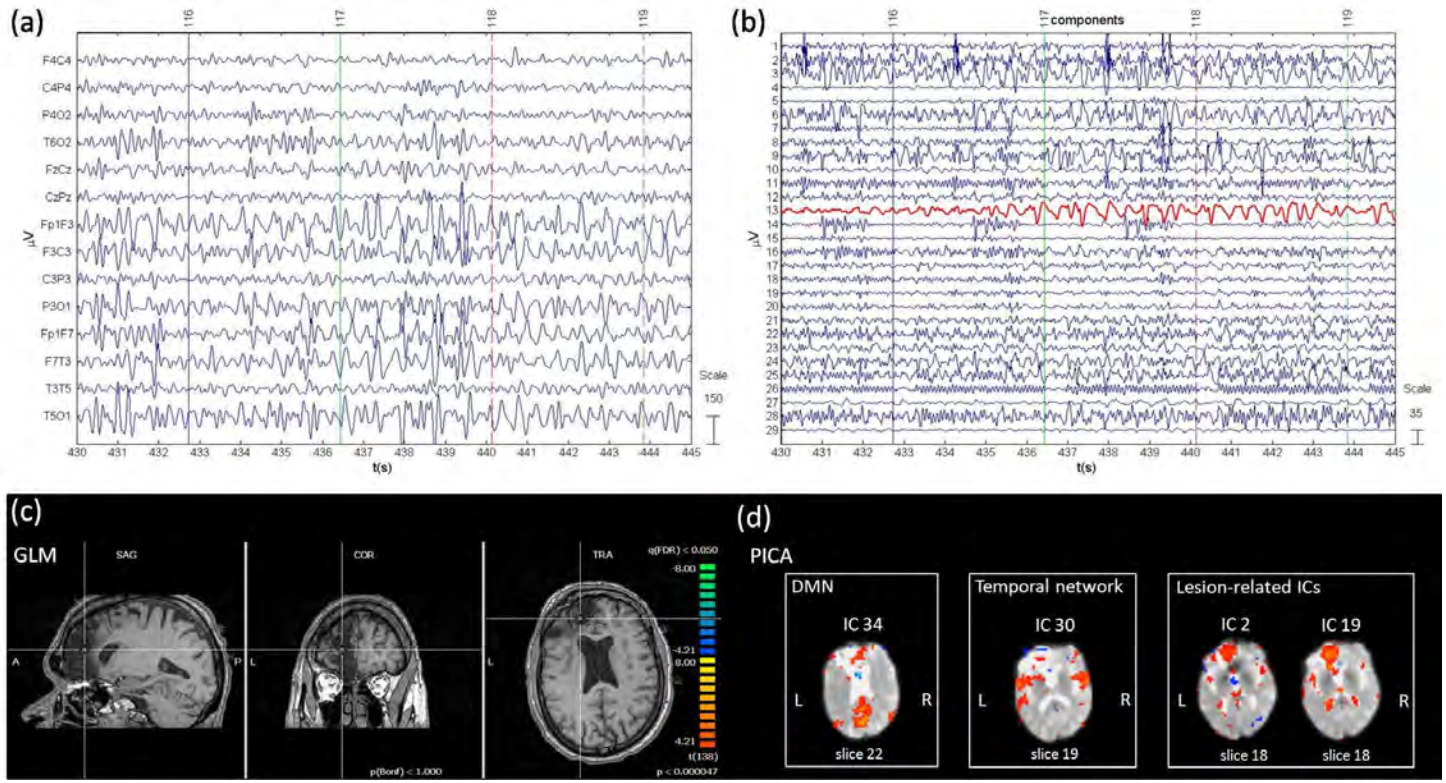


**Figure 6.5:** Patient No. 2. (a) EEG acquired during fMRI scanning after preprocessing. (b) EEG components obtained by ICA decomposition. EEG component no. 13 was selected. (c) EEG-fMRI results from the GLM analysis (FDR, $p<0.05$). (d) EEG-fMRI results from the PICA analysis.

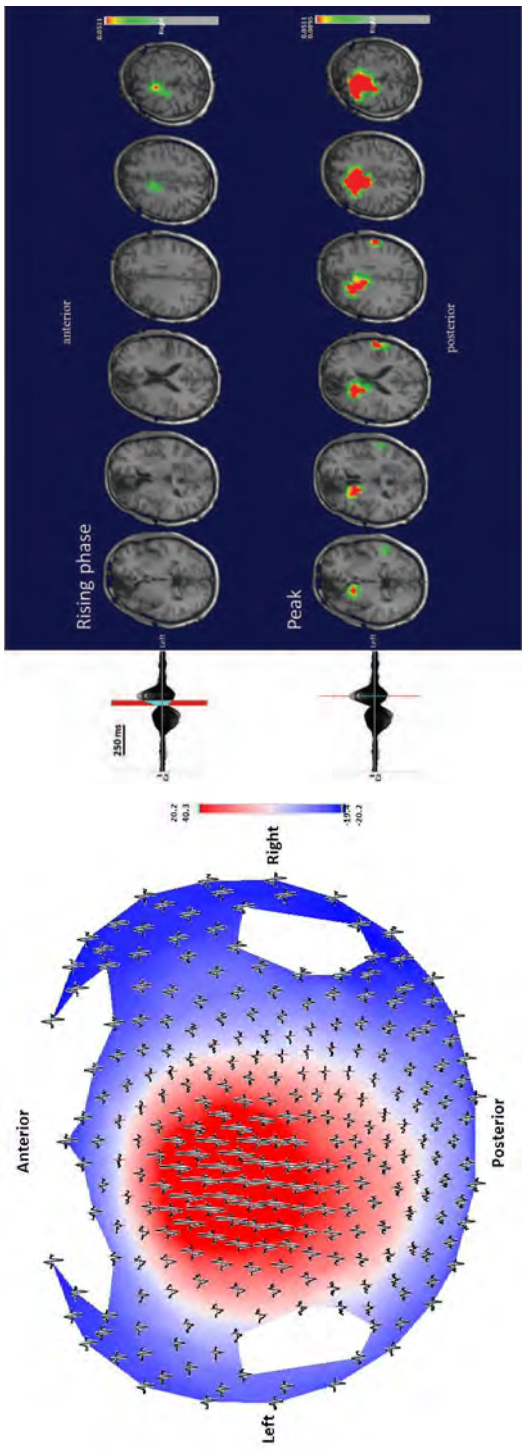


**Figure 6.6:** Patient No. 3. (a) HdEEG signal visualized according to the projected locations of the scalp electrodes (spike average). The representation of the potential is set at the maximum value of the global field power. (b) HdEEG source analysis results. On the left, 256-channel EEG traces with a duration of 1 s (spike average). The global field power is used for the onset (red line). On the right, EEG source imaging in the rising phase of the peak and at the peak. The maximum of the estimated source of the average interictal spike is indicated in red.

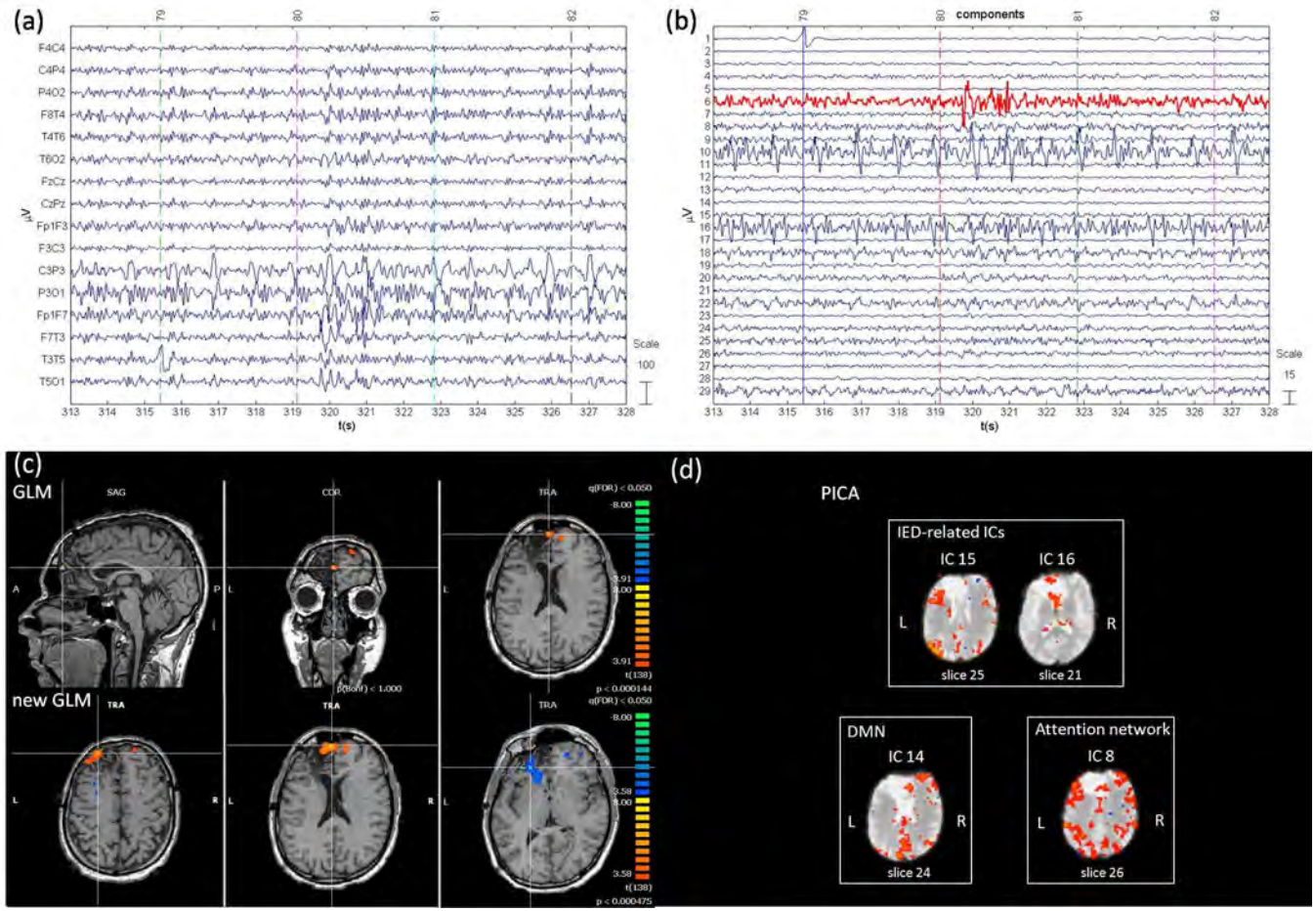


**Figure 6.7:** Patient No. 3. (a) EEG acquired during fMRI scanning after preprocessing. (b) EEG components obtained by ICA decomposition. EEG component no. 6 was selected. (c) EEG-fMRI results from the GLM analysis (FDR, p<0.05). (d) EEG-fMRI results from the PICA analysis.

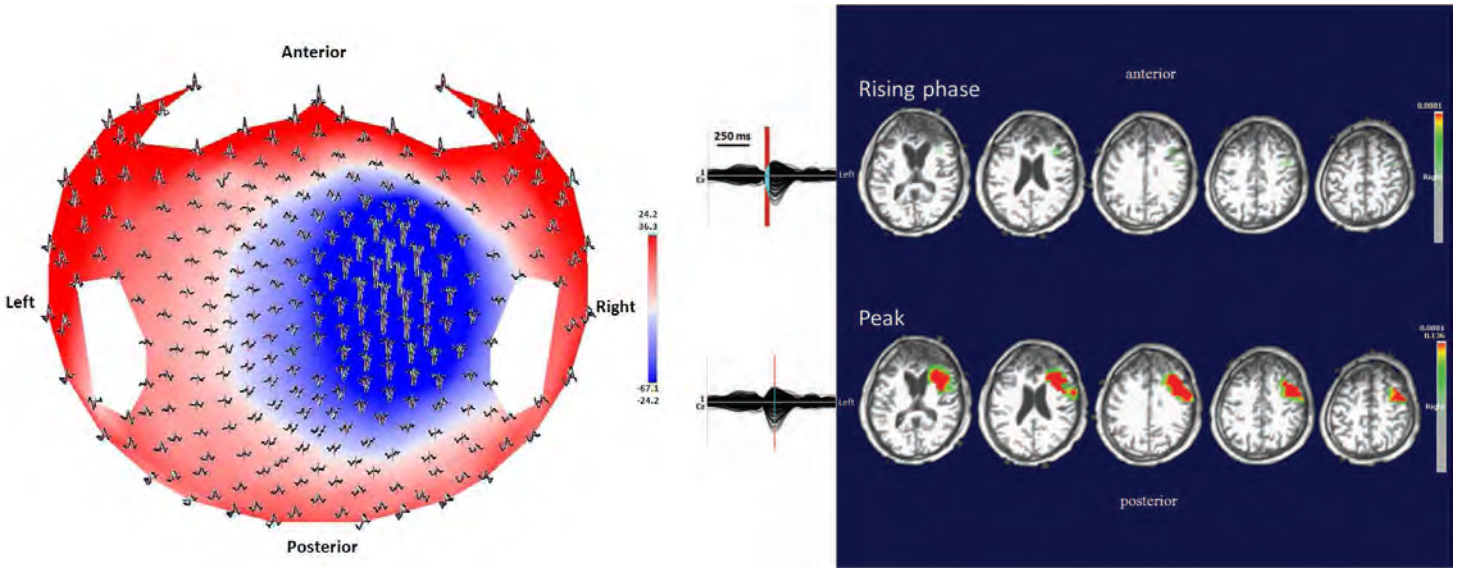


**Figure 6.8:** Patient No. 4. (a) HdEEG signal visualized according to the projected locations of the scalp electrodes (spike average). The representation of the potential is set at the maximum value of the global field power. (b) HdEEG source analysis results. On the left, 256-channel EEG traces with a duration of 1 s (spike average). The global field power is used for the onset (red line). On the right, EEG source imaging in the rising phase of the peak and at the peak. The maximum of the estimated source of the average interictal spike is indicated in red.

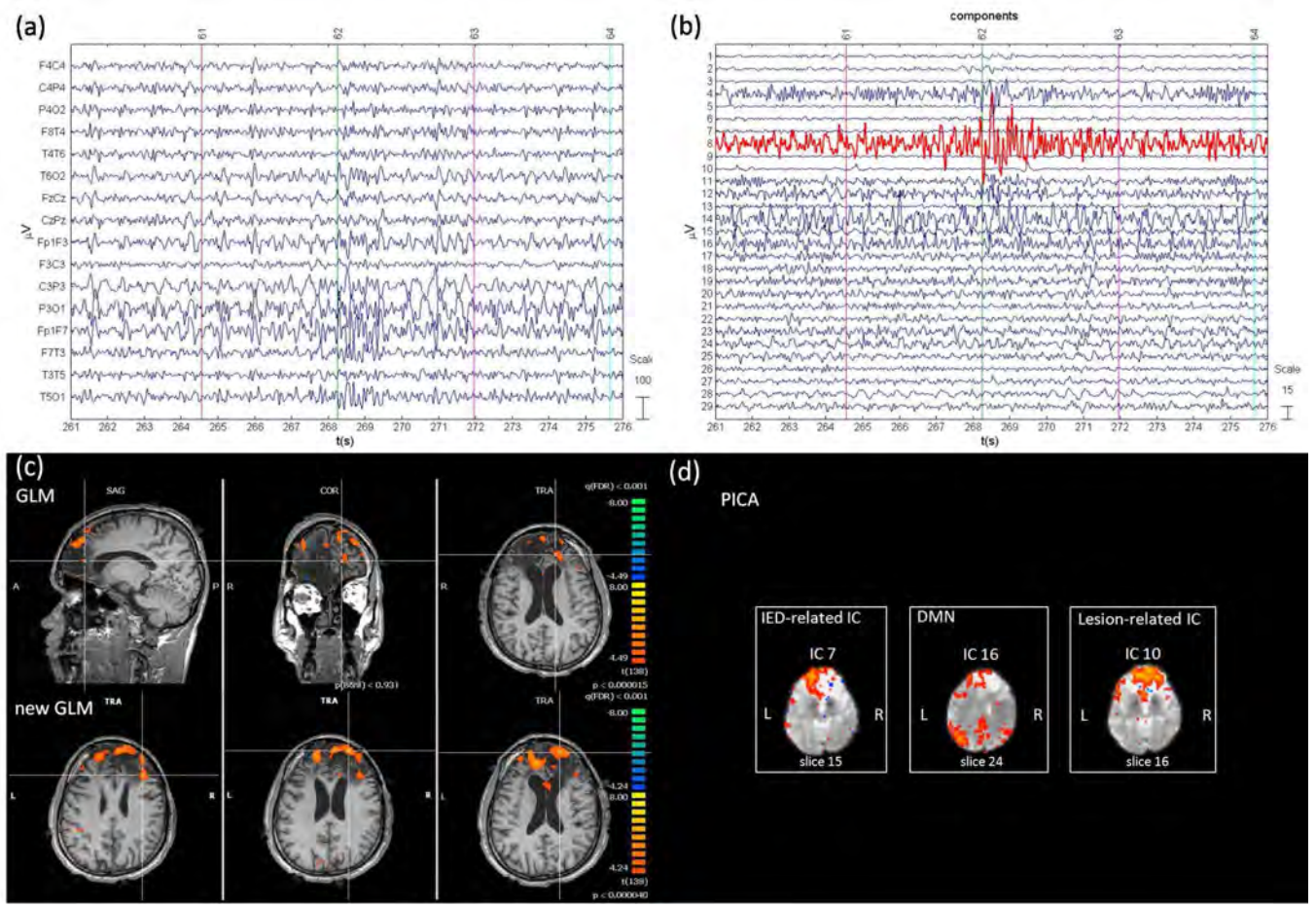


**Figure 6.9:** Patient No. 4. (a) EEG acquired during the second fMRI scanning after preprocessing. (b) EEG components obtained by ICA decomposition. EEG component no. 8 was selected. (c) EEG-fMRI results from the GLM analysis (FDR, p<0.001). (d) EEG-fMRI results from the PICA analysis.

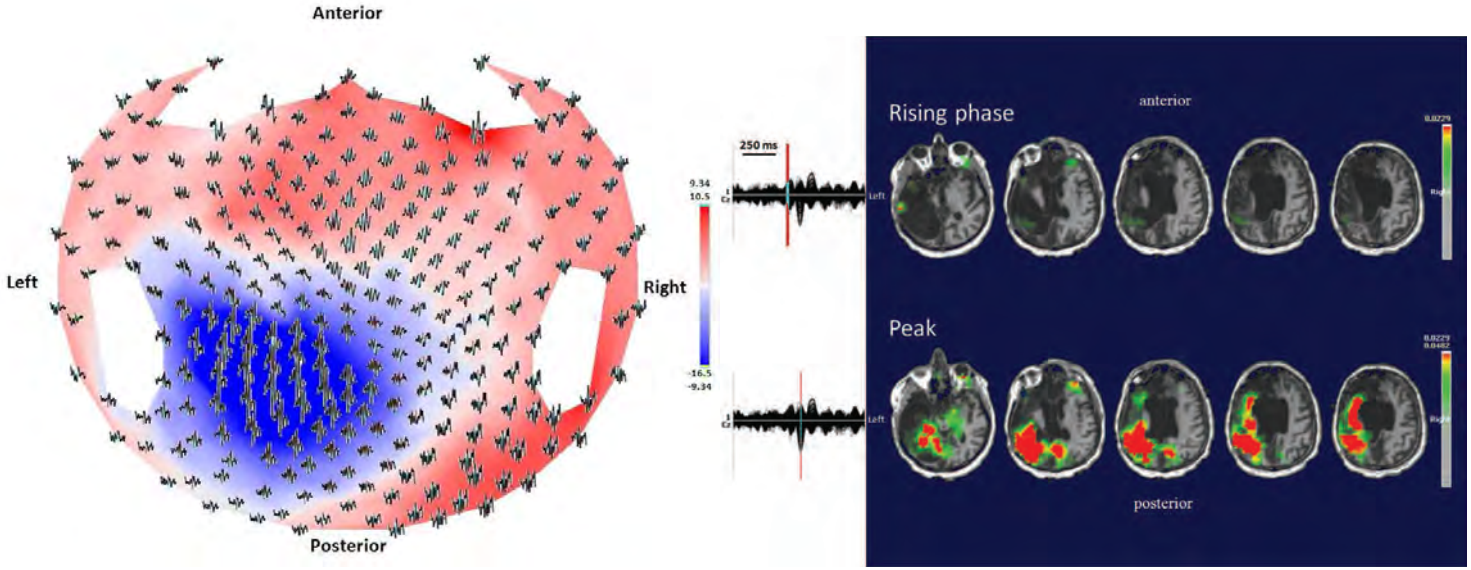


(a) (b)

**Figure 6.10:** Patient No. 5. (a) HdEEG signal visualized according to the projected locations of the scalp electrodes (spike average). The representation of the potential is set at the maximum value of the global field power. (b) HdEEG source analysis results. On the left, 256-channel EEG traces with a duration of 1 s (spike average). The global field power is used for the onset (red line). On the right, EEG source imaging in the rising phase of the peak and at the peak. The maximum of the estimated source of the average interictal spike is indicated in red.

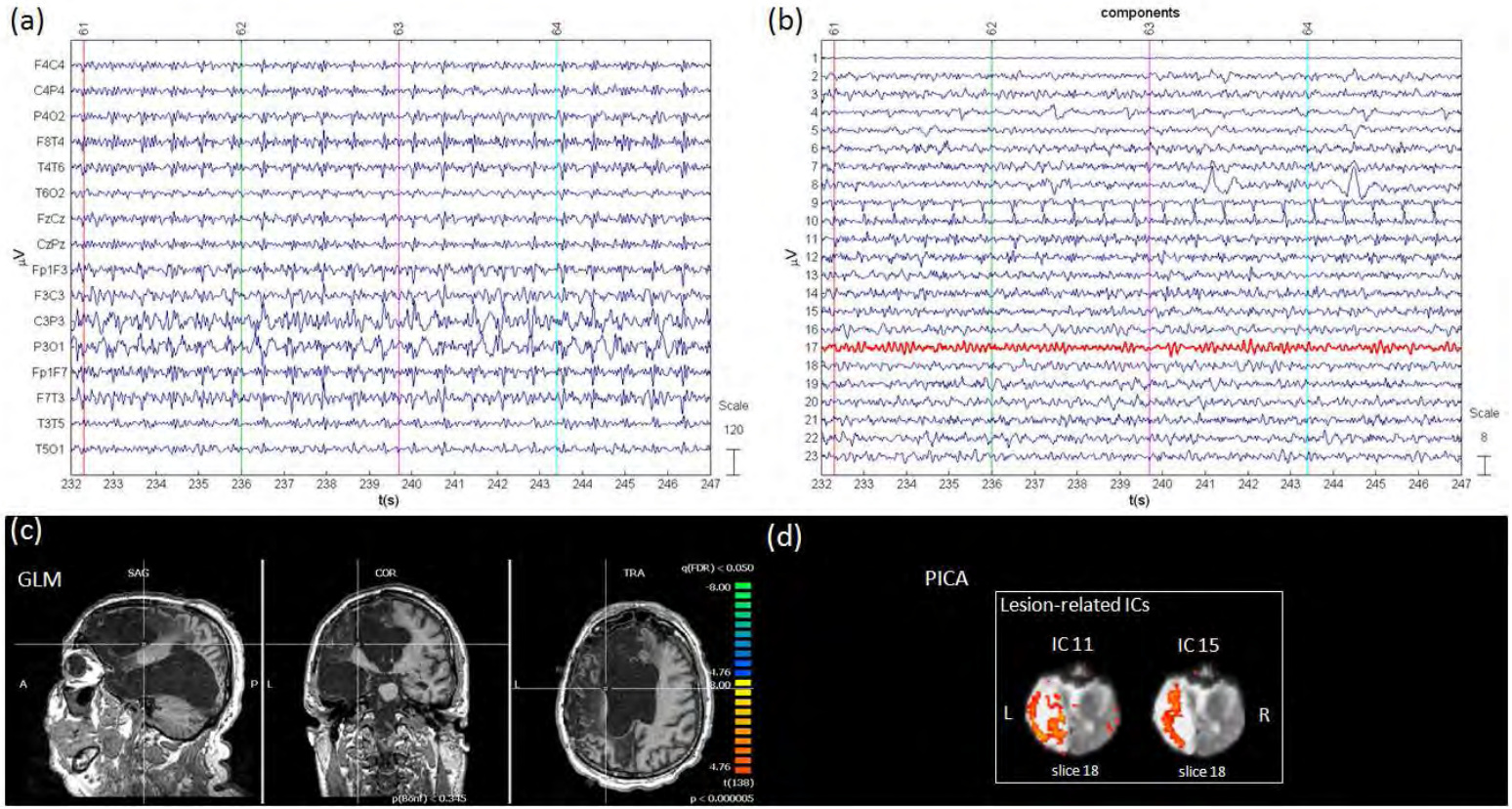


**Figure 6.11:** Patient No. 5 (a) EEG acquired during fMRI scanning after preprocessing. (b) EEG components obtained by ICA decomposition. EEG component no. 17 was selected. (c) EEG-fMRI results from the GLM analysis (FDR, $p<0.05$). (d) EEG-fMRI results from the PICA analysis.

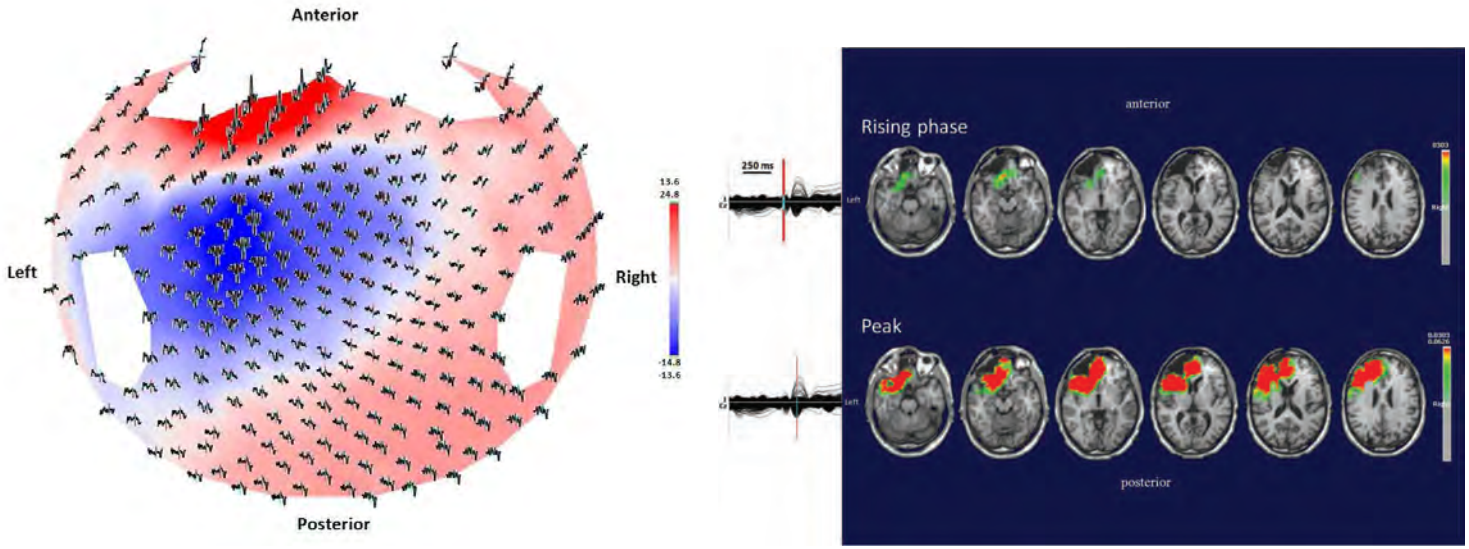


(a) (b)

**Figure 6.12:** Patient No. 6. (a) HdEEG signal visualized according to the projected locations of the scalp electrodes (spike average). The representation of the potential is set at the maximum value of the global field power. (b) HdEEG source analysis results. On the left, 256-channel EEG traces with a duration of 1 s (spike average). The global field power is used for the onset (red line). On the right, EEG source imaging in the rising phase of the peak and at the peak. The maximum of the estimated source of the average interictal spike is indicated in red.

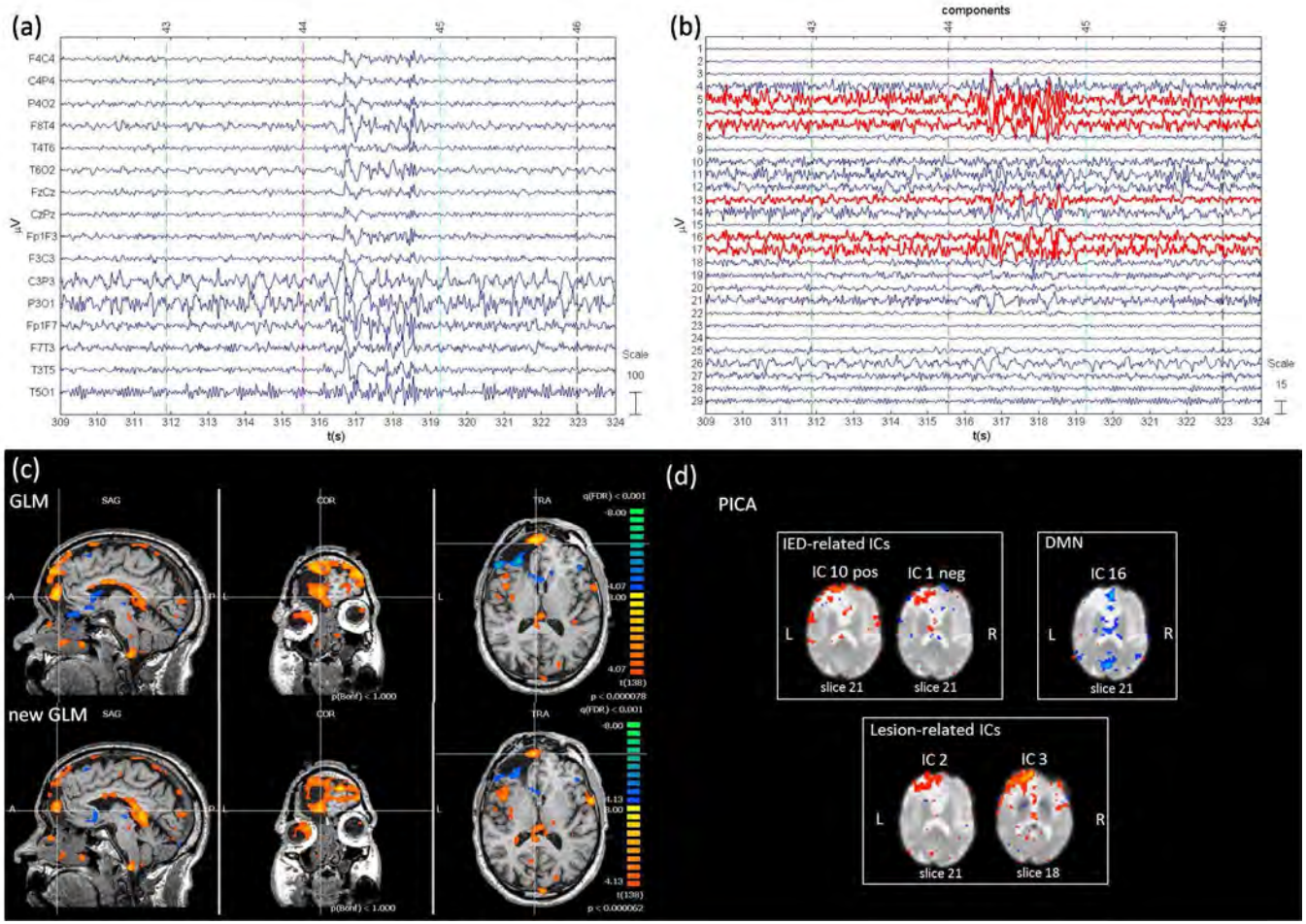


**Figure 6.13:** Patient No. 6. (a) EEG acquired during fMRI scanning after preprocessing. (b) EEG components obtained by ICA decomposition. EEG components nos. 5, 6, 7, 13, 16, and 17 were selected. (c) EEG-fMRI results from the GLM analysis (FDR, p<0.001). (d) EEG-fMRI results from the PICA analysis.

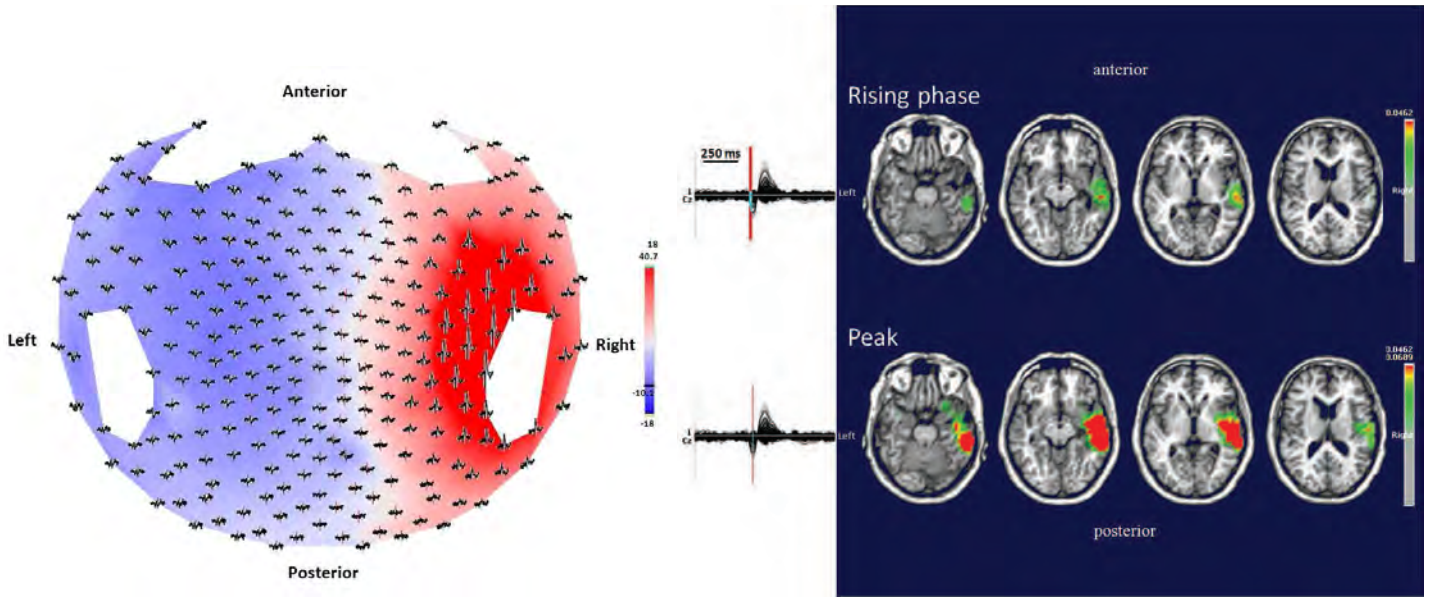


(a) (b)

**Figure 6.14:** Patient No. 7. (a) HdEEG signal visualized according to the projected locations of the scalp electrodes (spike average). The representation of the potential is set at the maximum value of the global field power. (b) HdEEG source analysis results. On the left, 256-channel EEG traces with a duration of 1 s (spike average). The global field power is used for the onset (red line). On the right, EEG source imaging in the rising phase of the peak and at the peak. The maximum of the estimated source of the average interictal spike is indicated in red.

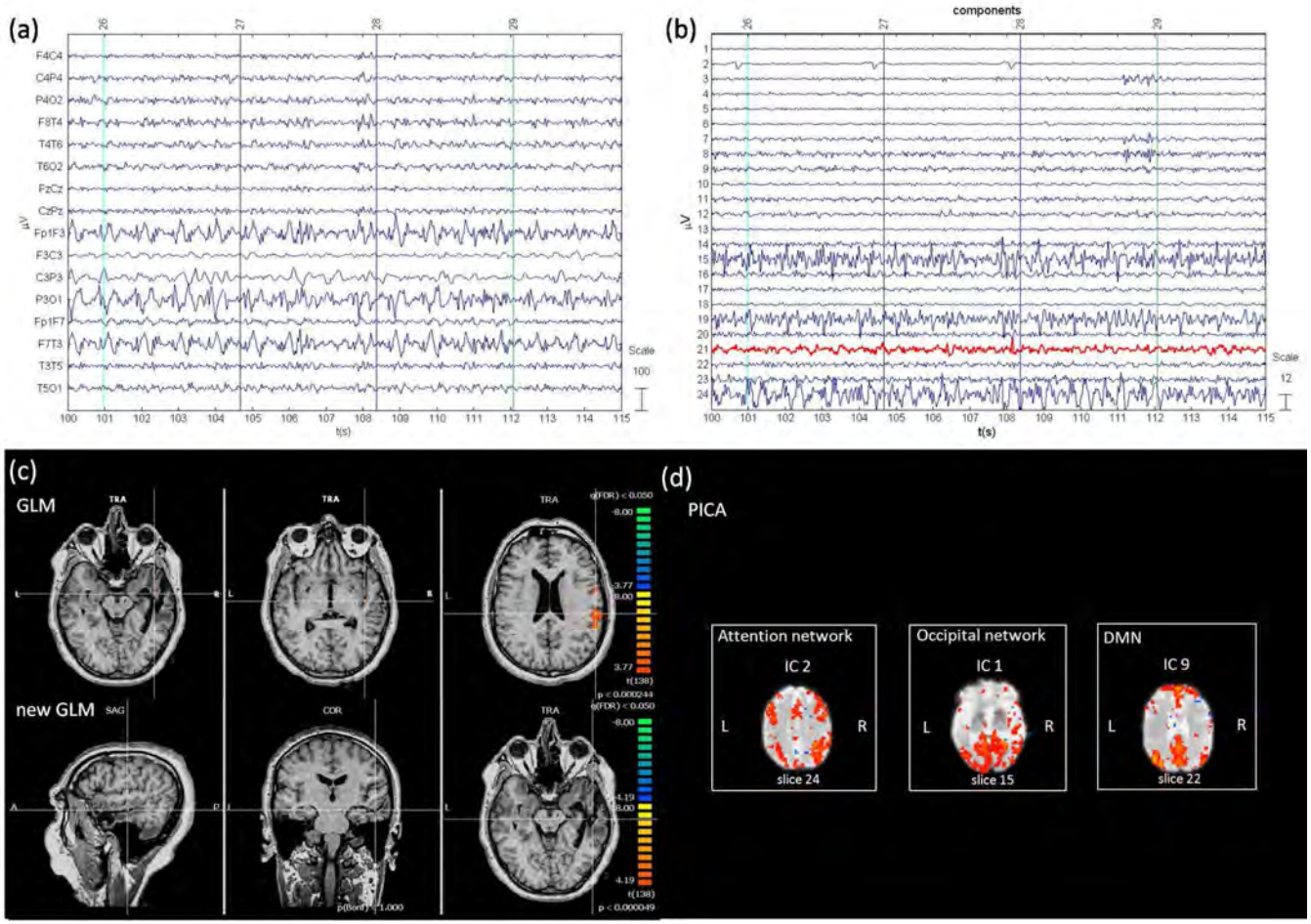


**Figure 6.15:** Patient No. 7. (a) EEG acquired during fMRI scanning after preprocessing. (b) EEG components obtained by ICA decomposition. EEG component no. 21 was selected. (c) EEG-fMRI results from the GLM analysis (FDR, $p<0.05$). (d) EEG-fMRI results from the PICA analysis.

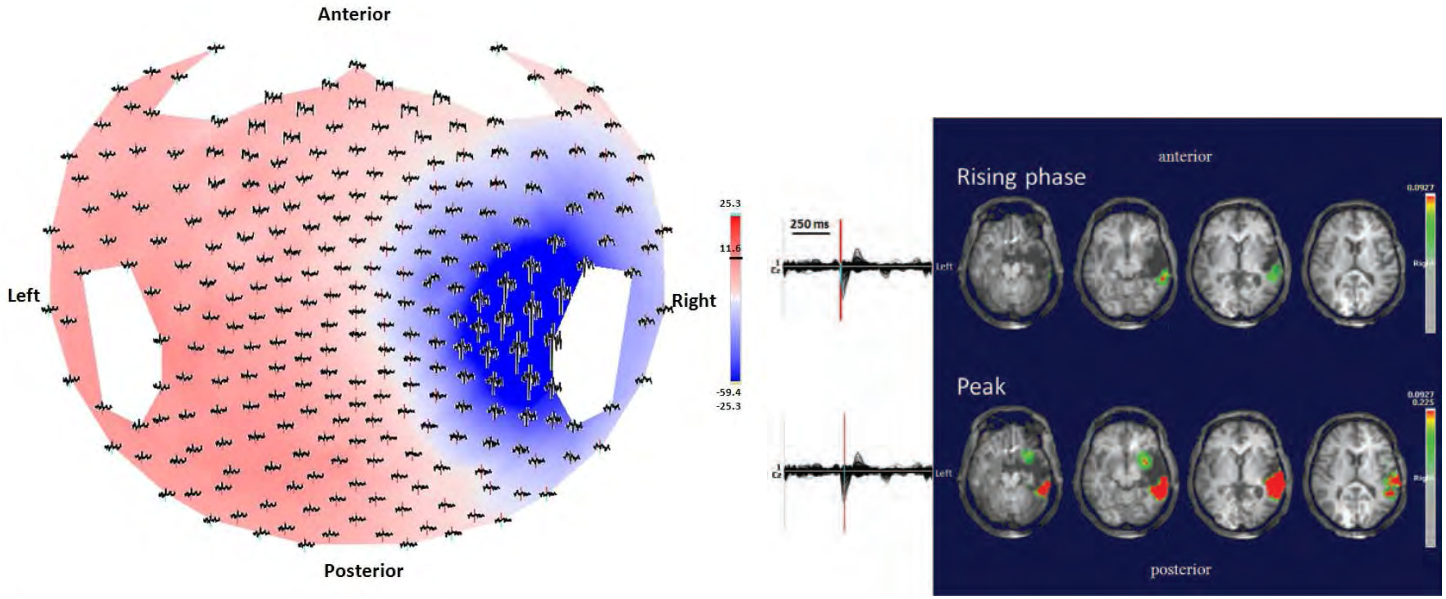


**Figure 6.16:** Patient No. 8. (a) HdEEG signal visualized according to the projected locations of the scalp electrodes (spike average). The representation of the potential is set at the maximum value of the global field power. (b) HdEEG source analysis results. On the left, 256-channel EEG traces with a duration of 1 s (spike average). The global field power is used for the onset (red line). On the right, EEG source imaging in the rising phase of the peak and at the peak. The maximum of the estimated source of the average interictal spike is indicated in red.

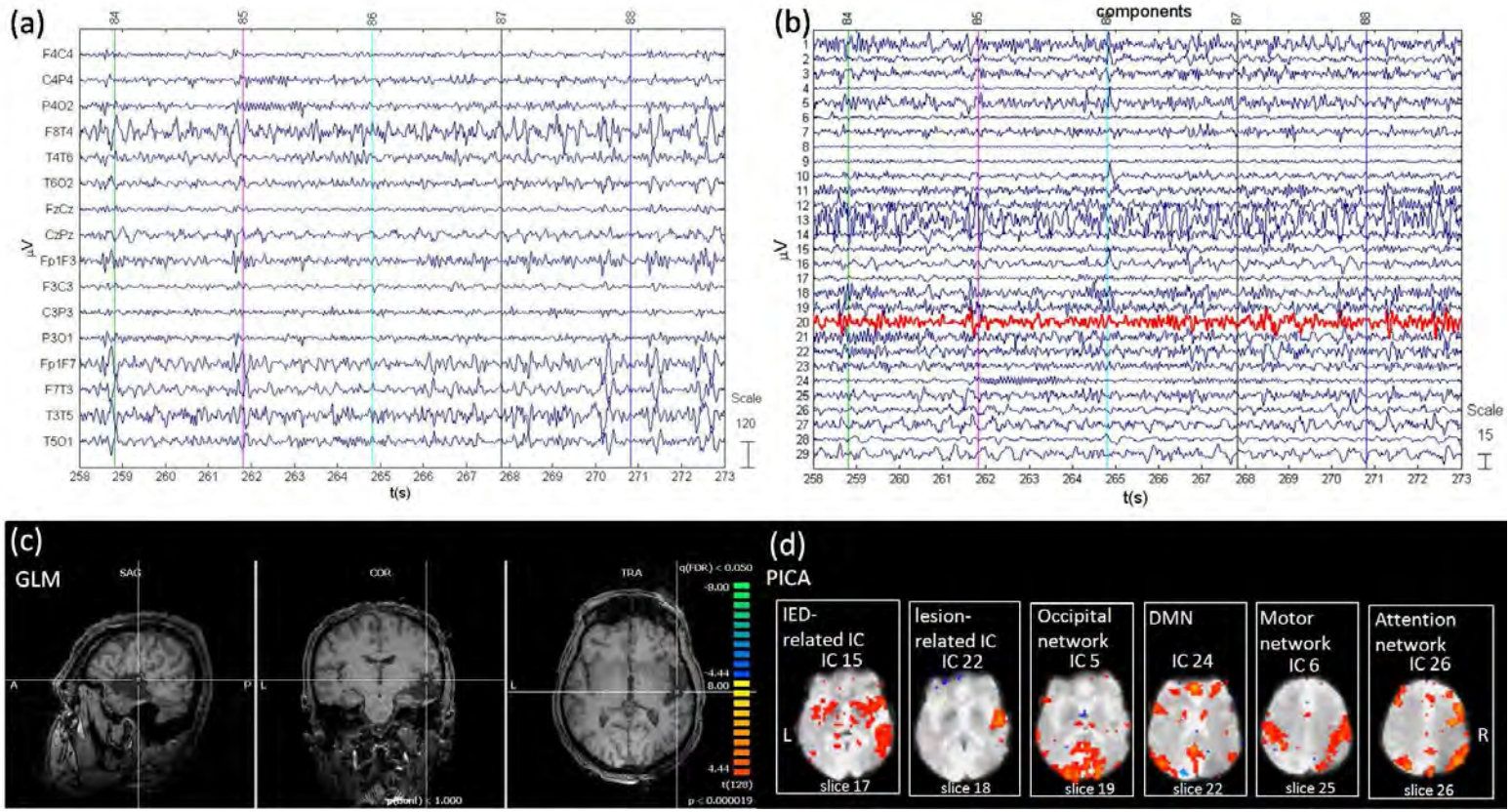


**Figure 6.17:** Patient No. 8. (a) EEG acquired during fMRI scanning after preprocessing. (b) EEG components obtained by ICA decomposition. EEG component no. 20 was selected. (c) EEG-fMRI results from the GLM analysis (FDR, p<0.05). (d) EEG-fMRI results from the PICA analysis.

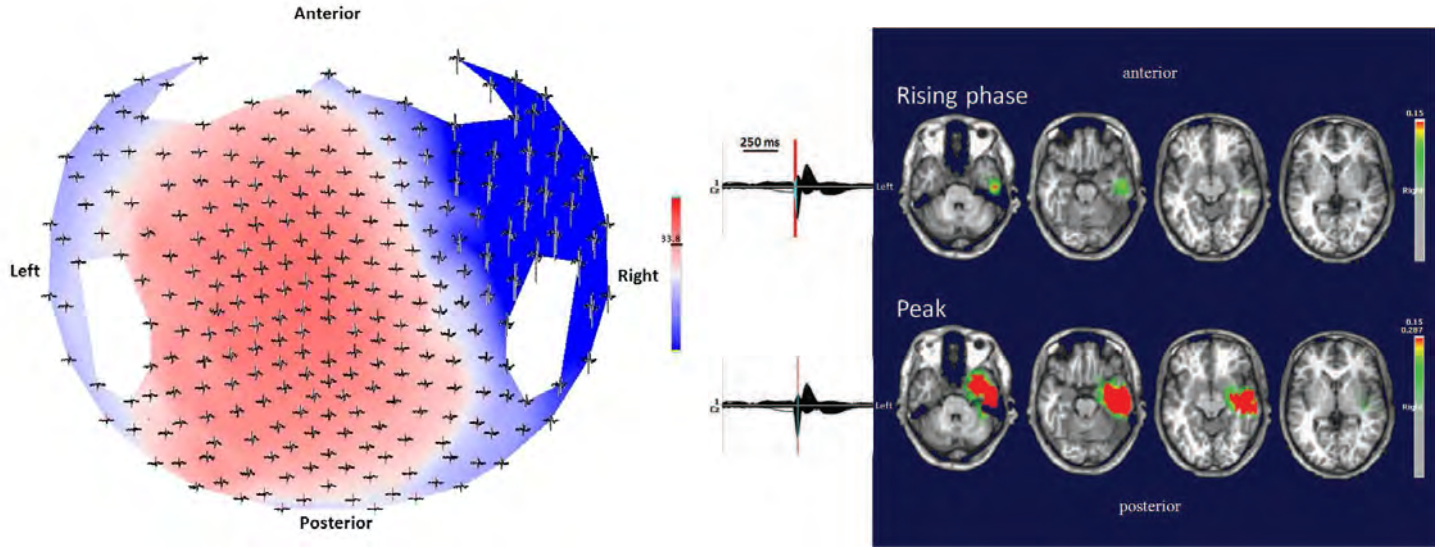


(a) (b)

**Figure 6.18:** Patient No. 9. (a) HdEEG signal visualized according to the projected locations of the scalp electrodes (spike average). The representation of the potential is set at the maximum value of the global field power. (b) HdEEG source analysis results. On the left, 256-channel EEG traces with a duration of 1 s (spike average). The global field power is used for the onset (red line). On the right, EEG source imaging in the rising phase of the peak and at the peak. The maximum of the estimated source of the average interictal spike is indicated in red.

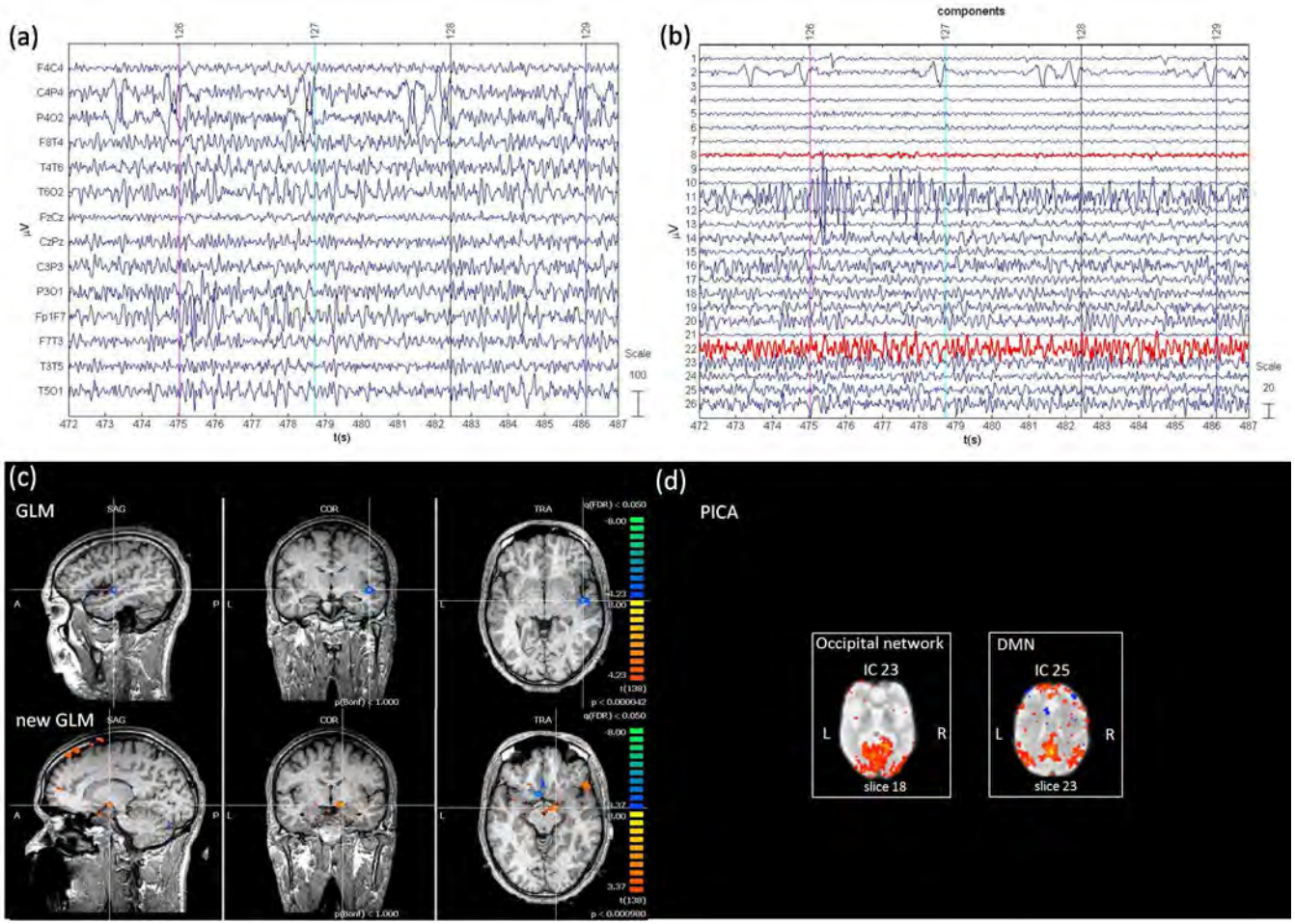


**Figure 6.19:** Patient No. 9. (a) EEG acquired during fMRI scanning after preprocessing. (b) EEG components obtained by ICA decomposition. EEG components nos. 8 and 22 were selected. (c) EEG-fMRI results from the GLM analysis (FDR, $p<0.05$). (d) EEG-fMRI results from the PICA analysis.

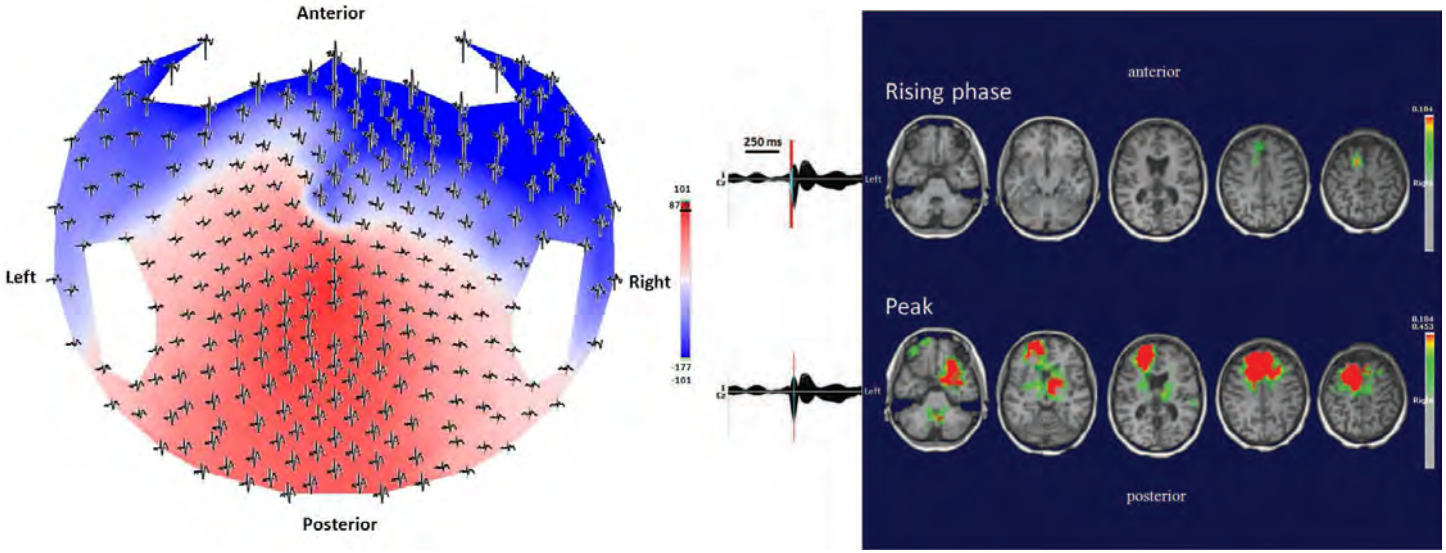


**Figure 6.20:** Patient No. 10. (a) HdEEG signal visualized according to the projected locations of the scalp electrodes (spike average). The representation of the potential is set at the maximum value of the global field power. (b) HdEEG source analysis results. On the left, 256-channel EEG traces with a duration of 1 s (spike average). The global field power is used for the onset (red line). On the right, EEG source imaging in the rising phase of the peak and at the peak. The maximum of the estimated source of the average interictal spike is indicated in red.

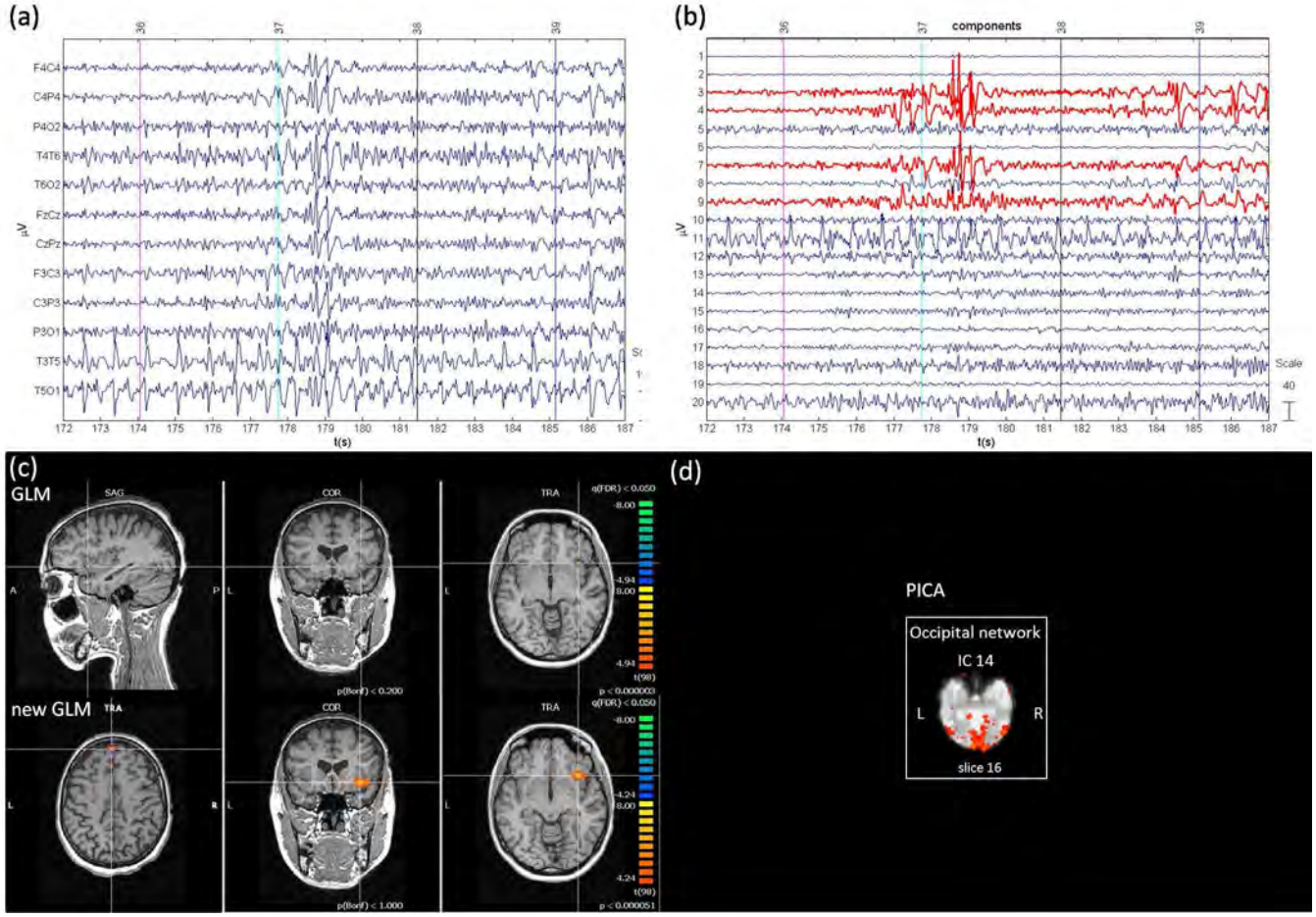


**Figure 6.21:** Patient No. 10. (a) EEG acquired during fMRI scanning after preprocessing. (b) EEG components obtained by ICA decomposition. EEG components nos. 3, 4, 7, and 9 were selected. (c) EEG-fMRI results from the GLM analysis (FDR, $p<0.05$). (d) EEG-fMRI results from the PICA analysis.

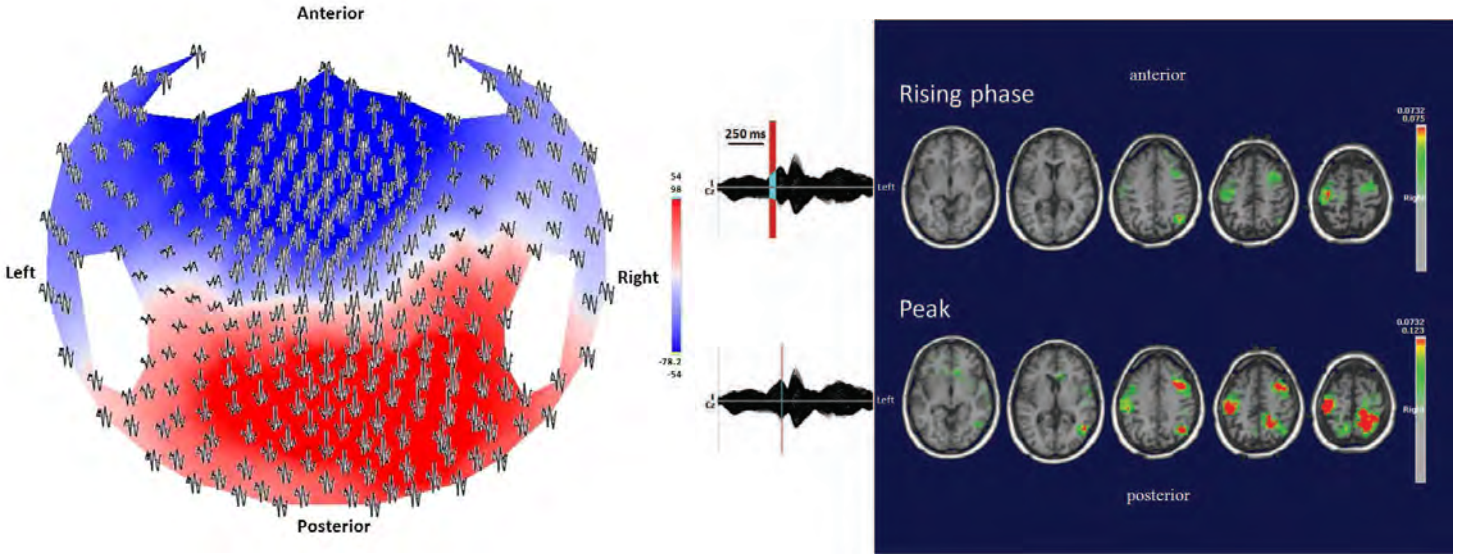


**Figure 6.22:** Patient No. 11. (a) HdEEG signal visualized according to the projected locations of the scalp electrodes (spike average). The representation of the potential is set at the maximum value of the global field power. (b) HdEEG source analysis results. On the left, 256-channel EEG traces with a duration of 1 s (spike average). The global field power is used for the onset (red line). On the right, EEG source imaging in the rising phase of the peak and at the peak. The maximum of the estimated source of the average interictal spike is indicated in red.

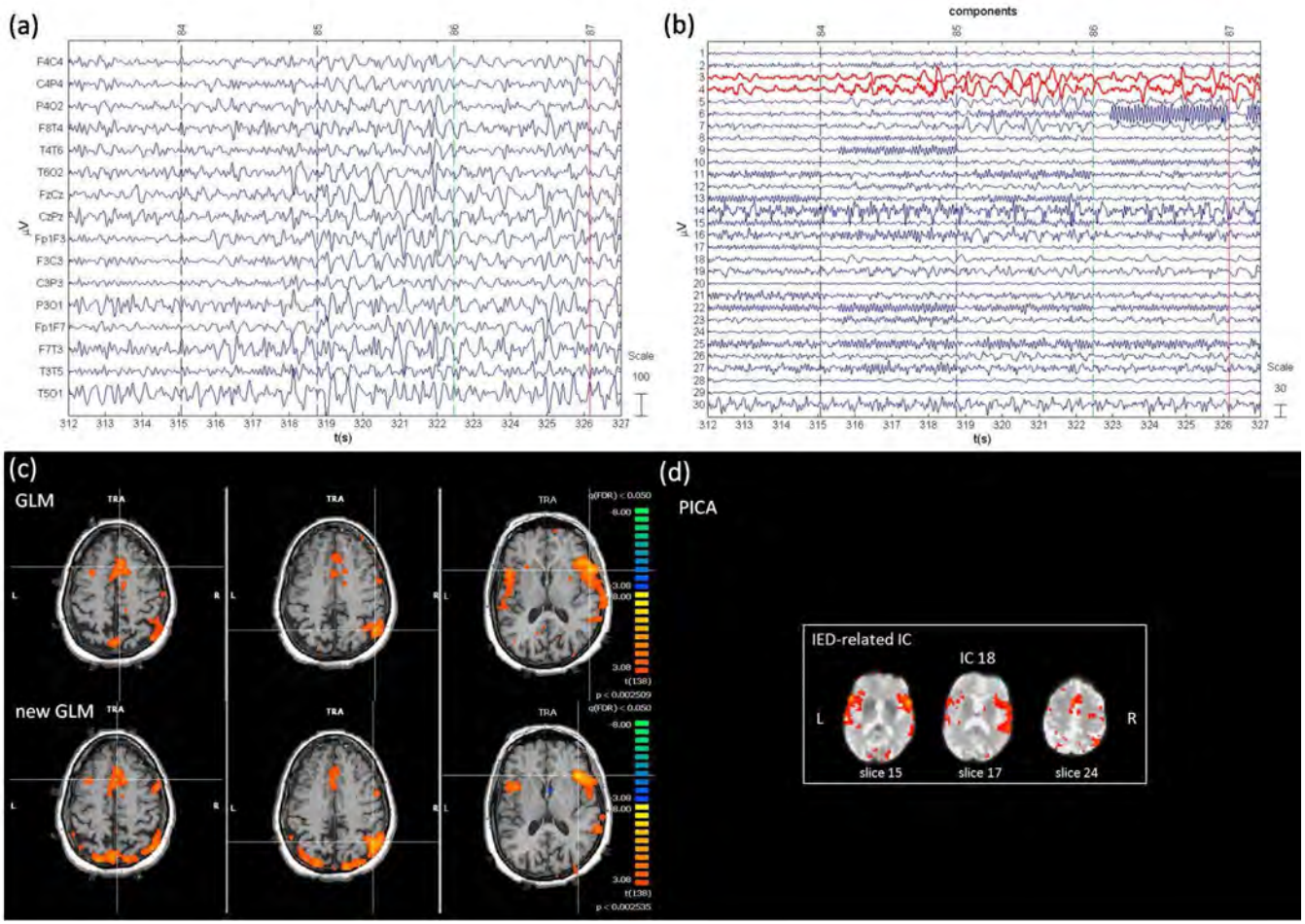


**Figure 6.23:** Patient No. 11. (a) EEG acquired during fMRI scanning after preprocessing. (b) EEG components obtained by ICA decomposition. EEG components nos. 3 and 4 were selected. (c) EEG-fMRI results from the GLM analysis (FDR, $p<0.05$). (d) EEG-fMRI results from the PICA analysis.

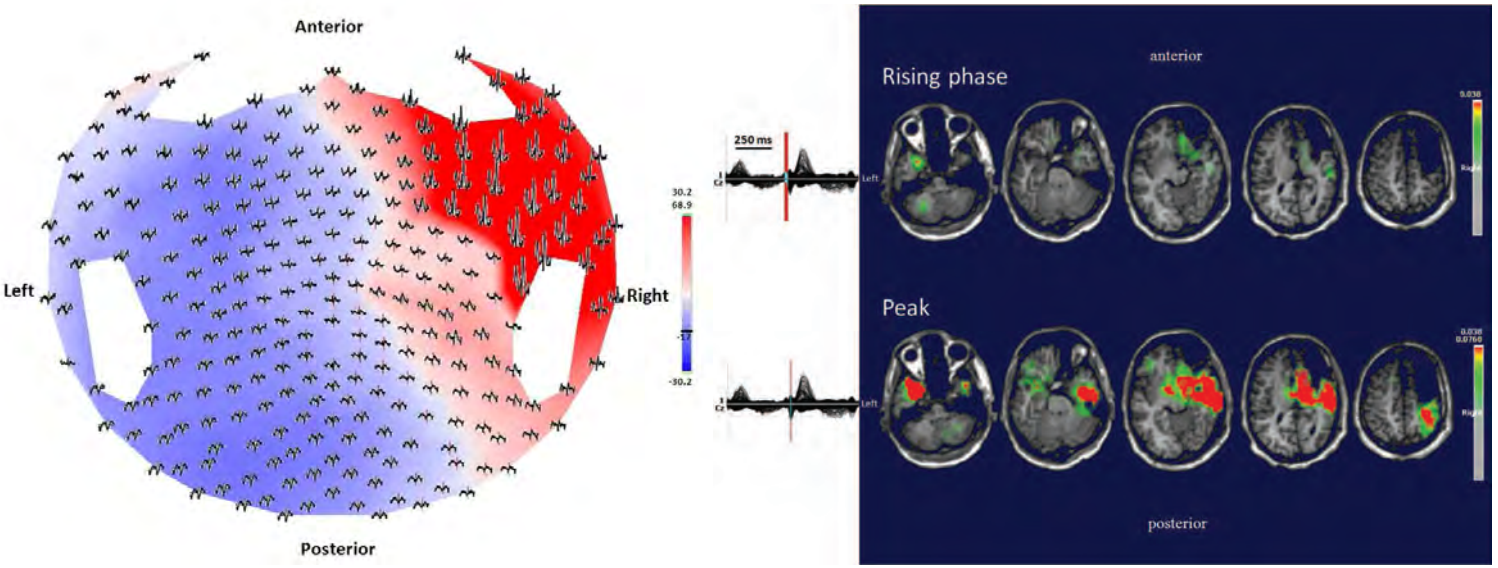


**Figure 6.24:** Patient No. 12. Right-lobe EEG activity (a) HdEEG signal visualized according to the projected locations of the scalp electrodes (spike average). The representation of the potential is set at the maximum value of the global field power. (b) HdEEG source analysis results. On the left, 256-channel EEG traces with a duration of 1 s (spike average). The global field power is used for the onset (red line). On the right, EEG source imaging in the rising phase of the peak and at the peak. The maximum of the estimated source of the average interictal spike is indicated in red.

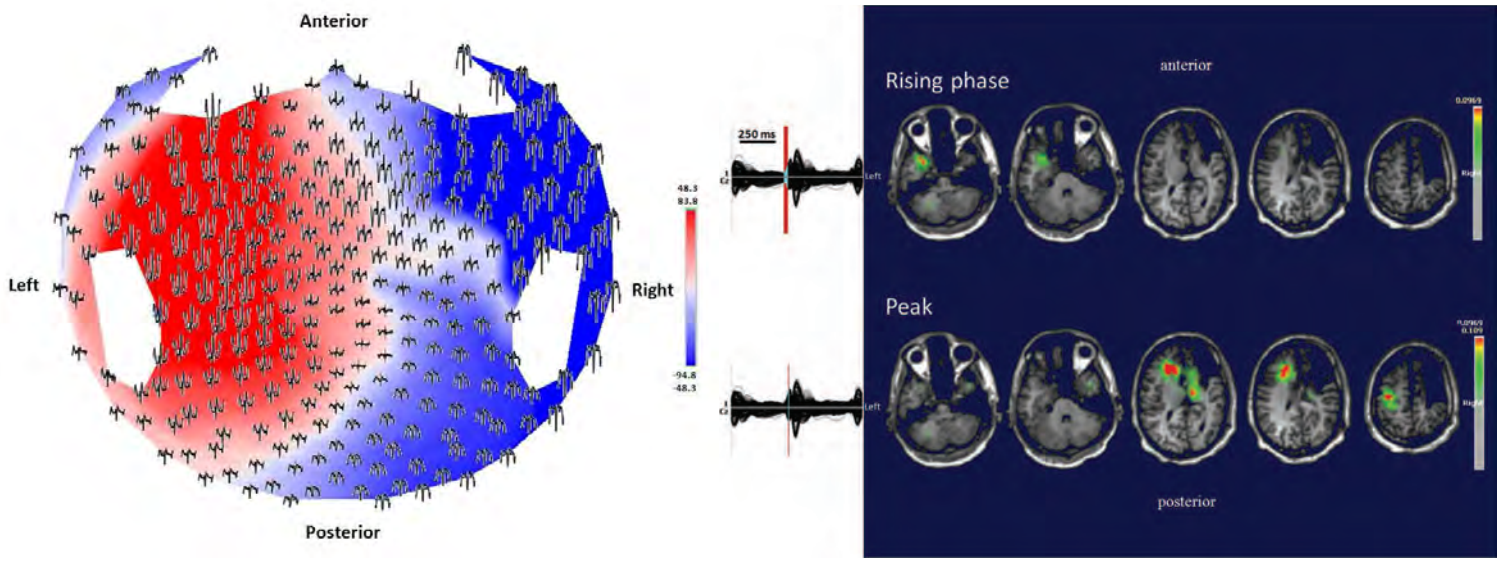


(a) (b)

**Figure 6.25:** Patient No. 12. Left-lobe EEG activity. (a) HdEEG signal visualized according to the projected locations of the scalp electrodes (spike average). (b) HdEEG source analysis results. On the left, 256-channel EEG traces with a duration of 1 s (spike average). The representation of the potential is set at the maximum value of the global field power. The global field power is used for the onset (red line). On the right, EEG source imaging in the rising phase of the peak and at the peak. The maximum of the estimated source of the average interictal spike is indicated in red.

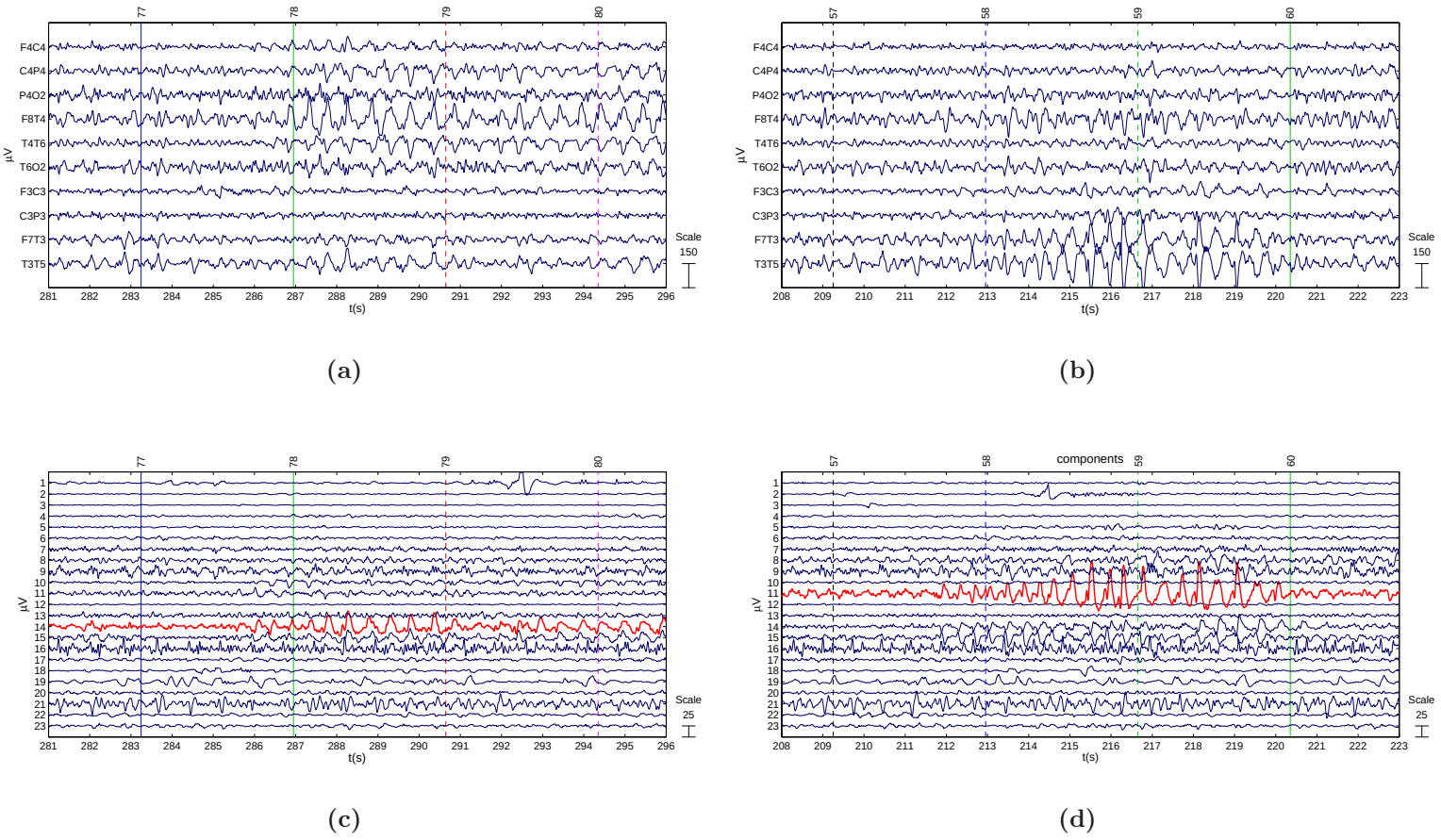


**Figure 6.26:** Patient No. 12. (a) EEG acquired during fMRI scanning with spike and waves in T4. (b) EEG acquired during fMRI scanning with spike and waves in T3. (c) EEG components obtained by ICA decomposition relative to (a). Component no. 14 shows the spike and wave waveform. (d) EEG components obtained by ICA decomposition relative to (b). Component no. 11 shows the spike and wave waveform.

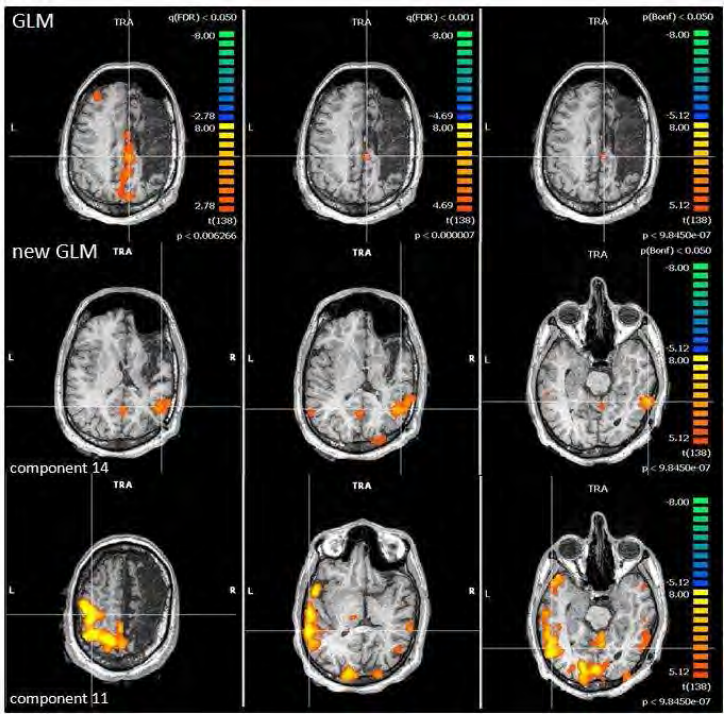


**(a)**

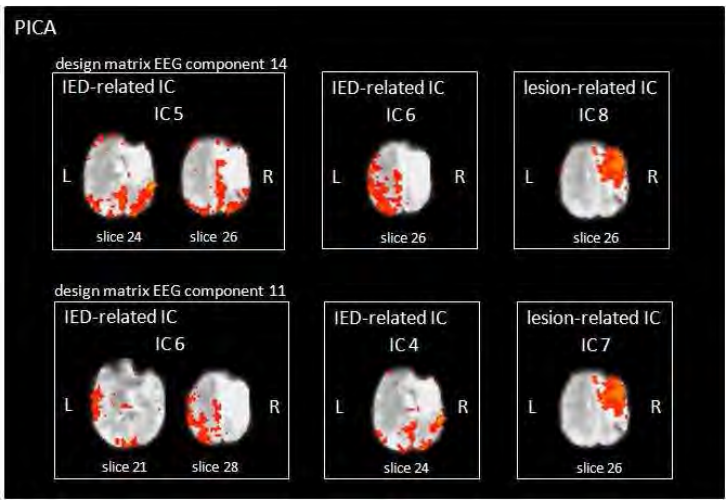


**(b)**

**Figure 6.27:** Patient No. 12. (a) EEG-fMRI results from the GLM analysis: conventional GLM analysis with three types of correction (q(FDR)<0.05, q(FDR)<0.001, and p(Bonferroni)<0.05); new GLM analysis using as regressor the component no. 14 (top) and component no. 11 (bottom), corrected p(Bonferroni)<0.05). (b) EEG-fMRI results from the PICA analysis. First PICA analysis (top): correlation with the regressor constructed on the component no. 14; second PICA analysis (bottom): correlation with the regressor constructed on the component no. 11.

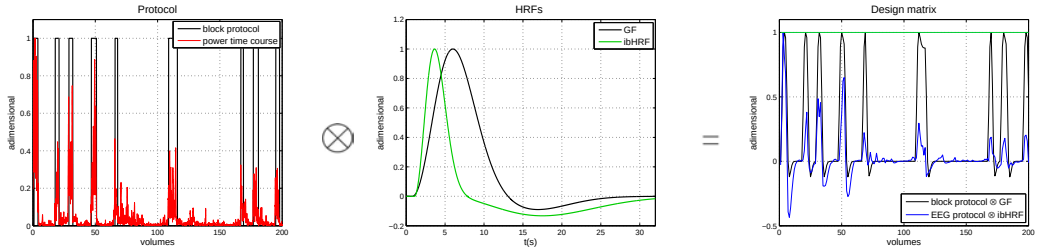


(a)

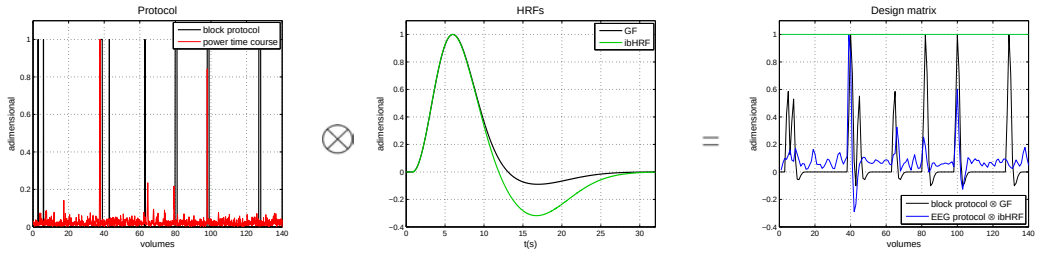


(b)

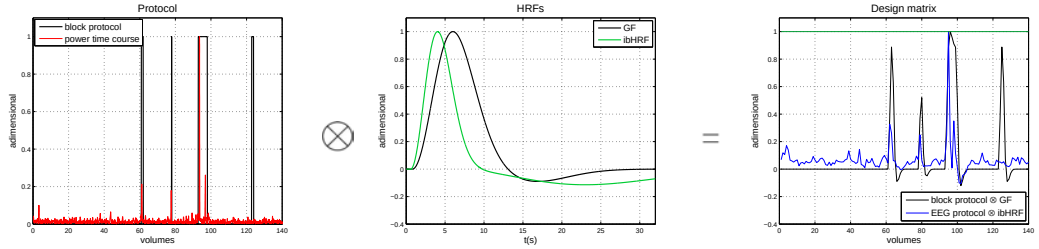


(c)

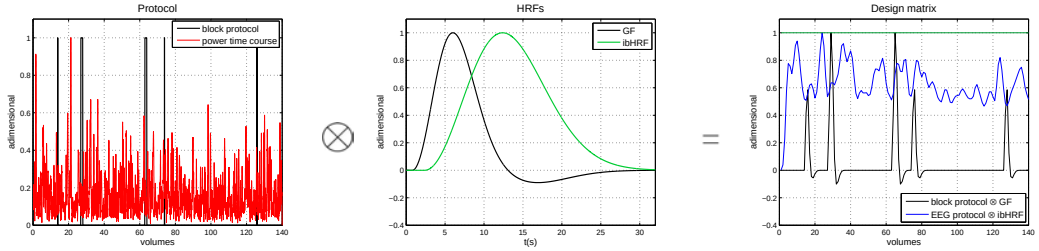


(d)

**Figure 6.28:** Patients Nos. 1 (a), 3 (b), 4 (c), and 7 (d). Left: Block protocol vs EEG protocol. Center: Standard GF HRF vs ibHRF. Right: Conventional regressor vs new regressor.

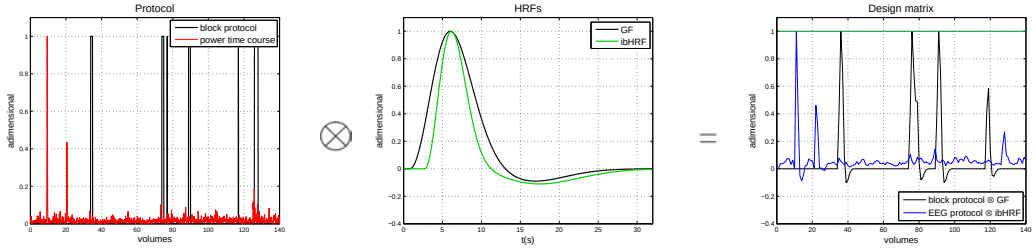


**(a)**

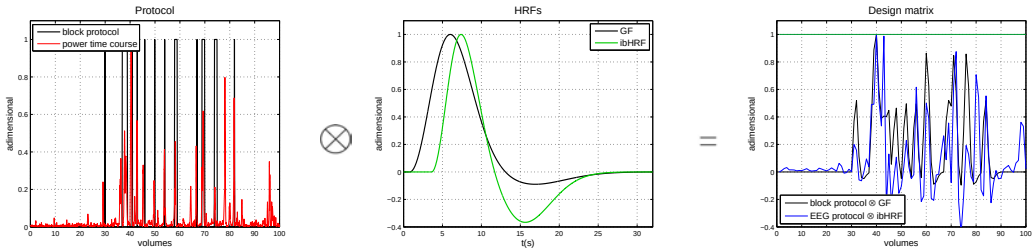


**(b)**

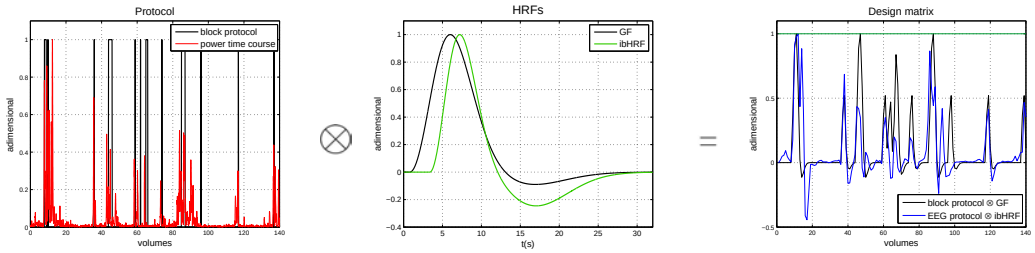


**(c)**

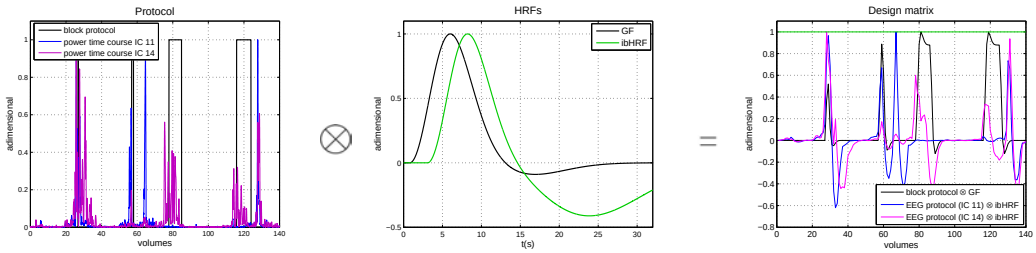


**(d)**

**Figure 6.29:** Patients Nos. 9 (a), 10 (b), 11 (c), and 12 (d). Left: Block protocol vs EEG protocol. Center: Standard GF HRF vs ibHRF. Right: Conventional regressor vs EEG regressor.

# Discussion

The main objective of EEG-fMRI and hdEEG, as independent electrophysiological and functional measurements, is to view brain function from various different perspectives and to detect and describe changes in neuronal activity. While IED recording and analysis of events can play a central role in the correct diagnosis of epilepsy, simple partial seizures may not have a definite location on scalp EEG. From EEG-fMRI and hdEEG registration, insights can be gained into networks associated with interictal epileptic activity [Gotman et al., 2006]; moreover, having two different methods to localize the same epileptic foci is clinically useful.

Unfortunately, it is not possible to detect BOLD activations related to IED activity in all patients, at least using conventional analysis [Al-Asmi et al., 2003, Salek-Haddadi et al., 2006, Thornton et al., 2010]. The aim of this thesis was to improve the sensitivity of the existing method of analysis for EEG-fMRI data and compare the results with the hdEEG source localizations.

***Automatic EEG method***

The main clinical finding in EEG-fMRI studies of patients with partial epilepsy is that focal interictal slow-wave activity was invariably associated with increased focal BOLD responses in a spatially related brain area. The new method here presented aimed to improve upon existing methods since it is fully automatic and the epileptiform activity, recorded from a scalp EEG, is used to modulate changes in BOLD signal. ICA decomposition and an automatic selection, based on wavelet analysis, was developed to identify signals representing the activity of interest, which is typically higher in amplitude than background activity and characterized by elevated power. The recon-

structed EEG signal, due to IED, was obtained with the only contribution of the selected components, thus removing the contribution of other components related to artifact or other activity. Its wavelet power is then used as GLM input. This offers a definite advantage with respect to the conventional approach, where all events are treated as equal, since it takes into account variations in amplitude and duration of epileptic spikes. Moreover, the conventional approach ignores the fact that IED activity is continuous and contains fluctuating sub-threshold epileptic activity, not clearly seen on surface EEG recordings. Such meaningful information is contained in the ICA factors employed in the method.

Analysis of in silico data provided a preliminary validation of the method, since it demonstrates the reliability of reconstructed IED regressor even in presence of other components, with similar frequency content as IED activity. The "true" and the estimated EEG regressors were compared using an index, equal to the difference between the areas under the two waveforms normalized to the area under the true waveform, and the results showed that EEG regressor estimated by the new method well matches the true one since the index is always below 2% [Formaggio et al., 2011]. The method, based on ICA decomposition, improves upon existing methods, since it eliminates subjectivity in classification of the IEDs and builds regressor for GLM in fMRI analysis modulated by epileptiform activity.

***Individual-based HRF***

Nowadays the EEG-fMRI has limited sensitivity to detect the significant BOLD signal changes. The sensitivity of EEG-fMRI can be improved with the use of different HRFs. Since HRF may vary in epileptic patients a major aim was to investigate the impact of a subject-specific HRF to describe the differences in hemodynamic response functions across patients versus the use of a standard HRF model. Since it is not possible to infer which is the best HRF model by looking at the activation maps, we developed a novel method and implemented a procedure to optimize in each patient the choice of HRF model from a set of four standard HRFs and a subject-specific HRF (ibHRF). Starting from a general template with flexible shape, we chose to model B HRF using the simple gamma function and GF by the sum of two gamma functions with fixed parameters. We also included GF HRF and its first temporal and dispersion derivatives [Friston et al., 1998]. In ibHRF five-parameters were estimated, constructing a model which balances the ac-

curacy of estimates and flexibility of the HRF model.

Once validated on in silico data, reproducing both usual and unusual patterns (Chapter 4), the method was applied on real data. Our results on real data show that the use of different HRFs influences the extension of active areas, thus the selection of the model best able to describe the hemodynamic response is a critical step in generation of activation maps by GLM. A subject-specific parametric HRF model takes into account intersubject variability in the hemodynamic response and thus, as suggested by the in silico analysis, it is likely to reduce false-positive and false-negative fMRI-BOLD responses in patients with epilepsy. Of note, in patients with epilepsy the characteristics of BOLD signal need to be especially well defined, in particular in delay and dispersion.

To summarize, a data analysis strategy was developed to identify a subject-specific HRF that parsimoniously describes the fMRI time course and provides reliable BOLD activation maps. We have assessed by simulations how the variations in HRF model affect the results of the statistical analysis. Using a suboptimal HRF to model the BOLD response may result in an over or under estimated activation. An individually chosen HRF is a prerequisite for obtaining adequate fMRI-BOLD activation maps. As future scope we will investigate whether the use of an individual pixel-based HRF provides further improvement of the method.

***The new GLM method***

The new GLM regressor based on the convolution of the automatic EEG protocol and the individual-based HRF was applied to twelve patients with epilepsy with frequent interictal focal slow wave activity on routine EEG. In all continuous EEG-fMRI recording sessions, after fMRI artifact removal, we obtained a good quality EEG that allowed us to detect spontaneous IEDs and analyze the related BOLD activation. In their focal distribution, BOLD activations resembled the focal IEDs seen on routine scalp EEG, as well as on EEG recorded during EEG-fMRI sessions and they were in good agreement with the clinical history of the patients. In the majority of the patients the results of the new analysis exhibited an increased sensitivity for the detection of brain regions associated with IED.

The main clinical finding in EEG-fMRI studies of patients with partial epilepsy is that focal interictal slow-wave activity was invariably associated with increased focal BOLD responses in a spatially related brain area. This

study extends current knowledge on epileptic foci localization and confirms previous reports suggesting that BOLD activation associated with slow activity might have a role in localizing the epileptogenic region even in the absence of clear interictal spikes.

***Correlation between BOLD and hdEEG source data***

On comparison of the hemodynamic and electrophysiological data, the results demonstrated a good correspondence in 7 out of 12 patients (patients Nos. 1, 3, 6, 9, 10, 11, and 12): in 4 patients no BOLD activation was found (patients Nos. 2, 5, 7, and 8) and in 1 patient the comparison showed a mismatch (patient No. 4). Unfortunately, a precise spatial overlap can not be found in all cases probably due to the different nature of two signals.

Compared to the GLM, ICA has the added advantage of detecting networks related to the IED activity and also resting-state networks such as the attention network, the posterior network, the temporal network and the DMN. The regions involved in the DMN have dense white matter connections, suggesting that they form part of the brain's structural core. Disruption of the DMN is clinically important, and abnormalities are observed in various neurological and psychiatric disorders. The DMN in PET and fMRI studies showed a consistent decrease from a relative baseline during a specific goal-directed behavioural task, as demonstrated in [Raichle et al., 2001]. According to published data, the interictal activity may disrupt the DMN [Laufs et al., 2007, Vaudano et al., 2009, Mulert and Lemieux, 2010]. In epileptic patients, a negative DMN was found as result of a suspension of the baseline state caused by the interictal activity [Aghakhani et al., 2004, Gotman et al., 2005, Hamandi et al., 2006, Laufs et al., 2006, 2007]. Of note is that DMN in the twelve epileptic patients was not always detected (i.e., patients Nos. 1, 5, 10, 11, and 12). A possible explanation is that the brain damage or long-term epileptic activity recorded inside the magnet does not allow activation (or at least in part) of the DMN.

The BOLD signal reflects the effect of electrical activity at the microvascular level, with high errors of measure (low signal-to-noise ratio), whereas imprecision in EEG source localization is related to an ill-posed nature of the problem, to errors of the head and source models. Other possible explanations may be sought in deep epileptic activities recognized by fMRI but not measured on scalp electrodes because of attenuation phenomena. Otherwise asynchronous neurons, which produce minimal metabolic activities, can be

measured by fMRI and not by EEG [Ritter and Villringer, 2006]. In other cases, the two signals can be negatively correlated. A high current density detected by the source localization is associated with hypo-hemodynamic activity in the same area.

Complementary information can be gleaned from a strategy that combines source analysis and coregistration, particularly in those forms of epilepsy in which clear focal activity is difficult to identify. A multimodal approach could be ideal for assessing patients with post-TBI epilepsy (patients 1-7) probably because of the long period of spiking alternating with rest periods and because patients with brain injury have sensitive metabolic changes in perilesional tissues. In such patients we can not exclude changes in perfusion during interictal period due to the functional and anatomical modifications of vessels in a injured brain [Mazzini et al., 2003]. In addition the post-traumatic brain has phenomena of maladaptitive plasticity due to fiber rearrangement after diffuse axonal injury that can be responsible for the epileptogenesis [Thom et al., 2011, Volman et al., 2011]. In these patients, who are not candidate for any surgical treatment, more information on the areas involved in the epileptic process are necessary in order to understand the physiopathological mechanisms. With the advent of simultaneous EEG and fMRI coregistration, complex transient hemodynamic responses associated with ictal and interictal events can be mapped noninvasively. Nevertheless, in patients with epilepsy, EEG remains the mainstay method to investigate functional brain abnormalities and to reveal characteristic paroxystic events reflecting neuronal synchronization. A caveat to this is that a wrong model of individual geometry and conductivity of the brain and a limited number of EEG channels can influence estimation of the sources. HdEEG technologies were developed to enhance the poor spatial information content of EEG activity. In addition, constraining the source analysis of high spatial resolution EEG to a patient's MRI provides more accurate localization of epileptic activity. The source localization on hdEEG data allows for precise mapping of IED activity when the same analysis on standard EEG fails (Fig. 1.12). With the use of the 256-electrode configuration, zygomatic and pre-frontal activity can also be detected. Furthermore, the sensitivity of interictal or ictal EEG can be significantly increased with the use of additional zygomatic electrodes.

The combination of multimodal techniques and their respectively methods of analysis are useful tools of a presurgical workup of epilepsy providing two different methods of localization of the same epileptic foci. To conclude,

the combined use of EEG-fMRI and hdEEG offers a new and more complete approach to the study of epilepsy and may play an increasingly important role in the evaluation of patients with refractory focal epilepsy.

# Appendix

## A The Novel Gradient Artifact Removal Method

After a realignment process of EEG data depending on slice repetition time, the algorithm performs an iterative subtraction of the estimated slice artifact, according to the following steps: artifact waveform analysis, computation of signal average waveform affected by gradient artifact, artifact estimate by least squares minimization, subtraction of estimated artifact.

*Realignment:* The operations to remove the artifact need to be executed within every channel, one volume at a time. Channel division in $nv$ volumes is performed by inserting automatic triggers in recorded EEG data for every scan interval, after a preliminary visual inspection in which first scan beginning is identified. Subsequently, volume subdivision in $ns$ slices is obtained by segmenting it in the same way.

*Algorithm:* The algorithm is based on the hypothesis that the recorded EEG signal $y(t)$ is the sum of a true underlying EEG signal $eeg(t)$ and a signal $u(t)$ containing artifact components:

$$y(t) = u(t) + eeg(t) \tag{A.1}$$

and consists in three fundamental steps that are repeated iteratively:
- *Signal affected by gradient artifact average.* A template for artifact waveform, $f(t)$, is computed by averaging all volume's slices.
- *Artifact estimate by least squares minimization.* Since artifact does not repeat identically at every slice, it was described by the following parametric expression:

$$\hat{u_i}(t) = a_i f(t), \quad i = 1...ns, \tag{A.2}$$

where $a_i$ is a proportional coefficient to be estimated for each slice by linear regression.
- *Subtraction of estimated artifact.* The estimated artifact is subtracted from the raw data, one slice at a time.

The algorithm terminates when the spectrum of the estimated artifact $\hat{u_i}(t)$ is similar to that of an artifact-free EEG, thus indicating that gradient artifact has been successfully removed. Finally, the output is smoothed by a Butterworth low pass filter with a cut-off frequency of 40 Hz applied in forward and reverse directions to give zero phase distortion in order to isolate EEG components in the range of interest (1-30 Hz).

## B Construction of Weight Matrix in GLM Analysis

There are various methods to construct the noise correlation and everyone have an influence on the performance of the estimation. We choose to estimate the temporal covariance structure of the noise with an autoregressive model as in [Bullmore et al., 1996, Jezzard et al., 2001]. In particular, we assume that the variability in time of error $\tilde{\epsilon}(n)$ is described by a first order autoregressive model AR(1) in which we suppose that the error from the previous scan is combined with white noise to produce the current scan:

$$\tilde{\epsilon}(n) = \rho \cdot \tilde{\epsilon}(n-1) + \xi_1(n) \tag{B.1}$$

where $|\rho| < 1$ and $\xi_1 \sim N(0, \sigma_1^2)$ is a Gaussian white noise with mean 0 and variance $\sigma_1^2$.

We identified the AR(1) model, estimating the parameters: the coefficient of model $\rho$ and the variance of white noise $\sigma_1^2$. We used the Yule-Walker equation that describes the autocorrelation of out process of the AR model, to construct matrix $V$. If a first order autoregressive model is used, the Yule Walker equation system yields a single equation:

$$R(0)\rho = R(1) \tag{B.2}$$

where $R$ is a known autocorrelation function and according to variance expression we obtain:

$$\sigma_1^2 = R(0) - \rho R(1) \tag{B.3}$$

Where $V$ is compound by coefficients of the Yule-Walker equation and is a Toeplitz matrix, a symmetric matrix whose diagonal or sub diagonal elements are equal. $V$ is an $N \times N$ matrix:

$$V = \begin{pmatrix} 1 & \rho & \rho^2 & \dots & \rho^{n-1} \\ \rho & 1 & \rho & \dots & \rho^{n-2} \\ \rho^2 & \rho & 1 & \dots & \rho^{n-3} \\ \vdots & \vdots & \vdots & \ddots & \vdots \\ \rho^{n-1} & \rho^{n-2} & \rho^{n-3} & \dots & 1 \end{pmatrix} \tag{B.4}$$

We estimated the variance of white noise and the coefficient $\rho$ for each voxel [Purdon et al., 2001].

First we estimated $\epsilon(n)$ with the $W$ identity matrix, we then applied the AR(1) model to the error. In this way we constructed $W$ for the next estimate. After estimating of $V$, in SOHIA we used a Cholesky factorization, inverting the transpose of the factor:

$$V = (H)^T \cdot H, \quad W = ((H)^T)^{-1}, \quad WVW^T = I, \tag{B.5}$$

where $I$ is the $N \times N$ identity matrix.
We constructed $W$ in this way:

$$W = \begin{pmatrix} 1 & 0 & 0 & \dots & 0 \\ -\rho R & R & 0 & \dots & 0 \\ 0 & -\rho R & R & \ddots & \vdots \\ \vdots & \ddots & \ddots & \ddots & 0 \\ 0 & \dots & 0 & -\rho R & R \end{pmatrix} \tag{B.6}$$

where $R = \frac{1}{\sqrt{1-\rho^2}}$.

**Acknowledgments**

The development of CARTOOL is supported by the Center for Biomedical Imaging (CIBM) of the Universities of Geneva and Lausanne, the Swiss Federal Institute of Technology, Lausanne (EPFL), and the University Hospitals of Geneva and Lausanne, Switzerland.

# Bibliography


Y. Aghakhani, A. P. Bagshaw, C. G. Benar, C. Hawco, F. Andermann, F. Dubeau, and J. Gotman. fMRI activation during spike and wave discharges in idiopathic generalized epilepsy. *Brain*, 127:1127–1144, May 2004.

Y. Aghakhani, E. Kobayashi, A. P. Bagshaw, C. Hawco, C. G. Benar, F. Dubeau, and J. Gotman. Cortical and thalamic fMRI responses in partial epilepsy with focal and bilateral synchronous spikes. *Clin Neurophysiol*, 117:177–191, Jan 2006.

G. K. Aguirre, E. Zarahn, and M. D'esposito. The variability of human, BOLD hemodynamic responses. *Neuroimage*, 8:360–369, Nov 1998.

H. Akaike. A new look at the statistical model identification. *IEEE Trans Automat Contr*, 19:716–723, 1974.

A. Al-Asmi, C. G. Benar, D. W. Gross, Y. A. Khani, F. Andermann, B. Pike, F. Dubeau, and J. Gotman. fMRI activation in continuous and spike-triggered EEG-fMRI studies of epileptic spikes. *Epilepsia*, 44:1328–1339, Oct 2003.

P. J. Allen, G. Polizzi, K. Krakow, D. R. Fish, and L. Lemieux. Identification of EEG events in the MR scanner: the problem of pulse artifact and a method for its subtraction. *Neuroimage*, 8:229–239, Oct 1998.

P. J. Allen, O. Josephs, and R. Turner. A method for removing imaging artifact from continuous EEG recorded during functional MRI. *Neuroimage*, 12:230–239, Aug 2000.

S-I. Amari, A. Cichocki, and H. H. Yang. A new learning algorithm for blind signal separation. *Proceedings of the 1995 Conference on Advances in Neural Information Processing Systems*, 8:757–763, 1995.

N. C. Andreasen, D. S. O'Leary, T. Cizadlo, S. Arndt, K. Rezai, G. L. Watkins, L. L. Ponto, and R. D. Hichwa. Remembering the past: two facets of episodic memory explored with positron emission tomography. *Am J Psychiatry*, 152:1576–1585, Nov 1995.

J. S. Archer, D. F. Abbott, A. B. Waites, and G. D. Jackson. fMRI "deactivation" of the posterior cingulate during generalized spike and wave. *Neuroimage*, 20:1915–1922, Dec 2003.

B. A. Ardekani, J. Kershaw, K. Kashikura, and I. Kanno. Activation detection in functional MRI using subspace modeling and maximum likelihood estimation. *IEEE Trans Med Imaging*, 18:101–114, Feb 1999.

M. Avesani, E. Formaggio, S. F. Storti, F. Alessandrini, A. Beltramello, A. Fiaschi, and P. Manganotti. f-MRI in Epilepsy with spike and wave activity evoked by eye closure: different BOLD activation in a patient with idiopatic partial epilepsy with occipital spikes and a control group. *The Neuroradiology Journal*, 21:159–165, Dec 2008.

K. A. Awada, D. R. Jackson, J. T. Williams, D. R. Wilton, S. B. Baumann, and A. C. Papanicolaou. Computational aspects of finite element modeling in EEG source localization. *IEEE Trans Biomed Eng*, 44:736–752, Aug 1997.

F. Babiloni, C. Babiloni, F. Carducci, G. L. Romani, P. M. Rossini, L. M. Angelone, and F. Cincotti. Multimodal integration of high-resolution EEG and functional magnetic resonance imaging data: a simulation study. *Neuroimage*, 19:1–15, May 2003.

F. Babiloni, F. Cincotti, C. Babiloni, F. Carducci, D. Mattia, L. Astolfi, A. Basilisco, P. M. Rossini, L. Ding, Y. Ni, J. Cheng, K. Christine, J. Sweeney, and B. He. Estimation of the cortical functional connectivity with the multimodal integration of high-resolution EEG and fMRI data by directed transfer function. *Neuroimage*, 24:118–131, Jan 2005.

A. P. Bagshaw, Y. Aghakhani, C. G. Benar, E. Kobayashi, C. Hawco, F. Dubeau, G. B. Pike, and J. Gotman. EEG-fMRI of focal epileptic spikes: analysis with multiple haemodynamic functions and comparison with gadolinium-enhanced MR angiograms. *Hum Brain Mapp*, 22:179–192, Jul 2004.

P. A. Bandettini, E. C. Wong, R. S. Hinks, R. S. Tikofsky, and J. S. Hyde. Time course EPI of human brain function during task activation. *Magn Reson Med*, 25:390–397, Jun 1992.

P. A. Bandettini, A. Jesmanowicz, E. C. Wong, and J. S. Hyde. Processing strategies for time-course data sets in functional MRI of the human brain. *Magn Reson Med*, 30:161–173, Aug 1993.

P. R. Bannister, C. F. Bekmann, and M. Jenkinson. Exploratory Motion Analysis in fMRI using ICA. *NeuroImage*, 13:S69, 2001.

J. Baudewig, H. J. Bittermann, W. Paulus, and J. Frahm. Simultaneous EEG and functional MRI of epileptic activity: a case report. *Clin Neurophysiol*, 112:1196–1200, Jul 2001.

C. Baumgartner, W. Serles, F. Leutmezer, E. Pataraia, S. Aull, T. Czech, U. Pietrzyk, A. Relic, and I. Podreka. Preictal SPECT in temporal lobe epilepsy: regional cerebral blood flow is increased prior to electroencephalography-seizure onset. *J. Nucl. Med.*, 39:978–982, Jun 1998.

C. F. Beckmann. Investigating the intrinsic dimensionality of FMRI data for ICA. *NeuroImage*, 13:S76, 2001.

C. F. Beckmann and S. M. Smith. Probabilistic independent component analysis for functional magnetic resonance imaging. *IEEE Trans Med Imaging*, 23:137–152, Feb 2004.

A. J. Bell and T. J. Sejnowski. An information-maximization approach to blind separation and blind deconvolution. *Neural Comput*, 7:1129–1159, Nov 1995.

C. G. Benar, D. W. Gross, Y. Wang, V. Petre, B. Pike, F. Dubeau, and J. Gotman. The BOLD response to interictal epileptiform discharges. *Neuroimage*, 17:1182–1192, Nov 2002.

C. G. Benar, C. Grova, E. Kobayashi, A. P. Bagshaw, Y. Aghakhani, F. Dubeau, and J. Gotman. EEG-fMRI of epileptic spikes: concordance with EEG source localization and intracranial EEG. *Neuroimage*, 30:1161–1170, May 2006.

H. Berger. Uber das Elektroenkephalogramm des Menschen. *Archiv fur Psychiatrie und Nervenkrankheiten*, 87:527–570, May 1929.

O. Bertrand, Thévenet M., and Perrin F. 3D finite element method in brain electrical activity studies. *In: Nenonen J., Rajala H., Katila T. (Eds.), Biomagnetic Localization and 3D Modelling. Report of the Dep. of Tech.Physics, Helsinki University of Technology.*, 1991.

B. Biswal, F. Z. Yetkin, V. M. Haughton, and J. S. Hyde. Functional connectivity in the motor cortex of resting human brain using echo-planar MRI. *Magn Reson Med*, 34:537–541, Oct 1995.

I. Blumcke, M. Thom, and O. D. Wiestler. Ammon's horn sclerosis: a maldevelopmental disorder associated with temporal lobe epilepsy. *Brain Pathol.*, 12:199–211, Apr 2002.

M. Boly, C. Phillips, L. Tshibanda, A. Vanhaudenhuyse, M. Schabus, T. T. Dang-Vu, G. Moonen, R. Hustinx, P. Maquet, and S. Laureys. Intrinsic brain activity in altered states of consciousness: how conscious is the default mode of brain function? *Ann. N. Y. Acad. Sci.*, 1129:119–129, 2008.

B. Bonakdarpour, T. B. Parrish, and C. K. Thompson. Hemodynamic response function in patients with stroke-induced aphasia: implications for fMRI data analysis. *Neuroimage*, 36:322–331, Jun 2007.

G. Bonmassar, K. Anami, J. Ives, and J. W. Belliveau. Visual evoked potential (VEP) measured by simultaneous 64-channel EEG and 3T fMRI. *Neuroreport*, 10:1893–1897, Jun 1999.

G. Bonmassar, P. L. Purdon, I. P. Jaaskelainen, K. Chiappa, V. Solo, E. N. Brown, and J. W. Belliveau. Motion and ballistocardiogram artifact removal for interleaved recording of EEG and EPs during MRI. *Neuroimage*, 16:1127–1141, Aug 2002.

G. Bonvento, N. Cholet, and J. Seylaz. Sustained attenuation of the cerebrovascular response to a 10 min whisker stimulation following neuronal nitric oxide synthase inhibition. *Neurosci. Res.*, 37:163–166, Jun 2000.

P. Borelli, M. Avesani, E. Formaggio, S. F. Storti, T. Zanoni, G. Moretto, A. Fiaschi, R. Cerini, and P. Manganotti. EEG-fMRI as an useful tool to detect epileptic foci associated with secondary bilateral synchrony. *Seizure*, 19:605–608, Nov 2010.

G. M. Boynton, S. A. Engel, G. H. Glover, and D. J. Heeger. Linear systems analysis of functional magnetic resonance imaging in human V1. *J. Neurosci.*, 16:4207–4221, Jul 1996.

V. Brodbeck, A. M. Lascano, L. Spinelli, M. Seeck, and C. M. Michel. Accuracy of EEG source imaging of epileptic spikes in patients with large brain lesions. *Clin Neurophysiol*, 120:679–685, Apr 2009.

V. Brodbeck, L. Spinelli, A. M. Lascano, M. Wissmeier, M. I. Vargas, S. Vulliemoz, C. Pollo, K. Schaller, C. M. Michel, and M. Seeck. Electroencephalographic source imaging: a prospective study of 152 operated epileptic patients. *Brain*, 134:2887–2897, Oct 2011.

M. J. Brookes, A. M. Gibson, S. D. Hall, P. L. Furlong, G. R. Barnes, A. Hillebrand, K. D. Singh, I. E. Holliday, S. T. Francis, and P. G. Morris. GLM-beamformer method demonstrates stationary field, alpha ERD and gamma ERS co-localisation with fMRI BOLD response in visual cortex. *Neuroimage*, 26:302–308, May 2005.

D. Brunet, M. M. Murray, and C. M. Michel. Spatiotemporal analysis of multichannel EEG: CARTOOL. *Comput Intell Neurosci*, 2011:813–870, 2011.

E. Bullmore, M. Brammer, S. C. Williams, S. Rabe-Hesketh, N. Janot, A. David, J. Mellers, R. Howard, and P. Sham. Statistical methods of estimation and inference for functional MR image analysis. *Magn Reson Med*, 35:261–277, Feb 1996.

V. D. Calhoun, T. Adali, G. D. Pearlson, and J. J. Pekar. Spatial and temporal independent component analysis of functional MRI data containing a pair of task-related waveforms. *Hum Brain Mapp*, 13:43–53, May 2001.

V. D. Calhoun, M. C. Stevens, G. D. Pearlson, and K. A. Kiehl. fMRI analysis with the general linear model: removal of latency-induced amplitude bias by incorporation of hemodynamic derivative terms. *Neuroimage*, 22:252–257, May 2004.

J. Cardoso and A. Souloumiac. Blind identification of independent components with higher-order statistics. *Proceedings of the Workshop on Higher-Order Spectral Analysis*, pages 157–162, 1989.

J. Cardoso and A. Souloumiac. Blind beamforming for non-Gaussian signals. *IEEE Proceedings*, 140:362–370, 1993.

C. Cobelli, D. Foster, and G. Toffolo. Tracer Kinetics in Biomedical Research. *New York: Kluwer Academic/Plenum Publishers*, 2000.

C. Cobelli, D. Foster, and G. Toffolo. Tracer Kinetics in Biomedical Research: From Data to Model. *London: Kluwer Academic/Plenum*, 2001.

M. S. Cohen. Parametric analysis of fMRI data using linear systems methods. *Neuroimage*, 6:93–103, Aug 1997.

P. Comon. Independent component analysis: A new concept? *Signal Processing*, 36:11–20, 1994.

D. Cordes and R. R. Nandy. Estimation of the intrinsic dimensionality of fMRI data. *Neuroimage*, 29:145–154, Jan 2006.

D. Cordes, V. M. Haughton, K. Arfanakis, G. J. Wendt, P. A. Turski, C. H. Moritz, M. A. Quigley, and M. E. Meyerand. Mapping functionally related regions of brain with functional connectivity MR imaging. *AJNR Am J Neuroradiol*, 21:1636–1644, Oct 2000.

D. Cordes, V. M. Haughton, K. Arfanakis, J. D. Carew, P. A. Turski, C. H. Moritz, M. A. Quigley, and M. E. Meyerand. Frequencies contributing to functional connectivity in the cerebral cortex in "resting-state" data. *AJNR Am J Neuroradiol*, 22:1326–1333, Aug 2001.

M. Cosottini, I. Pesaresi, P. Maritato, G. Belmonte, A. Taddei, F. Sartucci, M. Mascalchi, and L. Murri. EEG topography-specific BOLD changes: a continuous EEG-fMRI study in a patient with focal epilepsy. *Magn Reson Imaging*, 28:388–393, Apr 2010.

R. W. Cox. AFNI: software for analysis and visualization of functional magnetic resonance neuroimages. *Comput. Biomed. Res.*, 29:162–173, Jun 1996.

J. S. Damoiseaux, S. A. Rombouts, F. Barkhof, P. Scheltens, C. J. Stam, S. M. Smith, and C. F. Beckmann. Consistent resting-state networks across healthy subjects. *Proc. Natl. Acad. Sci. U.S.A.*, 103:13848–13853, Sep 2006.

F. De Martino, F. Gentile, F. Esposito, M. Balsi, F. Di Salle, R. Goebel, and E. Formisano. Classification of fMRI independent components using IC-fingerprints and support vector machine classifiers. *Neuroimage*, 34: 177–194, Jan 2007.

S. Debener, M. Ullsperger, M. Siegel, and A. K. Engel. Single-trial EEG-fMRI reveals the dynamics of cognitive function. *Trends Cogn. Sci. (Regul. Ed.)*, 10:558–563, Dec 2006.

A. Del Felice, T. Zanoni, M. Avesani, E. Formaggio, S. Storti, A. Fiaschi, G. Moretto, and P. Manganotti. EEG-fMRI coregistration in non-ketotic hyperglycemic occipital seizures. *Epilepsy Res.*, 85:321–324, Aug 2009.

A. Delorme and S. Makeig. EEGLAB: an open source toolbox for analysis of single-trial EEG dynamics including independent component analysis. *J. Neurosci. Methods*, 134:9–21, Mar 2004.

E. A. DeYoe, P. Bandettini, J. Neitz, D. Miller, and P. Winans. Functional magnetic resonance imaging (FMRI) of the human brain. *J. Neurosci. Methods*, 54:171–187, Oct 1994.

J. S. Ebersole. Non-invasive localization of the epileptogenic focus by EEG dipole modeling. *Acta Neurol. Scand., Suppl.*, 152:20–28, 1994.

M. L. Ellingson, E. Liebenthal, M. V. Spanaki, T. E. Prieto, J. R. Binder, and K. M. Ropella. Ballistocardiogram artifact reduction in the simultaneous acquisition of auditory ERPS and fMRI. *Neuroimage*, 22:1534–1542, Aug 2004.

N. Erbil and P. Ungan. Changes in the alpha and beta amplitudes of the central EEG during the onset, continuation, and offset of long-duration repetitive hand movements. *Brain Res.*, 1169:44–56, Sep 2007.

P. Federico, J. S. Archer, D. F. Abbott, and G. D. Jackson. Cortical/subcortical BOLD changes associated with epileptic discharges: an EEG-fMRI study at 3 T. *Neurology*, 64:1125–1130, Apr 2005.

J. Felblinger, J. Slotboom, R. Kreis, B. Jung, and C. Boesch. Restoration of electrophysiological signals distorted by inductive effects of magnetic field gradients during MR sequences. *Magn Reson Med*, 41:715–721, Apr 1999.

D. H. Fender. Source localization of the brain electrical activity. *Methods of Analysis of Brain Electrically activity and Magnetic Signals, Elsevier, Amsterdam, The Neverlands, Gevins AS and Remont A Eds.*, pages 355–403, 1987.

A. Ferretti, C. Del Gratta, C. Babiloni, M. Caulo, D. Arienzo, A. Tartaro, P. M. Rossini, and G. L. Romani. Functional topography of the secondary somatosensory cortex for nonpainful and painful stimulation of median and tibial nerve: an fMRI study. *Neuroimage*, 23:1217–1225, Nov 2004.

A. Ferretti, C. Babiloni, D. Arienzo, C. Del Gratta, P. M. Rossini, A. Tartaro, and G. L. Romani. Cortical brain responses during passive nonpainful median nerve stimulation at low frequencies (0.5-4 Hz): an fMRI study. *Hum Brain Mapp*, 28:645–653, Jul 2007.

E. Formaggio, M. Avesani, S. F. Storti, F. Milanese, A. Gasparini, M. Acler, R. Cerini, R. Pozzi Mucelli, A. Fiaschi, and P. Manganotti. Effect of a static magnetic field (1.5T) on brain oscillatory activities in resting state condition. *Neuroradiol J*, 21:629–635, 2008a.

E. Formaggio, S. F. Storti, M. Avesani, R. Cerini, F. Milanese, A. Gasparini, M. Acler, R. Pozzi Mucelli, A. Fiaschi, and P. Manganotti. EEG and FMRI coregistration to investigate the cortical oscillatory activities during finger movement. *Brain Topogr*, 21:100–111, Dec 2008b.

E. Formaggio, S. F. Storti, A. Bertoldo, P. Manganotti, A. Fiaschi, and G. M. Toffolo. Integrating EEG and fMRI in epilepsy. *Neuroimage*, 54:2719–2731, Feb 2011.

E. Formisano, F. Esposito, N. Kriegeskorte, G. Tedeschi, F. Di Salle, and R. Goebel. Spatial independent component analysis of functional magnetic resonance imaging time-series: characterization of the cortical components. *Neurocomputing*, 49:241–254, 2002.

M. D. Fox, M. Corbetta, A. Z. Snyder, J. L. Vincent, and M. E. Raichle. Spontaneous neuronal activity distinguishes human dorsal and ventral attention systems. *Proc. Natl. Acad. Sci. U.S.A.*, 103:10046–10051, Jun 2006.

K. J. Friston, P. Fletcher, O. Josephs, A. Holmes, M. D. Rugg, and R. Turner. Event-related fMRI: characterizing differential responses. *Neuroimage*, 7: 30–40, Jan 1998.

K. J. Friston, J.T. Ashburner, S.J. Kiebel, Nichols T.E., and Penny W.D. Statistical Parametric Mapping. *London: Academic Press*, page 182, 2007.

K.J. Friston, A.P. Holmes, K.J. Worsley, J-P. Poline, C.D. Frith, and R.S.J. Frackowiak. Statistical parametric maps in functional imaging: A general linear approach. *Hum Brain Mapp*, 2:189–210, Apr 1995.

H. Gastaut. Etude electrocorticographique de la re activite des rhythmes rolandiques. *Revue Neurologique Paris*, 87:176–182, 1952.

G. Glatting, P. Kletting, S. N. Reske, K. Hohl, and C. Ring. Choosing the optimal fit function: comparison of the Akaike information criterion and the F-test. *Med Phys*, 34:4285–4292, Nov 2007.

G. H. Glover. Deconvolution of impulse response in event-related BOLD fMRI. *Neuroimage*, 9:416–429, Apr 1999.

G. H. Glover, T. Q. Li, and D. Ress. Image-based method for retrospective correction of physiological motion effects in fMRI: RETROICOR. *Magn Reson Med*, 44:162–167, Jul 2000.

X. Golay, S. Kollias, G. Stoll, D. Meier, A. Valavanis, and P. Boesiger. A new correlation-based fuzzy logic clustering algorithm for fMRI. *Magn Reson Med*, 40:249–260, Aug 1998.

R. I. Goldman, J. M. Stern, J. Engel, and M. S. Cohen. Acquiring simultaneous EEG and functional MRI. *Clin Neurophysiol*, 111:1974–1980, Nov 2000.

S. I. Goncalves, P. J. Pouwels, J. P. Kuijer, R. M. Heethaar, and J. C. de Munck. Artifact removal in co-registered EEG/fMRI by selective average subtraction. *Clin Neurophysiol*, 118:2437–2450, Nov 2007.

S.L. Gonzalez Andino, R. Grave de Peralta Menendez, R. Biscay Lirio, J.C. Jimenez Sobrino, R.D. Pascual Marqui, J. Lemagne, and P.A. Valdes Sosa. Projective methods for the magnetic direct problem. *In: S.J. Williamson, M. Hoke, G. Stroink, and M. Kotani (Eds.) Advances in Biomagnetism, New York, Plenum*, pages 615–618, 1989.

I. F. Gorodnitsky, J. S. George, and B. D. Rao. Neuromagnetic source imaging with FOCUSS: a recursive weighted minimum norm algorithm. *Electroencephalogr Clin Neurophysiol*, 95:231–251, Oct 1995.

C. Gossl, D. P. Auer, and L. Fahrmeir. Bayesian spatiotemporal inference in functional magnetic resonance imaging. *Biometrics*, 57:554–562, Jun 2001a.

C. Gossl, L. Fahrmeir, and D. P. Auer. Bayesian modeling of the hemodynamic response function in BOLD fMRI. *Neuroimage*, 14:140–148, Jul 2001b.

J. Gotman. Epileptic networks studied with EEG-fMRI. *Epilepsia*, 49 Suppl 3:42–51, 2008.

J. Gotman, C. G. Benar, and F. Dubeau. Combining EEG and FMRI in epilepsy: methodological challenges and clinical results. *J Clin Neurophysiol*, 21:229–240, 2004.

J. Gotman, C. Grova, A. Bagshaw, E. Kobayashi, Y. Aghakhani, and F. Dubeau. Generalized epileptic discharges show thalamocortical activation and suspension of the default state of the brain. *Proc. Natl. Acad. Sci. U.S.A.*, 102:15236–15240, Oct 2005.

J. Gotman, E. Kobayashi, A. P. Bagshaw, C. G. Benar, and F. Dubeau. Combining EEG and fMRI: a multimodal tool for epilepsy research. *J Magn Reson Imaging*, 23:906–920, Jun 2006.

C. Goutte, P. Toft, E. Rostrup, F. Nielsen, and L. K. Hansen. On clustering fMRI time series. *Neuroimage*, 9:298–310, Mar 1999.

C. Goutte, F. A. Nielsen, and L. K. Hansen. Modeling the haemodynamic response in fMRI using smooth FIR filters. *IEEE Trans Med Imaging*, 19: 1188–1201, Dec 2000.

R. Grave de Peralta and S. Gonzalez. A critical analysis of linear inverse solutions. *IEEE Trans Biomed Eng*, 45:440–448, 1998.

R. Grave de Peralta and S. Gonzalez. Comparison of algorithms for the localization of focal sources: Evaluation with simulated data and analysis of experimental data. *International Journal of Bioelectromagnetism*, 4, 2002.

K. Groening, V. Brodbeck, F. Moeller, S. Wolff, A. van Baalen, C. M. Michel, O. Jansen, R. Boor, G. Wiegand, U. Stephani, and M. Siniatchkin. Combination of EEG-fMRI and EEG source analysis improves interpretation of spike-associated activation networks in paediatric pharmacoresistant focal epilepsies. *Neuroimage*, 46:827–833, Jul 2009.

F. Grouiller, L. Vercueil, A. Krainik, C. Segebarth, P. Kahane, and O. David. Characterization of the hemodynamic modes associated with interictal epileptic activity using a deformable model-based analysis of combined EEG and functional MRI recordings. *Hum Brain Mapp*, 31:1157–1173, Aug 2010.

F. Grouiller, R. C. Thornton, K. Groening, L. Spinelli, J. S. Duncan, K. Schaller, M. Siniatchkin, L. Lemieux, M. Seeck, C. M. Michel, and S. Vulliemoz. With or without spikes: localization of focal epileptic activity by simultaneous electroencephalography and functional magnetic resonance imaging. *Brain*, 134:2867–2886, Oct 2011.

A. G. Guggisberg, S. S. Dalal, J. M. Zumer, D. D. Wong, S. Dubovik, C. M. Michel, and A. Schnider. Localization of cortico-peripheral coherence with electroencephalography. *Neuroimage*, 57:1348–1357, Aug 2011.

M. Hamalainen and RJ. Ilmoniemi. Interpreting measured magnetic fields of the brain: estimates of current distribution (Technical Report TKK-F-A559). *Helsinki University of Technology, Finland*, 1984.

M. S. Hamalainen and R. J. Ilmoniemi. Interpreting magnetic fields of the brain: minimum norm estimates. *Med Biol Eng Comput*, 32:35–42, Jan 1994.

K. Hamandi, A. Salek-Haddadi, D. R. Fish, and L. Lemieux. EEG/functional MRI in epilepsy: The Queen Square Experience. *J Clin Neurophysiol*, 21: 241–248, 2004.

K. Hamandi, A. Salek-Haddadi, H. Laufs, A. Liston, K. Friston, D. R. Fish, J. S. Duncan, and L. Lemieux. EEG-fMRI of idiopathic and secondarily generalized epilepsies. *Neuroimage*, 31:1700–1710, Jul 2006.

K. Hamandi, H. Laufs, U. Noth, D. W. Carmichael, J. S. Duncan, and L. Lemieux. BOLD and perfusion changes during epileptic generalised spike wave activity. *Neuroimage*, 39:608–618, Jan 2008.

D. A. Handwerker, J. M. Ollinger, and M. D'Esposito. Variation of BOLD hemodynamic responses across subjects and brain regions and their effects on statistical analyses. *Neuroimage*, 21:1639–1651, Apr 2004.

N. Harel, S. P. Lee, T. Nagaoka, D. S. Kim, and S. G. Kim. Origin of negative blood oxygenation level-dependent fMRI signals. *J. Cereb. Blood Flow Metab.*, 22:908–917, Aug 2002.

C. S. Hawco, A. P. Bagshaw, Y. Lu, F. Dubeau, and J. Gotman. BOLD changes occur prior to epileptic spikes seen on scalp EEG. *Neuroimage*, 35:1450–1458, May 2007.

B. He, L. Yang, C. Wilke, and H. Yuan. Electrophysiological imaging of brain activity and connectivity-challenges and opportunities. *IEEE Trans Biomed Eng*, 58:1918–1931, Jul 2011.

D. J. Heeger, A. C. Huk, W. S. Geisler, and D. G. Albrecht. Spikes versus BOLD: what does neuroimaging tell us about neuronal activity? *Nat. Neurosci.*, 3:631–633, Jul 2000.

R. N. Henson. Repetition effects for words and nonwords as indexed by event-related fMRI: a preliminary study. *Scand J Psychol*, 42:179–186, Jul 2001.

R. N. Henson, C. J. Price, M. D. Rugg, R. Turner, and K. J. Friston. Detecting latency differences in event-related BOLD responses: application to words versus nonwords and initial versus repeated face presentations. *Neuroimage*, 15:83–97, Jan 2002.

A. Hoffmann, L. Jager, K. J. Werhahn, M. Jaschke, S. Noachtar, and M. Reiser. Electroencephalography during functional echo-planar imaging: detection of epileptic spikes using postprocessing methods. *Magn Res Med*, 4:791–798, Nov 2000.

M. D. Holmes, D. M. Tucker, J. M. Quiring, S. Hakimian, J. W. Miller, and J. G. Ojemann. Comparing noninvasive dense array and intracranial electroencephalography for localization of seizures. *Neurosurgery*, 66:354–362, Feb 2010.

F. R. Huang-Hellinger, H. C. Breiter, G. McCormack, M. S. Cohen, K. K. Kwong, J. P. Sutton, R. L. Savoy, R. M. Weisskoff, T. L. Davis, J. R. Baker, J. W. Belliveau, and B. R. Rosen. Simultaneous functional magnetic resonance imaging and electrophysiological recording. *Hum Brain Mapp*, 3:13–25, Oct 1995.

S. A. Huettel, A. W. Song, and G. McCarthy. Functional Magnetic Resonance Imaging. *Sinauer Associates: U.S.A.*, pages 334–335, 2004.

A. Hyvarinen. Fast and robust fixed-point algorithms for independent component analysis. *IEEE Trans Neural Netw*, 10:626–634, 1999.

G. V. Isaev and A. I. a. Supin. Ambiguity of the solution of the inverse problem of electroencephalography. *Biofizika*, 30:467–471, 1985.

J. R. Ives. Apparatus and method for recording an electroencephalogram during magnetic resonance imaging. *USA. Patent No: 5, 445, 162*, Aug 1995.

J. R. Ives, S. Warach, F. Schmitt, R. R. Edelman, and D. L. Schomer. Monitoring the patient's EEG during echo planar MRI. *Electroencephalogr Clin Neurophysiol*, 87:417–420, Dec 1993.

J. Jacobs, E. Kobayashi, R. Boor, H. Muhle, W. Stephan, C. Hawco, F. Dubeau, O. Jansen, U. Stephani, J. Gotman, and M. Siniatchkin. Hemodynamic responses to interictal epileptiform discharges in children with symptomatic epilepsy. *Epilepsia*, 48:2068–2078, Nov 2007.

J. Jacobs, P. Levan, F. Moeller, R. Boor, U. Stephani, J. Gotman, and M. Siniatchkin. Hemodynamic changes preceding the interictal EEG spike in patients with focal epilepsy investigated using simultaneous EEG-fMRI. *Neuroimage*, 45:1220–1231, May 2009.

K. Jann, R. Wiest, M. Hauf, K. Meyer, C. Boesch, J. Mathis, G. Schroth, T. Dierks, and T. Koenig. BOLD correlates of continuously fluctuating

epileptic activity isolated by independent component analysis. *Neuroimage*, 42:635–648, Aug 2008.

P. Jezzard, P. M. Matthews, and S. M. Smith. Functional MRI an introduction to methods. *Great Britain: Oxford University Press*, pages 255–265, 2001.

C. Jutten and J. Herault. Independent component analysis versus pca. *In proceedings, EUSIPCO*, pages 643–646, 1988.

D. Kandaswamy, T. Blu, L. Spinelli, C. Michel, and D. Van De Ville. EEG source localization by multi-planar analytic sensing. *5th IEEE international symposium on biomedical imaging: From nano to macro*, 2008.

S. S. Kannurpatti and B. B. Biswal. Negative functional response to sensory stimulation and its origins. *J. Cereb. Blood Flow Metab.*, 24:703–712, Jun 2004.

D. S. Kim, T. Q. Duong, and S. G. Kim. High-resolution mapping of iso-orientation columns by fMRI. *Nat. Neurosci.*, 3:164–169, Feb 2000.

D. S. Kim, I. Ronen, C. Olman, S. G. Kim, K. Ugurbil, and L. J. Toth. Spatial relationship between neuronal activity and BOLD functional MRI. *Neuroimage*, 21:876–885, Mar 2004.

V. Kiviniemi, J. Jauhiainen, O. Tervonen, E. Paakko, J. Oikarinen, V. Vainionpaa, H. Rantala, and B. Biswal. Slow vasomotor fluctuation in fMRI of anesthetized child brain. *Magn Reson Med*, 44:373–378, Sep 2000.

E. Kobayashi, A. P. Bagshaw, C. Grova, J. Gotman, and F. Dubeau. Grey matter heterotopia: what EEG-fMRI can tell us about epileptogenicity of neuronal migration disorders. *Brain*, 129:366–374, Feb 2006.

K. Krakow, F. G. Woermann, M. R. Symms, P. J. Allen, L. Lemieux, G. J. Barker, J. S. Duncan, and D. R. Fish. EEG-triggered functional MRI of interictal epileptiform activity in patients with partial seizures. *Brain*, 122 (Pt 9):1679–1688, Sep 1999.

Y. Lai, X. Zhang, W. van Drongelen, M. Korhman, K. Hecox, Y. Ni, and B. He. Noninvasive cortical imaging of epileptiform activities from interictal spikes in pediatric patients. *Neuroimage*, 54:244–252, Jan 2011.

E. M. Landaw and J. J. DiStefano. Multiexponential, multicompartmental, and noncompartmental modeling. II. Data analysis and statistical considerations. *Am. J. Physiol.*, 246:R665–677, May 1984.

N. Lange and S. L. Zeger. Non-linear fourier time series analysis for human brain mapping by functional magnetic resonance imaging (with discussion). *Applied Statistics, Journal of the Royal Statistical Society, Series C*, 46:1–29, 1997.

G. Lantz, R. Grave de Peralta Menendez, S. Gonzalez Andino, and C. M. Michel. Noninvasive localization of electromagnetic epileptic activity. II. Demonstration of sublobar accuracy in patients with simultaneous surface and depth recordings. *Brain Topogr*, 14:139–147, 2001.

G. Lantz, R. Grave de Peralta, L. Spinelli, M. Seeck, and C. M. Michel. Epileptic source localization with high density EEG: how many electrodes are needed? *Clin Neurophysiol*, 114:63–69, Jan 2003a.

G. Lantz, L. Spinelli, M. Seeck, R. G. de Peralta Menendez, C. C. Sottas, and C. M. Michel. Propagation of interictal epileptiform activity can lead to erroneous source localizations: a 128-channel EEG mapping study. *J Clin Neurophysiol*, 20:311–319, 2003b.

H. Laufs and J. S. Duncan. Electroencephalography/functional MRI in human epilepsy: what it currently can and cannot do. *Curr. Opin. Neurol.*, 20:417–423, Aug 2007.

H. Laufs, A. Kleinschmidt, A. Beyerle, E. Eger, A. Salek-Haddadi, C. Preibisch, and K. Krakow. EEG-correlated fMRI of human alpha activity. *Neuroimage*, 19:1463–1476, Aug 2003.

H. Laufs, U. Lengler, K. Hamandi, A. Kleinschmidt, and K. Krakow. Linking generalized spike-and-wave discharges and resting state brain activity by using EEG/fMRI in a patient with absence seizures. *Epilepsia*, 47:444–448, Feb 2006.

H. Laufs, K. Hamandi, A. Salek-Haddadi, A. K. Kleinschmidt, J. S. Duncan, and L. Lemieux. Temporal lobe interictal epileptic discharges affect cerebral activity in "default mode" brain regions. *Hum Brain Mapp*, 28: 1023–1032, Oct 2007.

L. Lemieux, P. J. Allen, F. Franconi, M. R. Symms, and D. R. Fish. Recording of EEG during fMRI experiments: patient safety. *Magn Reson Med*, 38: 943–952, Dec 1997.

L. Lemieux, K. Krakow, and D. R. Fish. Comparison of spike-triggered functional MRI BOLD activation and EEG dipole model localization. *Neuroimage*, 14:1097–1104, Nov 2001a.

L. Lemieux, A. Salek-Haddadi, O. Josephs, P. Allen, N. Toms, C. Scott, K. Krakow, R. Turner, and D. R. Fish. Event-related fMRI with simultaneous and continuous EEG: description of the method and initial case report. *Neuroimage*, 14:780–787, Sep 2001b.

L. Lemieux, H. Laufs, D. Carmichael, J. S. Paul, M. C. Walker, and J. S. Duncan. Noncanonical spike-related BOLD responses in focal epilepsy. *Hum Brain Mapp*, 29:329–345, Mar 2008.

L. Leocani, C. Toro, P. Manganotti, P. Zhuang, and M. Hallett. Event-related coherence and event-related desynchronization/synchronization in the 10 Hz and 20 Hz EEG during self-paced movements. *Electroencephalogr Clin Neurophysiol*, 104:199–206, May 1997.

P. LeVan, L. Tyvaert, and J. Gotman. Modulation by EEG features of BOLD responses to interictal epileptiform discharges. *Neuroimage*, 50:15–26, Mar 2010.

Q. Li, C. Luo, T. Yang, Z. Yao, L. He, L. Liu, H. Xu, Q. Gong, D. Yao, and D. Zhou. EEG-fMRI study on the interictal and ictal generalized spike-wave discharges in patients with childhood absence epilepsy. *Epilepsy Res.*, 87:160–168, Dec 2009.

M. A. Lindquist and T. D. Wager. Validity and power in hemodynamic response modeling: a comparison study and a new approach. *Hum Brain Mapp*, 28:764–784, Aug 2007.

A. D. Liston, J. C. De Munck, K. Hamandi, H. Laufs, P. Ossenblok, J. S. Duncan, and L. Lemieux. Analysis of EEG-fMRI data in focal epilepsy based on automated spike classification and Signal Space Projection. *Neuroimage*, 31:1015–1024, Jul 2006.

A. K. Liu, J. W. Belliveau, and A. M. Dale. Spatiotemporal imaging of human brain activity using functional MRI constrained magnetoencephalography data: Monte Carlo simulations. *Proc. Natl. Acad. Sci. U.S.A.*, 95:8945–8950, Jul 1998.

B. R. Logan and D. B. Rowe. An evaluation of thresholding techniques in fMRI analysis. *Neuroimage*, 22:95–108, May 2004.

N. K. Logothetis and J. Pfeuffer. On the nature of the BOLD fMRI contrast mechanism. *Magn Reson Imaging*, 22:1517–1531, Dec 2004.

N. K. Logothetis, J. Pauls, M. Augath, T. Trinath, and A. Oeltermann. Neurophysiological investigation of the basis of the fMRI signal. *Nature*, 412:150–157, Jul 2001.

F. H. Lopes da Silva. Electrical potentials. *In: V.S. Ramachandran, Editor, Encyclopedia of the human brain, Elsevier Science*, 2002.

F. H. Lopes da Silva and A. van Rotterdam. Biophysical aspects of EEG and magnetoencephalographic generation. *In: Niedermeyer E, Lopes da Silva F (eds) Electroencephalography: basic principles, clinical applications and related fields, 5th edn. Lippincott, Wlliams & Wilkins, New York*, 2005.

F. H. Lopes da Silva, J. P. Pijn, D. Velis, and P. C. Nijssen. Alpha rhythms: noise, dynamics and models. *Int J Psychophysiol*, 26:237–249, Jun 1997.

K. O. Lovblad, R. Thomas, P. M. Jakob, T. Scammell, C. Bassetti, M. Griswold, J. Ives, J. Matheson, R. R. Edelman, and S. Warach. Silent functional magnetic resonance imaging demonstrates focal activation in rapid eye movement sleep. *Neurology*, 53:2193–2195, Dec 1999.

W. Lu and J. C. Rajapakse. Eliminating indeterminacy in ICA. *Neuroimage*, 50:271–290, 2003.

Y. Lu, A. P. Bagshaw, C. Grova, E. Kobayashi, F. Dubeau, and J. Gotman. Using voxel-specific hemodynamic response function in EEG-fMRI data analysis. *Neuroimage*, 32:238–247, Aug 2006.

Y. Lu, C. Grova, E. Kobayashi, F. Dubeau, and J. Gotman. Using voxel-specific hemodynamic response function in EEG-fMRI data analysis: An estimation and detection model. *Neuroimage*, 34:195–203, Jan 2007.

T. E. Lund, K. H. Madsen, K. Sidaros, W. L. Luo, and T. E. Nichols. Non-white noise in fMRI: does modelling have an impact? *Neuroimage*, 29: 54–66, Jan 2006.

C. Luo, Z. Yao, Q. Li, X. Lei, D. Zhou, Y. Qin, Y. Xia, Y. Lai, Q. Gong, and D. Yao. Imaging foci of epileptic discharges from simultaneous EEG and fMRI using the canonical HRF. *Epilepsy Res.*, 91:133–142, Oct 2010.

H. Luo and S. Puthusserypady. Analysis of FMRI data with drift: modified general linear model and Bayesian estimator. *IEEE Trans Biomed Eng*, 55:1504–1511, May 2008.

J. B. MacQueen. Some Methods for classification and Analysis of Multivariate Observations. *Proceedings of 5-th Berkeley Symposium on Mathematical Statistics and Probability*, 1:281–297, 1967.

P. J. Magistretti and L. Pellerin. Cellular mechanisms of brain energy metabolism and their relevance to functional brain imaging. *Philos. Trans. R. Soc. Lond., B, Biol. Sci.*, 354:1155–1163, Jul 1999.

M. Makiranta, J. Ruohonen, K. Suominen, J. Niinimaki, E. Sonkajarvi, V. Kiviniemi, T. Seppanen, S. Alahuhta, V. Jantti, and O. Tervonen. BOLD signal increase preceeds EEG spike activity–a dynamic penicillin induced focal epilepsy in deep anesthesia. *Neuroimage*, 27:715–724, Oct 2005.

D. Malonek and A. Grinvald. Interactions between electrical activity and cortical microcirculation revealed by imaging spectroscopy: implications for functional brain mapping. *Science*, 272:551–554, Apr 1996.

P. Manganotti, E. Formaggio, A. Gasparini, R. Cerini, L. G. Bongiovanni, S. F. Storti, R. P. Mucelli, A. Fiaschi, and M. Avesani. Continuous EEG-fMRI in patients with partial epilepsy and focal interictal slow-wave discharges on EEG. *Magn Reson Imaging*, 26:1089–1100, Oct 2008.

P. Manganotti, S. F. Storti, E. Formaggio, M. Acler, G. Zoccatelli, F. B. Pizzini, F. Alessandrini, A. Bertoldo, G. M. Toffolo, P. Bovi, A. Beltramello, G. Moretto, and A. Fiaschi. Effect of median-nerve electrical stimulation on BOLD activity in acute ischemic stroke patients. *Clin Neurophysiol*, 123:142–153, Jan 2012.

S. Mangia, F. Giove, I. Tkac, N. K. Logothetis, P. G. Henry, C. A. Olman, B. Maraviglia, F. Di Salle, and K. Ugurbil. Metabolic and hemodynamic events after changes in neuronal activity: current hypotheses, theoretical predictions and in vivo NMR experimental findings. *J. Cereb. Blood Flow Metab.*, 29:441–463, Mar 2009.

D. Mantini, M. G. Perrucci, C. Del Gratta, G. L. Romani, and M. Corbetta. Electrophysiological signatures of resting state networks in the human brain. *Proc. Natl. Acad. Sci. U.S.A.*, 104:13170–13175, Aug 2007.

J. P. Marques, J. Rebola, P. Figueiredo, A. Pinto, F. Sales, and M. Castelo-Branco. ICA decomposition of EEG signal for fMRI processing in epilepsy. *Hum Brain Mapp*, 30:2986–2996, Sep 2009.

G. Marrelec and H. Benali. Non-parametric Bayesian deconvolution of fMRI hemodynamic response function using smoothing prior. *Neuroimage*, 13: S194, 2001.

G. Marrelec, H. Benali, P. Ciuciu, M. Pelegrini-Issac, and J. B. Poline. Robust Bayesian estimation of the hemodynamic response function in event-related BOLD fMRI using basic physiological information. *Hum Brain Mapp*, 19:1–17, May 2003.

R. A. Masterton, A. S. Harvey, J. S. Archer, L. M. Lillywhite, D. F. Abbott, I. E. Scheffer, and G. D. Jackson. Focal epileptiform spikes do not show a canonical BOLD response in patients with benign rolandic epilepsy (BECTS). *Neuroimage*, 51:252–260, May 2010.

L. Mazzini, F. M. Cossa, E. Angelino, R. Campini, I. Pastore, and F. Monaco. Posttraumatic epilepsy: neuroradiologic and neuropsychological assessment of long-term outcome. *Epilepsia*, 44:569–574, Apr 2003.

M. J. McKeown. Detection of consistently task-related activations in fMRI data with hybrid independent component analysis. *Neuroimage*, 11:24–35, Jan 2000.

M. J. McKeown, S. Makeig, G. G. Brown, T. P. Jung, S. S. Kindermann, A. J. Bell, and T. J. Sejnowski. Analysis of fMRI data by blind separation into independent spatial components. *Hum Brain Mapp*, 6:160–188, 1998.

M. J. McKeown, L. K. Hansen, and T. J. Sejnowsk. Independent component analysis of functional MRI: what is signal and what is noise? *Curr. Opin. Neurobiol.*, 13:620–629, Oct 2003.

J. W. Meijs, F. G. Bosch, M. J. Peters, and F. H. Lopes da Silva. On the magnetic field distribution generated by a dipolar current source situated in a realistically shaped compartment model of the head. *Electroencephalogr Clin Neurophysiol*, 66:286–298, Mar 1987.

R. S. Menon and B. G. Goodyear. Submillimeter functional localization in human striate cortex using BOLD contrast at 4 Tesla: implications for the vascular point-spread function. *Magn Reson Med*, 41:230–235, Feb 1999.

R. S. Menon and S. G. Kim. Spatial and temporal limits in cognitive neuroimaging with fMRI. *Trends Cogn. Sci. (Regul. Ed.)*, 3:207–216, Jun 1999.

V. Menon and S. Crottaz-Herbette. Combined EEG and fMRI studies of human brain function. *Int. Rev. Neurobiol.*, 66:291–321, 2005.

C. M. Michel and M. M. Murray. Towards the utilization of EEG as a brain imaging tool. *Neuroimage*, Dec 2011.

C. M. Michel, M. M. Murray, G. Lantz, S. Gonzalez, L. Spinelli, and R. Grave de Peralta. EEG source imaging. *Clin Neurophysiol*, 115:2195–2222, Oct 2004.

Minca. Automatic choice of dimensionality for PCA. *Technical Report 514, MIT Media Lab Vision and Modeling Group*, 2000.

F. Moeller, H. R. Siebner, S. Wolff, H. Muhle, R. Boor, O. Granert, O. Jansen, U. Stephani, and M. Siniatchkin. Changes in activity of striato-thalamo-cortical network precede generalized spike wave discharges. *Neuroimage*, 39:1839–1849, Feb 2008.

F. Moeller, P. LeVan, and J. Gotman. Independent component analysis (ICA) of generalized spike wave discharges in fMRI: comparison with general linear model-based EEG-fMRI. *Hum Brain Mapp*, 32:209–217, Feb 2011.

L. Molgedey and H. G. Schuster. Separation of a mixture of independent signals using time delayed correlations. *Phys. Rev. Lett.*, 72:3634–3637, Jun 1994.

M. Moosmann, P. Ritter, I. Krastel, A. Brink, S. Thees, F. Blankenburg, B. Taskin, H. Obrig, and A. Villringer. Correlates of alpha rhythm in functional magnetic resonance imaging and near infrared spectroscopy. *Neuroimage*, 20:145–158, Sep 2003.

C. H. Moritz, B. P. Rogers, and M. E. Meyerand. Power spectrum ranked independent component analysis of a periodic fMRI complex motor paradigm. *Hum Brain Mapp*, 18:111–122, Feb 2003.

J. C. Mosher and R. M. Leahy. Recursive MUSIC: a framework for EEG and MEG source localization. *IEEE Trans Biomed Eng*, 45:1342–1354, Nov 1998.

J. C. Mosher, R. M. Leahy, and P. S. Lewis. EEG and MEG: forward solutions for inverse methods. *IEEE Trans Biomed Eng*, 46:245–259, Mar 1999.

C. Mulert and L. Lemieux. EEG-fMRI. Physiological basis, technique, and applications. *Springer*, 2010.

C. Mulert, L. Jager, R. Schmitt, P. Bussfeld, O. Pogarell, H. J. Moller, G. Juckel, and U. Hegerl. Integration of fMRI and simultaneous EEG: towards a comprehensive understanding of localization and time-course of brain activity in target detection. *Neuroimage*, 22:83–94, May 2004.

R. M. Muri, J. Felblinger, K. M. Rosler, B. Jung, C. W. Hess, and C. Boesch. Recording of electrical brain activity in a magnetic resonance environment: distorting effects of the static magnetic field. *Magn Reson Med*, 39:18–22, Jan 1998.

R. K. Niazy, C. F. Beckmann, G. D. Iannetti, J. M. Brady, and S. M. Smith. Removal of FMRI environment artifacts from EEG data using optimal basis sets. *Neuroimage*, 28:720–737, Nov 2005.

E. Niedermeyer and F. H. Lopes da Silva. Electroencephalography: Basic principles, clinical applications, and related fields. *5th Ed Lippincott Williams & Wilkins Philadelphia*, 2004.

P. L. Nurez and R. Srinivasan. Electric fields of the brain: The neurophysics of EEG. *2nd Ed. Oxford University Press, New York*, 2006.

S. Ogawa, R. S. Menon, S. G. Kim, and K. Ugurbil. On the characteristics of functional magnetic resonance imaging of the brain. *Annu Rev Biophys Biomol Struct*, 27:447–474, 1998.

S. Ogawa, T. M. Lee, R. Stepnoski, W. Chen, X. H. Zhu, and K. Ugurbil. An approach to probe some neural systems interaction by functional MRI at neural time scale down to milliseconds. *Proc. Natl. Acad. Sci. U.S.A.*, 97:11026–11031, Sep 2000.

R. C. Oldfield. The assessment and analysis of handedness: the Edinburgh inventory. *Neuropsychologia*, 9:97–113, Mar 1971.

P. Ossenblok and H. Spekreijse. The extrastriate generators of the EP to checkerboard onset. A source localization approach. *Electroencephalogr Clin Neurophysiol*, 80:181–193, 1991.

P. Ossenblok, M. Fuchs, D. N. Velis, E. Veltman, J. P. Pijn, and F. H. da Silva. Source analysis of lesional frontal-lobe epilepsy. *IEEE Eng Med Biol Mag*, 18:67–77, 1999.

H. J. Park, J. S. Kwon, T. Youn, J. S. Pae, J. J. Kim, M. S. Kim, and K. S. Ha. Statistical parametric mapping of LORETA using high density EEG and individual MRI: application to mismatch negativities in schizophrenia. *Hum Brain Mapp*, 17:168–178, Nov 2002.

L. M. Parkes, M. C. Bastiaansen, and D. G. Norris. Combining EEG and fMRI to investigate the post-movement beta rebound. *Neuroimage*, 29: 685–696, Feb 2006.

R. D. Pascual-Marqui. Standardized low-resolution brain electromagnetic tomography (sLORETA): technical details. *Methods Find Exp Clin Pharmacol*, 24 Suppl D:5–12, 2002.

R. D. Pascual-Marqui. Discrete, 3D distributed, linear imaging methods of electric neuronal activity. Part 1: exact, zero error localization. *arXiv:0710.3341 [math-ph]*, http://arxiv.org/pdf/0710.3341, 2007.

R. D. Pascual-Marqui, C. M. Michel, and D. Lehmann. Low resolution electromagnetic tomography: a new method for localizing electrical activity in the brain. *Int J Psychophysiol*, 18:49–65, Oct 1994.

R. D. Pascual-Marqui, D. Lehmann, T. Koenig, K. Kochi, M. C. Merlo, D. Hell, and M. Koukkou. Low resolution brain electromagnetic tomography (LORETA) functional imaging in acute, neuroleptic-naive, first-episode, productive schizophrenia. *Psychiatry Res*, 90:169–179, Jun 1999.

M. R. Patel, A. Blum, J. D. Pearlman, N. Yousuf, J. R. Ives, S. Saeteng, D. L. Schomer, and R. R. Edelman. Echo-planar functional MR imaging of epilepsy with concurrent EEG monitoring. *AJNR Am J Neuroradiol*, 20:1916–1919, 1999.

G. Pfurtscheller. Event-related synchronization (ERS): an electrophysiological correlate of cortical areas at rest. *Electroencephalogr Clin Neurophysiol*, 83:62–69, Jul 1992.

G. Pfurtscheller and A. Aranibar. Evaluation of event-related desynchronization (ERD) preceding and following voluntary self-paced movement. *Electroencephalogr Clin Neurophysiol*, 46:138–146, Feb 1979.

C. Plummer, A. S. Harvey, and M. Cook. EEG source localization in focal epilepsy: where are we now? *Epilepsia*, 49:201–218, Feb 2008.

P. L. Purdon, V. Solo, R. M. Weisskoff, and E. N. Brown. Locally regularized spatiotemporal modeling and model comparison for functional MRI. *Neuroimage*, 14:912–923, Oct 2001.

M. E. Raichle, A. M. MacLeod, A. Z. Snyder, W. J. Powers, D. A. Gusnard, and G. L. Shulman. A default mode of brain function. *Proc. Natl. Acad. Sci. U.S.A.*, 98:676–682, Jan 2001.

J. C. Rajapakse, F. Kruggel, J. M. Maisog, and D. Y. von Cramon. Modeling hemodynamic response for analysis of functional MRI time-series. *Hum Brain Mapp*, 6:283–300, 1998.

R. Rathakrishnan, F. Moeller, P. Levan, F. Dubeau, and J. Gotman. BOLD signal changes preceding negative responses in EEG-fMRI in patients with focal epilepsy. *Epilepsia*, 51:1837–1845, Sep 2010.

G. Rees, K. Friston, and C. Koch. A direct quantitative relationship between the functional properties of human and macaque V5. *Nat. Neurosci.*, 3: 716–723, Jul 2000.

J. Riera, J. Bosch, O. Yamashita, R. Kawashima, N. Sadato, T. Okada, and T. Ozaki. fMRI activation maps based on the NN-ARx model. *Neuroimage*, 23:680–697, Oct 2004.

P. Ritter and A. Villringer. Simultaneous EEG-fMRI. *Neurosci Biobehav Rev*, 30:823–838, 2006.

P. Ritter, M. Moosmann, and A. Villringer. Rolandic alpha and beta EEG rhythms' strengths are inversely related to fMRI-BOLD signal in primary somatosensory and motor cortex. *Hum Brain Mapp*, 30:1168–1187, Apr 2009.

R. Rodionov, F. De Martino, H. Laufs, D. W. Carmichael, E. Formisano, M. Walker, J. S. Duncan, and L. Lemieux. Independent component analysis of interictal fMRI in focal epilepsy: comparison with general linear model-based EEG-correlated fMRI. *Neuroimage*, 38:488–500, Nov 2007.

K. Rosenkranz and L. Lemieux. Present and future of simultaneous EEG-fMRI. *Magn. Reson. Mater. Phy.*, 23:309–316, Dec 2010.

L. Sachs. Angewandte Statistik: Anwendung statistischer Methoden. *Berlin: Germany Springer, Verlag*, 2004.

A. Salek-Haddadi, L. Lemieux, M. Merschhemke, K. J. Friston, J. S. Duncan, and D. R. Fish. Functional magnetic resonance imaging of human absence seizures. *Ann. Neurol.*, 53:663–667, May 2003.

A. Salek-Haddadi, B. Diehl, K. Hamandi, M. Merschhemke, A. Liston, K. Friston, J. S. Duncan, D. R. Fish, and L. Lemieux. Hemodynamic correlates of epileptiform discharges: an EEG-fMRI study of 63 patients with focal epilepsy. *Brain Res.*, 1088:148–166, May 2006.

S. Salenius, A. Schnitzler, R. Salmelin, V. Jousmaki, and R. Hari. Modulation of human cortical rolandic rhythms during natural sensorimotor tasks. *Neuroimage*, 5:221–228, Apr 1997.

R. Salmelin and R. Hari. Spatiotemporal characteristics of sensorimotor neuromagnetic rhythms related to thumb movement. *Neuroscience*, 60: 537–550, May 1994.

S. Sanei and J. A. Chambers. EEG Signal Processing. *John Wiley & Sons, Ltd, England*, 2007.

E. Sartori, E. Formaggio, S. F. Storti, A. Bertoldo, P. Manganotti, A. Fiaschi, and G. M. Toffolo. Gradient artifact removal in co-registration EEG/fMRI. *WC, IFMBE Proceedings 25/IV*, pages 1143–1146, 2009.

R. L. Savoy, K. M. O'Craven, R. M. Weisskoff, T. L. Davis, J. R. Baker, and B. R. Rosen. Exploring the temporal boundaries of fMRI: measuring responses to very brief visual stimuli. *Society for Neuroscience 24th Annual Meeting, Miami Beach, FL*, page 518, 1994.

R. Scheeringa, M. C. Bastiaansen, K. M. Petersson, R. Oostenveld, D. G. Norris, and P. Hagoort. Frontal theta EEG activity correlates negatively with the default mode network in resting state. *Int J Psychophysiol*, 67: 242–251, Mar 2008.

M. Scherg. Fundamentals of dipole source potential analysis. *Adv Audiol*, 6: 40–69, 1990.

M. Scherg and D. Von Cramon. Two bilateral sources of the late AEP as identified by a spatio-temporal dipole model. *Electroencephalogr Clin Neurophysiol*, 62:32–44, Jan 1985.

V. Schopf, C. H. Kasess, R. Lanzenberger, F. Fischmeister, C. Windischberger, and E. Moser. Fully exploratory network ICA (FENICA) on resting-state fMRI data. *J. Neurosci. Methods*, 192:207–213, Oct 2010.

M. Seeck, F. Lazeyras, C. M. Michel, O. Blanke, C. A. Gericke, J. Ives, J. Delavelle, X. Golay, C. A. Haenggeli, N. de Tribolet, and T. Landis. Non-invasive epileptic focus localization using EEG-triggered functional MRI and electromagnetic tomography. *Electroencephalogr Clin Neurophysiol*, 106:508–512, Jun 1998.

A. Shmuel, E. Yacoub, J. Pfeuffer, P. F. Van de Moortele, G. Adriany, X. Hu, and K. Ugurbil. Sustained negative BOLD, blood flow and oxygen consumption response and its coupling to the positive response in the human brain. *Neuron*, 36:1195–1210, Dec 2002.

A. M. Siegel, B. C. Jobst, V. M. Thadani, C. H. Rhodes, P. J. Lewis, D. W. Roberts, and P. D. Williamson. Medically intractable, localization-related

epilepsy with normal MRI: presurgical evaluation and surgical outcome in 43 patients. *Epilepsia*, 42:883–888, Jul 2001.

J. Sijbers, I. Michiels, M. Verhoye, J. Van Audekerke, A. Van der Linden, and D. Van Dyck. Restoration of MR-induced artifacts in simultaneously recorded MR/EEG data. *Magn Reson Imaging*, 17:1383–1391, Nov 1999.

J. Sijbers, J. Van Audekerke, M. Verhoye, A. Van der Linden, and D. Van Dyck. Reduction of ECG and gradient related artifacts in simultaneously recorded human EEG/MRI data. *Magn Reson Imaging*, 18: 881–886, Sep 2000.

M. Siniatchkin, K. Groening, J. Moehring, F. Moeller, R. Boor, V. Brodbeck, C. M. Michel, R. Rodionov, L. Lemieux, and U. Stephani. Neuronal networks in children with continuous spikes and waves during slow sleep. *Brain*, 133:2798–2813, Sep 2010.

N. Soldati, S. Robinson, C. Persello, J. Jovicich, and L. Bruzzone. Automatic classification of brain resting states using fMRI temporal signals. *Electronic Letters*, 45, 2009.

L. Spinelli, S. G. Andino, G. Lantz, M. Seeck, and C. M. Michel. Electromagnetic inverse solutions in anatomically constrained spherical head models. *Brain Topogr*, 13:115–125, 2000.

G. Srivastava, S. Crottaz-Herbette, K. M. Lau, G. H. Glover, and V. Menon. ICA-based procedures for removing ballistocardiogram artifacts from EEG data acquired in the MRI scanner. *Neuroimage*, 24:50–60, Jan 2005.

C. W. Steele. Numerical Computation of Electric and Magnetic Fields. *Kluwer, Dordrecht, The Netherlands*, 1996.

B. Stefanovic, J. M. Warnking, and G. B. Pike. Hemodynamic and metabolic responses to neuronal inhibition. *Neuroimage*, 22:771–778, Jun 2004.

B. Stefanovic, J. M. Warnking, E. Kobayashi, A. P. Bagshaw, C. Hawco, F. Dubeau, J. Gotman, and G. B. Pike. Hemodynamic and metabolic responses to activation, deactivation and epileptic discharges. *Neuroimage*, 28:205–215, Oct 2005.

M. Steriade and F. Amzica. Intracortical and corticothalamic coherency of fast spontaneous oscillations. *Proc. Natl. Acad. Sci. U.S.A.*, 93:2533–2538, Mar 1996.

S. F. Storti, E. Formaggio, A. Bertoldo, E. Sartori, A. Manganotti, P. Fiaschi, and Toffolo GM. Selection of Optimal Hemodynamic Response Function for fMRI Analysis on Acute Stroke Patients. *IFMBE Proceedings 25/IV*, pages 253–256, 2009.

S. F. Storti, E. Formaggio, A. Beltramello, A. Fiaschi, and P. Manganotti. Wavelet analysis as a tool for investigating movement-related cortical oscillations in EEG-fMRI coregistration. *Brain Topogr*, 23:46–57, Mar 2010.

F. T. Sun, L. M. Miller, and M. D'Esposito. Measuring interregional functional connectivity using coherence and partial coherence analyses of fMRI data. *Neuroimage*, 21:647–658, Feb 2004.

M. R. Symms, P. J. Allen, F. G. Woermann, G. Polizzi, K. Krakow, G. J. Barker, D. R. Fish, and J. S. Duncan. Reproducible localization of interictal epileptiform discharges using EEG-triggered fMRI. *Phys Med Biol*, 44:N161–168, Jul 1999.

J. Talairach and P. Tournoux. Co-planar stereotaxic atlas of the human brain. *Thieme, New York*, 1988.

C. Tallon-Baudry, O. Bertrand, C. Delpuech, and J. Permier. Oscillatory gamma-band (30-70 Hz) activity induced by a visual search task in humans. *J. Neurosci.*, 17:722–734, Jan 1997.

B. Thirion, S. Dodel, and J. B. Poline. Detection of signal synchronizations in resting-state fMRI datasets. *Neuroimage*, 29:321–327, Jan 2006.

M. Thom, J. Y. Liu, P. Thompson, R. Phadke, M. Narkiewicz, L. Martinian, D. Marsdon, M. Koepp, L. Caboclo, C. B. Catarino, and S. M. Sisodiya. Neurofibrillary tangle pathology and Braak staging in chronic epilepsy in relation to traumatic brain injury and hippocampal sclerosis: a post-mortem study. *Brain*, 134:2969–2981, Oct 2011.

R. Thornton, H. Laufs, R. Rodionov, S. Cannadathu, D. W. Carmichael, S. Vulliemoz, A. Salek-Haddadi, A. W. McEvoy, S. M. Smith, S. Lhatoo, R. D. Elwes, M. Guye, M. C. Walker, L. Lemieux, and J. S. Duncan. EEG

correlated functional MRI and postoperative outcome in focal epilepsy. *J. Neurol. Neurosurg. Psychiatr.*, 81:922–927, Aug 2010.

J. Tiihonen, R. Hari, M. Kajola, J. Karhu, S. Ahlfors, and S. Tissari. Magnetoencephalographic 10-Hz rhythm from the human auditory cortex. *Neurosci. Lett.*, 129:303–305, Aug 1991.

F. E. Turkheimer, R. Hinz, and V. J. Cunningham. On the undecidability among kinetic models: from model selection to model averaging. *J. Cereb. Blood Flow Metab.*, 23:490–498, Apr 2003.

L. Q. Uddin, A. M. Kelly, B. B. Biswal, F. Xavier Castellanos, and M. P. Milham. Functional connectivity of default mode network components: correlation, anticorrelation, and causality. *Hum Brain Mapp*, 30:625–637, Feb 2009.

K. Ugurbil. Mapping brain function with magnetic resonance imaging. *Acta Anaesthesiol Scand Suppl*, 110:113–115, 1997.

M. Ullsperger and S. Debener. Simultaneous EGG and FMRI. Recording, Analysis and Application. *Oxford University Press*, 2010.

K. Uutela, M. Hamalainen, and R. Salmelin. Global optimization in the localization of neuromagnetic sources. *IEEE Trans Biomed Eng*, 45:716–723, Jun 1998.

B. D. Van Veen, W. van Drongelen, M. Yuchtman, and A. Suzuki. Localization of brain electrical activity via linearly constrained minimum variance spatial filtering. *IEEE Trans Biomed Eng*, 44:867–880, Sep 1997.

A. E. Vaudano, H. Laufs, S. J. Kiebel, D. W. Carmichael, K. Hamandi, M. Guye, R. Thornton, R. Rodionov, K. J. Friston, J. S. Duncan, and L. Lemieux. Causal hierarchy within the thalamo-cortical network in spike and wave discharges. *PLoS ONE*, 4:e6475, 2009.

J. L. Vincent, G. H. Patel, M. D. Fox, A. Z. Snyder, J. T. Baker, D. C. Van Essen, J. M. Zempel, L. H. Snyder, M. Corbetta, and M. E. Raichle. Intrinsic functional architecture in the anaesthetized monkey brain. *Nature*, 447:83–86, May 2007.

V. Volman, T. J. Sejnowski, and M. Bazhenov. Topological basis of epileptogenesis in a model of severe cortical trauma. *J. Neurophysiol.*, 106: 1933–1942, Oct 2011.

S. Vulliemoz, R. Thornton, R. Rodionov, D. W. Carmichael, M. Guye, S. Lhatoo, A. W. McEvoy, L. Spinelli, C. M. Michel, J. S. Duncan, and L. Lemieux. The spatio-temporal mapping of epileptic networks: combination of EEG-fMRI and EEG source imaging. *Neuroimage*, 46:834–843, Jul 2009.

S. Vulliemoz, L. Lemieux, J. Daunizeau, C. M. Michel, and J. S. Duncan. The combination of EEG source imaging and EEG-correlated functional MRI to map epileptic networks. *Epilepsia*, 51:491–505, Apr 2010a.

S. Vulliemoz, R. Rodionov, D. W. Carmichael, R. Thornton, M. Guye, S. D. Lhatoo, C. M. Michel, J. S. Duncan, and L. Lemieux. Continuous EEG source imaging enhances analysis of EEG-fMRI in focal epilepsy. *Neuroimage*, 49:3219–3229, Feb 2010b.

S. Warach, J. R. Ives, G. Schlaug, M. R. Patel, D. G. Darby, V. Thangaraj, R. R. Edelman, and D. L. Schomer. EEG-triggered echo-planar functional MRI in epilepsy. *Neurology*, 47:89–93, Jul 1996.

S. Warach, J. R. Ives, G. Schlaug, M. R. Patel, D. G. Darby, V. Thangaraj, R. R. Edelman, and D. L. Schomer. Deconvolution analysis of fMRI time series data AFNI 3d deconvolve documentation. *Medical College of Wisconsin*, 2000.

M. E. Weinand, L. P. Carter, W. F. el Saadany, P. J. Sioutos, D. M. Labiner, and K. J. Oommen. Cerebral blood flow and temporal lobe epileptogenicity. *J. Neurosurg.*, 86:226–232, Feb 1997.

H. G. Wieser. ILAE Commission Report. Mesial temporal lobe epilepsy with hippocampal sclerosis. *Epilepsia*, 45:695–714, Jun 2004.

C. Windischberger, H. Langenberger, T. Sycha, E. M. Tschernko, G. Fuchsjager-Mayerl, L. Schmetterer, and E. Moser. On the origin of respiratory artifacts in BOLD-EPI of the human brain. *Magn Reson Imaging*, 20:575–582, Oct 2002.

M. W. Woolrich, M. Jenkinson, J. M. Brady, and S. M. Smith. Fully Bayesian spatio-temporal modeling of FMRI data. *IEEE Trans Med Imaging*, 23: 213–231, Feb 2004.

K. J. Worsley, C. H. Liao, J. Aston, V. Petre, G. H. Duncan, F. Morales, and A. C. Evans. A general statistical analysis for fMRI data. *Neuroimage*, 15: 1–15, Jan 2002.

G. Yang and C. Iadecola. Glutamate microinjections in cerebellar cortex reproduce cerebrovascular effects of parallel fiber stimulation. *Am. J. Physiol.*, 271:R1568–1575, Dec 1996.

J. Ylipaavalniemi and R. Vigario. Analyzing consistency of independent components: an fMRI illustration. *Neuroimage*, 39:169–180, Jan 2008.

A. Ziehe and K. R. Muller. TDSEP-an efficient algorithm for blind separation using time structure. *In Proc. Int. Conf. on Artificial Neural Networks (ICANN'98)*, pages 675–680, 1998.

M. Zijlmans, G. Huiskamp, M. Hersevoort, J. H. Seppenwoolde, A. C. van Huffelen, and F. S. Leijten. EEG-fMRI in the preoperative work-up for epilepsy surgery. *Brain*, 130:2343–2353, Sep 2007.